DOCTORAL (PhD) THESIS

"ELECTROCHEMICAL TECHNIQUES OF INVESTIGATIONS—A TOOL FOR DIFFERENT APPLICATIONS"

Compiled within the framework of the
University of Pannonia
Doctoral School of Chemical Engineering and Material Sciences

DOI:10.18136/PE.2025.956

Written by:

Juan Santiago Hidalgo Viteri

MSc in Applied Chemical Engineering

Supervisor:

Mrs. Prof. dr. Galambos Ildiko
Associate professor

Mrs. Prof. habil. dr. eng. Graziella Liana Turdean
Associate professor

SOOS – Erno Research Centre, Faculty of Engineering
University of Pannonia

Veszprém, Hungary
September 2025

ELECTROCHEMICAL TECHNIQUES OF INVESTIGATIONS—A TOOL FOR DIFFERENT APPLICATIONS

The thesis was prepared for the award of a doctoral degree (PhD) within the framework of the Doctoral School of Chemical Engineering and Material Sciences at University of Pannonia

in the discipline of bio-, environmental-, and chemical engineering sciences

written by: Juan Santiago Hidalgo Viteri

Supervisors: Dr. Ildikó Galambos, Prof. habil. dr. eng. Graziella Liana Turdean

I recommend the dissertation for acceptance: **yes** / no.

……..…….
Dr. Ildikó Galambos
supervisor

I recommend the dissertation for acceptance: **yes** / no.

……
Prof. habil. dr. eng. Graziella Liana Turdean
supervisor

I recommend the dissertation for peer review.

……
chair of the DDHC

The PhD-candidate has achieved ……. % at the public debate.

The composition of the Final Examination Committee:

chair:……..……

reviewers:. Rosa Maria Magalhães Rego, Maria Teresa Fernandez Abedul.

members:…….

Veszprém,

……
chair of the committee

Qualification of degree: ….....

Veszprém,

……..
chair of the UDHC

ABSTRACT

Electrochemical methods have been used to produce devices that can be applied to different purposes. With this regard, in the present dissertation, I proposed to produce devices that can be used to solve existing environmental problems. Therefore, the research activities were divided into three main chapters, which correspond to the production of methodology to evaluate the delivery of a drug into the saliva by means of a non-destructive electrochemical impedance spectroscopy. This novel approach has not been used, and we planned to take advantage of the easiness and cheapness of the methodology in comparison to the current applied techniques, such as UV-vis. Then, the second chapter was focused on the production of coatings and plant extract inhibitors to prevent the corrosion of titanium alloys and mild steel. The novelty of this chapter lay in the use for the first time of a polymeric matrix crosslinked with expired drugs in the case of the coatings and the use for the first time of Ecuadorian plants, which were not studied for other purposes, to produce green inhibitors. The most notable advantages regarding the proposed products are the use of cheap products, the mitigation of the contamination by avoiding the production of potentially environmentally harmful waste, and the technical viability of produced plant extracts. Finally, the third chapter was focused on chemically modified electrodes to be used as platforms for diclofenac detection in different real samples. The advantages of the methodology proposed are based on the easiness of the modification; for that, a simple drop casting method was used; the ability to combine different nanomaterials; thus, engineering filaments were combined with different nanoparticles; and the possibility of miniaturizing the electrodes. Overall, by using electrochemical techniques, such as cyclic voltammetry, electrochemical impedance spectroscopy, square voltammetry, it was possible to build devices that can be applicable to a wide range of applications such as medicine (drug delivery systems), industry (corrosion protection), and at the environmental monitoring (chemically modified electrodes). Moreover, the excellent performances of the prepared devices were evaluated throughout the chapters and the advantages over other technologies were highlighted.

List of tables

List of figures

List of abbreviations and acronyms

Ag/AgCl/KClsat: Silver chloride electrode (Ag/AgCl/KClsaturaded)

CV: Cyclic Voltammetry

SWV: Square Wave Voltammetry

DPV: Differential pulse voltammetry

WE: Working Electrode

SAMs: Self-Assemble monolayer

SPE: Screen-printed electrodes

AE: Auxiliary Electrode

F: Faraday constant

DA: Dick diffusion coefficient

I: Current

FRA: Frequency response analyzer

dc: Direct Current

ac: Alternative current

SEM: Scanning electron microscopy

AFM: Atomic force microscopy

BSE: Backscattered electrons

EDS: Energy Dispersive X-ray

IR: Infrared Spectroscopy

FTIR: Fourier transformation infrared spectroscopy

UPLC-MS/MS: Ultra-high performance liquid chromatography- Tandem Mass Spectrometry

LOD: Limit of Detection

DDS: Drug Delivery System

PEDOT: Poly(3,4-ethylenedioxythiophene)

SDS: Sodium dodecyl sulfate

NSAID: Nonsteroidal anti-inflammatory drug

PBS: Phosphate buffer saline

IBU: Ibuprofen

SE: Soxhlet Extraction

ME: Maceration

CME: Chemically modified electrode

f-MWCNTs: Functionalized multiwalled carbon nanotubes

NPs: Nanoparticles

CCVD: Catalytic chemical vapour deposition

DS: Sodium Diclofenac

NSAID: Non steroidal anti-inflammatory drugs

PA: Paracetamol

BBD: Boro Dopped Diamond

PMMA: Poly(methyl methacrylate)

Ibuf: Ibuprofen

LP: Linear Polarization

OCP: Open circuit potential

PDP: Potentiodynamic Polarization

EIS: Electrochemical Impedance Spectroscopy

Acknowledgment

Agradezco profundamente a todas las personas que me han acompañado a lo largo de este proceso. En primer lugar, a Dios, a mi familia, por su apoyo incondicional, su cariño y su confianza en mí en cada etapa. También quiero expresar mi gratitud y tutores Profesora Graziella and Profesora Ildiko, quienes con su orientación y consejo han contribuido significativamente a mi formación académica y personal.

A mis compañeros y amigos, gracias por su compañía, su generosidad y por todos los momentos compartidos que han hecho este camino más ameno y enriquecedor. No puedo dejar de agradecer a todas aquellas personas que, de una u otra manera, aportaron a este logro, brindándome ánimo, apoyo y herramientas para seguir adelante.

Por último, reconozco el valor del esfuerzo, la constancia y la dedicación como pilares fundamentales para alcanzar este objetivo. Este logro es también de todos los que creyeron en mí y me acompañaron en este trayecto. ¡Muchas gracias!

1. Introduction

Electrochemistry has been studied over the decades as a tool for different applications due to its capacity to connect the chemical characteristics of a system with electric energy [1]. In fact, the field of electrochemistry encompasses a huge array of different phenomena, such as corrosion, devices such as analytical sensors, and technologies such as drug delivery systems. Thus, the use of electrochemistry becomes a powerful and cheap strategy that can be extended from basic to complex technology analysis [1].

Drug delivery systems (DDS) is a technological formulation which enables to introduce a drug compound into a human body and to control the release of the active compound into a specific target [2]. Therefore, most of the time DDS are used to (a) reduce the possible side-effects of the drug, (b) to ensure a proper drug profile into the human plasma, and (c) to maintain the action properties of the drug by avoiding rapid metabolic degradation of it [3]. The development and production of DDS have been studied over the last decades as effect of huge number of new drugs on the market and as effect of the apparition of new most aggressive human illness. The researchers are moving towards two directions: (a) the production of novel nanocarriers with a high load capacity; or (b) new methodologies to control the release profile into the human body. Therefore, the production of novel materials to be used as drug carriers has become the principal concern between the researchers. Thus, the DDS new materials are based on the production of intelligent nanocarriers which include materials such as polymers, nanoparticles, liposomes, dendrimers, and porous materials (e.g., mesoporous silica materials [4], bentonite [5]). The proper materials for DDS development should be nontoxic, biodegradable, biocompatible, mechanically resistant, and able to contain a high drug dosage [6]. Among all the tested materials, smart polymers have been demonstrating the excellent accomplishment of the cited properties, because smart polymers reports significant advantages in comparison with other smart materials such as (a) capability to incorporate a high dose of different drugs, (b) they can incorporate mesoporous structure which increase the drug loading capacity; (c) they providing the possibility of controlled drug release as function of a response to external stimuli such as light, electric and magnetic fields, pH [7]. The electric responsive have been starting to explore due to their properties. The most remarkable are (i) tunable mechanical properties as well as complex (re-programmable) shape morphing (SM) capabilities at different length scales [8], (ii) the capability to tune the inner structure by the application of the proper electric field, (iii) fast actuation/ response time, and (iv) compatibility in biological

environment [9]. The conductive polymers are capable of react towards the electric stimulus. Conductive polymers (CP), a special type of polymers possess electrical conductivity due to the movement of electrons within their chains [10], are extensively used for the DDS preparation. They can incorporate a widely number of drugs in an anodic state in a process called doping (oxidation) and to controlled release the incorporated drug in a process known as de-doping (reduction). This increase considerably the drug loading capacity [4]. Therefore, several types of conductive polymers such as polypyrrole [11], 3,4-ethylenedioxypyrrole [3], polyaniline, polyacrylic acid, polyvinyl alcohol, poly(N-vinylpyrrolidone), acrylic resin, poly(styrene sulfonate), methylcellulose [12]. Among them, poly(3,4-ethylenedioxythiophene) (PEDOT), a polymer from the aniline family, is gained more attention due to their superior properties when it is compared with other polymers. These properties are (i) fast charging/discharging mechanism, (ii) good electrocatalytic properties; (iii) ability to be doped by different compounds; (iv) high load capacity, (v) environmental friendliness [13], (vi) high stability, (vii) and undoubtedly its biocompatible make it the best candidate to produce DDS systems for a widely range of drugs. For example, it was used to carried anti-inflammatory drugs such as Ibuprofen [14], or antibiotic drugs [4], or anticarcinogenic drugs [15], or other kinds of medicaments such as glucose [16]. On the other hand, there is not a widely extended studies in the new techniques to study the release profile and the release kinetics of the delivered drugs. They are limited to classical techniques such as UV-vis, HPLC, fluorescence spectrometry, or electrochemical method (e.g., square-wave voltammetry). Therefore, the first part of the present research was devoted in the production a novel Ti-6Al-4V alloy coated with a DDS using a PEDOT polymeric membrane to carry Paracetamol, which was not reported anywhere else. This configuration was selected because of two main reasons: (i) Ti and its alloys are widely used as a biomaterial to produce dental and orthopaedic implants because of its optimal properties such as biocompatibility and proper corrosion resistance; (ii) researchers have developed drug-eluting titanium implants by coating them with polymers or composites that carry therapeutic agents to prolongated the lifetime of the prothesis as well as to ensure the success of the treatment. Also, it was for the first study the release of the PEDOT in saliva solution by using electrochemical impedances spectroscopy (EIS). The study of the release onto saliva solution can be important for several interdisciplinary reasons, especially in the context of oral health, pharmacokinetics, and implant biocompatibility.

Corrosion is defined as the deterioration of the material as an effect of the interaction with the surrounding medium [17]. Therefore, the term corrosion can be applied to all kinds of materials, but in the present investigation, it is going to refer to the corrosion of metals. Corrosion is led by the apparition of chemical or electrochemical reactions, which alters the structure of the metal. Corrosion is amongst the most serious problems that humankind faces because it represents an annual cost of $2.2 trillion US, or 3 % of global gross domestic product (GDP) [18]. Corrosion also represents a problem for the environment and the worker's health. Therefore, many strategies have been studied for reduced corrosion-related failures and to reduce the expenses related to the apparition of corrosion [19]. These include strategies such as proper design and material construction of the machinery and constant monitoring. However, these techniques could represent a time-consuming activity [19]. So, other possibilities appear to be cost-effective and less time-consuming. One of them is the design and synthesis of coatings. The coating methodology consists in applying a physical layer, such as an organic, inorganic, or hybrid coating, which makes the interaction of the metal with the environment difficult. This represents the most effective technique to control the corrosion [20]. Therefore, the challenging part is the selection of the proper material according to the medium conditions, the resistance of the coating materials, or the operational conditions of the material. Hybrid polymers arrive as an optimal technology to produce polymeric coatings. They are preferred because of (i) their ability to form adsorption sites for bonding with the metal surface, which enables a higher attachment to the metal surface; (ii) their ability to replace adsorbed water molecules, which limits the corrosion process due to the increase of the entropy; and (iii) their good mechanical properties, such as good mechanical strength and proper flexibility, which ensure proper resistance to the metal operational conditions [21]. Different organic or inorganic polymers have been used as a coating material; among them, polymethyl methacrylate (PMMA) emerges as a promising material because of its good properties, such as biological non-degradability, thermal stability, high electrical conductivity, and low cost of production [22], which make PMMA a good candidate for anticorrosion applications. In this sense, the second part of the research was focused on the production of a PMMA polymer coating by combining it with expired Ibuprofen. The coating was used to evaluate the corrosion protection over Ti-6Al-4V metallic plates exposed to a saline corrosive medium (3.50 % sodium chloride). Also, another technique widely used to prevent corrosion is corrosion inhibitors. They are substances added to the corrosion medium that reduce the rate of

corrosion by forming a protective layer on the metallic surface or by interacting with the medium [23]. In general, corrosion inhibitors are organic, inorganic, or naturally derived products that are composed of rich electron atomic centers such as N, S, P, and O atoms, or they are composed of polar groups or heterocyclic compounds, or they have double or triple bonds and aromatic rings, which enable the strong interaction of the inhibitors with the metal surface. From them, many of the organic and inorganic inhibitors have been banned due to their proved toxicity to the environment and human health, especially the inhibitors that are chromium derived [24]. So, nowadays plant-derived inhibitors are preferred because of their good performances, good cost-efficiency, and environmental safety [24]. These types of inhibitors are obtained from the plants, and they are applied directly to the corrosive medium (e.g., processing water flowing through a pipe that needs protection). The green inhibitors are rich in phytochemicals, which can interact with the metal surface, and by these interactions the inhibitor is incorporated into the metal surface, forming a protective layer. This process reduces the interaction of the metal surface with the medium and increases the charge transfer resistance, which limits the corrosion reactions. Therefore, the third part of the research work was focused on producing a plant-based green inhibitor by using Tara or Guayusa, Ecuadorean plants, which were used as corrosion inhibitors for mild steel exposed to an acid medium (0.10 M nitric acid).

Chemically modified electrodes (CME) are electrodes with an altered surface by the addition of a thin layer of a specific substance such as polymers, nanoparticles, biomolecules [25]. The modifications enable to obtain desirable properties such as good catalytic properties, enhanced the conductivity, high surface area-to-ratio, etc. Consequently, CME have been used for different purposes which ranging from batteries to sensing device. In electrochemical sensing platforms the CME are preferred because of their reduced sample preparation necessity, their robustness, capacity to continuous detection, and cost effectiveness [26]. Therefore, CME are gaining much more space in the detection of microcontaminants in different sources. They arrived as an alternative solution to the most sophisticated and complicated methods such as gas chromatographic method [27], liquid chromatography [28] or chromatography coupled with tandem mass spectrometry [29]. These techniques are highly robust, but they are limited because of their high cost, necessity of sample pretreatment before analysis, time-consuming, inability routine analysis [29]. Diclofenac sodium (DS), a non-steroidal anti-inflammatory drug (NSAID), is among the most worldwide consumed drugs to treat

different illness such as ankylosing spondylitis, rheumatoid arthritis, and osteoarthritis [30]. Some environmental problems arrived from its consumption, because not all the administered DS remains in the body and it is sending to water bodies. The presence of DS in water bodies represent an ecological risk because prolongated exposed period raises health concerns for vultures, aquatic organisms, and higher plants but also causes serious threats to mammals [31]. Consequently, DS has been including in the watch list of the European Framework. Thus, the continuing monitoring is necessary to have a proper mitigation program to avoid the cited problems. For this, the last part of this research work was focused on the modification of glassy carbon electrodes (GCE) to be used as an electrochemical platform for the detection of DS in different real samples named tablets or wastewater.

2. Literature review

2.1. Drug Delivery systems

2.1.1. Definition

A drug delivery system (DDS) is defined as a technology which enables the optimal therapeutical effect of a drug through precise control of their disposition profiles in the body [32]. The DDS systems include the administration of the therapeutic substance, the release of the active compound, and the transport of the active compound through the molecular membrane to the desired site of action [33]. To achieve an optimal delivery of the drug, key factors such as delivery the drug in a precise area and at the specific time and concentration are necessary to control, but there are many impediments to achieving successful drug delivery including low solubility, environmental or enzymatic degradation, fast clearance rates from the body, nonspecific toxicity, and inability to cross the biological barriers [34]. Thus, DDS systems should be designed to ensure the availability of the drug at the desired site of action at specific time and within the desired concentrations over the time [35]. To control and achieve a good performance, drug delivery is a complicated topic in which scientists have been discovering new methods and techniques to improve the efficiency of delivery. In this sense, it appears the controlled release systems aim to deliver the drug at different rates for a definite period, which can vary from hours to years, independent of the local environment. There are also different carriers in these devices that let you control how the drug is released into the target tissue or organ. This attacks the active site and makes sure that the drug is released as effectively as possible. To make this drug release happen, engineers use materials that

can react to various signals, including changes in pH, electronic signals, temperature signals, chemical signals, and pressure signals.

2.1.2. Classification of drug delivery systems

2.1.2.1. Conventional drug delivery systems

This type of DDS is the most common and the most used systems to carry a drug and to deliver to the target. Generally, this type of DDS is widely used when it is necessary a quick absorption of the drug without controlling the delivery parameters [36]. Nowadays, DDS is the most used technology, because of its simplicity, low cost and good rate of delivery. The most used conventional DDS are simple oral, topical, inhaled, or injections methods [37]. However, the major disadvantages of the conventional DDS systems are (a) the inability to keep the drug concentration at a fixed and constant level for a given period (temporal delivery), (b) the inability to control the release towards the target organ [35]. The first problem has been overcome by administrating multiple doses of the drug at regular intervals (repeated doses), but the effectiveness of this solution depends on the patient's responsibility to take the drug at the planned time. In most cases it was studied that the concentration of the drug varies up and down irregularly in blood plasma because of the not controlled time in the delivery [38]. While the problems related to achieving the desired target have not been solved. Thus, the necessity to explore more sophisticated methods for delivering a drug has emerged as an important topic.

2.1.2.2. Controlled-release drug delivery system

Controlled-release drug delivery systems (CRDDS) are a special kind of material which combines advanced engineering materials and new drug dosage form to introduce better drug potency, control drug release, provide greater safety, and target a drug specifically to a desired tissue enabling predictability and reproducibility in the release kinetics [35]. CRDDS are specifically designed to maintain the drug in the therapeutical range during an extended period providing sustained and controlled release of the drug. These systems employ various mechanisms, such as diffusion, osmosis, dissolution, or stimuli-responsive materials, to regulate drug release [39]. The purpose of CDDS is to overcome limitations associated with conventional drug delivery methods, such as frequent dosing, erratic drug concentrations, and inadequate targeting. By providing controlled release, CDDS offers several advantages, including improved patient compliance, reduced drug toxicity, enhanced therapeutic efficacy, and the potential for

personalized medicine. Table 1 describes the advantages and disadvantages of CRDDS compared with conventional DDS.

Table 1. Advantages and disadvantages of controlled-release drug delivery

Advantages	Disadvantages
Prolongated delivery time and bioavailability of the drug	Possibility of the toxicity of the DDS materials
Lower drug degradation and prevention of losing its therapeutical effect	Toxic degradation of the material
Reduction of the drug dosage frequency	Difficulty in application. It is necessary in most of the cases a surgery to implant or remove the DDS
Control in the concentration of the drug in the plasma	High cost of final product due to carrier cost or fabrication procedure
Improved drug usage	
Maintaining drug concentration in therapeutically range	
Elimination of the side effect by local administration	
Facilitated administration in underprivileged areas	

Source: [35]

Moreover, the main characteristics that a CRDDS should have to achieve proper delivery of the drug are as follows [6]: (i) drug-carrier solubility: the drug should be soluble in the carrier to ensure an incorporation; (ii) stability: the drug should maintains its chemical composition and potency trough the release process; (iii) Pharmacokinetics: the kinetics parameters of the drug must be considered to produce a proper CRDDS. It should include drug absorption, distribution, metabolism, and excretion; (iv) mode of action: drugs which have locally action may require a delivery system that maintains a constant concentration at the target site, while drugs with systemic effects may necessitate sustained release throughout the body; (v) biocompatibility: the drug and the carried should be biocompatible and non-toxic to ensure patient safety. Thus, if the drug and the carrier accomplish the cited characteristics, they can be used as CRDDS. Therefore, it is

necessary to study methods of preparing the DDS and their main parameters which are going to be considered in the following section.

Methods for preparing drug delivery systems

The physicochemical properties of the DDS are going to be controlled by the production method. Therefore, it is necessary to choose the most appropriate method of preparation/production at the initial stage of development. This is going to depend on the type of carrier and the type of drug that is used [40]. These methods vary based on the type of drug, desired release profile, and route of administration. The next sections describe the conditions, material uses, technologies, etc., used in each type of methodology and the final characteristics of the DDS.

2.1.2.3. Drug Encapsulation

Encapsulation is the process of stabilizing the drug agent through the structuring of systems capable of preserving their chemical, physical, and biological properties. This construction can change its properties to release or deliver the drug compound under certain condition (). In this process, the therapeutical active compounds are coated with an especial design membrane. The first element is known as active material or core material, while the second element is known as carrier or shell. Encapsulation has innumerable advantages, such as improved stability, increased shelf life, protection against degradation in process and storage, masks undesirable tastes and odors, increases stability, protects drugs against gastrointestinal fluids, allows controlled release, among others [41]. Therefore, the most common techniques to produce drug encapsulation are: (a) nanoprecipitation; (b) layer-by-layer synthesis; (c) spray-drying, and (d) in-situ polymerization. They are described in the following sections.

2.1.2.3.1. Nanoprecipitation

Nanoprecipitation is a widely used method to produce drug delivery systems. It is based on the precipitation of a dissolved drug into a solid shell by adding an anti-solvent. In depth, nanoprecipitation is based on the interfacial deposition of a polymer following the displacement of a semi-polar solvent miscible with water from a lipophilic solution. In this method solvent and nonsolvent phases preparation is required which is followed by the addition of one phase to another under moderate magnetic stirring. Then, the solvent is evaporated which forms the nanoparticles (NPs) in water. The final stage comprises the removal of the aqueous phase. After this procedure, film-forming material

is obtained. It contains one or more drug molecules, a lipophilic surfactant, and one or more organic solvents [42]. Film-forming materials could be (a) natural, (b) synthetic, or (c) semi-synthetic polymers.

Natural polymers are among the most used materials because of their bioavailability and their high drug charging capacity. In this sense, Wembo Y et. al. (2022) [43] prepared a DDS based on polysaccharide-stabilized zein nanoparticles by flash nanoprecipitation to deliver doxorubicin (DOX). The DDS was prepared by dissolving flash nanoprecipitation (FNP) using a two-stream mixer. The first stream contained zein, the main storage protein widely found in corn, dissolved in dimethyl sulfoxide (DMSO) (100 mg/mL) and 20% of DOX forming the solution a, while the second stream contained polysaccharide dissolved in deionized water (10 mg/mL) forming the solution b. Then, 1 mL of solution a was loaded in a 1 mL gastight syringe and 10 mL of solution b was loaded in a 10 mL syringe. After docking to the inlets of the mixer, the solutions were purged into the micro-cavity of the mixer at a high velocity and the preparation was completed in 10 s. The NPs were collected via a Teflon tubing connected to the outlet of the mixer. The efficiency of the prepared DDS was analyzed via cumulative release of DOX from DOX-loaded NPs. For that, a phosphate buffer (10 mM, pH 5.50 or 7.40) at 37 °C, these conditions mimic the acidic intracellular or tumoral microenvironment and the physiological environment, and 2 mL of DOX@NPs (weight ratio of DOX to NPs is 1:10) dispersion was placed in a dialysis bag and immersed in 40 mL of phosphate buffer with continuous shaking in the dark. At predetermined time points, 4 mL of the dialysis buffer was taken out for the measurements of DOX concentration using UV–vis spectrophotometer and 4 mL of fresh buffer was added back to keep the total volume of dialysis buffer constant. The results showed that the release of DOX was very fast in the first 2 h and reached a plateau in about 12 h. Also, the author Rizwan Ahmed Bhutto et. al., (2021) [44] prepared a drug delivery system by flash nanoprecipitation loading ß-carotene into a sodium caseinate membrane. The DDS was prepared by using a multi-inlet vortex mixer which was fed by four inlets as follows: (i) inlet 1 was a solution of sodium caseinate in sodium acetate buffer at pH 7; (ii) inlet 2 was carotene dissolved in tetrahydrofuran (THF); (iii) streams 3 and 4 were sodium acetic buffer solution at pH 7. All streams had velocities ranging from 5 to 100 mL/min through pumps. The prepared DDS solution was subsequently dialyzed for 24 h at room temperature against deionized water. Afterwards, the DDS were dried for further analysis. Thus, the drug release was

studied in PBS solution at 37°C, by mixing 10 mg of the prepared DDS with a 10 mL of PBS solution for 4 hours. The release of the carotene after 4 hours was equal to 50%.

Synthetic polymers are less used for producing DDS via nanoprecipitation as an effect of the toxicity of the polymers. However, the authors Zahra Roshan et. al., (2024) [45] prepared a curcumin-encapsulated Poly(lactic-co-glycolic acid) (PLGA) drug delivery system. The nanoprecipitation was executed by the following steps: (a) a solution containing 10 mg/L of PLGA and 10 mL acetone was prepared by mixing the cited components in a magnetic stirrer for 3 h; (b) 0.01 g curcumin was added to the previous solution, and stirring continued for 24 h until a completely uniform solution was reached. The resultant solution was labeled as solution a; (d) a solution containing 2 g/L of poly (vinyl alcohol) (PVA) and 100 mL was prepared by mixing both components in a magnetic stirred for 2 hours and labeled as solution b; (e) solution a was dropwise injected in the solution b under stirred at room temperature. The solution was left on a magnetic stirrer for 24 h at room temperature; (f) the particles were washed by three centrifugation cycles using a Hettich centrifuge at 7500 rpm for 10 min, discarding supernatant and resuspending the pellet nanoparticles in deionized water; (g) the curcumin-PLGA particles were freeze-dried for 48 h. Therefore, the drug release was evaluated by dissolving 10 mg of the prepared DDS into 10 mL phosphate buffer saline (PBS, pH = 7.4). The determination was carried out by centrifuging the mixture at 3000 rpm for 10 min, and the released curcumin was then dissolved in 1 mL ethanol to measure the absorption at 426 nm wavelengths in the UV vis spectrophotometer. Therefore, the release of the curcumin reported a biphasic release pattern divided in an initial burst followed by a sustained release. At the initial burst, 25.50% of curcumin was released within 4 hours, and the total released of the curcumin occurred within 2 weeks after the analysis.

Semi-synthetic polymers are a good alternative to be used in the nanoprecipitation to produce DDS when there is not possible to use natural polymers, for example, the authors Sadaf Hasankhan, et. al (2020) [46], prepared a curcumin-zein-ethyl cellulose DDS via nanoprecipitation method. The preparation of the DDS consisted in the following steps: (i) 0.16% w/v of zein were dissolved in 10 mL ethanol 80% v/v and were stirred at 500 rpm at room temperature (25 °C) for 30 min; (ii) 10 mg of curcumin were added and stirred in darkness 500 rpm for 90 min; (iii) 20 mL water was added to the solution as anti-solvent phase under stirring at 1000 rpm for 5 min. The formed colloid was identified as Cu-Zn; (iv) 0.09% w/v ethyl cellulose (EC) was dissolved in ethyl acetate under

magnetic stirring at 500 rpm for at least 1 h at ambient temperature. The prepared solution was labeled as EC-EA; (v) 8.3 g of EC-EA were added to 100 mL of solution Cu-Zn by using a syringe injection with a feeding rate of 2 mL/h; (vi) the ethanol and ethyl acetate was removed from the sample with rotary evaporation at 45°C for 10 min under vacuum. The drug release profile of the prepared DDS was studied by dissolving 20 mg of the prepared DDS system in 10 mL of 0.10 M acetic acid medium adjusted to a pH of 3,4,6 and 8. This solution simulated the gastrointestinal condition. The solution was centrifuged for 10 min and the obtained supernatant was centrifuged again. Finally, the amount of free curcumin in the supernatant was measured using UV spectrophotometer after dilution with 80% ethanol solution, and the free curcumin absorption band was clearly detectable at 429 nm. The principal findings were: (i) the released amount of curcumin after 2 h at pH 3 and 4 were below 1%; (ii) the release profile was not apparent changed in pHs from 3 to 8.

Overall, nanoprecipitation is a highly advantageous method to produce drug delivery nanocarriers. Hence, this method is the most used in pharmaceutical applications. The advantages of this methos includes simplicity, scalability, and ability to produce nanoparticles with controlled size and high drug loading [47] which enables its use with a wide range of pharmaceutical active compound, varying from small hydrophobic drugs to complex biomolecules. However, this method is primarily effective for hydrophobic drugs, while it is limited when hydrophilic molecules need to be loaded because they tend to diffuse rapidly into the aqueous phase, leading to poor encapsulation efficiency and rapid drug leakage [47].

2.1.2.3.2. Layer by layer synthesis

The layer-by-layer (LbL) method is an easy and versatile bottom-up method to produce DDS based on the assembly of charged polyelectrolytes from aqueous solution forming a thin film coating over a flat or spherical substrate forming a hollow polyelectrolyte capsule, which have then been used for encapsulation and release of several active ingredients [48]. The LbL production process involves the following steps: i) a charged nanoparticulate template is immersed in polyelectrolyte solution of oppositely charged polymer-forming first layer on the template; ii) removal of excess polymer by washing or centrifugation method to prevent the contamination of oppositely charged colloid and iii) formation of the second layer by depositing oppositely charged polymer solution. The process continues until the desired coating is achieved on pharmaceutical nanoparticles

[48]. So, as one layer is formed, it interacts with the new layer by hydrophobic bonds and covalent bonding. Thus, at this stage the active drug ingredient is included in the polyelectrolyte solution and the polymer continues to the grown stage [49]. Therefore, the LbL method is widely used because by tuning the kinds of materials and deposition sequences, various nanostructured components with distinct structure and composition can be closely and harmoniously combined. This results in the production of hybrid nanostructures with promising collective and improved functional properties for target applications [50]. Therefore, a huge number of researchers studied the production of DDS by LbL methods. For example, Parinaz Mofazali et. al. (2024) [51] produced a layer-by-layer self-assembly containing IGF-1 (Insulin-like growth factor 1), and cefazolin, a therapeutical drug. The final goal of the DDS was to prevent infections and improve bone regeneration of porous Ti-6Al-4V scaffolds. Thus, the production of the DDS consisted in coating the scaffold with multiple layers. This was achieved by the following procedure: (a) scaffold preparation: Cubic-dodethin-shaped Ti64 porous scaffolds were etched using a solution of HF, HNO_3, and deionized water (2:3:5). Then, the scaffolds were washed with ionized water and immersed in a 5 M NaOH solution at 60ºC for 24 h. Subsequently, they were heated to 600ºC for 1 h at a controlled rate of 5 ºC/min; (b) two solutions were prepared at the same time. The first contained IGF-1 (0.02 mg/mL) and an optimum blend of polymer gelatine. It was labeled as solution 1, while the second solution contained 10 mL chitosan and 0.40 mg/mL of cefazolin. It was labeled at solution 2; (c) the prepared scaffolds were dipped in a flask containing the solution 1 at room conditions; (d) the scaffolds + solution 1 were dipped in the solution 2 at room temperature, (e) the steps c and d were subsequently repeated 5 times to form the LbL DDS. Afterwards, the prepared scaffolds were immersed in 500 µL PBS (pH = 7.20–7.40, 0.01 M) in a bain-marie at 37ºC, and the concentration of IGF-1 and cefazolin in the samples at indicated time points were measured to determine drug release. The concentration of IGF-1 was measured using an ELISA kit for human IGF-1 (Abcam, ab100545), and the concentration of cefazolin was measured using ultra-performance liquid chromatography with UV detection (UPLC-UV). Thus, the release profile of the cefazolin corresponded to a biphasic release pattern divided into an initial burst followed by a sustained release. So, the total release of the drug was completed within 10 days. Also, the authors Cristiana Sousa et. al. (2023) prepared a DDS by loading drug fluoresce in isothiocyanate-labelled bovine serum albumin (FITC-BSA) in a membrane film containing Chitosan and alginate via LbL method. The release of the drug was determined by the incubation of the

membranes, in triplicates, into 1 mL of 10 mM PBS aqueous solution at pH 7.40 at 50 rpm and 37ºC for 4 days. At each predetermined time-point (0.1, 0.5, 1, 2, 4, 7, 24, 48, 72 and 96 h), 0.50 mL of the release medium was collected and freeze-dried, and 0.50 mL of fresh PBS was added to the sample. The drug released was studied via fluorescence microscopy micrographs at excitation (λ_{exc}) and emission (λ_{em}) wavelengths of 495 and 520 nm, respectively. Therefore, the prepared membrane prevented the initial burst release and promoted a much more sustained release of FITC-BSA over time, suggesting a quasi-zero-order release kinetics, and the total amount of FITC-BSA released was equal to 8.10±0.60 $\mu g \cdot mL^{-1} \cdot mm^{-2}$ of the loaded FITC-BSA within 4 days. Moreover, the authors Krzysztof Szczepanowicz et. al., (2016) [52] produced pegylated polyelectrolyte nanoparticles to carry paclitaxel, an anticancer drug. The DDS were built by LbL assembly using a solution of poly-L-glutamic acid (PGA) poly-l-lysine (PPL). Therefore, the membrane was built via multiple dipping into the solutions up to 5 or 6 layers. The efficiency in the production was assed via analyzing the Lactate dehydrogenase (LDH) release. Therefore, the amounts of formazan, which correspond to the level of LDH released from the cells, were quantified by absorbance measurement at 492 nm in a culture media and in control cells. As a principal outcome it was obtained that the activity of LDH released to the culture medium from the cells incubated with nanoparticles was like that released from the control cells. This result clearly indicates that multi-layer nanoparticles and multi-layer nanoparticles with functionalized surfaces have no adverse effects on cell membrane integrity and the prepared membrane may serve as a vehicle for passive tumor targeting.

From the collected investigations, it can be concluded that the principal advantages of using LbL to produce drug delivery systems are: (a) the possibility to monitory the growth rate of the film; (b) the release profiles reports a biphasic behavior divided into an initial burst followed by a sustained release, which can be controlled by choosing the appropriate parameters; (c) this method improves the permeability and the stability of the DDS; (d) the release of the drug occurred in a sustained manner which increases the therapeutical properties. On the other hand, the main limitation is the limited deposition of targeted molecules within the films owing to the unfavorable stability of the films and, moreover, the need for pre-deposition [52].

2.1.2.3.3. Spray drying method

Spray-drying consists in the process of converting an emulsion, suspension, dispersion, or liquid into fine, dispersible particles using an atomizer into a hot drying gas

medium, most commonly air [54]. This method consisted in a single-step process which reduces energy and time consumption because it does not require freezing or high vacuum. In this sense, spray drying method is widely used for the conversion of a liquid solution, emulsion, paste or suspension into a solid dry powder, granule or agglomerate [54]. The preparation of drug delivery systems through this method consisted in these stages: (i) atomization of the liquid feed into very small droplets; (ii) drying of the atomized droplets into solid particles of specific size; (iii) collection of the drying product. By this single three-step method it is possible to control the size, morphology, drug loaded capacity by controlling the process parameters such as flow rate, inlet/outlet temperature, drying rate, pressure, feed composition, feed viscosity, feed density, and equipment configuration (counter or co-current flow, collector type). Therefore, the number of investigations related to the production of DDS via spray drying method have been increased in the last years. As an example, the authors Nian-Qiu Shi et. al., [55] prepared a DDS by spray drying method to deliver luteinizing hormone. The DDS was prepared by a single water-in-oil emulsion of aqueous leuprolide/gelatin solution in poly (lactic-co-glycolic acid) (PLGA) 75/25 acid capped (13 kDa·Mw) dissolved in methylene chloride (DCM) was spray-dried before washing the microspheres in cold double distillated water (ddH_2O) and freeze-drying. The efficiency of the spray drying method was studied through long-term release. This was tested over 9 weeks in PBS + 0.02% Tween 80 + 0.02% sodium azide pH 7.40 (PBST) at 37°C. The amount of leuprolide released was determined by UPLC. As a result, the leuprolide release profile reported biphasic behavior where at the initial burst 26% of the model drug was released within one day. Following the initial burst release, slow and continuous release was observed throughout 9 days. In the same trend, the authors Arwa Omar Al Khatib et. al., (2025) [56] pimozide spray dried lipid nanoparticles to control the release of the active compound towards the non-small cell lung cancer. The DDS was prepared by preparing two different phases as follows: (a) Lipid phase: it was prepared by dissolving 50 mg of pimozide in 200 mg of stearic acid; (b) Liquid phase: it was prepared by dissolving 200 mg Poloxamer 407 and 100 µL PEG 400 dissolved in 50 mL water. Then, 1 mL of the lipid phase was mixed with 50 mL of the liquid phase and heated at 85ºC for 1 hour. Afterwards, the product was cooling down and 300 mg of methocel E5 and 60 mg of trehalose were added to the mixture with continuous stirring. The resulting nanoparticle dispersion was then spray-dried to obtain the final powder formulation. Hence, the DDS release profile was evaluated. For that, 10 mg of the prepared DDS was suspended in 5

mL of simulated lung fluid (SLF) which contained 100 mM NaCl, 5 mM KCl, 2 mM $CaCl_2$, 25 mM $NaHCO_3$, 5 mM Na_2HPO_4, 1 mM NaH_2PO_4, 1 mM $MgCl_2$ hexahydrate at pH equal to 7.40. The suspension was placed in a dialysis bag and immersed in a vial containing 20 mL of SLF under constant stirring at 800 rpm at 37ºC. The released was evaluated by taking 1 mL of the SLF containing the released pimozide and measuring its concentration via HPLC method. The concentration of pimozide was evaluated within 72 hours. Moving to the results, a biphasic release pattern was observed composed by an initial burst followed by a sustained release phase. Therefore, the initial release was equal to 18.90% ± 2.07% after 2 h. The release rate then reached 51.80% ± 4.21% by 8 h. This phase continued over the 72-h period, peaking at a mean release of 89.20% ± 3.08. Also, the authors Monireh Abbassi et. al., (2025) (https://doi.org/10.1038/s41598-025-05948-4) prepared a DDS by optimizing the spray drying technique to carrier zinc, a vital trace element plays a crucial role in various physiological functions. It was prepared two phases for the production of the DDS, these were according to: (a) liposome phase: it was prepared a maltodextrin solution (10% w/v) in purified water and homogenized using a temperature controlled magnetic stirrer at 50°C for 2 h; (b) solid phase: it was prepared by mixing 90 mg soybean-derived L-α-phosphatidylcholine (PC), 10 mg cholesterol (molar ratio 9:1), 10 mg cholesterol (molar ratio 9:1) and the mixture was dissolved in 30 mL of 10 mM NaCl solution (pH 5.50) containing zinc sulfate at a concentration of 10 $mg \cdot mL^{-1}$ (expressed as zinc ion concentration). Then, it was dropwise added the solid phase to the liposome phase in a ratio of 1:1 (v/v) under continuous stirring in room conditions. Finally, the resulting dispersion underwent spray drying at 90ºC. The showed sustained zinc release, with 94.98% cumulative release over 12 h. Therefore, the release was controlled, and the materials accomplish their objectives.

Therefore, the spray dying method is gaining attention due to their advantages which can be summarized as follows: (i) good reproducibility as an effect of the control of the conditions and the characteristics of the powder quality during the entire process; (ii) rapid production. The production consists only in a single step; (iii) bench-to-bedside translation. This represents their easiness in scale up the process which enables its use in the industry; (iv) suitable for formulation of poorly water-soluble compounds into amorphous solid dispersions; (v) broad spectrum. It can be used with a huge number of active ingredients including some compounds that require specific controlled release protection (e.g. ascorbic acid); (vi) very fast solvent evaporation as an effect of the atomization of the liquid. On the other hand, this preparation method still overcomes some

problems which are: (i) time consuming applications because of the necessity to optimize the production parameter; (ii) necessity of computational and mathematical modeling techniques to avoid production risks during the development stage; (iii) low yielding process varying from 20 to 70% which can be translated into the loss of particles. They get stuck into the walls of the drying chamber; (iv) difficulty in separate fine particles because of the poor capacity of the cyclones.

2.1.2.3.4. In-situ polymerization

The term in-situ polymerization in the production of DDS implies the development of the system within the polymerization mixture [57]. In most cases, this methodology is used to design DDS that can withstand the harsh conditions of the gastric system to protect the active ingredients and prevent its degradation [58]. The in-situ polymerization is widely used because the production process can be undertaken at temperatures and pH values within the physiological range which prevents the degradation of the active ingredient. Also, it is important to highlight that during the production steps of the polymer such as free radical formation and interfacial polymerizations the cross-linking density can be controlled to modulate drug release [59]. Therefore, this production technique has been used for a long time, specially to design drug delivery systems for oral applications. Thus, the researchers have been building more complex systems which are able to reduce the loss of the active ingredients and to produce more controlled systems. In this sense, the authors Escobar et. al. (2023) [60] produced a local drug delivery system with cyclodextrin for breast implants by using in-situ polymerization. This procedure was carried out as follows: (a) chitosan solution preparation: 1 gram of chitosan was dissolved in 570 µL of 100 mM glacial acetic acid and 90 mL of distilled water. Then, the solution was stirred over night at room conditions.

After this time, the pH solution was adjusted to 4; (b) cyclodextrin solution preparation: 10 g of cyclodextrin was mixed with 3 g $NaH_2PO_2 \cdot H_2O$ and 10 g of citric acid at room conditions. The mixture was dissolved in 100 mL of distilled water. Then, the solution was stirred for 1 h on a magnetic stirrer; (c) drug loaded: the previous prepared cyclodextrin solution was mixed with pirfenidone in a ratio of 1 mg/mL and stirred for 1 hour at room conditions; (d) breast implants pretreatment: implants samples were oxidized with oxygen plasma in a Harrick Plasma Cleaner. Immediately after oxidation, the samples were immersed in the previously prepared chitosan solution preparation and placed in a horizontal shaker at 100 rpm for 15 minutes. Then, the

samples obtained were rinsed with distillated water until obtained a pH equal to 4 and dried at room temperature; (e) in-situ polymerization: the pretreated implants were immersed in the solution prepared at step (c) and stirred at 100 rpm for 15 min, followed by drying at 30°C. Afterwards, the solution was introduced in an oven at 140°C for 30 min. Finally, the obtained DDS was rinsed with distillated water and ethanol to remove unpolymerized residues and dried at room temperature until further studies. The efficacy in the production of the proposed DDS was evaluated via building the drug release profiles. For that, the prepared DDS were loaded into vials filled with 5 mL of PBS at 37°C in a horizontal shaker (100 rpm). Then, the supernatant solution was completely renewed at pre-determined time intervals, and the drug content in the withdrawn bulk fluid was analyzed by UV spectrophotometry. Hence, the pirfenidone was detected at 310 nm. The principal results reported for the authors were: (i) the drug release mechanism reported a biphasic behavior which is formed by a rapid release of the drug at the initial time and after 50 minutes of analysis the release was stable; (ii) 82% of the loaded pirfenidone was released after 48 hours of analysis; (iii) the release mechanism of the active compound was controlled by both diffusion and erosion mechanisms. In the same context, the authors Attia et. al. (2021) [61] prepared a DDS by in-situ polymerization of acrylamide hydrogel to load ibuprofen. Thus, the elaboration process of the DDS was produced in two consecutive steps as follows: (i) synthesis of electrospun cellulose acetate nanofibers (CANFs) loaded with Ibuprofen: cellulose acetate (18 wt/ %v) was dissolved in dimethyl acetamide/acetone in a ratio of 2:1 m/m. Then the prepared solution was loaded with 5% m/m of ibuprofen. Then, the previous prepared solution was loaded in a 5 mL syringe and connected to a metal capillary needle with an exit orifice diameter of 0.6 mm. Subsequently, the solution was injected into the electrospinning machine at a flow rate equal to 2 $mL \cdot h^{-1}$. Finally, the cellulose acetate nanofibers loaded with Ibuprofen were collected and dry under vacuum at 100ºC for 2 hours; (ii) in situ UV-polymerization of acrylamide hydrogel coating on drug-loaded CANFs: 15 mg of acrylamide was mixed with 5% wt methylene bisacrylamide, 0.75% wt of 2,2-dimethoxy-2 phenylacetophenone, and 10 mL of N, N-dimethyl formamide to form a polymeric solution. Then, 100 mg of the solution prepared in step (i) was soaked in 7 mL of the polymeric solution and the mixture was exposed to UV radiation (365 nm) from the top at 45ºC for 2 hours. Finally, the product obtained after two hours was air dried at 100ºC for 1 hour and kept for further analysis. Hence, the drug release properties of the prepared DDS were evaluated in a solution in phosphate-buffered saline at pH 7.40. This was executed by immersing 50 mg

of the DDS in 10 mL PBS in a regenerated cellulose dialysis bag. The closed bag was then immersed into a beaker containing 100mL of release medium, PBS at pH = 4. The dialysis bag stirred and the temperature in the medium was kept at 37 ± 0.5ºC. Finally, at fixed slot time 1 mL of solution was taken and UV-vis analysis at 264 nm were performed in triplicate to evaluate the concentration of release Ibuprofen. The principal findings of the prepared DDS were the following: (a) the loading efficiency of the prepared DDS was equal to 96.90%; (b) the release capacity of the system was equal to 84.20%; (c) the total release of the ibuprofen was achieved after 8 hours, (d) the half-time elimination period was equal to 2 hours; (e) the coating process facilitated a constant release rate of drug as opposed to a more conventional burst release profiles obtained by other DDS. By another in-situ polymerization process, the authors Huapan Fang et. al. (2023) [62] prepare a DDS to release therapeutic proteins by oral delivery. This system was prepared by dissolving 2.5 mg of bovine serum albumin (BSA) in 2.50 mL of sodium bicarbonate buffer. Then, 4.50 mg of methylacrylic acid (MAA) was dissolved in 1 mL of sodium bicarbonate buffer. The MMA solution was added to BSA solution and stirred for 5 minutes. Then, 0.50 mg of ammonium persulfate (APS) was added into the previous solution and degasses with N_2 for 5 minutes. Next, 5 mg of N,N,N′,N′,-tetramethylethylenediamine (TMEDA) was added and degassed again for 5 minutes. Finally, the solution was stirred for two hours and the polymer/BSA complexes solution was further dialyzed for 4 h in PBS buffer (pH 7.40) to obtain the DDS. Then the DDS was characterized by measuring the bioavailability of the drug into the saliva of the patient. Therefore, the principal outcomes were as follows: (a) after oral administration of the prepared DDS, the entire coating is degraded once the capsule enters the intestine, releasing the protein; (b) the oral bioavalability of the protein in the saliva was equal to 16.90%; (d) no significant toxic effect was observed for such oral protein formulations in the treated animals.

The conclusions of the reported studies agreed that the main advantages of the in-situ polymerization to prepare DDS are: (i) the polymer chain can be adjusted in length or molecular weight that enables a proper drug loaded capacity. These parameters can be controlled by adjusting the concentration of the initiator or by adjusting the grown stage of the polymerization; (ii) the desired released profile of the active ingredient can be controlled in contrast with the other previously reported technologies which suffer from an initial burst release. On the other hand, some challenges that this method faces are: (i) potential of drug degradation during the polymerization as an effect of the harsh condition of production; (ii) stability issues due to chemical degradation when the DDS gets in

contact with the saliva or the gastric juices in the organism which can inhibit the functionality of the system.

Overall, there are different methods to synthesis and produce DDS systems. Therefore, the selection of the technique used is based on the properties of the drug model, the characteristics of the materials used, and the desired target. However, one thing that the different methods have in common is that production most of the time involves the use of polymeric matrices which can carry the active ingredients and to deliver them into the human body. These polymers, no matter what they route of synthesis, play a crucial role in the success of the preparation of DDS. Therefore, the next section covers the importance of them, their properties and the role in the preparation of DDS.

2.1.3. Role of polymers in the drug delivery systems

Researchers have studied polymers in drug release devices for almost 25 years. The development of the polymers in this sense has been rapid and is nowadays considered the most valuable technology in the production of drug delivery devices. Polymers, whether natural or synthetic, are used to produced a wide range of DDS which can be classified as: (a) diffusion-controlled DDS, which are consistent in two parts, the reservoir-drug core in liquid or powdered form and the matrix—a layer of non-biodegradable polymer; (b) solvent/activated DDS, composed of an external fluid (containing a low concentration of the drug) and a permeable polymeric membrane (containing a high concentration of the drug); (c) chemically controlled DDS, in this type of DDS, the drug is chemically linked to the backbone of the polymer; (d) magnetically controlled systems, composed of albumin and magnetic microspheres charge in a polymeric film [63].

Therefore, to consider a polymer as a candidate to build a DDS system, it should be soluble, biodegradable or bioerodible, and mucoadhesive [64]. In terms of solubility, a polymer should be able to produce polymer-drug linkages, it should have a suitable molecular weight, it should be able to incorporate residues that will facilitate direction, and the polymer should be non-toxic, and it should be easy to eliminate from the organism [64]. In terms of biodegradability, three characteristics are evolved, which are (a) erosion of the polymer surface with concomitant release of physically entrapped drug; (b) cleavage of covalent bonds formed between the drug and the polymer and the ability to diffuse the drug; and (c) the ability to control the diffusion of the drug with bioabsorption of the polymer delayed until after drug depletion [64]. Therefore, the list of polymers which accomplish these conditions is vast, it goes from natural polymers (chitosan,

collagen) to artificial polymers (polyamides, polyurethanes) and in most of the cases semiartificial polymers are preferred among the other polymers. These are synthesized to increase the thermogelling properties, mechanical strength, and degradation rates of the natural polymers or artificial polymers [63]. Among the studied polymers, a new branch of polymers is studied for the construction of DDS which are called the conductive polymers.

2.1.3.1. Conductive polymers

Conductive polymers are a new generation of intelligent engineering biomaterials that can deliver electrical stimulation trough the membrane cell, which enables their use in the preparation of biomedical devices such as DDS. So, the main characteristic of these materials is the capacity of conducting electricity, which is contrary to the normal polymers that in general are electrical insulators because of their firmly covalent bond across the polymeric chain. However, not all polymers are insulators, it is known that some natural polymers can conduct electricity. It is an intrinsic characteristic of these natural polymers. These polymers can be modified to increase the capacity to conduct the electricity; them these kinds of modified polymers are known as conductive [64]. Therefore, the most notable characteristics of them are the ability to precisely control the electrical/current stimulation, and they remain tunable whilst maintaining biocompatibility, biodegradability and porosity [64]. In this regard, these properties are attributed to their composition and especially the conjugated and alternating single and double carbon- carbon bonds located along the polymeric backbone. So, the backbone structure is composed of localized σ-bonds, which provide excellent mechanical stability, and π-electrons provided by double bond carbons, which offer excellent electrical conductivity. Additionally, there are also synthetic conductive polymers that have stable carbon-carbon double bonds found within the polymer backbone. Enhanced stability is achieved by removing or adding electrons by the specific polymer's redox states while providing a band gap that is more reflective of conductive materials than insulators [65]. In this context, there are at least 10 described conductive polymers which have been produced by different doping methods (chemically, electrochemically, photodoping), therefore, the present research is based on electrochemical methods, so, the most used electrochemical doping conductive polymer is the PEDOT (Poly(3,4-ethylenedioxythiophene) which is going to be described in the bellow section.

2.1.3.1.1. Poly (3,4-ethylenedioxythiophene)

Poly(3,4-ethylenedioxythiophene) (PEDOT) is the polymerized form of the EDOT, a monomer from the aniline family, which is produced via electropolymerization, thus the current is the initiator agent of the oxidative polymerization [65]. This polymer was developed by the Bayer AG research laboratory to give a conductive soluble polymer that lacked the presence of undesired α, β, and β, β- coupling within the polymer backbone. These couplings are highly toxic. Moreover, due to the insolubility of this monomer in the presence of water, it was necessary to perform polymerization by adding poly (styrene sulfonic acid) (PSS), as the charge balanced dopant agent [65]. This combination results in a soluble high resistances polyelectrolyte polymer which has excellent film forming properties, high conductivity (ca. 10 S/cm), high visible light transmissivity, and excellent stability [66]. In depth, there are several ways to produce the PEDOT-PSS polymer; however, in the present, it is going to study the electropolymerization technique (this is the technology used in the present research), which is preferred due to the small quantities and short time used to produce the polymer. Electropolymerization is based on the generation of radicals by inducing different potentials. These radicals are formed near the working electrode, and they are polymerized by the coupling of these radicals, which decreases the solubility of the polymer and causes a fast condensation and precipitation onto the working electrode, so the polymerization takes place on all of the surface of the electrode (even in the porous), and all of the surface porous scaffold can be coated with a layer of active material [66]. The electropolymerization of the EDOT allows obtaining a polymer that has exceptional electrochemical and spectroscopic properties, characteristics that include strong cathodically coloring, relatively broad cyclic voltammetric response with an $E_{1/2}$ of about 0 V vs. Ag/Ag+, capacity of being doped without the use of a supporting electrolyte, electrochromic contrast accessible with films, and redox properties [65]. Overall, the PEDOT is among the most used conductive polymers, and its properties enable it to be used in a wide range of applications, including the preparation of DDS devices because of its biocompatibility.

2.1.4. Titanium-based alloys

Titanium is a strong, light, metallic element (symbol Ti; atomic no. 22) that is mostly found as oxides in minerals such as anatase, brookite, ilmenite, rutile, and sphene, and also as the antimonate in lewisite. The extended use of the titanium and its alloys is promoted by their superior characteristics in comparison with other metals used in

human-body implants such as mild steel, cobalt-chromium alloys (see table 2). Moreover, titanium and titanium-based alloys have been widely applied in the orthopedic field, thanks to their excellent corrosion resistance to body fluids and their Young's modulus, which are more like bone compared with other alloys (see Table 2) [67]. The Ti-6Al-4V is the most used (50% of the Ti production is destinated to produce this alloy) among the different titanium-alloys in medical prosthesis because of its good fabricability, including high yield strength at room temperature. It provides rapid osseointegration by progressively producing a TiO_2/OH film on the bone surface besides triggering cell adhesion after implantation [68]. Therefore, Ti-6Al-4V alloys can be produced by different processes such as divided in traditional methods (forging, casting and rolling of bulk feedstock materials, followed by subsequent machining to final shapes and dimensions) or additive manufacturing (AM) production which includes (a) DED (directed energy deposition), (b) selective laser melting (SLM), and (c) EBM (electron beam melting). In this context, traditional methods are still preferable, but these methods result in a large amount of material waste, high manufacturing cost and long lead time [69].

Once the Ti-4Al-6V is obtained it can be shaped to obtain prothesis which mimics the behavior of bones, or dents which can last for 10 or 15 years depending on different factors such as patient health habits, quality of the alloy, part of the body, health issues problems. Then, failure of orthopedic implants can occur for various reasons, including inflammation, or poor 'osseointegration' (i.e. firm attachment of the implant's surface with bone tissues) because Ti-6Al-4V demonstrated to be time times stiffer than bone, that leads to stress shielding and aseptic loosening, leading to implant's loosening and/or complete detachment [70].

To prevent the failure, the construction of local drug delivery systems (e.g., antimicrobial drug delivery systems, anti-bone resorption drug delivery systems, etc.) on titanium-based implants has been proved to be an effective strategy to improve osseointegration. Furthermore, addition of drug delivery feature to bone implants has the potential to not only enhance the osseointegration and lifespan of such implants but also provide effective treatment for conditions like osteoporosis, bone infection (i.e. osteomyelitis) and related inflammation as well as malignant conditions such as bone carcinoma, etc. [70].

Table 2. The tensile and compressive properties of materials developed for orthopedic implantation.

Materials	Benefit	Drawback	Biomedical applications	Tensile strength (MPa)	References
316 L Stainless Steel	Low-priced, readily accessible, good biocompatibility, can cause an allergic reaction.	High modulus, poor resistance to corrosion, can cause an allergic reaction.	Fracture plates and screw, Ilizarov frames.	490–1350	[71]
Chromium Based Alloys	Higher oxidation and corrosion resistance, fatigue strength.	Expensive, high modulus.	Total hip replacement, k wire fixation and bone plates.	655–1793	[71]

Titanium-based Alloys	MRI (Magnetic Resonance Imaging)-compatible, corrosion-resistant, lightweight, lower modulus.	Low wear resistance.	Total Hip replacement, fracture fixation elements (Illizarov frames, plates, screws)	690–1100	[71]

Releasing drugs locally can help to minimize systemic therapy side effects while simultaneously providing more optimum drug concentration inside the bone microenvironment [72].

Thus, some researchers have studied the production of DDS to increase the lifetime of body–protheses. For example, Kanike Rajesh et. al. (2022) [73] produce a multilayered porous hydroxyapatite to coat Ti-6Al-4V plates to enhance the delivery of antibiotic components and to increase the antimicrobial properties. The production of the coating was carried out by the following steps: (a) prothesis coating: the coating of the Ti-6Al-4V was performed via plasma spraying coating. Thus, commercial grade HA (hydroxyapatite) powder was spraying at a current voltage equal to 699 V, at a feed rate equal to 10 g/min to form the first layer. Then, 4 more layers of HA were formed by the same procedure but changing the parameters. The current voltage was equal to 263 V, 254 V, and 242 V for the second, third- and fourth-layer formation, while the feed rate was kept at 10 g/min; (b) vancomycin loaded chitosan polymer preparation: 10 ml of 3% w/v chitosan polymer solution was prepared by dissolving the 300 mg of chitosan in 10 ml of distilled water with 1% acetic acid, and this mixture was stirred for overnight at 70ºC to get the homogenous polymer solution. Later, add 20 mg of vancomycin drug to 1 ml of chitosan solution and mix well through a vortex shaker for 10 min; (c) polymer addition to the coated prothesis: at this stage the coated samples prepared at step (a) were kept inside a vacuum chamber. Then, it was applied a vacuum pressure equal to 1 mbar for 5 minutes. After the evacuation, the polymer prepared at stage (b) was released slowly through the nozzle to fill the pores. Subsequently, it was applied a vacuum pressure equal to 3 bar for 10 minutes. Finally, the samples were taken out of the chamber and cured at room temperature to further study. The prepared DDS was mechanically characterized, and drug release kinetics were performed in simulated body fluid (SBF). Therefore, the DDS was immersed in 10 mL of SBF solution containing falcon tube and kept in an incubate shaker and set the temperature at 37ºC with 80 rpm. Then, at specific time, a 2 mL solution was withdrawn from the falcon tubes and replaced with an equal amount of fresh SBF solution. The drug concentration was measured through UV–Visible spectroscopy. The amount of drug (vancomycin) release was quantified by determining the absorbance peak at a wavelength of 280 nm. The principal findings from the release studies are as follows: (a) the release profile reported two release zones, an initial burst release followed by a sustained slow release. Thus, at the initial stage 64% of the drug is release during 80 hours, while 20% of the drug is release after 80 to 170 h; (b) the prepared

structure offered an improvement in drug loading by 145% (16 μ g/mm^2) and increased the drug release duration (in days) by almost 4 times; (c) effective filling of the pores with polymer improved the fracture toughness of the HA coating significantly, by restricting the crack growth. Other example is reported by the authors Mingyue Wang et. al. (2021) [74]. The authors produced a polymeric coating on titanium plate to release dopamine. The production of the coating was performed by the following steps: (a) Ti plates coating: the plates were coated with calcium carbonate by using crystallization method. Thus, titanium sheets were sonicated in a calcium chloride solution for 10 min. Then, 1 mL of a sodium carbonate solution was added, and ultrasonication was performed for 30 s (20ºC and 40 Hz). Afterwards, the former mixture was allowed to rest in a Petri dish for 1 min to complete the crystallization process, followed by 3 wash steps with deionized water. Finally, samples were sterilized in an autoclave (120ºC and 30 min) and labeled as SLA/$CaCO_3$; (b) hydrogel precursor solution preparation: the dopamine was loaded in the prepared samples by using the hydrogel method. For this, a hydrogel solution was produced by dissolving sodium alginate in 0.10 M 2-(N-morpholino)ethanesulfonic acid (MES) buffer (pH 6.5, 0.3 M NaCl) and stirred over night at room conditions. Then, it was added 27.40 mg of sulfo-N-hydroxysulfosuccinimide, 48.42 mg of N-(3-dimethylaminopropyl)-N′-ethylcarbodiimide, and 16.7 mg of arginine-glycine-aspartic acid peptide. The flask was stirred at room temperature for 20 h and then quenched with an appropriate amount of hydroxylamine. Finally, 1 mg of dopamine was added to the mixture and dissolved overnight at 37ºC; (c) drug loaded: 70 μL of the solution prepared in step (b) was loaded on the SLA/$CaCO_3$ interface and incubated for 10 minutes. Finally, the treated samples were immersed in 2 mL of a $CaCl_2$ solution (0.50 M) for 10 min to crosslink the hydrogel. Hence, the DDS was physically characterized by scanning electron microscopy (SEM) to observe the surface morphology, while the drug release profile was analyzed at 37ºC in PBS at various pH values (pH 6.50, 7.40 and 8). One milliliter of the release media was obtained at each indicated time point and used to measure the DA content by HPLC method. The principal outcomes obtained were: (a) the release profile was divided into two parts. An initial burst release in which 50% of dopamine was released withing 24 hours of analysis, preceded by a controlled release in which 80% of dopamine was released after 14 days; (b) the pH of the medium did not affect change significantly before and after the release of DA, (c) the releases of the dopamine ensured to have a positive therapeutical effect.

Overall, it can be concluded that the use of Ti-6Al-4V is preferred over other metal alloys to produce body-protheses. This is because of its superior biocompatibility, corrosion resistance, and normal to high mechanical properties such as high tensile stress resistance and high flexibility. Therefore, most of the human protheses (e.g. dental screw, bone screw, hip joint, k-wires) are built by using this alloy. However, there is still limitation in their use because of the reduced lifetime, or their side effects when the protheses are not well designed. Hence, DDS coating has appeared to prevent the damage of the alloys. The main advantages which offer the coating of the Ti alloys with DDS are: (a) In-vitro antibacterial study revealed the drug impregnated of the protheses effectively combated the bacterial attack; (b) impregnated alloy samples showed good bioactivity properties; (c) drug loaded polymer impregnated coatings samples reduce the coefficient of friction and specific wear rate [76]. This is mainly due to the lubricating nature of polymer and improved fracture toughness; (d) localized drug release is an effective method to prevent bacterial infection and other implant-related problems [76]; (e) under degenerative conditions, such as those in osteoporosis, surface-modified and drug-loaded implants undoubtedly show better osseointegration than implants alone. Therefore, new findings are needed to improve the coating of the Ti-6V-4Al based prothesis, to increase their timeline and to reduce the health risk on the patient. Thus, the tendency moves forward to the production of bioavailable polymers, such as PEDOT, which can load high content of pharmaceuticals and deliver them in a controlled way over a long period of time.

2.1.5. Paracetamol

Paracetamol (PA) is a p-aminophenol derivative that exhibits analgesic and antipyretic activity. It does not possess anti-inflammatory activity. Paracetamol is thought to produce analgesia through a central inhibition of prostaglandin synthesis [77]. Paracetamol is among the most consumed analgesic antipyretic drug. Therefore, PA has been a standard and first-line treatment for fever and acute pain over the decades. Their extended use is derived from the non-side effects, the easiness of synthesis and production, and because it is non-prescriptive drug in most of the countries, so the patients can easily access to it [78]. So, PA is used for the management of various types of acute painful conditions that include headache, musculoskeletal pain, period pain, osteoarthritic pain, back pain, dental pain [77]. The standard therapeutic dose of paracetamol for adults is 2 tablets of 500 mg each taken orally every 4 hours up to a maximum of 8 tablets for any 24-hour period. In

children, paracetamol is marketed in dosages depending on age and range from 60 mg (2–3 months) to 480–750 mg (12–16-year-olds). Also, it can be taken safely by nearly everyone including pregnant and breastfeeding women as well as children over 2 months of age [78]. Regarding this, the PA therapy face some problems as effect of its fast release and absorption (this can take 10 – 20 minutes) which increase the frequency of the dosing, approximately 4 times per day dosing is needed [79]. Thus, it is necessary to consume more PA for effective treatment which is not desirable because it increases the chances of intoxication by overdoses. This can derivate in liver damage, which can lead to total hepatic necrosis, leukopenia, and thrombocytopenia. Also, the overconsumption of PA can create environmental problems. It is probed that the median rate of absorption of PA in the human body is 65 %. The rest is discarded from the human body to the environment. To overcome this problematic situation, scientists are developing intelligent DDS which ensures the maximum efficacy in the delivery of the PA by maintaining it concentration at a constant desired value over the time at least for 24 hours into the body. Therefore, several materials (e.g. polymers, nanocarriers, nanoparticles) can be found in the literature to formulate a proper DDS. For example, the authors Mahboubeh Pishnamazi et. al. (2019) [80] design a controlled release system for Paracetamol based on modified lignin, the authors Joanna Goscianska et. al. (2020) [81] design wrinkled mesoporous carbon spheres, the authors S. Gautam et. al. (2022) [82] produced a metal-organic frameworks (HKUST-1) as a drug carrier, Sourav Adhikary et. al. (2023) [83] entrapped the PA in nanoporous silica nanoparticles for transdermal delivery, or the authors H. Asci et. al. (2020) [84] produced a supralingual administrator by using polyvinyl alcohol nanofibers. Therefore, from the cited researchers it can be discussed that the PA served as an excellent drug model because of its large consumption, it releases properties and its capacity to be administrated in several ways ranging from oral to transdermal routes. Also, the characteristics and advantages of using intelligent materials to produce DDS which can carry, and release PA can be outlined in the following points:

- Innovative uses of novel materials to carry and release PA allow an effective PA blood plasma concentration, especially in children.
- Morphological irregularities and specific functional groups created new adsorption sites for paracetamol, supporting host-guest interactions that enable high drug loading.

- Zero-order kinetic release of paracetamol is preferred in gastric fluid which enables to achieve a constant rate within 24 h to eliminate the initial burst drug delivery carrier. This is beneficial for biomedical applications and for reducing the toxicity of drugs.
- The capacity of drug loading is strongly associated to the pore size and pore volume of the drug.
- The main goal of the DDS is to reduce the possible hepatotoxicity associated with paracetamol over-dose.

While some of the challenges face during the production of DDS are:

- Side effects created by the addition of some nanomaterials.
- Impossibility of industrial scale-up the system
- Difficulty to online evaluation of the profile release.

Therefore, it is still needed to produce new technologies to ensure a proper release of the PA into the human body, because the consumption of the PA is growing day by day, so the way of administration of this drug should be as optimal as possible. Moreover, biocompatible materials such as PEDOT are preferred to study because of the reduction of side-effect problems. Also, the PA can be used as a coating component of Ti-6Al-4V to reduce the problems associated with the loos of the properties of this alloy when is applied as human protheses based material.

2.1.6. Drug release kinetics

Pharmaceutical compounds can be administered to the human body through exposure; medium, e.g. oral, dermal, or intramuscular, but in most of the cases the drug did not accomplish it final target because of the null consideration of the pharmacokinetics, the body interacts with administered substances for the entire duration of exposure, thus, it is reported that 50% of the global population should consume more than one dose of the medicament to ensure its optimal therapeutical effect. This causes several problems in terms of (i) economical loses of about 5.80 billion were dispensed in 2018, (ii) side effects which can be considerable represent a humanitarian problem due to the apparition of aggressive health illness, (iii) possibility of the destruction of the flora and fauna as effect of the present of high toxic pollutants in water bodies or in the soil [85]. Therefore, the classical methods for delivering medicines are limited by their pharmacokinetic profile,

which is characterized by initial rapid drug distribution pushing systemic levels above the minimum effective concentration (MEC) but below the minimum toxic concentration (MTC) followed by a drop below the MEC over time as the drug is metabolized and cleared from the body [85]. More sophisticated systems have been proposed to avoid the problems related with the classical methods; hence, it is necessary to study and develop a proper drug release profile which ensures the availability of the medicine over a long period of time. In these senses, to establish specific, planned release profiles, it is essential to understand the precise mass transport processes governing drug release and to quantitatively forecast the resultant drug release kinetics to ensures an optimal release of the drug to ensure its maximum effect. The study release of the drug can be undertaken using empirical models in which the most used ones are the (a) Zero order model, (b) Higuchi model, and (c) Korsmeyer-Peppas model. These mathematical models are an important tool to design pharmaceutical formulations, evaluate drug release processes in vitro and in vivo and, in general, come up with the optimal design for new systems. It is important that to highlight that the mathematical equations give a quantitative interpretation of the values obtained from a dissolution or drug release assay. Therefore, their use, and conditions are going to be described below.

2.1.6.1. Zero order model

Zero order kinetics model refers to a constant rate drug release process from a DDS. Therefore, the model stated that the same amount of drug is deliver per time independently of the concentration of the drug remaining in the DDS [86]. Therefore, the considerations needed to build this model are as follows [87]: (i) velocity consideration: the dissolution of the drug is a kinetic process; thus, the velocity of the dissolution can be stated as:

$$\frac{dC}{dt} = \frac{DS}{Vl}(C_S - C) \quad (1)$$

where dc/dt is the velocity of dissolution, V is the volume of solution., D is the coefficient of diffusion of solute in the solution, S is the solute area exposed, l is the thickness of the diffusion layer, Cs is the solid solubility, and C is the solute concentration into the solution on time t; (ii) slow drug release: the dissolution of active agents contained in non-disintegrating dosage forms is very slow, so it can be represented as $W_0 - W_i = K \cdot t$ where W_0 is the initial mass of active agent in the dosage form; W_i is the remaining mass in the dosage form, on time t and K is the constant of proportionality; (iii) the drug release is only a function of time and it occurs at constant rate independent of the drug

concentration in the system (see Figure1). This is state by the equation $C_t = C_o \cdot K_o t$ where C_t represents the amount of active agent released during the time t, C_0 is the initial concentration of active released (generally, $C_0 = 0$), and K_0 is the zero-order constant; (iv) the active compound is diffusing through the coating membrane, and reaching the target; (v) saturation of the core coating membrane produce the stationary concentration; (vi) when the stationary concentration falls below saturation concentration, the delivery rate decays to zero.

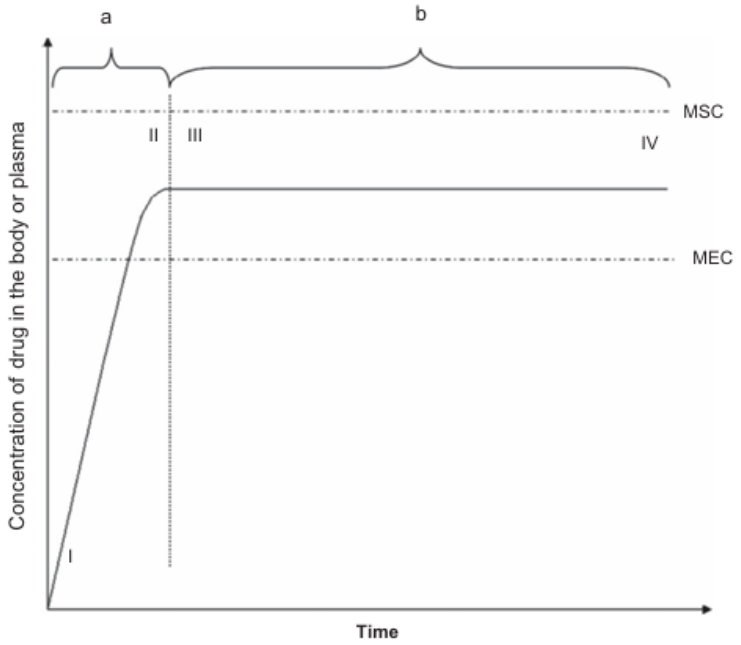

Figure 1. Drug level versus time profile of zero-order, controlled release: (a) absorption phase; (b) elimination phase; (I and II) rate of drug absorption higher than rate of drug
Source: [87]

The main advantages of Zero order model are:

- Zero-order delivery systems are a form of controlled drug delivery that can potentially further expand and improve the performance of therapeutics beyond what is possible using current FDA-approved controlled-release systems, including drugs with small therapeutic windows or hepatic toxicity [88].
- After enough time, the DDS which are adjusted to Zero-order model would lead to virtually constant drug concentrations in the biological media, resulting in improved safety, efficacy, and patient compliance.

On the other hand, decoupling the release rate from the amount of drug remaining in the device is challenging, especially for passive systems [88].

2.1.6.2. Higuchi model

The mathematical model developed by Higuchi is related to particles of active ingredients dispersed in a homogenous matrices submitted to a diffusing medium. The mathematical model makes the following considerations: (i) the dissolution of the active ingredient in a planar, homogenous matrix can be written as:

$$f_1 = Q = \sqrt{D \cdot (2C - C_s) \cdot C_s \cdot t} \quad (2)$$

where Q is the amount of drug released on time t by area unit, C is the initial amount of drug contained in dosage form, Cs is the solubility of active agent in the matrix medium and D is the diffusion coefficient in the matrix medium; (ii) the amount of the release drug is proportional to the square root and it can be describe by:

$$f_1 = Q = K_H\sqrt{t} \quad (3)$$

where K_H is the release constant of Higuchi; (iii) the matrix contains an initial drug concentration much higher than the solubility of the drug; (iv) the diffusion is unidirectional, because the edge effects are negligible; (v) the swelling or dissolution of the matrix is negligible; (vi) the diffusivity of the drug is constant; (vii) the perfect sink conditions are attained in the release environment; (viii) the mathematical model is only applicable to carries that do not significantly swell upon contact with water; (ix) when the concentration of the active ingredient is much lower than that of saturation (typically from 1/10 to 1/3 of saturation) the dissolution system is working under sink conditions, and the driving force of dissolution is higher (see Figure 2) [86].

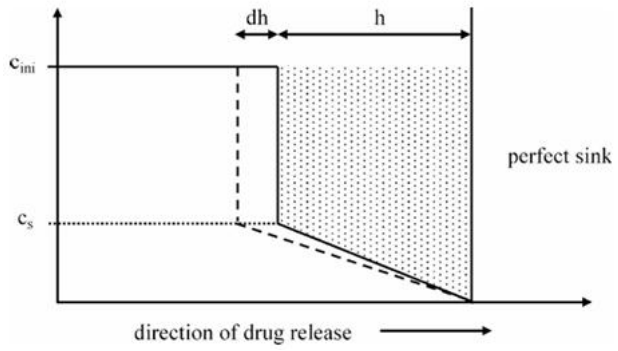

Figure 2. Schematic presentation of the drug concentration–distance-profile within the ointment base after exposure to perfect sink conditions at time t (solid line) and at time t + dt (dashed line).
Source: [86]

2.1.6.3. Korsmeyer–Peppas model

It is known as the power law, and it represents a more sophisticated model to describe the release of an active ingredient. The model was developed by Korsmeyer, Gurny, Doelker, Buri, and Peppas (1983) as a semi-empirical model, establishing the exponential relationship between the release and the time by the following equation [86]:

$$f_1 = \frac{M_i}{M_\infty} = Kt^n \quad (4)$$

where f_1 is the amount of drug released, M is the amount of drug at the equilibrium state (sometimes very close to the amount of drug contained in the dosage form at the beginning of the release process), Mi is the amount of drug released over time t, K is the constant of incorporation of structural modifications and geometrical characteristics of the system (also considered the release velocity constant), and n is the exponent of release (related to the drug release mechanism) in function of time t. The model was developed exclusively for the release studies of an compounds carried in polymeric films, such as hydrogel [86]. This model superposes two different apparently independent process named diffusion and relaxation which completed the drug transport from the membrane to the solution. So, the drug release profile is divided into four different cases which are (i) Fickian model (n = 0.5), so this process is controlled by diffusion, and this process is dominant again the chain relaxation; (ii) non-Fickian (n = 1) in this case, the release process is somewhat like the zero order model and the controlled process is swelling or relaxation of polymeric chains; (iii) non-Fickian or anomalous transport ($0.5 < n < 1$), in this the mechanism of drug release is governed by diffusion and swelling; (iv) super case II ($n > 1$), in this case the controlled process is the sorption process. During this process the polymeric film is breaking, and as the process advance, also the nucleus is breaking. So, the n is calculated at the portion of release curve in which $\frac{M_i}{M_\infty} = 0.6$ [86].

2.2. Corrosion

2.2.1. Definition

Corrosion is a surface process between a material and its environment that destroys it. Therefore, the corrosion is extended to all classes of materials (polymers, wood, cement, metals, ceramics) [89]; however, in the present thesis, the term will be applied to the metals. So, when the deterioration of a material is involved, corrosion can represent a dangerous process that includes plant shutdown, loss of products, loss of efficiency, contamination as the effect of the apparition of corrosion products, and health and safety

problems. Moreover, the economic cost of corrosion is also several problems because it is estimated that in the developed countries, the cost of corrosion is around 1000 billion US dollars per year, which represents approximately 3-4% of the annual gross domestic product (GDP). Thus, major industries, such as petroleum, automotive, petrochemical, construction, manufacturing, pulp and paper, and transportation, are among the most affected by the apparition of the corrosion. This apparition causes several damages to the equipment, and the main problems are (a) loss of impermeability, (b) loss of mechanical strength, (c) loss of physical properties, (d) contamination of the product, and overall, when the corrosion is observed, it creates in some cases irreversible damage to the machines, the pipes, etc. [89].

2.2.2. Types of corrosion

The corrosion can be associated with a certain point of the material or to the whole material. It can be also appeared in different shapes or at different positions in the crystal structure of the metal. So, it is necessary to categorize the form of corrosion, to monetarize and prevent the apparition of corrosion sites. Therefore, the types of corrosion are classified according to:

- Uniform corrosion: this type of corrosion occurs in a homogeneous manner over the entire surface of the corrosion. It is produced by the continual shifting of anode and cathode regions of the surface of a metal in contact with the electrolyte. The uniform corrosion can be inspected by simple visual test because its apparitions is easy to detect. This type of corrosion is the least damaging form of corrosion because it is predictable if the corrosion rate is known. Therefore, a well-known uniform corrosion process is observed as rusting of steel plate exposed to corrosive environments for example seawater or high humidity zones. The apparition of this type of corrosion in the metal surface can be successfully controlled can by using coatings and paints, cathodic protection or simply by stipulating a specific allowance of it [90].
- Localized corrosion: In contrast with the uniform corrosion, the localized corrosion attack appears in certain points zones of the metal surface leaving other zones of the metal free of corrosion. The mechanism of the localized corrosion is driven by the apparition of a fixed anodic sites (oxidation reactions dominates) surrounding by a cathodic zone where the reduction reaction takes place. Localized corrosion rates are often several orders of magnitude higher than the

corrosion rates for general corrosion, thus, this type of corrosion penetrates very fast onto the metallic surface. Moreover, localized corrosion is by far the most difficult to monitor and control, so it can lead unexpected damage with disastrous consequences [91]. The most common types of localized corrosion are (a) crevice corrosion: it occurs when crevices, formed by lapped joints, or areas of partial shielding, are exposed to corrosive environments. So, around this zone is often distinguish two types of concentration cells, the oxygen concentration cell which is characterized by the depletion of oxygen and the area acts as an anode relative to the oxide region, and the metal ion cell which is characterized by the apparition of shielded area that accumulates corrosion products and becomes cathodic to the regions outside of the crevice where corrosion products are kept washed away [90]; (b) pitting corrosion: pitting is an extremely localized corrosion process that derives in the apparition of holes in the metallic structure. The pitting corrosion is very challenging to detect and control because the formed holes are very small and they are covered by corrosion products in most cases. Therefore, it is not detected on time, the apparition of a pit can derive in chemical attacks, mechanical attacks, or crevice attacks which could irreversibly destroy the metal [90]. The pitting corrosion is caused by halides attack (generally chloride pitting of stainless steel) or by oxygen attack. Therefore, it is important to detect on time the apparition of small pits. This can be achieved by ultrasonic testing or eddy current testing which gives information about the formation of subsurface pits, or by electrochemical methods which are used to predict the susceptibility of the material to undergo of pitting corrosion. In general, the localized corrosion can be prevented by a proper selection of the materials, by a proper surface treatment (applying protective layer – coating), or by a proper maintenance of the machinery.

- Galvanic corrosion: This type of corrosion is known as contact or bimetallic corrosion because the mechanism is controlled by the coupling of two metals with different potentials in a conductive electrolyte solution which results in accelerated attack to the anodic metal and reduced attack (so protection) to the cathodic metal [90]. So, the galvanic corrosion is composed by less noble metal (anode) and a more noble metal (cathode) and an electrical conductor, in most of the cases the surrounding medium. Therefore, this type of corrosion is not so common to occur in the industrial machines, but it is still needed to prevent their

apparition. The most common methods to prevent the galvanic corrosion are (a) selection compatibles materials. It is needed metals with similar electrochemical potential; (b) insulating dissimilar metals: if there is not possible to chose similar metals, the dissimilar materials should be insulating by non-conductive barriers to prevent the electric contact; (c) using protective coatings: it is preferring to coat the less noble metal to avoid the apparition of the galvanic cell.

Overall, corrosion can appear in different types as effect the normal and daily use of the metals. However, it is fundamental to control the apparition of this process in its early stages to prevent significant damage which can produce several economic and environmental problems. Therefore, monitoring corrosion is fundamental to having a general idea how to prevent or contrast corrosion, so the next section is going to describe briefly the most used corrosion techniques in the industry.

2.2.3. Corrosion monitoring

Corrosion monitoring refers to all the activities reported to study the conditions of the metal structures and the report of the losses by the apparition of the corrosion. Therefore, there is not a standard procedure to control the corrosion, because there are plenty of variables, such as material design, medium, time of operation, which can be considerer to select and appropriate time and type of monitoring control. The corrosion monitoring is classified according to the type of used method as follow: (a) coupons: this method consisted in the introduction of a preweighed metallic coupons into the machine to mimic the operation conditions, then, at certain period, they are taken off and examined though visual inspection and weight to see the extension of the corrosion attack. It is the simplest technique because it does not require any specialized instrument [94]; (b) electrical resistance measurements: In this technique, the electrical resistance of a wire or strip element of a probe is measured. Therefore, the continuous monitoring of the electrical resistance as function of time can be correlated with the corrosion, and the corrosion rate can be calculated from the obtained data. The advantages of this technique are that it can be used in any environment, and it is unaffected by rapid fluctuations in corrosion rate, for the response time of the probe is usually about a day or more. On the other hand, the main disadvantage of this technique is the necessity of sophisticated and sensitive electronic apparatus to reduce the background noise. Therefore, this technique is most applied for monitoring internal corrosion on pipelines and vessels on process plants [94];

(c) electrochemical method: this method consisted in connecting two or three cylindrical electrodes of a similar material to that of the plant and immersing them into a medium which simulates the operation conditions, then a small d.c. voltage , of about 10 ± 20 mV is applied across the connected electrodes, then, the current flow is measured between the polarized electrodes after a few minutes and it is used to calculated the corrosion rate. The most common types of electrochemical monitoring methods are linear polarization (Lp), potentiodynamic polarization (PDP), and electrochemical impedance spectroscopy (EIS). From them, the EIS is the most complicated method because it requires specialized operator to interpret the results. Therefore, the main advantages in using this type of method are the simplicity of the needed machinery, the speed (response time a few minutes) and the capacity of obtaining instantaneous corrosion rates. On the other hand, the corrosion rates estimated with electrochemical measurements need to be substantiated by independent means (e.g., coupons) in cases where parasitic redox reactions are suspected to occur on the electrodes. Anyways, the electrochemical methods are used for process control and optimizing dosages of corrosion inhibitors or adjusting other plant parameters [95]; (d) ultrasonic method: this is a non-destructive method based on the use of high-frequency sound waves which pass through the material and give information about the thickness of materials and the size of defects [96]. The main advantage of this method is the ability to obtained information outside wall while the plant is operating. This allows to have a in-situ information during the operation of the machinery. On the other hand, the main disadvantages of this method are dependence on operator skill, limitations in penetrating certain materials, the need for thorough surface preparation, and potential cost implications. Anyways, ultrasonic methods are widely used in inspection and NDT (non-destructive test) surveys to assess the condition of pipes, vessels, and structures [97].

All the mentioned types of monitoring can be connected between each other to offer a wide panoramic view of the corrosion process. Therefore, the main information that can be obtained from them are (i)remaining life or life extension of the machinery, (ii) process control, (iii) product quality control by minimizing metallic contamination, (iv) safety, (v) preservation, and (vi) uninterrupted performance. Thus, the information about the state and the rate of corrosion let us move to the next step, which is the corrosion protection methods which are going to be covered in the next sections.

2.2.4. Corrosion protection methods

There are several ways to protect the materials against the corrosion process, which are: (a) cathodic protection, which consists in supplying electrons to reduce the anodic reactions; (b) control by inhibition, which consist in adding substances (inhibitors) which can eliminated or retard the corrosion reactions; (c) coatings, which consist in the addition of a coating material to increase the resistivity of the electrolyte and to retard the electron flux; and (e) corrosion by design, which consist in the reduction of corrosion from the selection of the proper materials to avoid corrosion reactions. From the cited technologies, the ones that are going to be described in detail are b and c because they were studied, and they were the focus point of this research.

2.2.4.1. Control corrosion by coatings

For over a thousand years, people have used coating technology to protect different metals from corrosion. This technique consists of recovering the metallic surface with a special membrane that decreases the interaction of the metallic parts with the environment [60]. Therefore, to prepare an acceptable coating, it should have (a) a high degree of adhesion in the metal, (b) a minimum porosity, (c) a high resistance against the electron flow, (d) a sufficient thickness, and (e) a low diffusion rate for Cl^- and H_2O. Moreover, there are several different types of coating, but polymeric coatings are gaining more applications due to their high performance. In this context, epoxy, polyurethane, chlorinated rubber, polyvinyl chloride has been used in the industry for a long time ago. Therefore, hoosing the proper polymeric coating is a challenging task, and it relies on the ability of the polymer to adapt to different environments, the ability to fix into the metallic surface, and the cost of production. Another advantage of using the polymers as a coating agent is the ability to be doped by another substance, which allows for an increase in the corrosion protection. On the other hand, the most problematic thing about using a polymer is how easily it breaks. For these reasons, the polymer should be very rough and flexible to ensure a proper functionality at the metal working conditions [98]. Therefore, the below section is going to cover the polymethyl methacrylate as a potential polymer for producing anticorrosive coatings.

2.2.4.1.1. Polymethyl methacrylate

The polymethyl methacrylate or poly-methyl 2-methylpropenoate (PMMA) is a polymer from the methyl methacrylate family with a chemical formula $(C_5H_8O_2)_n$. This polymer is clear and colorless, which is one of the most produced polymers due to its

highly extended applications (bags, computers, bottles, etc). PMMA is obtained by the free radical polymerization of methyl methacrylate. Moreover, this polymer lacks methyl groups in their backbone carbon chain; as a result, this polymer is a soft thermoplastic. Furthermore, the ability of the PMMA to be potentially used as corrosion inhibitors lies in the high mechanical resistances; thus, it has a large Young's modulus, a low elongation at break, high scratch resistances (one of the hardest thermoplastics), low water absorption capacity, sunshine resistance, medium thermal stability, low cost, and high electrical charge resistances [99].

2.2.4.1.2. Expired drugs

The ability of the expired drugs to prevent corrosion lies in their chemical structure; thus, they contain organic compounds with different heteroatom structures (N, P, S), which can be adsorbed onto the metallic surface under certain conditions [100]. These molecules have lone pair electrons or π double bond electrons, so when these electrons are fixed on the metallic surface, they prevent the change in potential and increase the charge transfer resistance by slowing the corrosion reaction rate, thus reducing the rate of corrosion reactions. Moreover, the use of expired drugs as inhibitors also solves the problem regarding the contamination generated by the final deposition into the waste of these drugs [100]. Thus, a wide range of expired drugs have been studied; therefore, the below section is going to describe ibuprofen, a highly used expired drug, in the production of inhibitors of corrosion.

2.2.4.1.3. Ibuprofen

Ibuprofen ($C_{13}H_{18}O_2$), (RS)-2-(4-(2-methylpropyl) phenyl) propanoic acid, is among the most used nonsteroidal anti-inflammatory (NSAID) drugs to treat muscle pain and rheumatic diseases. It belongs to the propionic acid family, and its chemical structure is composed of hydroxyl groups and an aromatic ring. Moreover, the properties of ibuprofen are low solubility in water but high solubility in phosphate buffer saline (5.20 mg/ml), a normal melting range (75 - 78ºC), and a crystalline structure [101]. Because of its chemical structure, ibuprofen can serve as a potential inhibitor of corrosion.

2.2.4.2. Corrosion control by inhibition

The corrosion control by inhibition consists of adding a substance (organic or inorganic) which can convert the active corrosion process into passive process, and this results in the suppression of the corrosion process. The inhibitors can be organic or

inorganic molecules, and they are classified according to the type of protection into cathodic and anodic inhibitors. Basically, this classification arrives from the change in potential that the addition produces into the system [100]. Moreover, the addition of the inhibitor can be implemented without changing any process in the system. Therefore, the selection of the inhibitor constitutes the key parameter in this technology. The principal characteristics that an inhibitor should fulfill are high solubility and dispersibility with respect to the electrolyte, capacity to be absorbed into the metallic surface, presences of different functional groups which can slow down the corrosion reactions, long range effectiveness, possibility to produce bimetallic coupling, high resistances against different temperatures, low toxicity and non-adverse effects produced when they release on the environment, economic and technical competitiveness against other forms of corrosion inhibitors [98]. On the other hand, the main disadvantages of using inhibitors are inhibitors are they are limited (a) when the equipment and components are subjected to turbulent flow; (b) when the systems operating above the stability limits of inhibitor; and (c) when the equipment subjected to high velocity, beyond 4 m/s. Beyond the limitations, the inhibitors are highly used in industrial sector, so it is necessary to develop more effective inhibitors, so, the following section is going to describe a new trend in the production of the inhibitors.

2.2.4.2.1. Plant extracts

Plant extracts have been investigated to be used as inhibitors of corrosion to replace synthetic corrosion, which is very toxic to the environment. The reason to study the plant's extract is that they have a huge range of chemical compounds in their structure, which especially regards the high number of heterocyclic compounds actively involved in the corrosion protection reactions [102]. These heterocycle compounds can be chemically or physically adsorbed in the metals. Therefore, a protective covering layer is formed on the metal surface, which denies the access of corrosive environments. Hence, the corrosion protection is given by the following mechanisms: (a) polarization of the anodic and cathodic potential; (b) reduction of the diffusion rate of the reactants to the metal surface; (c) increase of the charge transfer resistance; and (d) decrease of the double layer capacitance because of the protective layer formed on the metal surface as effect of the interaction between the rich functional groups of the plant extract and the empty electron orbitals of the metal [61]. Thus, choosing the appropriate plan extract is considered the most challenging part of the preparation of inhibitors.

In this context, researchers have been paying attention to the preparation of plant extracts to use them as anticorrosive inhibitors. Thus, the author Haiquin Ren, et al., [103] prepared an environmentally friendly corrosion inhibitor by using Pumpkin leaf extract (PLE) crop waste for copper in 0.5 M H_2SO_4. The results reported that the inhibition efficiency of the PLE against copper reached 89.98 % when the concentration of the PLE reached 800 mg/L. Furthermore, when the temperature and soaking time increased, the corrosion protection efficiency of 800 mg/L PLE on copper consistently remained above 85%. In this same trend, the author Bouchan Tan, et al., [104] prepared an environmentally friendly corrosion inhibitor by using Pyracantha fortuneana alcohol extracts (PFAE) for copper in sulfuric acid. The principal outcomes of the study demonstrated an inhibition efficiency upper of 95% when it was added 600 mg/L of PFAE. Also, after 4 h of immersion in a H_2SO_4 solution containing PFAE, the copper could still maintain more than 80 % of the anti-corrosion performance. In addition, Shahmoradi et al. [105] thoroughly investigated the anti-corrosion performance of quince seed extract on steel, employing QC calculations, MD simulations and various experimental methods. When the concentration of quince seed extract is 800 ppm, its corrosion inhibition efficiency was found to surpass 90 %. Moreover, Aicha Rizi, et al., [106] prepared a green inhibitor based on the use of Cuminum cyminum (CC), a native plant from India, to protect mild steel in 0.5 M HCl. This extract reported an inhibition efficiency ranging from 79.69 to 98.76 %. The optimal inhibition concentration was 2 g/L, and surface analysis confirmed the formation of a protective layer. Table 3 gathered a summary of the recent used plants as ecofriendly corrosion inhibitors.

Compared with the present research, the inhibition efficiency of our extract reported similar values, thus probe the applicability of the Tara as corrosion inhibitor due to its composition. Moreover, Tara was not reported as a corrosion inhibitor in all the research that by consulting many references. So, it is important to establish the inhibition protection mechanism by means of different analyses. Therefore, plant extract may form a complex protective film through the synergistic effect of multiple components (antioxidants, terpene-based, tannins), which not only physically blocks the corrosive medium, but also may inhibit the corrosion reaction through electro chemical or chemical means [107].

So, there are a huge number of possible plant candidates to be used as inhibitors; that is why the present research is studying the Caesalpinia Spinosa (Tara) and the Guayusa Ilex as potential inhibitors of corrosion.

2.2.4.2.2. Caesalpinia Spinosa – Tara

The Caesalpinia Spinosa, known as Tara, is an arborescent native species native to South America, and they are cultivated in arid zones from Argentina to Ecuador. This plant represents an economical income to the indigenous people of these zones due to their extensive application; unfortunately, they only obtain limited economic benefits because of the null industrial transformation. The characteristic of this plant is the high content of different chemical compounds in all their structures, in the pods, shells, and leaves. In this sense, the plant has a high number of gums and tannins. The latest (tannins) represents the possibility of the application of this plant as an anticorrosive inhibitor [62]. Tannins are a type of polyphenolic compound that has at least one phenyl ring and one or more hydroxyl substituents. Thus, the phenyl ring can be adsorbed on the metallic surface, and this ability can be used to probe the Tara as a potential green inhibitor for the corrosion protection of metals.

2.2.4.2.3. Guayusa Ilex

Guayusa (Ilex guayusa Loes) is a native plant cultivated in the Amazonian region of Ecuador, Colombia, and Peru. Guayusa belongs to the only extant genus of the family Aquifoliaceae. The guayusa is a wild plant, and it has not been cultivated in any region of the cited countries. Thus, the wild Guayusa plants reach a height of approximately 25 m and a stem diameter of approximately 50 cm at breast height. This plant has not been studied in detail; however, as within the genus plants, Guayusa has a big quantity of alkaloids (caffeine and theobromine). The alkaloids are heterocyclic organic compound, nitrogenous, basic, with restricted distribution, and endowed, in small doses in the plant [113]. Moreover, the alkaloids have been studied as inhibitors due to the presence of the nitrogen groups, which are able to slow down the corrosion reactions, and they are easily absorbed on the metallic surface [114]. Thus, the Guayusa can be exploited as an inhibitor of corrosion.

Table 3. Principal investigation for producing environmentally friendly corrosion inhibitor by using plant extracts

Plant Extract name	Substrate	Corrosion Medium	Concentration	Inhibition efficiency	References
PLE	Cupper	0.5 M HCl	800 mg/L	89.98%	[103]
PFAE	Cupper	0.1 M H_2SO_4	600 mg/L	95%	[104]
QSE	Mild Steel	1 M HCl	800 ppm	90%	[105]
CC	Mild Steel	0.5 M HCl	2 g/L	79.69 to 98.76%	[106]
WLE	Mild Steel	0.5 M HCl and 0.5 M HNO_3	0.6 g/L	82% and 90%	[108]
PCOE	Carbon Steel	1 M H_2NSO_3H	300 ppm	96%	[109]
IPMFE	Cupper	0.5 M H_2SO_4	300 mg/L	93.3%	[110]
WPE	Mild steel	1M HCl	2000 ppm	92%	[111]
SCLE	Steel	1 M HCl	2500 ppm	98%	[112]

PLE: Pumpkin leaf extract, PFAE: Pyracantha fortuneana alcohol extracts, QSE: quince seed extract, CC: Cuminum cyminum, WLE: Willow Leaf Extract, PCOE: Pipper cubeba official extract, IPMFE: Idesia polycarpa Maxim fruits extract, WPE: Wormwood plant extract, SCLE: *S. caseolaris* leaf extra

2.3. Chemically modified electrodes

2.3.1. Definition

A chemically modified electrode (CME) is a conductor or semiconductor material that is coated with a monomolecular, multi-molecular, ionic, or polymeric film to change the electrochemical, optimal, mechanical, and other properties on the interface [69]. The modification starts with a pretreatment of the electrode. In this step, the electrode is cleaned and sometimes turned on to make sure it has good crystalline, roughness, and chemically active sites where the modifier can attach. Then, it comes the fixation of the modifier into the electrode surface; this process is the heart of the modification, and the final properties of the CME are going to highly depend on this process. There are several ways to attach the modifiers; however, the most commonly used are (a) Langmuir-Blodgett, which is an assembly method that consists of transferring organized mono-molecular films from a liquid phase in a Langmuir trough onto a solid support; (b) self-assembly, which is a modification by spontaneous chemisorption through the formation of strong covalent bonds; and (c) covalent attachment, which consists of the formation of new covalent bonds between the modifier and the electrode. The process is highly dependent on the chemical composition of the substance involved. The latter is the most common method to produce CME, especially when it is necessary to modify carbon electrodes [115]. Thus, carbon electrodes, in most cases, are composed of aromatic rings distributed along the carbon backbone, so these parts are rich in reactive sites in which different functional groups can form covalent bonds [115].

2.3.2. Classification

The classification of the chemically modified electrodes can be studied from different points of view; however, the scientific community agree to classified them according to their film–substrate attachment method and film composition to avoid a long extension of CME electrode classification. Anyway, as the field advance this classification only serve as a reference because it can be interjoined according to the necessities and the characteristics of the modifiers [116]. Therefore, the CME are divided into three main categories which are Langmuir-Blodgett, self-assembly and covalent attachment modifications. The characteristics, composition, mode of modification and applications are going to be discussed in the following sections.

2.3.2.1. Langmuir-Blodgett electrode modification technique

The Langmuir-Blodgett (L-B) technique creates and transfer monomolecular films from a Langmuir layer which is composed by amphiphilic molecules at the liquid/gas interphase; thus, the hydrophobic tail is oriented towards the gas phase and a hydrophilic head is oriented towards the liquid interphase onto a solid support by the self-organization of amphiphilic molecules at the liquid-solid interface to a solid substrate [116]. Therefore, at the solid substrate (electrode surface) the film is attached by attractive noncovalent interactions. Therefore, the properties of the modified electrode depend in the characteristics of the Langmuir layers. Moreover, this type of electrode modification is widely used in biological studies because its mimics the lipid membrane's structure, so transport phenomena and enzyme activity can be replicated. Other application of L-B electrodes includes the preparation of molecular recognition sensors or in molecular electronics [116].

The method of preparation of L-B modified electrodes follows these stages: (a) Langmuir film layer preparation: generally, this stage consisted in sparingly dissolved an amphiphilic solution (organic acids, esters, alcohols, amides, amines, nitriles in combination with polar solvents) into an aqueous phase. Then, lateral pressure is applied to increase the two-dimensional film concentration. Hence, as the pressure increase the solution changes its phase, from liquid to gas and there is formed a gas-liquid interface where the hydrophilic component (head part) is partial soluble in the liquid phase, while hydrophobic tail group extends partially into the gaseous phase to minimize the free energy of the system. At the end of the compression cycle, a highly ordered two-dimensional film is formed [116]; (b) electrode modification: the previous formed layer is transfer to the solid electrode surface by dipping the electrode into the solution. Here, the attractive forces between the surface and the head groups of the Langmuir solution result in transfer of the layer, such that the film physisorbs on the electrode surface [116]. Step (b) can be repeated several times to form a multilayer film which enhances better architecture. Therefore, the main advantage of this method is that L-B films possess unique characteristics compared to other films: they can achieve ultra-thin thickness ranging from a fraction of a nanometer to several nanometers, exhibit highly anisotropic lamellar structures, and theoretically offer monomolecular layers with minimal defects. On the other hand, the main disadvantages relating to L-B modification are [116]:

- Attractive forces between the Langmuir solution and solid electrode are much smaller than those resulting in chemical bond formation. Thus, L-B layers may not be stable for long periods of time or in harsh environments.
- Specialized equipment is required to create them, and special care must be taken to ensure reproducible and well-ordered films.
- This approach is particularly demanding with respect to high-purity reagents and liquids, and surface preparation procedures.

These disadvantages limit the use of L-B modifications in sensing applications; however, some investigations can be found in the literature with respect to this topic. For example, Inci Capan et. al. (2022) [116] produces a lipophilic calix[4]arene phosphonate-based Langmuir-Blodgett thin film for detection of organic vapors. The synthesis process was divided into two parts as follows: (a) Langmuir solution preparation: calixarene based lipophilic phosphonate derivatives were synthesised. Then, clevelage P–O–Si bond was necessary to form the Langmuir solution. This was performed by treatment of the trimethylsilyl esters with absolute methanol at room conditions for 20 h. This solution was labelled as CTPO4; (b) thin film fabrication: the CTPO4 solution was dissolved in appropriate amount of chloroform to obtain a final concentration equal to 1 $mg{\cdot}mL^{-1}$. The prepared solution was sprinkled onto a clean water surface with a syringe and let to rest for 10 to 15 minutes for solvent evaporation. Finally, a gold solid substrate was fixed in the upper part of a NIMA 622 model LB thin film fabrication, and it was immersed in the previous prepared solution at constant pressure. The prepared electrode was used to sense volatile organic compounds (VOCs) in a controlled environment. Therefore, the obtained electrodes are highly sensitive to benzene, toluene, chloroform and dichloromethane vapours with two-region interactions; i) fast diffusion of the surface interaction ii) slow diffusion of the bulk interaction. Moreover, the authors Lu Wang et. al. (2015) [117] prepared a modified electrode to detect methylparaben by using multiwalled carbon nanotubes (MWCNTs) modified electrode with Langmuir-Blodgett film. Therefore, glassy carbon electrode (GCE) was modified by the following steps: (a) electrode pretreatment: GCE was polished by using aluminium slurry, rinsed thoroughly with redistilled water and sonicated successively in ethanol and redistilled water respectively, (b) MCNTs functionalization (f-MWCNTs): commercial MWCNTs chloroform solution and sonicated for 2 h to obtain a uniformly black suspension of 1 $mg{\cdot}mL^{-1}$; (c) electrode modification: first, octadecyl amine (ODA) was dissolved in

chloroform and sonicated for 2 h to obtain a uniformly black suspension of concentration equal to 1 mg·mL^{-1}. Then, this solution was suspended onto a pure water surface and let to rest at room condition for 3 hours to chloroform evaporation. After, pressure was applied to obtain a layer of ODA which was floated on the subphase surface. Subsequently, f-MWCNTs were spread into the ODA solution. This suspension was let in rest for one hour. After this time, the prepared Langmuir film was compressed at rate of 10 mm·min^{-1}and then transferred onto the GCE surface with rate of 1.50 mm·min^{-1} via vertical dipping under surface pressure of 30 mN·min^{-1}. This process was repeated for at least 4 times to form a multilayer film. The obtained modified electrode was labelled as MWCNTs-LB/GCE. Then, the MWCNTs-LB/GCE was used to determine the redox behaviour of methylparaben cycle voltammetry (CV) or linear sweep voltammetry (LSV) performed in 2 × 10^{-5} mol·L^{-1} methyl paraben dissolved in 0.10 mol L^{-1} PBS (pH 3). The principal finding of the modified electrodes were: (a) From the EIS, it was demonstrated that the addition of MWCNTs via L-B modification reduce in a considerable manner the charge transfer resistances which ensures a better interaction between the analyte and the electrode. Also, the electrode which was modified two times with the L-B layer report the smallest charge transfer resistance; (b) From the CV, it was reported an irreversible peak potential at 1.06 V in the presences of methyl paraben. Thus, the MWCNTS-LB/GCE can sense the analyte; (c) From voltammetric, it was obtained a limit of detection equal to 4 × 10^{-7}mol·L^{-1} in a concentration range varying from 1 × 10^{-6} mol·L^{-1} to 8 × 10^{-5} mol·L^{-1}; (d) the modified electrode was tested in skin toner real sample achieving a percentage of apparent recovery equal to 97.90%. From the reported literature, it can be stated that even do the L-B method is complicated and time-consuming, there is some possibility to used in the production of sophisticated electrochemical sensing devices.

2.3.2.2. Self-assembly electrode modification technique

The self-assembly modification is carried out by attaching a modifier to the electrode surface by spontaneous adsorption forming a highly ordered layer. The film is typically formed by the chemisorption bonding between the substrate and the electrode. The term chemisorption is related to the strong adsorption of a molecule onto a surface through the spontaneous formation of a chemical bond and it is the controlled process in the modification. However, other intermolecular forces between the film are also important for the final characteristic of it [118]. These interactions allow the formation of bonds between the functional groups of the substrate and the and an active site of the electrode

surface. As a product of this interaction, it is formed monomolecular layers known as self-assembled monolayers (SAMs). These SAMs layers can be used to impart the desired function to the electrode directly or can serve as a foundation for more complex electrode architectures. The main advantages of the layer by layer (LbL) self-assembly technique are (i) it is possible to precise control the thickness and composition of the layer at nanoscale levels through the alternating deposition of oppositely charged polyelectrolytes or other interactive species [119]; (ii) it is possible to incorporate different functional materials including polymers, nanoparticles, and biomolecules, into the sensing interface; (iii) by the addition of more SAMs it is possible to control the architecture of the electrode enhanced stability and reproducibility compared to single-layer modifications; (iv) it is possible to tailoring the electrode surface properties (e.g. charge, hydrophilicity, and porosity) which derived in a better sensor's interaction with target analytes [120]. The explained advantages are the reason that LbL method is for now the most used technique to chemically modified electrodes to obtain electrochemical sensing devices. On the other hand, some problems such as (i) challenges in achieving complete and uniform monolayers [119], (ii) potential instability in harsh environments, (iii) the possibility of non-specific interactions, (iv) hinder electron transfer, and (iv) difficult to integrate with certain materials are still needed to overcome to enhance a better characteristic of the modified electrodes [120].

Anyways, more of the self-assembled electrodes are produced by the exposition of an adsorbate precursor (liquid or vapor) to a suitable substrate. Therefore, the most used LbL mechanism is carried out by immersing a substrate in a dilute solution (10^{-4} or 10^{-3} M) which contains the modifier for a long or short period of time (from seconds to days). Subsequently, the modified substrate is removed, rinsed copiously with neat solvent, and dried before use. Moreover, multiple mixed monolayers can be produced by simultaneous deposition of multiple precursors from the same solution, but this is not recommended because of the difficulty in controlling the concentration [120].

The LbL technique is widely used in the production of biosensors because of the ability of the sulphur-containing functional groups (founded in biomolecules) to be chemisorb onto some metallic surfaces such as gold, silver, copper, platinum, and mercury or in glassy carbon. For example, Yuqiong Liu (2024) [121] prepared a modified glassy carbon electon (GCE) by LbL self-assembled poly(diallyldimethylammonium chloride)/cyclodextrin composite for the electrochemical detection of paracetamol. The LbL electrode modification was carried out by simple dip coating method in which the

GCE were immersed in the modifier solution, then, it was taken off, dried with distilled water and dried under a stream of nitrogen gas. Or the authors Myungsang Park et. al. (2020) who prepared an electrochemical immunosensor for human immunoglobulin E using ferrocene self-assembled monolayers to modify an indium tin oxide (ITO) electrode. In their case, they produce the modification by incubating the ITO into the modifier solution; while the authors Xiaoyun Qin (2021) [122] prepared a modified electrode self-assembled, close-packed AuNPs to detect dopamine. In their case, they modified the electrode by drop-casting method. Also, by using drop casting the authors Mahmoud A. Hefnawy et. al. (2022) [123] modified a GCE using self-assembly Pd(II)-Schiff base complex to detect paracetamol.

Overall, the cited authors agree that the parameters of the production of the SAMs should be adjusted and optimized to produce a highly sensitive electrode modification. Also, the reported platforms are optimal to detect a wide range of analytes varied from pharmaceutical compounds to viruses or bacteria. Also, the analytes can be detected from a wide range of electrochemical techniques such as CV, square wave voltammetry, and EIS which allows the rapid determination of them. Overall, there is needed more research oriented to the production of better electrodes architecture and the inclusion of novel nanomaterials which aims to improve the stability, reproducibility, or the sensitivity.

2.3.2.3. Covalent attachment

The covalent attachment method is based on the formation of new covalent bonds between the modifier and the electrode substrate by the interaction between the functional groups of the modifier and the active sites of the electrode [124]. Thus, the final characteristic of the modified electrode highly depends on the chemical structure, physical properties such as crystallinity, area-to-ratio volume, or the nature of the electrode of the modifiers. As in the other modification techniques, it can be formed a single layer or a multiple layer film by changing how many times the modification is carried out. This is studied to produce better architecture electrodes structures. However, adlayer stability is not guaranteed (especially for organosilane linkages) and increased robustness may be offset by the complicated preparation required for many covalent modification schemes. Also, the preferred electrode substrates are carbon-based materials, however, the modification of some metallic, metallic oxide and semiconductor surfaces is also possible but the modification could be more complicate. In general terms, the advantages of the covalent attachment method are: (a) the addition of novel

nanomaterials (e.g. carbon nanotubes, metal and metal oxide nanoparticles, polymers) to the modifier suspension allows to produce highly stabile, selective, and sensitive electrodes compared to non-modified electrodes [125]; (ii) the covalent interactions, which are the most stable bond interaction, allows to form strong, irreversible bonds between the modifier and the electrode surface; (iii) the leaching or detachment is prevented by the strong covalent interactions. This leads a reliable and long-lasting electrode performance; (iv) it is possible to precise control the surface interaction which enables the production of electrodes with tailored properties for specific applications. On the other hand, the challenge of this method release in the difficulty of produced highly organized layers, thus, the reproducibility of the fine structure of the layer can be limited which limited the analytical application of the sensors. However, this can be solved by the development of more sophisticated modifier which can be tunned to achieve the desired layer structure.

The covalent attachment is the most used method to produce chemically modified electrodes in electrochemical sensing applications, therefore, the preparation of them can follow different paths, but a general view of the preparation follows the next steps [125]: (a) electrode pretreatment: this step is mandatory for all the electrodes. In the case of metals, this step includes surface homogenisation and cleaning, while in the case of carbon electrodes in many cases it is necessary an activation process. The activation allows to enrich the active functional groups presented in the carbon electrodes or allows to convert the functional group to a more reactive form. This is typically achieved through various methods, including physical activation with oxidizing gases, chemical activation using agents like potassium hydroxide or sulfuric acid and electrochemical activation through processes like anodization [126]. Then, the carbon electrodes are polished and cleaned; (b) modifier solution preparation: this step consisted in prepare a solution which is formed by the immobilized agent (e.g. polymer) which can form new covalent bonds with the electrode surface, and the nanomaterial (e.g. nanoparticles, biomolecules). The modifier solution preparation can be achieved by different techniques such as chemical methods, electrochemical method, gravimetric methods. The selection of the proper method is highly dependent on the nanomaterial necessities. Moreover, in the case of graphite electrodes this process is not needed; (c) modifier – electrode bonding: this stage consists in putting in contact the modifier and the electrode. By this interaction the new bonds are formed. Therefore, this step can be performed by direct mixing, dip coating,

spinning coating, layer deposition, etc. This step is the key factor to control the electrode architecture.

Because of its simplicity and the reported advantages, this method is the most preferred among the modification methods to produced chemically modified electrodes for electrochemical sensing applications. Thus, the literature in this topic is extended, however, some examples can be discussed in this section. For example, Zeyun Yang et. al. [127] produced a Cu(II) modified covalent organic framework for electrochemical detection of glutathione. Therefore, they first prepared the Cu(II) modified TADH ((N,N,N′,N′-tetra(3-aminopropyl)-1,6-diaminohexane)-covalent organic framework (COF) via condensation reaction. Then, this nanomaterial was dispersed in distillate water and drop casting over the GCE surface/ Thus, the covalent attachment was achieved via O(–OH) and N (C N) binding sites. Also, the authors Esam. M Dief (10.1039/d5cc00857c) prepared an electrochemical aptasensor for vancomycin voltammetric detection via direct aryl diazonium grafting approach. The aptasensor was prepared via gold–carbon covalent bonding. The aryl diazonium salt-derived introduce more functional groups to create more stable covalent bonds in comparison with other techniques performed to produce aptasensor such as LbL formation. Also, authors such as Satar Jabbar Rahi, et. al (2025) [128], or Yawen Xiao (2022) [129] or the authors Ting Zhang et. al. (2018) [130] chemically modified electrodes via covalent attachment and they were applied in different samples varied from medicaments to food.

In the reported studies, the authors agree that the potential used of the covalent attachment is the ability to prepare a huge number of electrodes by using different nanomaterials and different electrode substrate. Thus, the architecture of the sensor can be controlled by the nanomaterial which aims to increase the catalytic activity of the sensors. Therefore, the modifiers are different in composition, and due to the huge amount of them, the following sections are going to describe the modifiers used during the research stage. This includes the chitosan and different nanoparticles. Also, the working electrodes can be from different types such as glassy carbon, graphite, screen printed electrodes, gold, boron diamond electrode. From them, it is going to be described the carbon-based electrodes because they were used in the further chapters.

2.3.3. Glassy carbon electrodes

Glassy carbon (GC) is a gas impermeable, electrically conductive type, and highly chemical resistant type of carbonaceous material [131]. GC is produced by thermal

carbonization treatment of the graphite at about ≥1000ºC. After the treatment the material is composed of aromatic ribbon molecules, randomly oriented and tangled in a complicated manner [131]. The GC tends to form a stable wide variety of allotropes due to its hybridization, lent C-C bonds purely sp^2 hybridized, containing three σ and one delocalized π bond per coordination. Thus, it is relatively simple to perform modifications on its structure, which has been studied over the decades, to produce the most advanced materials [132]. However, glassy carbon (GC) does not present a well-defined crystal or amorphous structure, which allows for a potentially infinite number of symmetrical states, albeit such that every order has a finite degree of disorder and vice versa [133]. Moreover, due to their crystal structure and carbon orientation, the GC reports an optimal characteristic such as high hardness, brittleness, low toughness, high electrical conductivity, high thermal resistance, low density, impermeability to gases and liquids, inertness to corrosion and other forms of chemical attack, resistance to abrasion, low friction and the characteristic glossy exterior [133]. Furthermore, GC electrodes become indispensable tools in electrochemistry due to it large electrically conductive nature. This property is consequences of GC high ratio of sp^2/sp^3 content, due to the delocalized electrons contributed by the sp^2 bonding [134]. Other unique characteristics of the GC materials which are anomalous from other type of carbonaceous materials are the negative magnetoresistance, thermal conductivity proportional to the orientation of the turbostratic structural elements, reversible structural changes, biocompatibility. Overall, the GC electrodes have the best properties in comparison with other metal or carbon electrodes, however the synthesis and production are still a challenge, and this should be solved because the properties of the GC electrodes depend in high amount to their structure.

2.3.4. Electrode modifiers

2.3.4.1. Chitosan

Chitosan is a deacetylated derivative of the chitin coming from the family of the polysaccharides composed of a varying amount of (β1→4) linked residues of N-acetyl-2 amino-2-deoxy D-glucose (glucosamine, GlcN) and 2-amino-2-deoxy-D-glucose (N-acetyl-glucosamine, GlcNAc) residues [134]. Chitosan is soluble in aqueous acid media as a function of the primary amine protonation. This polymer can be extracted from insects, yeast, mushroom, cell wall of fungi, and marine shellfish such as crab, lobster, krill, cuttlefish, shrimp, and squid pens [135]. Moreover, this polymer has been used because of its notable myriad biological and technological properties. This includes high

molecular weight varying from 10000 to 1000000 Da, water solubility at pH acid, high degree of deacetylation (>90), high crystallinity, ability to form complex with transition metals. Furthermore, the importance of using chitosan to chemically modified electrodes lie on high reactivity of its functional groups (primary amino groups-C_2, and primary and secondary hydroxyl groups- C_1, C_2), which can created covalent bonds by interacting with other particles to produce stable compounds [136]. Overall, chitosan encountered a wide range of applications in the academic and industrial field. Thus, nowadays chitosan applications include agriculture, food processing, biotechnology, chemistry, cosmetics, dentistry, medicine, textiles, veterinary medicine, and environmental sciences. Therefore, the polyelectrolyte characteristics and the existence of reactive functional groups account for chitosan's gel-forming capability, elevated adsorption capacity, biodegradability, and antibacterial capabilities, which are crucial for its applications as a modifier of working electrodes [135].

2.3.4.2. Titanium dioxide nanoparticles

TiO_2NPs are nanoparticles derived from titanium dioxide (TiO_2) with diameters less than 10 nm. TiO_2 has three crystal structures, namely anatase, rutile, and brookite. For TiO_2 small nanoparticles, anatase is the most stable structure. Moreover, the extended use of the TiO_2NPs in all three crystal structures is connected to the good characteristics of these NPs. The characteristics include a high melting point (2972ºC), high dielectric constant, nontoxicity, stability in the presence of oxygen, hydrogen sulfide, sulfur dioxide, carbon dioxide, and ammonia, and a large band semiconductor (3.20, 3.02, and 2.96 eV for the anatase, rutile, and brookite phases, respectively), and high oxidation power [136]. The synthesis of TiO_2NPs, which includes sol-gel, hydro- and solvothermal, and electrodeposition, is the key parameter to obtain one crystal structure over the other, and this is important because the anatase phase is preferred because of its abundance, higher reactivity, longer charge carrier lifetimes, and highly tetragonal crystalline structure. However, the three crystal structures are widely used in different industrial applications such as photocatalysis, production of solar cells, production of lithium-ion batteries, production of biomedical devices, and production of sensors [137]. Overall, TiO_2NPs constitutes an interesting nanomaterial; however, there is still much necessary research to improve its characteristics.

2.3.4.3. Carbon nanotubes

The term carbon nanotube (CNTs) refers to a single layer of hexagonal-shaped carbon atoms rolled into a tube shape. CNTs are allotropes of carbon like the graphene and fullerene. There are two types of CNTs, the single-walled carbon nanotubes (SWCNTs) and the multiwalled carbon nanotubes (MWCNTs), depending on the number of carbon sheets [139]. Moreover, to produce CNTs there is three accepted technologies which are (a) catalytic chemical vapor deposition method (CCVD), which consist in produce a heterogeneous reaction in which both solid and volatile products are formed from a volatile precursor through chemical reaction, and the solid products are deposited on a substrate; (b) electric arc discharge, which consist in irradiated the graphite with an arc which has a voltage equal to 20 V in an inert atmosphere of 500 Torr of helium or argon; and (c) laser ablation, which consists in the vaporization of a piece of graphite by laser irradiation under an inert atmosphere [139]. The most used produced technology is the CCVD due to its low cost and high efficiency. After the production process, a CNTs structure with notable characteristics such as good electrical conductivity, high mechanical resistance (high Young´s module from 900 to 1700 GPa), high elongation, and high thermal conductivity (around 5800 $W{\cdot}\mathrm{m}{\cdot}K$). Overall, CNTs are a high-performance nanoparticle and because of their properties, CNTs have already attracted industrial interest, with carbon nanotube commercialization in sectors such as automotive, electrical, electronics, sporting goods, renewable energy, and drug delivery, amongst others [139].

2.3.4.4. Bioengineered flagellin nanofilaments

Bacterial flagella are extensions on the cell body that facilitate movement. The quantity of flagella per cell varies according to the species. Monotrichous species possess a singular flagellum at one pole (e.g., Pseudomonas aeruginosa); lophotrichous species exhibit multiple flagella at the same pole (e.g., Helicobacter pylori); amphitrichous species feature one flagellum at each pole (e.g., Campylobacter jejuni); and peritrichous bacteria possess multiple flagella distributed in all directions (e.g., Escherichia coli, Salmonella enterica) [140]. Moreover, the flagella are composed of three components (a) membrane embedded basal body; (b) a hook; (c) a filament. In this sense, filaments are a long part (longer than the flagella body) and during smooth swimming they adopt a left-handed supercoiled corkscrew shape, while clockwise rotation changes the handedness [140].

Flagellin is an elongated protein that constitutes the only component of flagellar filaments. The molecular weight of flagellins in Salmonella bacteria typically ranges around 51 kDa, with the terminal sections exhibiting great homology across species, forming the core of the filament. Furthermore, filaments are tubular structures composed of 20,000 copies of the flagellin protein organized in a helical configuration. Flagellin undergoes 11 rotations and translations along the screw axis, completing two full turns before returning to its initial position. This configuration produces 11 stacks of flagellin along the axis known as protofilaments, which serve as the fundamental functional components of the filament. The interaction among flagellin molecules within a protofilament facilitates a transition between two distinct states, left-handed (L) and right-handed (R), in relation to the longitudinal axis, independent of adjacent protofilaments. Furthermore, the cross-section of the Salmonella filament exhibits a densely packed helical core of 115 Å in diameter, surrounding a central channel around 25 Å wide, with an outside portion exposed to the surface where the domains of individual molecules are distinctly separated [141-142]. The diameter of the entire filament is around 230 Å. The core has two tubes, inner and outer, linked by eleven small spokes, whereas the outer section features two distinctly defined domains [141-143]. The filaments are intricate biomolecules, and their creation is documented in several stages: (i) strain selection, (ii) culture media preparation, (iii) culture growth, and (iv) flagellin purification. Consequently, advancements in purification and characterization techniques have rendered flagellin increasingly significant in biomedicine (drug and vaccine production), water treatment, and, more recently, in the development of biosensors owing to their capacity to recognize various analytes.

2.3.5. Applications for sodium diclofenac detection

2.3.5.1. Sodium diclofenac

Sodium diclofenac (DS) is among the most consumed non-steroidal anti-inflammatory drugs (NSAIDs), which are taken to reduce inflammation and used as an analgesic to reduce certain types of pain [144]. The structural formula is $C_{14}H_{11}Cl_2NO_2$. Moreover, the mechanism of action in the human or animal organism is not well understood yet; however, it is assumed that it involves the inhibition of cyclooxygenase (COX-1 and COX-2). DS is an odorless, white to off-white crystal powder, slightly hygroscopic, with a high melting point (ranging from 283 to 285ºC), high stability, and high solubility in water (≥9 mg/L) and PBS at pH 7 (6 mg/L) [145]. Moreover, the DS comprises two

aromatic rings and two chloride substitutes. The major problem with the administration of DS is its complete adsorption. It is studied that depending on the organism, the diet, and other parameters, the maximum reported adsorption on them is between 50-60%. Thus, the rest of the active compounds are released into the water; hence, the appearance of DS reported a concentration equal to 0.1 µg/l in inland surface waters (including rivers, lakes, and related artificial or heavily modified water bodies) and 0.01 µg/L in other (coastal) surface waters [146]. Therefore, DS has been put on the newly introduced "watch list" mechanism to collect European Union-wide monitoring data to monitor and control its presence in different water sources [146]. Therefore, multiple analytical methods have been proposed to determine its concentration in water sources, such as GC, LC, UPLC-MS/MS, NMR, and chemical-modified sensors [147].

2.3.5.2. Chemically modified electrodes for sodium diclofenac detection

The preparation of chemically modified electrodes for the detection of sodium diclofenac have been studied since the earlies 1970. They arrive as an alternative solution to detect the presences of this analyte in environmental sources, and in less cases for the application in the pharmaceutical industry to quality control application. Therefore, the literature is vast regarding this topic. However, the present section describes the most recent advances in the production of these electrodes, they feature and their analytical parameters. For example, Ana-Raluca Măghinici et. al. (2025) [148] detect DS in pharmaceutical samples by a screen-printed electrode (SPE) modified with graphene oxide and phenanthroline. Also, Sudip Das et. al. (2023) [149] detect DS in tablets via differential pulse voltammetry by using a SPE graphene/gadolinium oxide composite. Moreover, Sudip Da et. al. (2024) [150] use a chemically modified SPE by using graphene/MWCNT/copper-nanoparticle to detect DS in water samples and milk samples, or Linghui Tang et. all. (2025) [151] who produced a GC modified electrode by using carbon nanotube-doped hydrogel in pharmaceutical tablets via square wave voltammetry (SWV) or the authors Heba T. Elbalkiny et. all. (2019) [152] who used functionalized iron oxide (Fe_3O_4) magnetite nanoparticles to potentiometric detect DS in wastewater samples. Therefore, the analytical parameters of the prepared electrodes are gathered in Table 4, and from the results, it can be discussed that the application of the modified electrodes enables their used in a wide range of real samples and to detect DS in concentration even lower than micromoles.

Therefore, the authors agree that the modified electrodes presented the following advantages when they are compared with traditional methods:

- In most of the cases it is necessary to modify the pristine electrode because it cannot detect the redox process of DS in small concentrations.
- The electrocatalytic effect of the modifiers improves sensitivity, increases process reversibility, and reduces the activation energy of the DS redox electrochemical processes.
- The development and application of electrochemical methods for the determination of active compounds in various samples, including pharmaceutical ones, is favoured due to their rapid response, high selectivity and sensitivity, improved versatility, cost-effectiveness, and low toxicity, making this method environmentally friendly.
- The evaluation of DS in real world sample analysis also confirmed the efficacy of the modified sensors in complex matrices.

On the other hand, there is still needed to overcome some problems related to the modified electrodes such as selectivity, sensor stability and reusability. Therefore, studies are necessary to needs to be investigated with respect to the long-term study of the sensor for cost-effective and sustainable applications which as outcome is going to enable the replacement of the traditional detection methods by easier and more novel electrochemical modifier electrode.

Table 4. Principal parameters obtained from the collected chemically modified electrodes to detect sodium diclofenac in different real samples

Modified Electrode	Methods of detection	Linearity Range / µM	Limit of detection / µM	Real Sample
Carbon modified with graphene oxide and phenanthroline [148]	CV	0.01 – 0.07	1.53×10^{-3}	Tablets and injectable solution
SPE modified with graphene/ gadolinium oxide [152]	DPV	5.86 – 66.60	0.03	Tablets
SPE modified with MWCNT/copper nanoparticles [149]	DPV	17.41– 206.45	0.06	Drinking water and Milk
GCE modified with carbon nanotube-doped hydrogel [150]	SWV	10 – 80	3.5	pharmaceutical tablets
poly (vinylchloride) matrix modified with factionalized magnetite ferric oxide nanoparticle [151]	Potentiometric	0.10 to 10000	0.11	Wastewater
GC electrode modified with ZnO core@Cu shell nanoparticles [153]	SWV	0.01–300	0.03	Human urine and pharmaceutical samples

2.4. Morpho-structural methods of investigation

2.4.1. Scanning electron microscopy

Scanning electron microscopy is a device that use a focus beam of electrons to scan the surface of the sample [154]. It is among the most versatile instruments for analysing the micro- morphological structure of wide range of samples [155]. SEM analysed are based on bombarding with a fine beam of electrons the analysed sampled, scanning trough it by the scan coils. In this sense, the resulting imagines are going to depend on the interaction between the electron bean and the sample; thus, these interactions are classified in two: elastics and inelastic interaction. The first type is obtained by the deflection of the incident bean from the specimen atomic nucleus or by outer shell electrons of similar energy [156]. It is characterized by negligible energy loss during the collision of the particles and a wide-angle directional change of the scattered electron. Thus, it appears incident electrons which are called backscattered electron (BSE). These electrons are backscattered through an angle equal to or higher than 90º. While the second interaction type (inelastic scattering) occurs by different interactions between the particles and results in the primary beam electron transferring substantial energy to that atom [156]. From this process, secondary electrons, conventionally defined as possessing energies of less than 5 eV, are obtained, and these can be used to imagine or analysed the sample. Moreover, the secondary electrons can only escape within a few micrometres from the sample due to their low energy (commonly 3-5 eV), so they can precisely mark the position of the beam and give topographic information of the sample with good resolution. Moreover, due to their low energy, they can be attracted by the microscopic detector carrying some applied bias. This is accomplished by the Everhart Thornley (ET) detector, the most used detector in the SEM apparatus, which applies both a bias (+10 kV) to the scintillator and a lower bias (+300 V) to the Faraday cage, which screens the detector [157]. Then, the scintillator converts the energy of the electrons into photo visible light (photons). They travel down to the Plexiglas or polished quartz light pipe and move out to the specimen chamber wall, and into a photomultiplier tube (PMT) which converts the quantum energy of the photons back into electrons. The output voltage from the PMT is further amplified before being output as brightness modulation on the display screen of the SEM [156]. Therefore, the quality of the pictures depends on how much secondary electrons reach the detector.

To build the microscopic images, the SEM apparatus is composed of the following elements: (a) an electron gun, which is on the top the equipment, and it is on charge of

produce and accelerated the incident beam to an energy level of 0.1 – 30 keV; (b) electromagnetic lenses and aperture, which are used to focus and define the electron beam and to form a small focused electron spot on the specimen; (c) high vacuum pump, which generates a vacuum on the chamber and allows the travel of the electrons without suffering from scattering by the air; (d) electron beam coils which allows the deflection of the electron beam so that it can scan on the specimen surface along x- or y-axis; (e) processing system provide real-time observation and image recording of the specimen surface.

The SEM technique can build microscopic images of the sample, in which the structure can be observed in an amplification equal to or lower than 10 nm, but the secondary electrons that do not reach the amplifier should be separated in some way; otherwise, they produce shadows or unclear imagines. Overall, the SEM images can be studied in detail to learn useful things about the samples' surface structure. However, it is important to get the clearest images possible to figure out why these features are important for making electrochemical devices.

2.4.1.1. Scanning electron microscopy applied to the electrochemistry

SEM imagistic method is widely applied in the construction of electrochemical devices to evaluate the surface morphology which is determinant in electrochemical analysis methods because the surface morphology in one of the variables which controls the redox process extension than can be occurred in the electrode/electrolyte surface [157]. Moreover, by the study of the microstructure, it can be obtaining information about the arrangement, size, shape, orientation, and distribution of grains, phases, pores, and defects within a material. These properties profoundly influence a wide array of electrochemical behaviours in the devices [158]. Therefore, it is necessary to explain this with some examples of the SEM was used in the production of DDS, green inhibitors, and chemically modified electrodes.

The SEM is a potent technique in the analysis of preparation of DSS and is widely studied. For example, the authors Shawn Zhang [159] studied the transport mechanisms for controlled release polymer membranes via SEM methodology. They studied the efficiency of the production of DDS for example by analysing the morphology changes after the delivery of the drug, or by analysing the change in the porosity when the DDS was produced by different methods and how the porosity affects the DDS release. In the same way, the authors Thilo Faber (2023) [160] studied the principal insights of a DDS

via SEM imagens. In their work, he stated that the SEM images can help to understand the mechanism of action of the DDS, because it is possible to observe the distribution of the active compound in the inner part of the carries and how this system responds to the stimulus. Also, by the correct sampling it can be studied the interaction of DDS with their respective targets, as well as uncovering structural features within advanced DDS. From the reported studied, the following conclusions arrives: (a) the SEM is a powerful tool to study the surface of the DDS and the distribution of the active ingredients in the core part of the system, but the sample should be carry with extra care to ensure that it was not damage due to melting, re-deposition, and particle plucking; (b) the SEM operational conditions should be carefully control to avoid high voltage which can destroy the polymer; (c) SEM images grand opportunities in the understanding, design, and optimization of controlled release systems, but the DDS SEM images should be accompanied with other characterization techniques (e.j. FTIR, HPLC, UV-vis) to have a complete panorama about DDS functionality.

SEM images are highly used in corrosion studies, because it can give a narrow panorama about the state of corrosion of a metallic sample, the properties of the crystal structure and the efficiency in the protection, so, it can be applied as a supplementary technique for corrosion studies. For example, Frederick O. Pessu et. al. (2022) [161] studied the apparition of local pitting corrosion in mild steel exposed to CO_2 corrosion experiments by mapping the surface thought SEM images. Thus, by the SEM pictures analysis, the researcher realizes that the pitting initiation can be observed by the apparition of amorphous ferrous carbonate ($FeCO_3$) corrosion surface layer at the top surface. The formation of this layer was an indication of the corrosion process as it was probed by Raman, Linear polarization and EIS measurements in the same sample. Also, Ashraful Alam [162] explain the behaviour of pure aluminium and its alloys in aqueous sulfuric acid medium using as a first approach SEM images. They observed some light spots in the aluminium plates, and some smaller pit shaped pores were present in the surfaces of Al alloys 7S10 and 7003H. Thus, they concluded that all the aluminium plates presented corrosion. Also, the aluminium is less corroded at the analysed conditions. This was probe by other techniques. Moreover, the SEM images can also be used as a first approach to analyse the effectiveness of the protection via corrosion inhibitors obtained from plant extract. For example, the authors S. Abdelaziz (2021) [163] produced a green corrosion inhibition of mild steel in HCl medium using leaves extract of Arbutus unedo L. plant and studied its efficacy by different method taking as starting point SEM pictures.

They analyzed the metallic SEM when they were exposed to the acid medium without and with the inhibitor. Therefore, the pictures of the surface of the metal samples reported a destruction of the crystal structure and the apparition of pits when the samples were exposed to the acid medium after 24 h of exposition. On the other hand, pits were not reported when the extract was added, and the surface of the metal remains almost equal compared to the metallic samples which were not exposed to the acid medium. So, the authors agree that SEM microscopy is a power tool for corrosion analysis, because it can be observing pitting or metallic surface destruction as effect of the corrosion process. However, the SEM technique is still limited to be used in industrial applications because of its difficulty and elevate price. Another limitation is the sampling, because if there is not chosen the right sample it can be cover up the apparition of corrosion. But SEM technique still a good analysis method but it should be combined with other corrosion analysis methods to have a complete picture of the corrosion in metal samples.

Finally, SEM applied to the production of CME are widely used to obtain information about the morphological structure of the electrode and it is a hint to observed if the modification was successful and the distribution of the modifier into the electrode surface. For example, Ruimiao Qin et. al. (2023) [164] produced a carbon cloth modified electrode by using gold NPs. The SEM imagens reported a small round nanoparticle distributed randomly on the electrode surface which was an excellent proof of the modification. Also, the authors Ademar Wong (2016) [165] modified a GC electrode by the used of graphene oxide and gold nanoparticles crosslinked chitosan film. From SEM imagens they discussed that the graphene oxide was well attached to the electrode surface because it can be observed some portions with a leaves or wrinkled paper shape which is the characteristic shape of the graphene oxide. Also, between the graphene oxide some sphere NPs particles appear randomly distributed which are a proof of the presences of gold NPs. They conclude that the presences of both nanoparticles increase the active area of the electrode which is desired because it increases the active sites in which the redox reactions can occurred. Overall, the SEM images are widely applied to the determination of the quality of the modification because they can give the researcher a valuable tool to evaluate the architecture of the electrode, and how this architecture control the final analytical parameters of the electrode.

2.4.2. Atomic Force microscopy

Atomic force microscopy is an imagistic technique that is based on building images by applying different forces between a cantilever and the sample and measuring and transforming these forces into images [166]. Therefore, the qualitative sketch of these forces is given as a function of the distance between the tip and the sample. These distances are distributed in three different zones: (i) the tip is far away from the sample—not possible to calculate the force; (ii) the tip is close to the sample—a negative (attractive) force is obtained; (iii) the tip is very close to the sample—a strong repulsive force occurs between the sample and the tip [166]. Hence, the applied forces are measured by a part of the AFM machine called a cantilever, the deflection of a cuboid-shaped flat spring, which acts as a spring, and its deflection is proportional to the applied force. This force can be calculated by Hook's law (assuming that the cantilever spring is constant), which states $F_{spring} = -kz$, where F_{spring} is the spring force and z is the distance the cantilever spring is bent relative to its equilibrium position without the sample present. This deflection is measured by a laser beam reflected from the back of the cantilever [166].

Furthermore, at the static mode of operation, the surface contour is mapped while scanning by the change of the z-position or the tip in a way that produces different forces between the sample and the tip, and the distance between both parts remains constant. Thus, the z-signal is recorded in the form of topographic images. On the other hand, if the measurements are executed in zone (ii), the operating mode is called contact mode. In this mode, the surface atoms of the sample are in contact with the tip. Another mode in which the AFM can work is known as dynamic mode, in which the cantilever is oscillating around the sample [166]. This mode occurs in the attractive zone, and it is applied when the sample (polymer or biological samples) is susceptible to the touch and can be easily destroyed by the tip. The principle behind this type of operation is that the cantilever is excited to vibrate close to its free resonance frequency, and when the cantilever approaches the sample, the interaction between the sample and the tip changes the oscillation frequency of the cantilever. Thus, the interaction can be explained by another spring acting in addition to the cantilever. Overall, the idea behind the AFM technique is to scan a probe over the surface, and the chemical or physical properties of the sample can be determined with high spatial resolution [166].

2.4.2.1. Atomic force microscopy applied to the electrochemical devices

In the present case AFM was used to evaluate the film properties. Thus, AFM is a valuable tool to study this kind of technology. AFM allows to observer the characteristics of the film at nanoscale level, providing insight information about the formation above the metallic surface, or information about of the coating degradation, or information about the ability of the polymer to be crosslinked, or even in other cases to obtain information about the metallic state by studying the inner dimension of the metallic surface [167]. Therefore, several research can be found in the literature about the AFM characterization of the coatings. For example, the authors Ahed Almalla et. al. (2022) [167] proposed a methodology based on AFM imagen analysis to study the corrosion process in an epoxy-like model organic film used to protect aluminum alloy. The methodology was based on analysing the changes in the thickness of the film at the buried interface between the coating and the metal surface expose to an aqueous electrolyte solution. They reported that the surface film was thick when the metal surface was immersed in the solution under a certain, but the metal surface remained with the same thickness. On the other hand, when the metal surface without coating was evaluated in saline environment, the thickness decreased considerably, therefore they confirmed the corrosion process over the metal when it was not cover with the polymeric membrane. Also, the authors Joan M. Perry et.al. (2000) [168] evaluated the corrosion behavior of a spraying coating by AFM measurements. They prepared a Co-Cr polymeric coating over a mild steel plate which was exposed to saline environment. The principal finding. From AFM imagens they can observed apparition of small pits in the non coated mild steel as effect of the corrosion attack. However, the pits did not appear in the case of the coated sample which confirms the protection of the metallic sample. Overall, AFM reported some advantages to be used in the corrosion protection control such as (a) this technique serve to have a clear panorama of the corrosion over metallic surfaces by measuring its surface thickness and homogeneity; (b) AFM provide information from the buried polymer/metal interfaces to be able to observe corrosion induced delamination [168]. On the hand, the AFM is still limited to be used only in laboratory conditions as effect of the time-consuming sample preparation and as effect of the complexity in the manipulation of the equipment [168]. So, more development is still needed to facilitate the sample preparation and to facilitate the operational conditions of the machinery.

2.5. Other characterization techniques

2.5.1. Infrared spectroscopy

Infrared spectroscopy (IR) is undoubtedly one of the important analytical techniques available in chemical laboratories. This technique is based on measuring the vibration of atoms in a molecule. The experiment is accomplished by passing infrared radiation through a sample, and thus, a fraction of the incident radiation is adsorbed at a certain amount of energy value [169]. This vibration results in the formation of an infrared spectrum. So, in this diagram, some peaks appear, which represent the vibration of a part of a particular sample. Vibration occurs in heterogeneous molecules in which the dipole moment can expand or contract to follow the movements of molecules. Therefore, the interaction of the molecules with the infrared radiation is understood in terms of vibrations and rotations because the molecules, in a simple view, are represented by a system of masses joined by bonds with spring-like properties [169]. Thus, a simple diatomic molecule has three degrees of translational freedom and two degrees of rotational freedom. Stretching and bending movements, also known as vibrations, occur when the atoms move about each other (bond length variation). Hence, only one movement is possible for a diatomic molecule, while for polyatomic molecules (containing N atoms), the allowed movements are going to have 3N degrees of freedom. The vibrations can involve a change in bond length (stretching) or a change in bond angle (asymmetric stretching). Other contributions to the infrared spectra are the bending vibrations; these can be deformation, rocking, wagging, or twisting. Furthermore, it can be observed from the spectra something that is called a fingerprint, which consists of the coupling of the vibrations over a large part or the whole molecule [169].

In this sense, a special type of IR is called Fourier-transformation infrared spectroscopy which lies in the principle of the interferences of the radiation created by two beams which yield an interferogram [170]. Therefore, the domains of the frequency and the distances are interconvertible by the application of Fourier-transformation mathematical model. So, the basic components of the FTIR equipment are (a) radiation source. It is typically a tungsten–halogen lamp; (b) Interferometer, composed by moving mirrors capable of scanning two distances so that the path difference corresponds to a known value; (c) sample, most general organic molecules; (d) detector, a pyroelectric device incorporating deuterium tryglycine sulfate; (e) amplifier, (f) Analog-to-digital converter with a Fourier transformation software; (g) computer to obtain the final FTIR spectrum [50-52]. The advantages of using the FTIR machines include the Fellgett (or

multiplex) advantage, an improvement in the signal-to-noise ratio -proportional to the square root of the number of resolution elements being monitored-, and the Jacquinot (or throughput) advantage, gain energy at the detector, thus is translated as higher signals and lower signal-to-noise ratio. Another advantage of the FTIR is the speed in performing the analysis, it is possible to obtain the spectra in millisecond timescale [50-52].

2.5.2. Ultra-high performance liquid chromatography- Tandem Mass Spectrometry

The ultra-high performance liquid chromatography-mass spectrometry/mass spectrometry (UPLC - MS/MS) is an analytical method that combines high liquid chromatography with mass spectrometry to analyze the characteristics of a chemical compound [171]. For this, an interface is necessary to remove the chromatographic mobile phase. Therefore, due to the incompatibility of both techniques (UPLC – MS/MS), they cannot be linked directly. However, this combination allows one to overcome the problems reported by one or the other characterization technique; thus, the main role of the UPLC is to separate the compounds of a mixture and quantitatively or qualitatively analyze these compounds, while the mass spectrometry provides the information of the compound with a high degree of precision. So, the main advantage of using this combination is to overcome the UPLC problems (inability to provide an unequivocal identification of the components of a mixture even if they can be completely separated from each other) and the MS/MS problems (difficulty of identification of a compound when it is in a mixture, with special regard when this analyte is the minor component of that mixture). Therefore, the high performance of this combination lies in the ability of the UPLC to separate the components of a mixture and in the ability of the MS to provide the information of an analyte when it is not in a mixture [171]. This is especially advantageous when the components of a mixture have similar retention characteristics.

Consequently, to accomplish a good combination of both techniques, the capabilities of both techniques should not be affected by their link. These include the following criteria [172]:

- The interface should not affect the chromatography capacity. It is important when it is necessary to analyze complex multi-component mixtures. In this case the performance of the MS is reduce to a tolerable point

- It is necessary to eliminate any uncontrolled chemical modification of the analyte when it passes through the UPLC and when it is introduced in the MS
- It is necessary to have a high rate of analyte transferred from the UPLC to the MS, or a high ionization transfer rate if the process occurs in the UPLC - MS/MS interface. This is fundamental when it is analyzed a trace level of analyte or when it is analyzed polar and/or labile analytes
- The chemical background should keep at low as possible in the interface to avoid possible interactions with the analyte
- The interface should be precise and easy to use
- The interface should operate at all the UPLC conditions including flow rates 20 $nL \cdot min^{-1}$ to around 2 $nL \cdot min^{-1}$, solvent systems from 100% organic phase to 100% aqueous phase, gradient elution, wide range of polarity, volatile or involatile buffers
- The vacuum on the interface should not be affected by the operation of the UPLC, to ensure the optimal working conditions of the MS equipment.
- The MS should provide unambiguous molecular weight information from the wide range of compounds, including biomolecules with molecular weights more than 1000 Da.
- The structural information provides by the MS should reproducible, interpretable, amenable to library matching. Thus, an electro ionization spectrum should be generated.
- The quantitative information provided by the interface should be better 10% reproducible with low detection limit (LOD) and a linear response over a wide range of particle size (from low picograms to µg)

In depth, the UPLC-MS/MS equipment is composed of both UPLC-MSMS components. Thus, this equipment is composed of (a) mobile phase reservoir; (b) pump, which is on charge to provide a stable rate flow between 10 $\mu L \cdot min^{-1}$ and 2 $mL \cdot min^{-1}$; (c) sample injector, a loop injector to introduce liquid samples into a liquid flow stream; (d) mobile phase, in which the analytes are soluble; (e) stationary phase, generally a chemically modified silica; (f) detector, could be UV, fluorescence, electrochemical, conductivity and refractive index detectors depending on the analyte; (g) ions source, generally a tungsten lamp; (h) quadrupole rods, where fragmentation of ions transmitted by the first set of quadrupole rods is carried out [171].

Overall, the coupling of both equipment presents a wide range of advantages which includes the speed of analysis, the convenience, particularly for the analysis of multi-component mixtures, the reduced possibility of sample loss, the ability to carry out accurate quantitation using isotopically labelled internal standards, and the ability to carry out certain tasks, such as the evaluation of peak purity, which would not otherwise be possible [171]. On the other hand, there is some problems related with major incompatibilities between UPLC and MS/MS spectroscopy. The first is that the differences in the vacuum pressure because of the different operational conditions. Thus, the UPLC typical operates with a rate flow equal to 1 $mL \cdot min^{-1}$, while the mass spectrometer operates at a pressure of around 10^{-6} torr. So, it is not possible to pump the directly the mobile phase to the MS equipment, and a portion of the mobile phase should be removed. The second is that most analytes that are likely to be separated by UPLC are relatively involatile and/or thermally labile and therefore not amenable to ionization, this complicates the analysis in the MS/MS part [171]. However, these limitations have been solved through the last decades, and more powerful UPLC - MS/MS equipment are disponible nowadays. Thus, this technique is in present one of the most powerful and used characterization method due to their high precision and their capacity to give a high accurate quantitative and qualitative information of a wide range of analytes.

2.6. Electrochemical characterization methods

The electrochemical process is always occurring in a heterogeneous system, thus, most of the time the electron transfer process which are on solution reacts in a solid or gas surface (working electrode). To understand this heterogeneity, it is necessary to understand that the heterogeneity creates a phase boundary. There is no matter of the chemical species involved in the process there are divided in two types: the molecules which are far from the electrode, they do not take part in the process, and the molecules which are near to the electrode-electrolyte solution (bulk phase), they take part in the electrochemical process. Moreover, at the electrode-electrolyte surface the environment is not homogeneous, which is the main differences with respect to other analytical technologies, it originates the different process which occurs in the electrochemical techniques, and they include phenomenon such as mass transport, adsorption, chemisorption, homogeneous-phase chemical reactions, and convention [172]. All this process is studied at the three-electrode configuration which is going to be described in the next section.

2.6.1. Voltammetric Techniques

The term voltammetry is derived from volt-amperometry, and it explains that these techniques relate the measured current as a function of the voltage, in other words, as a function of the electrode potential [173]. The voltammetric techniques have their origin in the polarography technique (this term expressed that the polarization of an electrode was graphically recorded as current–potential curves, so if there is a current flow, the electrode is depolarized, and if there is no current flow, the electrode is polarized, so the minimal current response is obtained by the change in the potential). Moreover, the application of the voltammetric techniques enables the researchers to correlate the concentration and the change in the current or voltage of the system. This relation is explained by the faradic current, an electric current generated by the reduction of oxidation of a chemical substance. Thus, for the generation of the faradic currents, the molecules or ions need to reach the working electrode surface [36]. Therefore, the controlled mechanism is the mass transport of them, so the paths that the molecules can follow are: (i) diffusion because of concentration gradient, (ii) migration of ions because of potential gradient, and (iii) convection [173]. Also, another key parameter to consider is the geometrical area of the working electrode, so for example when the electrode area has a value in the range of μm, the edge effects become the controlled parameter, and the diffusion layer is having a circular shape [36]. Moreover, the stirred is also a parameter to consider, thus, when the solution or the electrode are moving the diffusion layer shrinks because of the movement [174].

Overall, the voltammetric techniques are based on the Nerst equation (equation 5) [174].

$$E = E^{o} - \frac{RT}{nF}\log\left(\frac{a_{ox}}{a_{red}}\right) \qquad (5)$$

Where E is the potential (V), E^{o} is the standard potential (V), R is the universal ideal gas constant (8.31 $J \cdot K^{-1} \cdot mol^{-1}$), a_{ox} is the activity of the oxidase form of the species at equilibrium, a_{red} is the activity of the reduced form of the species at equilibrium. This equation can connect the redox reactions with the change in the potential of the system when it achieves equilibrium. Furthermore, voltammetric techniques intentionally alter the charge transfer and mass transfer rates up to a specific value [174]. Therefore, the way of measuring the potential, the current, and the relation with the Nernst equation are the main differences between the different applied voltammetry techniques that will be considered in the following sections.

2.6.1.1. Cyclic Voltammetry

The Cyclic Voltammetry (CV) is a voltammetry technique which consists of cycling the potential of an electrode immersed in an unstirred electrolyte and measuring the resulting current [175]. The changes in the potential of the working electrode should be measured against a reference electrode (calomel, Ag/AgCl, Ag). The CV method is simple, thus converts the CV in the most versatile electroanalytical technique for the study of a wide range of electroactive species [175]. Moreover, to understand the behaviour of an electrochemical system, the CV is the first applied technique, because it allows the researcher to rapidly observed the redox behaviour of the involved species under a wide potential range. In depth, the controlled applied potential is studied as an excitation signal. This is a linear potential scan which results in a triangular wave form. The triangular potential excitation signal sweeps the WE potential between two values, these are called switching potentials [175]. Hence, the variation of potential and the obtained current respond in the working electrode is draw in a diagram known as cyclic voltammogram. In this, the x-axis represents the voltage, and the y-axis represents the response current signal, and the slope of the curve represents the scan rate of the analysis [175]. Moreover, the CV technique is composed by a forward scan (scanned negatively) and a reverse scan (scanned positively). Thus, the CV has the advantages to rapidly produce new oxidation states during the forward scan and then proving its fate on the reverse scan [175]. This constitutes a particularly important aspect of technique. CV is understanding more in depth by the application of the Nerst equation (equation 5) which stablish the relationship between the change in potential and the changes in the concentration of the species in the solution during the electrolysis. Moreover, from the relation it can be observed that the control variable is the change in potential which exerts control over the change in the concentration of the participant species at the electrode surface.

2.6.1.2. Square wave voltammetry

Square wave voltammetry is a powerful electrochemical technique which relies on the imposition of a small amplitude, short pulses on a staircase potential-time function and the current is measured before the pulse application and after each imposed pulse, and the differences between both currents is calculated [176]. So, the main features of the SWV are the scan increment ΔE and the duration of each potential step τ. Therefore, the scan rate as definition is the ratio of the scan increment and the step duration, $v = \Delta E / \tau$. The

overall potential modulation can be understood by studying the potential variation during a single potential step. At each potential step, two small and opposite oriented potentials are imposed. So, the duration of the two pulses is identical, and it is designated as t_p which is equal $\tau/2$. Moreover, the height of the single pulse potential is defined as square-wave amplitude (E_{sw}). Hence, the main parameters of the square wave potential modulation are the scan increment ΔE of the staircase ramp, the SW amplitude (E_{sw}) and the duration of the potential pulse t_p know as square wave frequency [176]. So, one cycle of the SWV method is composed of the two neighbouring potential pulses imposed at a single potential step.

In terms of evaluating the mechanistic properties of the system, the SWV is more powerful than the CV technique, because of the ability to check the mechanistic aspects of the electrode reactions at the potential value corresponding to each potential step, starting from the E_s to the final E_f potential, thus avoiding the necessity to reverse the overall potential modulation [176] as it occurs in the CV technique. Likewise, at each potential step two currents are measured. So, another curve can be built from these data (subtraction of the forward and backward current) and it is termed as net current ($I_{net}=I_{for}-I_{back}$). This simple approach allows to draw the over SW voltammogram which is a well-defined peak, no matter if the backward and forward elements have a square shape. The advantages of this are the obtention of a peak-like shape of net SW, because it can be obtained readable measurement parameters such as peak height, peak position, thus it can be correlated the concentration of the analytes with these parameters. Therefore, SWV unifies the advantages of cyclic voltammetry, as a tool for mechanistic studies, with the advanced sensitivity, typical for pulse voltammetric techniques [177].

2.6.2. Electrochemical Impedances Spectroscopy

Electrochemical impedance spectroscopy (EIS) is a powerful electrochemical technique that is based on the perturbation of a system in an equilibrium or steady state by the application of a sinusoidal signal (ac voltage or ac current) over a huge range of frequencies, and the obtained signal, which can be a change in potential or in current, is monitored towards the applied perturbation [178]. So, the EIS can be used in many areas, including corrosion, semiconductor science, chemical sensing and biosensing, drug release systems, non-invasive diagnostics, and more. It is important to highlight that the system remains invariant on time, so the impedance is a transfer function that models the

inlet signal against the outlet signal. Hence, the result gives kinetics or mechanistic data of different electrochemical systems. The τ constant of the system is given by:

$$\tau = R \times C \qquad (6)$$

where R is the resistance of a resistor (Ω) and C is the capacitances of a capacitor (F), thus allows the EIS results to be simulated by an equivalent circuit, which is composed commonly of passive component (such as resistor, capacitors and inductors) and other more complicated elements (distributed elements) connected each other differently according to the system [178]. The main advantage of the EIS when compared to other described electrochemical techniques is the ability to simplify the most complex electrochemical process by deconvoluting it in individual processes with different time constants. Thus, very slow electrochemical processes can be studied at very low frequency values, while rapid electrochemical processes can be studied at high frequency values. Therefore, the potentiostats power will significantly influence the accuracy of the technique. Most of the commercial potentiostats span the frequency in a range between 10 μHz and 1 MHz. Moreover, most of the electrochemical processes are governed by three main processes: the charging/discharging of the electric double layer at the electrode/electrolyte interface, the kinetics of the faradaic reaction, and the diffusion of the redox species from the bulk solution to the electrode surface [179]. They can be observed in the different frequencies of the study and are represented by the formation of a semicircle (charging/discharging process) and the formation of a line (faradic and diffusion process) connected in a graph called a Nyquist plot.

3. Original Contribution

3.1. Drug Delivery systems

3.1.1. General Objective

- To build a methodology for analyzing the release profile of paracetamol in artificial saliva solution using the electrochemical impedance spectroscopy technique.

3.1.2. Specific Objective

The proposed specific objectives for the present chapter were:

- To construct a composite film containing PEDOT and paracetamol (PA) over a titanium plate working electrode.
- To obtain information about the PA release profile in artificial saliva solution as effect of the pH of the medium.

- To investigate the functionalization of the PEDOT and the PA by analyzing the principal features of the cyclic voltammograms, the morphological characteristics, and the chemical characteristics.
- To describe the appropriated kinetic model for the release of the PA in artificial saliva solution utilizing the decrease of the solution resistances over the time.

3.1.3. Materials and methods

3.1.3.1. Reagents

The following chemicals were used during this experimental part: 3,4-ethylenedioxythiophene (EDOT, from Sigma-Aldrich, 97% purity), sodium dodecyl sulfate (SDS, from Merck, 99% purity), lithium perchlorate ($LiClO_4$, from Fluka, 95% purity), Paracetamol (PA, from Sum-Pharma/Romania, 98% purity), sodium chloride (NaCl, from Merck, 99% purity), potassium chloride (KCl, from Merck, 99% purity), calcium chloride ($CaCl_2 \cdot 2H_2O$, from Sigma-Aldrich, 95% purity), citric acid ($C_6H_8O_7$, from Merck, 99% purity), sodium sulfide nonahydrate ($Na_2S \cdot 9H_2O$, from Merck, 98% purity), sodium phosphate monobasic monohydrate ($NaH_2PO_4 \cdot H_2O$, from Sigma-Aldrich, 98% purity), urea (NH_2CONH_2, form Merck, 95% purity), ammonium sulphate ($(NH_4)_2SO_4$, from Merck, 99% purity), sodium bicarbonate ($NaHCO_3$, from Merck, 99.50% purity). hydrochloric acid (HCl, from Sigma-Aldrich, 37% purity), sodium hydroxide (NaOH, from Merck, 99% purity), and distilled water. All the cited chemicals were used as the provider supply without further purification to avoid excessive preparation of the reagents.

3.1.3.2. Equipment

The electrochemical experiments were carried out by using a controlled AutoLab potentiostat (PGSTAT302N EcoChemie, Utrecht, Netherlands) operated by GPES 4.7 and FRA 2.1. Hence, a conventional three cell configuration (equipped with a working electrode of Ti-modified electrode or boron-doped diamond (BDD) electrode, an Ag/AgCl, KCl_{sat} reference electrode, and a platinum wire auxiliary electrode) was employed. The morphological characteristics of the prepared composite films were evaluated by using a SU8230 scanning electron microscope (Hitachi, Japan) equipped with Dual EDX System (X-Max N100TLE Silicon Drift Detector) from Oxford Instruments.

The chemical characterization of the films was executed by using a Nicolet 6700 FTIR Spectrometer, and the pH was measured by using a glass combined electrode (HI 11310) connected to a pH meter (type MV 870, Pracitronic, Germany).

3.1.4. Methodology

3.1.4.1. Preparation of the monomer solution

10 mM of EDOT, 0.10 M of SDS, and 0.10 M of $LiClO_4$ were added to a 25 mL volumetric flask to prepare the monomer solution. Then, the flask was agitated in a magnetic stirrer for an hour; subsequently, the flask was sonicated in an ultrasonic machine for an hour. The prepared solution was stored in the fridge at 4ºC.

3.1.4.2. Preparation of the artificial saliva solution

An artificial saliva solution was prepared by following the Mondely [180] receipt. Thus, in a volumetric flask of 1 liter, the following components were added: 0.50 g of NaCl, 0.50 g of KCl, 0.79 g of $CaCl_2 \cdot H_2O$, 5×10^{-3} g of $C_6H_8O_7$, 0.50 g of $Na_2S \cdot 9H_2O$, 0.30 g of $(NH_4)\ SO_4$, 0.78 g of $NaH_2PO_4 \cdot H_2O$, 1 g of NH_2CONH_2, 0.30 g of $(NH_4)_2SO_4$, and 0.10 g of $NaHCO_3$. Distilled water was added until the flask was flushed. This solution was agitated in a magnetic stirrer for 20 minutes or until it was colorless. Subsequently, drops of HCl or a solution of 1 M NaOH were added (depending on the acidity of the solution) until the pH was adjusted to 5. The same procedure was repeated for a second solution, but at the last step, the pH of the solution was adjusted to 6. Also, a third solution was prepared with the same procedure, but, in this case, the pH was adjusted to 7. The three solutions were labeled (according to the pH value) and stored in the fridge at 4ºC until they were used.

3.1.4.3. Preparation of the working electrode

Metallic titanium plates were cut in a cylindrical shape with a diameter of 3 mm and covered with a Teflon tube to isolate the pieces and control the area, which was approximately 7.65×10^{-2} cm^2, so that it was immersed in the saliva solution. This configuration constitutes the working electrode. Before use, the electrode was mechanically polished by using an abundant amount of alumina (from Buehler), then it was rinsed with abundant distilled water, and finally, it was dried at room temperature. Three working electrodes were prepared by following the procedure described.

3.1.4.4. Polymeric film preparation

The cleaned Ti electrode was immersed in an electrochemical cell that contained 10 mL of the solution prepared according to section 3.1.3.3.2. Additionally, to this solution was added 1 or 2 mM of PA (according to the required composition of the membrane). The setup was then connected to the potentiostat, and the references and auxiliary electrode were submerged in the cell. The polymeric film was prepared via electropolymerization; thus, a cyclic voltammetry experiment was conducted. Therefore, the working electrode was cyclic with the voltage from -1 to 1 vs. Ag/AgCl/KCl_{sat} with a scan rate of 5 or 10 $mV \cdot s^{-1}$ (depending on the requirement of the experiment) for 10 cycles. Finally, the electrodes were taken out of the solution, rinsed with distilled water, and labeled according to the experimental conditions used.

This procedure was repeated 3 times for each experimental condition. Therefore, the obtained working electrodes were labeled as follows: 5-Ti/PEDOT-PA, 5-Ti/PEDOT-2PA, 10-Ti/PEDOT-PA, and 10-Ti/PEDOT-2PA were 5 or 10, corresponding to the scan rate, and 1 or 2-PA corresponds to the paracetamol concentration. These electrodes were stored at room temperature until the experiments were carried out. All experiments were performed at ambient temperature and repeated three times.

3.1.4.5. Drug release analysis

The drug release analysis was performed by evaluating the solution resistant obtained by using EIS technique. The prepared working electrodes (section 3.1.3.3.4) were immersed into 10 mL of saliva solution; the pH of it varies from 5 to 7 according to the required condition, and impedance spectra were recorded for 6 h with a delay of 1 min between the measurements by using an AC signal with an amplitude of ±10 mV and a frequency interval from 10 kHz down to 0.01 Hz. The EIS data was plotted as Nyquist and Bode diagrams. Using an equivalent electric circuit, the experimental impedance data were fitted using ZSimpWin 3.2.1 software, and the values of circuit components were subsequently correlated with the processes occurring in the electrochemical cell. Moreover, to contrast the EIS results, the determination of released paracetamol in the saliva solution was monitored by using differential pulse voltammetry (DPV) analysis with a pristine BBD electrode. The experiments were carried out in the previous prepared artificial saliva solution (pH 6). The set up for the DPV measurements was as follow: (a) deposition potential, -1 V; (b) deposition time, 180 s; (c) module time, 0.05 s; (d) interval

time, 0.1 s; (e) initial potential 0.5 V; (f) step potential, 0.005 V; (g) module amplitude, 0.1 V. Moreover, the release of the PA was evaluated every 40 minutes for 6 hours.

3.1.4.6. Kinetic mathematical model construction

The kinetic mathematical model was built by correlating the resistances obtained from the EIS analysis against time. Therefore, the solution resistances obtained from the equivalent circuit analysis were plotted against time and correlated according to the zero order, Higuchi, and Korsmeyer-Peppas models (equations 7, 8, and 9 respectively), which are calculated according to the following formulas:

$$Q_t = Q + K_0 \cdot t \quad (7)$$

$$Q_t = K_H \cdot t^{\frac{1}{2}} \quad (8)$$

$$\frac{Q_t}{Q_\infty} = K_{KP} \cdot t^n \quad (9)$$

Where, Qt is the amount of PA dissolved at time t, Q_0 is the initial amount of PA in the solution (assuming, Q_0 =0), Q_∞ is the amount of PA released after infinite time, K_0 is the zero-order model constant (concentration/time), K_H is the Higuchi model constant, K_{KP} is Korsmeyer-Peppas rate constant (compromising the structural and geometric characteristics of the PA formulation), and n is the diffusional exponent or drug release exponent which is indicative of the mechanism of drug release. Hence, the most affordable mathematical model was chosen by the comparison of the chi-square value.

3.1.5. Results and discussion

3.1.5.1. Chemical Characterization of the polymeric film

The chemical characterization of the prepared polymeric films was evaluated by means of FTIR measurements. For that, 1 ± 0.01 g of each compound involved was introduced in the machine cantilever, and then the spectra were obtained and analyzed. Moreover, the samples from the electropolymerization of PEDOT: PSS with PA and 2PA were compared with the spectra of PA alone to verify if paracetamol was doped into the PEDOT during the process. Therefore, in Figure 3 is clearly defined three different spectra, the one obtained from the PEDOT, the one obtained from the paracetamol and the other which has similar vibration peaks obtained from the PEDOT + PA indifferent from the amount of the drug added during the polymerization.

In this sense, PEDOT spectra is divided into two well appreciable parts. Thus, at the high frequency it is observed a vibrational peak at position 3326 cm^{-1} which indicates the

presence of N–H components. In the same part, there is observed another vibrational peak at peak position 3162.49 cm^{-1} which corresponds to the O-H groups [183]. In the second part of the spectra, it is observed a vibration peak at 1530 cm^{-1} attributed to the C=C asymmetric stretching vibrations. Then, it is observed a C-C and C=C stretches of the thiophene ring at peak position 1350 and 1275 cm^{-1} respectively.

Moreover, at the peak position of 830, 722, and 629 cm^{-1} belong to the thiophene ring structure (C−S−C) [180]. On the other hand, for the paracetamol, the spectra show three well-defined parts, at the high frequency it is observed a vibrational stretching at the position 3320 cm^{-1} which corresponds to the O-H group, and another vibrational stretching is observed at position 3055 cm^{-1} which corresponds to the C-H vibration. At the second part it can be distinguish three different bending and vibrational peaks, the first one at position 1656 cm^{-1} which correspond to the C=O vibration, and C=C stretching is observed at 1565 cm^{-1}, finally at peak 1440 cm^{-1} it can be observed a bending of the N-H amide. At the third part of the spectra, it is observed two adsorption peaks. The first one at position 837 cm^{-1} are assigned to the C-O stretching, and the second peak at 688 cm^{-1} it is assigned para-disubstituted aromatic ring [181,182].

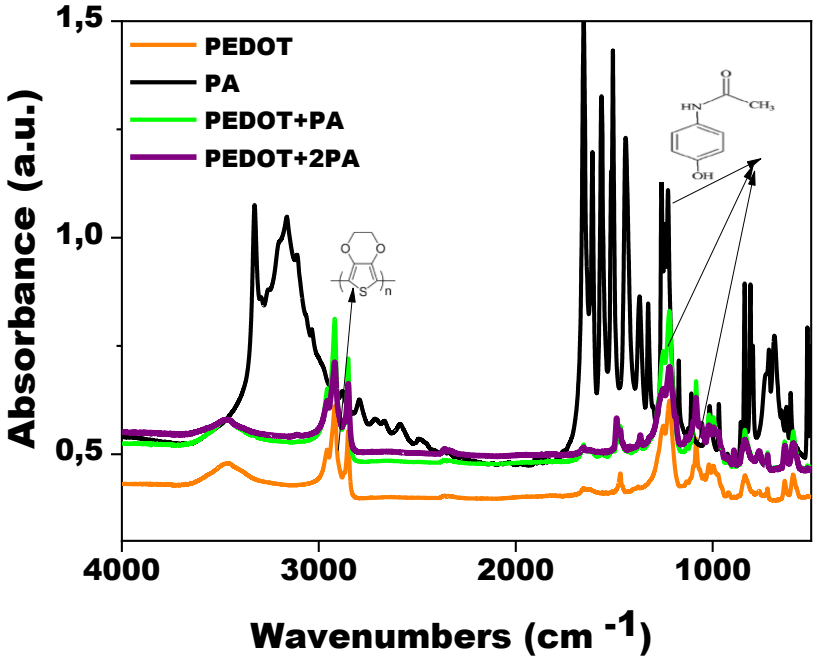

Figure 3. FTIR spectra of the PEDOT (orange), paracetamol (black), PEDOT + 1 mm paracetamol (green) and PEDOT + 2 mm paracetamol (purple).

Likewise, the PEDOT+PA and PEDOT+2PA spectrum shows the characteristic stretching, vibration, and bending peak of the combination of both detailed spectra (PEDOT, PA) in separate. The main differences that it can be observed between both spectra is that at the 2PA the peaks have more intensity in contrast with the PA, that confirms the effect of the doping of the PEDOT by the addition of the PA, and as much as PA is included, it is crosslinked with the PEDOT as it is going be described in detail in the next sections. As a first approach, it can be predicted that during the electropolymerization the PEDOT and the PA interact to form the polymeric film.

3.1.5.2. Morphological characterization

The morphological characteristics of the film are indispensable to achieving the desired film conductivity, surface coverage, and film uniformity (fewer pinholes). Therefore, the scan rate and concentration of PA influences the electropolymerized film surface and composition, using the SEM microscopy images and Energy Dispersive X-ray analysis (EDX) spectra. Thus, comparing Figures 4A and 4B, it is observed that for both scan rates, a flower-like morphology is extended all over the electrode surface. It is noted that when the scan rate increases, the presence of more flower-like structures appears because of the greater content of PEDOT on the electrode structure, which is demonstrated by the EDX spectra. When the scan rate is higher, there is more oxygen and sulfur content (see FS1A and FS1B).

The reported structure of the polymeric film has a similar flower-like structure to the ones reported by the authors (Cheng, Y.) [180], (Patra, et. al.) [184], and (Sangam, et. al.) [185], which prepared the PEDOT film under different conditions (different scan rate, addition of different NPs, etc.). Moreover, there is a clear variation in the morphological structure when the potential range is shifted for the electropolymerization, and at a range between -1 to 1 V, the morphological structure presented more porosity; thus, the spaces forming in the film can be filled by a doping agent [184]. Therefore, according to the purpose of the presented research, the chosen voltage range is appropriate, and the inclusion of the PA is viable because of the chance to occupy the present porous.

Moreover, the change in the PA concentration was studied by the pictures shown in Figures 4C and 4D. They reported a flower-like structure with some agglomerates randomly distributed into the electrode surface; these are caused by the PA doping during the electropolymerization process. Additionally, the appearance of the agglomerates is more notable when more PA is added to the monomer solution. Thus, it is evident that

the inclusion of the PA occurs, and the film can be cross-linked depending on the concentration of the drug. The observed distribution is probably due to an intermolecular structure based on π-π stacking interaction between PEDOT and PA leading to a porous surface, having advantageous properties from the perspective of biomedical applications.

When the EDX spectra between PA and 2 PA are compared, it is observed that the carbon content decreases and the O increases when more PA is added (see FS 1C and FS 1D). Thus, because of the presence of the PA, which in its structure has oxygen atoms, and lower presences of the PEDOT, which is replaced by the PA. These results are in accordance with the FTIR measurements. Moreover, all the membrane films presented a high porosity that would be favorable for improving the active sites at the electrode/electrolyte interface [184].

(A)

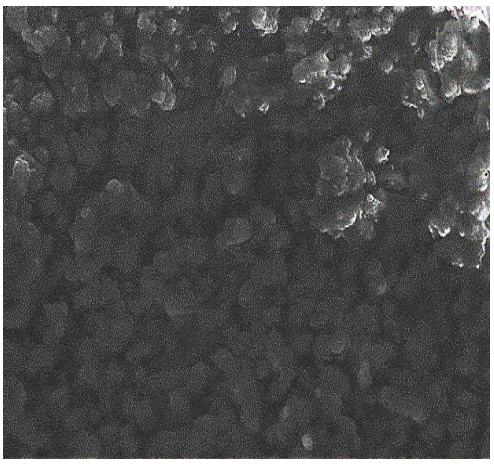

(B)

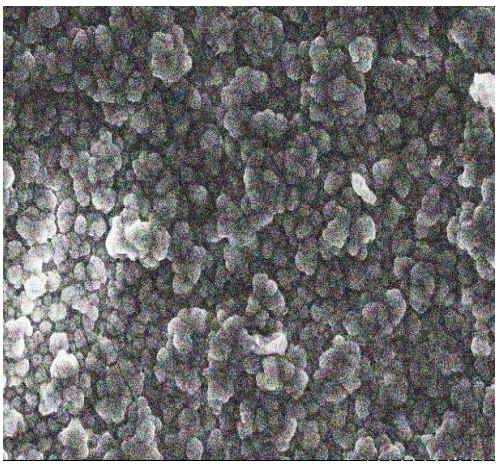

(C)

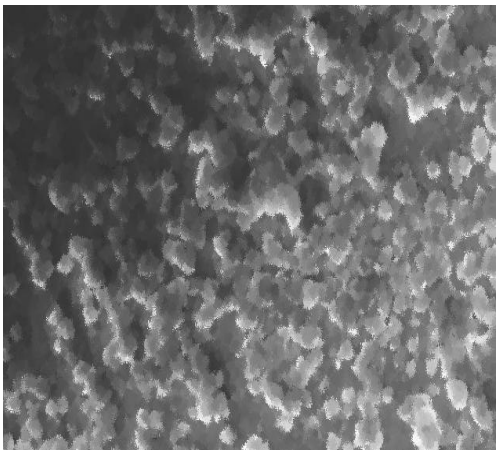

(D)

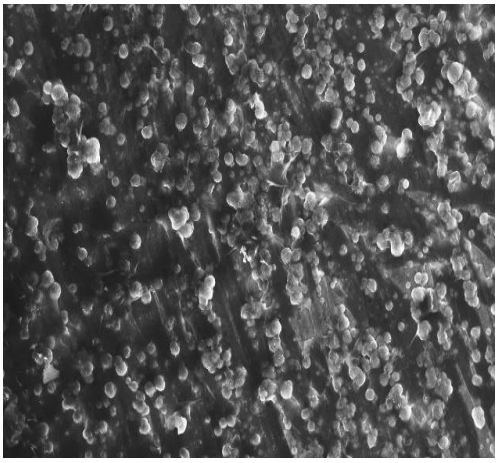

Figure 4. SEM imagines of PEDOT/Ti prepared at 5 $mV \cdot s^{-1}$ (A), PEDOT/Ti prepared at 10 $mV \cdot s^{-1}$ (B), PEDOT+PA/Ti prepared at 5 $mV \cdot s^{-1}$ (C), and PEDOT+2PA/Ti prepared at 10 $mV \cdot s^{-1}$ (D) at a scale equal to 50 nm and magnification equal to 800x.

3.1.5.3. Drug Immobilization

The membrane was produced by taking advantage of the PEDOT characteristics. Thus, the production of them was performed by using a cyclic voltammetry technique, varying the potential from -1 to 1 V vs. Ag/AgCl/KCl_{sat}. This enables the electropolymerization of the EDOT in the presence of counterions and these counterions are integrated into the structure as the resulting PEDOT oligomers are oxidized [185].

After the oxidation, it is forming a positively charged polymer bond structure that is stabilized by the doping of anions from the reaction environment [186]. The first process is demonstrated at Figures 5A and 5B. Here, there is an observed oxidation peak that occurs at 0.6 V vs. Ag/AgCl/KCl_{sat}. The oxidation process is irreversible; as a result, there is no peak at the reverse scan.

Likewise, the rate of the oxidation process increases as the number of cycles increases, as shown by the increasing oxidation peak potential of each performed cycle. Thus, on the first cycle, this process is not observed at all, while in the 10th cycle, the peak oxidation peak at 0.6 V vs. Ag/AgCl, KCl_{sat} is visible. Furthermore, it is important to remark that the scan rate of the voltammetry seems to influence the electropolymerizing rate; thus, if it is compared to the 10th cycle at 5 and 10 $mV \cdot s^{-1}$, it can be noted that the oxidation peak increases. Thus, it is explained that the fact of the positively charged polymer chains is produced and stabilized faster when the rate of scan increases, ensuring a high rate of electropolymerization [186].

Moreover, the second process in film production, the doping and stabilization of the polymer, is reported at the Figures 5C and 5D. From here, the effect of the addition of different quantities of PA during the film production can be studied. As a primary approach it is established that the polymerisation/doping process occurs at positive potentials applied to the electrolyte solution containing monomer. Therefore, at this step occurs the noncovalent π-π stacking interactions between the aromatic moieties of PEDOT and PA [187]. The comparison between the addition of different levels of PA (0, 1, and 2 mM) demonstrated the doping of the PEDOT. This, when PA was not added to the formulation the current is very high, because the stabilization of the cations only

occurred by the presences of the Cl^- ions (presented in the $LiClO_4$). This is confirmed, by the considerable decrease in the current capacitance of the figures 5C and 5D.

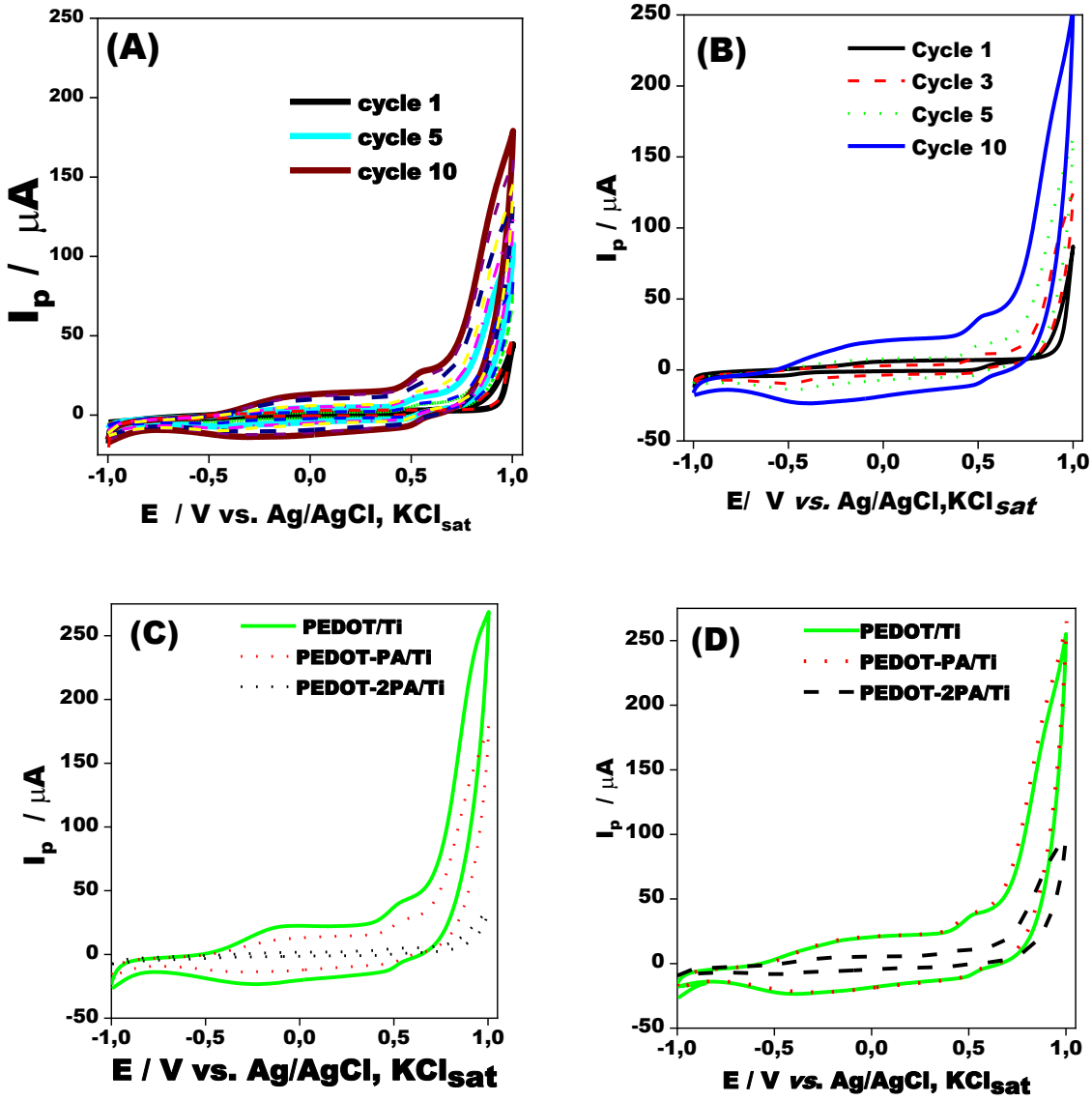

Figure 5. Film preparation by electropolymerization at 5 $mV{\cdot}s^{-1}$ (A) and 10 $mV{\cdot}s^{-1}$ (B). Comparison between the last CV cycle (10^{th}) at PEDOT-PA and PEDOT-2PA modified titanium electrodes (C, D). Experimental conditions: electrolyte, PEDOT, PEDOT-PA and PEDOT-2PA solutions; scan rate, 5 $mV{\cdot}s^{-1}$ (A, C) and 10 $mV{\cdot}s^{-1}$ (B, D); starting potential, -1 V vs. Ag/AgCl, KCl_{sat}; number of cycles, 1, 3, 5, 10.

The tendency of these decreasing is the following: 80.50 µC (Ti/PEDOT) > 50.20 µC (Ti/ PEDOT-PA) > 7 µC (Ti/PEDOT-2PA), and 79.30 µC (Ti/PEDOT) ≅80.20 µC (Ti/PEDOT-PA) > 23 µC (Ti/PEDOT-2PA), at 5 $mV{\cdot}s^{-1}$ and 10 $mV{\cdot}s^{-1}$ respectively.

Higher PA concentrations increase the likelihood of doping, which spatially favors the stabilization of cations [187].

The lower charge transfer capacitances are due to the formation of a bigger polymer film. This decrease is caused by two things: (a) the PA molecules are stable at experimental conditions (pKa value of the PA is 9.38), which lets them keep their biological effect; and (b) the PA molecules are much bigger than the PEDOT film, so they take up more space in the polymer matrix, which lowers the charge transfer [187]. On the other hand, the increase in the current values ($I_{p=}$ 20.10 μA at E = 0.14 V for PA and I_p = 11.81 μA at E = 0.14 V vs. Ag/AgCl, KCl_{sat} for the sample without the addition of PA) is an insight into the capacity of the PA to act as a doping agent, and it indicates that the PA is introduced in the matrix and the Cl^- ions are less preferred due to their size; therefore, these ions are not interact as co-dopant agent.

3.1.5.4. Electrochemical Impedances Spectra

Electrochemical impedance spectroscopy (EIS) provided information on the kinetics at the electrode/electrolyte interface without destroying the polymeric matrix, which is the foundation of this proposed method in contrast with other destructive techniques. Therefore, the behavior of the polymeric matrix was evaluated by means of EIS in different pH conditions to establish the best performance of this technique under the controlled conditions. Moreover, for each pH value (5, 6, and 7), the influence of the PA concentration on the electrochemical characteristics of the polymeric film. These results were correlated with the time in which it was carried out in the EIS to profile the release of the PA into the saliva solution. In this sense, EIS spectra were obtained every hour until 6 hours of experimentation were completed with a predetermined interval of 1 min between each measurement.

The EIS was presented as Nyquist plots. Thus, it was first necessary to compare the effect of the addition of PA to the polymeric matrix prepared at the same rate. In this sense, from figures 6A and 6B, there are notable differences between both spectra. Thus, when PA was added, the EIS spectra were represented by two well-distinguished parts, which are (a) higher frequency values, an arc that represents the charge transfer resistance against the interfacial process, and (b) a straight line (almost 90ºC) that appears, which represents the diffusion process from the matrix to the electrode. While, in the case of the addition of 2PA, the arc does not have a clear shape, and it is mixed with the diffusion process.

Therefore, when the components of the EIS were fitted with the equivalent circuit, the following ($R_{sol}(Q_{dl}(R_{ct}Q_{film}))$) equivalent circuit was obtained (this circuit was used for all the experiments in this section, see inset Figure 6A), which is composed of $R_{sol,}$ which stands for the solution resistance, Q_{dl} for the constant phase element involving an n exponent to represent C_{dl}, R_{ct} stands for the charge transfer resistance, and Q_{film} for a constant phase element at the low-frequency limits [188].

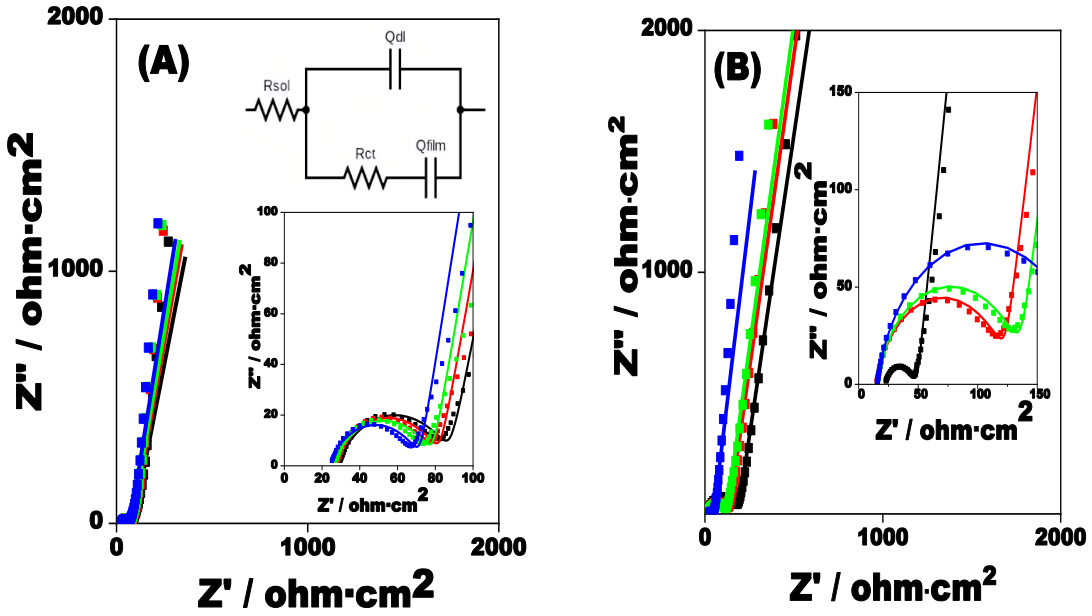

Figure 6. Nyquist diagram for Ti/PEDOT-PA (A) and Ti/PEDOT-2PA (B) composite modified electrode. Experimental conditions: scan rate of electropolymerization, 5 $mV{\cdot}s^{-1}$; test solution, artificial saliva pH 5; time of experiment, 0 h (■), 1 h (■), 3 h (■), 6 h (■)

Consequently, to have evidence in the influences of the scan rate and the PA concentration it was compared the charge transfer resistance (R_{ct}) because it gives information about the kinetic process into the polymeric matrix, while for the analysis of the PA release it was employed the R_{sol}, because it gives information about the electrode/electrolyte interaction.

Thus, the charge transfer resistances compared at the initial time (t= 0 min) when the film was produced at 5 $mV{\cdot}s^{-1}$ reported higher values when it was added lower concentration of PA (59.17 ± 2.30 $ohm{\cdot}cm^{-2}$ and 32.19 ± 0.47 $ohm{\cdot}cm^{-2}$ for the PEDOT-PA and PEDOT-2PA respectively) while after 6 hours the tendency did not change (47.87 ± 2.22 $ohm{\cdot}cm^{-2}$, and 27.82 ± 1.34 $ohm{\cdot}cm^{-2}$ for the PEDOT-PA and PEDOT-2PA respectively) as it is indicated in Table S1.

The change in charge transfer resistant from one to the other layer is in accordance with the CV reported in the upper section, thus, when there is more PA in the solution,

the electrode is less porous, that reduces the transfer of the charge as effect of the homogeneity of the electrode surface. While, when the polymeric matrix was polymerized at 10 $mV \cdot s^{-1}$ the increased charge resistances was keep for both the PEDOT-PA/Ti and PEDOT-2PA, reporting a charge transfer resistance equal to 35.28 ± 2.66 and 136.70 ± 2.36 $ohm \cdot cm^{-2}$ respectively at the time equal to 0, and values equal to 20.32 ± 2.26 $ohm \cdot cm^{-2}$, and 90.27 ± 3.01 $ohm \cdot cm^{-2}$ at time 6 h for the PEDOT-PA/Ti and PEDOT-2PA respectively.

From this, it can be observed that the charge transfer dismisses when there is more PA in the formulation indifferent of the scan rate and comparing both scan rate (5 and 10 $mV \cdot s^{-1}$); the charge transfer resistances decrease when the scan rate increases. Because, as the scan rate increases, the surface homogeneity also increases as it was observed in SEM imagens. Thus, if the surface is more homogenous the charge transfer interaction at electrode/electrolyte increases, so, the charge transfer resistances decrease [189]. As a first approximation, at saliva pH equal to 5, the R_{ct} decreases when the concentration and the scan rate increases. Moreover, the R_{ct} at this condition is reduced when the time passes.

When the pH of the saliva was adjusted to 6 the following results were observed:

- The same evaluation was carried out when the saliva has a pH equal to 6. Hence, first it was evaluated the effect of the scan rate over the charge transfer resistance when it was added the same amount of PA (1- or 2-mM PA). In this context, when it was added 1 mM of PA, the R_{ct} values at time equal to 0 were equal to 59.17 ± 2.30, and 35.28 ± 2.60 $ohm \cdot cm^{-2}$ produced at scan rate of 5 and 10 $mV \cdot s^{-1}$ respectively. The charge transfer resistances decrease until values equal to 47.87 ± 2.22, and 20.32 ± 2.26 $ohm \cdot cm^{-2}$ evaluating the samples evaluating after 6 hours (see Table S2).
- In addition, it was studied the effect of the concentration of the PA in the production of the polymeric film. For example, when the polymeric films were produced at scan rate equal to 5 $m \cdot V^{-1}$, it was evaluated the change in the R_{ct} when it was applied 1 or 2 mM of PA. In this context, at time 0 the R_{ct} values were equal to 59.17 ± 2.30, and 32.19 ± 0.47 $ohm \cdot cm^{-2}$ respectively. The same tendency was maintained when it was evaluated the R_{ct} at time equal to 360 min. The results obtained for the PEDOT-PA/Ti, and PEDOT-2PA/Ti were equal to 47.87 ± 2.22, and 27.82 ± 1.34 $ohm \cdot cm^{-2}$ respectively.

- The R_{ct} decreases as effect of the PA added and as effect of the scan rate of the electropolymerizing, this occurs in all the times when it was performed the EIS measurements. Thus, the resistances charge can be related with other parameters such as the capacitances of the double layer (Q_{dl}) which for the case of the PEDOT-PA/Ti produced at scan rate equal to 5 $mV \cdot s^{-1}$ was equal to 9.00 ± 1.00 $mS \cdot s^{n} \cdot cm^{-2}$, while when it was increased the scan rate (10 $mV \cdot s^{-1}$) was equal to 8.00 ± 1.13 $mS \cdot s^{n} \cdot cm^{-2}$, thus maintaining the same tendency with respect to the R_{ct} at all conditions tested when the pH of the saliva was equal to 5.
- The increased the scan rate and the decrease in the content of the PA, the polymeric membrane is more homogeneous. This is also confirmed by the change in n, and n_1 values (see Table S2) with obtained the highest value when it was evaluated the PEDOT-PA/Ti electropolymerized at 10 $mV \cdot s^{-1}$ reported values of n and n_1 equal to 0.94 and 0.90 respectively.
- In this context, when the process is faster, the initiated process is faster; thus, there are more cations available to be oxidized, and these produce an even distribution of them on the Ti surface. While, in the case of a larger quantity of PEDOT+PA/Ti, it tends to form agglomerates randomly distributed in the polymeric surface, thus decreasing the homogeneity of the film, and because of the non-conductive characteristics of the PA, they are not interacted with in the electrode/electrolyte process. As a result, the resistances increase while the capacitances decrease [187].

When the pH of the saliva was adjusted to 7 the following results were observed:

- It was evaluated first how the speed in the scan rate changes the characteristics of the membrane. It was compared to the PEDOT+PA/Ti membranes produced at different scan rates (5 and 10 $mV \cdot s^{-1}$), and the parameter that denotes the change is the R_{ct}. Consequently, the values of the R_{ct} evaluated at time 0 were equal to 108.20 ± 0.38 and 9.87 ± 0.69 $ohm \cdot cm^{-2}$, respectively. These values decreased to 96.03 ± 3.22 and 8.72 ± 0.70 $ohm \cdot cm^{-2}$, respectively, when the EIS was performed at 360 minutes (further results in Table S3).
- The resistances against the charge transfer are clearly influenced by the scan rate of the preparation of the polymeric film. Moreover, when it was evaluated the effect of the concentration of the PA in the polymeric film, it was obtained

R_{ct} (at time equal to 0) values equal to 108.20 ± 0.38 ohm·cm^{-2}, and 32.30 ± 0.28 ohm·cm^{-2} at the PEDOT-PA/Ti, and PEDOT-2PA/Ti produced at scan rate of 5 mV·s^{-1} respectively. The R_{ct} maintained the same decreased tendency as a function of time, hence, at time 360 the R_{ct} was equal to 96.03 ± 3.22 ohm·cm^{-2}, and 8.72 ± 0.70 ohm·cm^{-2}. This behavior was obtained in all the studied pH. It is explained by the fact of the similarity of the produced film. Thus, at the electrode/electrolyte interface the controlled process is determined by the characteristics of the DDS and the pH of the solution is not widely affecting because the structure of the membrane remain constant [190].

- On the other hand, the change in Q_{dl} went in the opposite direction, except for Ti/PEDOT-2PA. This phenomenon means that the capacitances of the double layer go up when more PA is added to the polymeric matrix. For example, when it was evaluated, this parameter at time equal to zero obtained values equal to 5.16×10^{-2} ± 0.02 mS·s^{n}·cm^{-2} and 0.15 ± 0.22 mS·s^{n}·cm^{-2} when it was produced at 5 mV·s^{-1} in the PEDOT-PA/Ti and PEDOT-2PA/Ti polymeric films, respectively. However, the tendency was not kept in the time, as it is shown analyzing the Q_{dl} after 360 minutes of the analysis, the results were equal to 15.10 ± 0.21 mS·s^{n} ·cm^{-2}, and 0.17 ± 0.21 mS·s^{n} ·cm^{-2} when it was analyzed the PEDOT-PA/Ti and PEDOT-2PA/Ti produced at 5 mV. Hence, for this case the EIS behavior of the prepared membrane at pH 7 is not well stablished, this can be due to the protonation state of the PA, as a consequence of the proximity of the neutrality of the medium, the PA is not protonated (pK_a = 9.70), thus it is not interfering directly in the process, but, the great change in the R_{ct} indicates that a part of the PA agglomerates creates a resistance to transfer of the electrons. Figure 7A, 7B, and 7C summarized the interaction between the scan rate in CV, the concentration of the PA, and the time as effect of the pH of the saliva solution.

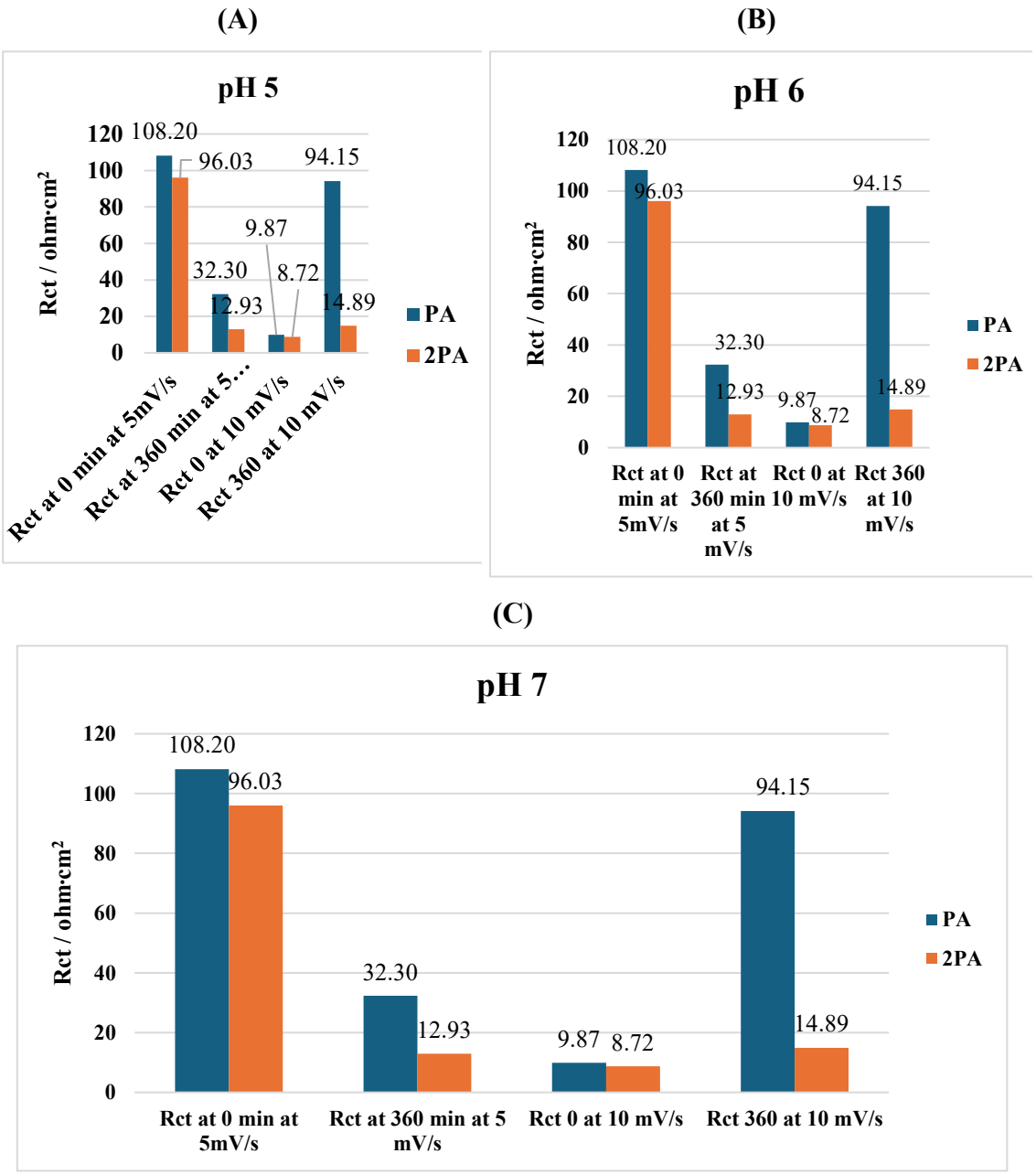

Figure 7. Interaction between the scan rate in CV, the concentration of the PA, and the time as effect of the pH of the saliva solution

Overall, from the reported results, it can be established that the values of the scan rate and the concentration of the PA influence the electrochemical characteristics of the prepared films, as obtained from the chemical and morphological characterizations. Therefore, for the EIS characterization of the PEDOT at different conditions, it can be assumed that the film thickness is the key parameter that controls the kinetic characteristics of the double layer and the electrode/electrolyte interface. Thus, the decrease in the thickness of the film decreases considerably the diffusion coefficient,

causing an increase in the impedance module as effect of the slower move of the electrons and increases the electron transport [191].

In this sense, it can be explained that when a conductive polymer is investigated using the EIS, the redox sites remain at the polymeric membrane layer, and the charge is propagated from the electrode/electrolyte by creating an electron holes and by the diffusion of the free-moving ions (in the present case the ions of the PA indifferent of the pH of the solution); therefore, some electrons can cross the polymeric-metal structure and other electrons can be incorporated into the polymeric structure [192].

The shape of the Nyquist plot, as interpreted by the equivalent circuit, demonstrates the electron hopping and diffusion. The Nyquist plot exhibits an "ideal response" distinct from the Randles circuit behavior at high frequencies, suggesting that at an intermediate frequency, the system functions solely as a capacitor, thanks to the redox capacitances present at low frequencies. While it can be observed, the dispersion of the high-frequency capacitance is attributed to the microscopic roughness of the electrode surface [192,193].

Furthermore, homogeneity plays a fundamental role in controlling the kinetics in the interface; thus, at low frequencies, the capacitive behavior depends on the homogeneity of the polymeric surface, in which the dopants and the counterions are binding to different sites depending on the energy [194]. So, the scan rate is the dominant parameter in the case of the roughness of the polymeric matrices because of its ability to control the rate at which the oxidation of the PEDOT occurs. This effect is observed as an example of the highest value of n being reported at the PEDOT produced at 10 $mV \cdot s^{-1}$, which is between 0.90 and 0.95. Also, this phenomenon was observed at the SEM imagens. When the electropolymerization rate increases the surface was more homogenous (see Figure 4) and the polymeric membrane covered better the Ti-6V-4Al surface, thus the charge transfer resistance is decrease because there is more polymer which in nature is conductive.

The Nyquist plots tend to stay in the shape of a half-circle process at high frequencies and diffusion at low frequencies. This shows that pH doesn't have a big effect on how the polymeric matrices behave. This means that the prepared polymeric matrix is a good approximation for a drug delivery system.

This approximation is positive for the preparation of the DDS because the saliva of the patients varies according to different conditions, such as habits, diet, etc., so the obtained results give a good approximation of the behavior of the polymeric matrix, as it will be demonstrated in the following section.

3.1.5.5. Drug releases studies

The EIS technique enables understanding the interaction between the electrode surface and the electrolyte; thus, it is a primordial approach to establishing a system that evaluates the drug release profile of the PA in the saliva solution. To find out how this parameter can be linked to the concentration of PA, the main method was to look at how it changed over 6 hours in different specimens that had different amounts of PA and were tested in artificial saliva at different pH values.

Therefore, the values of the R_s collected at different times were evaluated at pH values of 5, 6, and 7 (see Table TS4). The solution resistances reported two different conducts in relation to the time. Hence, it is observed that a primary linear decrease during the 200 minutes and another linear decrease was reported at time < 200 for all the pH and the film matrices evaluated.

The relation between the R_s and the concentration of PA is understood by the evaluation of the strong interaction of the dissolved PA with the components of the saliva solution. In this sense, it can be understood that when the dc-current or voltage inputs are applied to the system, the double layer is charged as an effect of the movement of the PA ions from the matrix to the interfaces as a result of the increase of the available electron in the electrolyte, which creates more holes in the system [192].

Therefore, the PA charge ions generate a strong interaction with the electrolyte, from which the first values of the R_s can be extracted; however, when the times of the analysis pass, the interactions begin to reduce as a result of the competition of the holes on the matrices to catch the PA ions to return to the steady state, and at this point the R_s decreases [192]. Hence, at time equal to 200 min, it can be observed that this process does not report a linear behavior because of the leakage of the spaces in the polymeric matrices, which need to return to their initial condition, and it catches the available PA in the electrolyte; thus, the solution resistances decrease abruptly [187].

However, when the PEDOT returns to its initial state, the process is repeated, and again, there is reported a linear decrease of the R_s as an effect of the release of the PA and the increase in the electron interaction between the saliva and the PA. This is maintained until the finalization of the voltage or current input, and the system returns to its initial state.

The above process is confirmed by comparing the obtained results with a DPV analysis. It was executed by the construction of an electrochemical detector for PA by using a BDD working electrode without any modification. The determination of the PA

concentration in the saliva was executed at different times, as in the case of the EIS (the time range was from 0 to 150 minutes), this is reported in Figure 8. As the release profile has an equal tendency for all the prepared matrices exposed to all the pH values, it was chosen as an example of the release process, the PEDOT-2PA/Ti polymeric matrix prepared at 5 $mV \cdot s^{-1}$.

Therefore, Figure 8A shows the PA release into the saliva. It can be observed that the release again shows that until 200 minutes the release keeps a liner tendency (Figure 8B), then from 120 to 130, the process is altered from the linearity, and the tendency becomes linear again until the final time of analysis. Moreover, it was evaluated the analytical parameters in the determination of the PA of the prepared electrode (Figure 8C). Hence, the calibration curve was performed within a linear concentration range equal to 0.20 – 2.20 µM, following the equation:

$I/A = (3.86 \times 10^{8} \pm 2.53 \times 10^{9}) + (0.05 \pm 1.95 \times 10^{-3})\ [PA]/M$ (9), R = 0.9914, n = 12 points.

From the linear equation it was calculated the limit of detection which was equal to 0.16×10^{-6} M (0.02 $\mu g \cdot ml^{-1}$) as it is reported at Figure 8D.

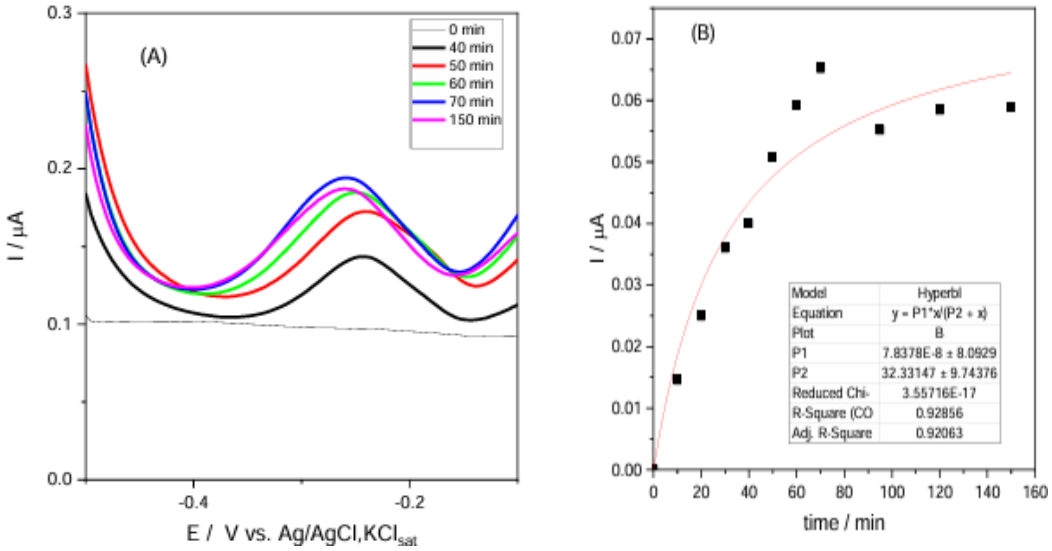

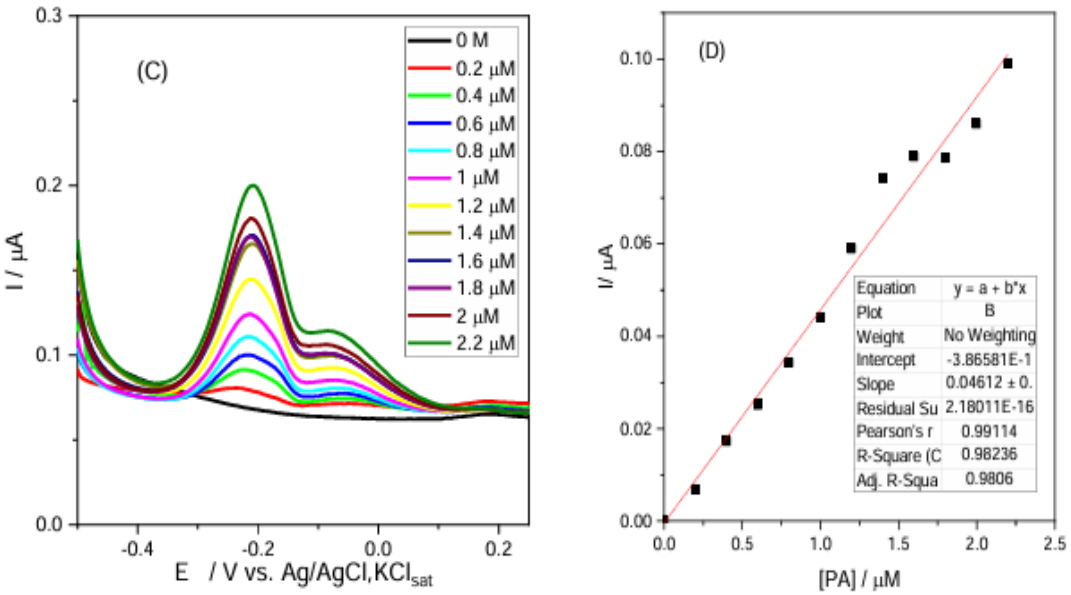

Figure 8. Differential Pulse voltammograms at bare Boro Dopped Diamond (BDD) electrode in the presence of Ti/PEDOT-2PA and artificial saliva (pH 6) recorded at different periods of time (A) and the corresponding release profile (B). DPV at bare BDD electrode in artificial saliva (pH 6) (C) and the corresponding calibration curve (D).
Source: [195]

According to the results obtained with the prepared BBD electrode are comparable with the decreased tendency of the R_s as function of time obtained by EIS technique, therefore, it is necessary to stablish the release profile of the drug into the saliva, to understand the process which is occurring in the inner part of the polymeric matrix.

In this context, it was analyzed the drug profile of the PA at different pH values by correlation the R_s changes over 6 hours. From these values, zero – order, Higuchi and Korsmeyer–Peppas (see equation of the models at section 3.1.4.6) were built. Hence, the mathematical models explained enables to explain the proportionality between the R_{sol} and the ionic strength of the solution.

To find the best mathematical model, the adj-R^2 statistical parameter was compared, which is a common way to do this when models with different numbers of parameters are for comparison. Hence, the drug release profiles were established for all the prepared polymeric matrices (PEDOT/PA and PEDOT/2PA prepared at 5 or 10 $m \cdot V^{-1}$). The profiles were divided into two sections (before and after 200 min), because of the complexity in explaining the interaction between the saliva solution and the PA, and the complexity of the interaction of the PA and the PEDOT.

The division was proper to see only both linear processes, and to evaluate the drug release process in small time intervals, without the necessity to study the whole releases process, which is difficult to describe with a linear mathematical model. Thus, the results of the slopes and adj-R^2 are reported in Tables TS4, TS5, and TS6 for the pH values equal to 5, 6, and 7, respectively.

Therefore, comparing the adj-R^2 for all the mathematical models, it can be observed that for times before of 200 minutes, the zero-order linear method describes better the releases profile for all the analyses matrices. The adj-R^2 achieves values between 0.9551 to 0.9987 (representing a good linear approximation) when it was evaluated all the pH ranges of the polymeric materials, these values were superior in comparison to the adj-R^2 obtained when the R_s values were adjusted to the Higuchi and the Korsmeyer–Peppas mathematical models.

The obtained results were the same when the studied time was > 200 min (see Tables TS4, TS5, and TS6), so the zero-order model also was the one that reported the highest values of adj-R^2, which vary from 0.9551 to 0.9954 regardless of the concentration of PA and the scan rate. The mathematical models which describe the release profile of PA before and after 200 minutes are reported in Figure 9. The approximation to obtain these results is that the PA is released by a diffusion-controlled process in the saliva solution. Moreover, for all the releases experiments, the adj-R^2 values were lower when it was applied the Korsmeyer – Peppas model in contrast with the values obtained with the zero-order model; it is because the matrix in contact with saliva does not accomplish the conditions of this mathematical model, hence, $Qt/Q\infty < 0.60$ can not be reached by the system [196].

In this context, the diffusion-controlled process can be observed in the low frequency region at the Nyquist plot; thus, the straight line tends to increase as the time of the experiments pass for all the pH studied values. Moreover, this process is clearly observed at the pH 5 when the polymer matrix has 1 mM of PA prepared a 5 $mV \cdot s^{-1}$ (see Figure S4) and this is correlated with the differences in the morphology characteristics obtained in the SEM imagens (see Figure 4A and 4B).

Therefore, the straight line in the Nyquist plots tend to move to the positive site as the time passes, showing that the release of the PA is controlled by the diffusion of it on the double layer interface as effect the existence of acidic organic groups inside the coating matrix establishes a persistent acidic microenvironment within the composite film, regardless of the external pH level. Consequently, in an acidic microenvironment, the

solubility of a basic PA (pKa of 9.38), will be increased, resulting in a more rapid and typically complete release of the drug from the matrix [197].

Consequently, the main insights that it can be observed from the release of the PA in the saliva are: (a) the pH does not affect significative to the release profile of the PA in the saliva, thus at every pH values, the tendency is that the process is controlled-diffusion which is notorious at the increase in the straight line values of the lower-frequency portion of the Nyquist plot, (b) the scan rate for the production of the polymeric matrix, also does not represent a determinant step in the release of the process, thus it cannot be observed any differences in the profiles when the polymer was prepared at 5 or 10 $mV \cdot s^{-1}$; (c) the PA concentration also does not show a significant influence on the release profile of the PA, thus the R_s of the solution is affected by the release of the drug, however it is a controlled process, so the major content of the PA in the polymer matrix is not expected to increase the ionic strength of the solution, because the process is kinetic controlled; and (d) the R_s can be correlated with the concentration of the PA in the solution as it is demonstrated by the concentration profile analysis performed by means of DPV measurements.

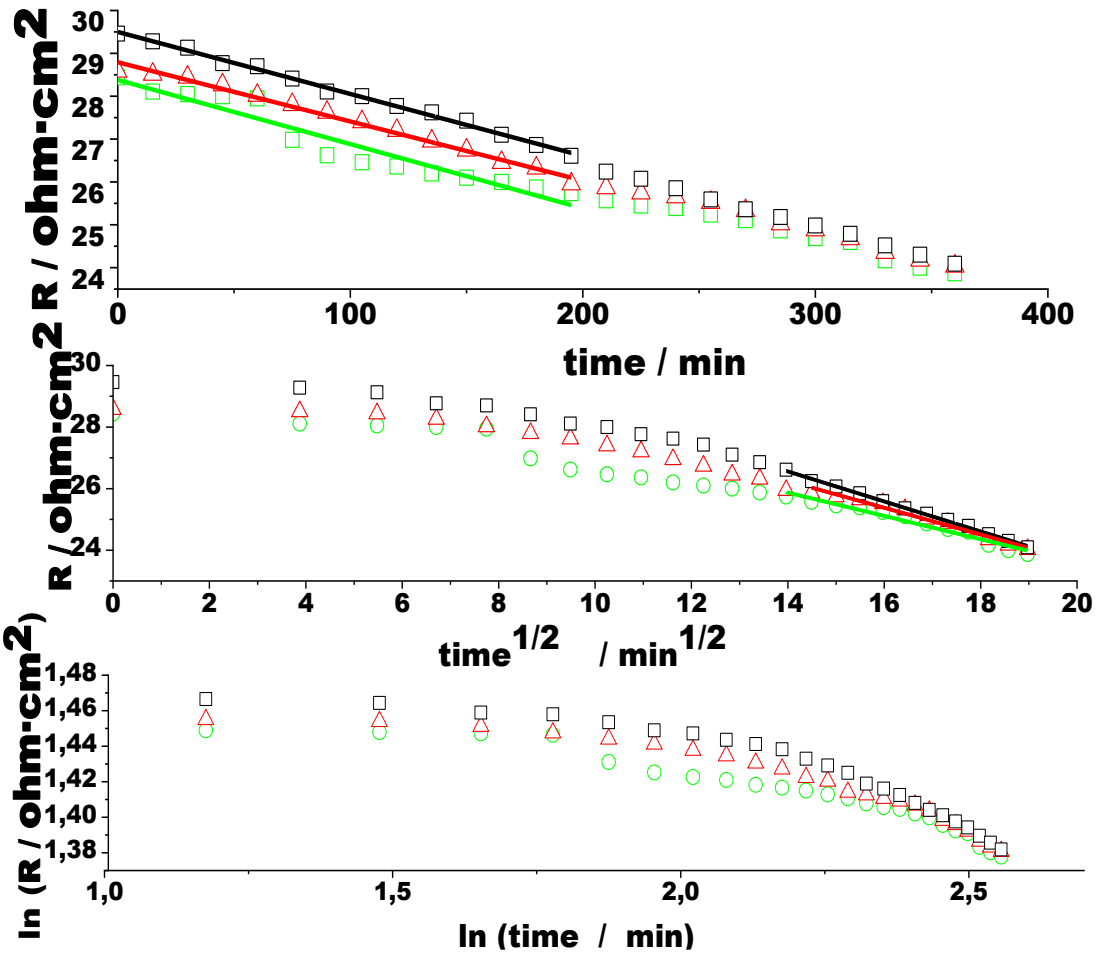

Figure 9. Mathematical models for the description of the release profile of PA from PA-PEDOT/Ti (v = 5 $mV \cdot s^{-1}$) membrane film, following zero-order model (A), Higuchi model (B), and Korsmeyer–Peppas (C). Experimental conditions: EIS spectra recorded in artificial saliva of pH 5 (□, black), 6 (△, red), and 7 (□, green), for 0-6 hours.

3.1.6. Partial Conclusions

A novel methodology was built to analyze the drug release profile of paracetamol in saliva by applying a non-destructive electrochemical impedance spectroscopy methodology based on the analysis of the decrease of the resistance of the solution as a function of time. Therefore, it was necessary to build the matrix in which the PA was loaded. This outcome was achieved by the electropolymerization of the EDOT in situ with the PA over the Ti metallic plates. It was carried out by means of the cyclic voltammetry technique. Therefore, it was carried out by changing the potential from -1 to 1 vs. $Ag/AgCl/KCl_{sat}$ for 10 cycles. Hence, the effect of the cycle scan rate was studied by varying its value (5 or 10 $mV \cdot s^{-1}$), and the effect of the PA concentration (1 or 2 mM) were studied.

Thus, the inclusion of the PA on the polymeric matrix was confirmed by the analysis of the FTIR spectra of the films. In these, it was observed that the prepared films reported the typical vibrational peaks of both the PEDOT and the PA. Also, it was observed that when a larger quantity of PA was added, the spectrum vibrational peaks increased. Moreover, the influences of both variables (scan rate and PA content) on the properties of the polymeric matrix were analyzed by SEM images. They show the typical flower-like structure of the PEDOT, which was homogenously distributed on the metal surface, and when the PA was added, some agglomerate points appeared, located randomly in the polymeric structure. These points were more notorious when it included more concentration of PA in the monomer formulation.

After the characterization of the Ti/PEDOT-PA or Ti/PEDOT-2PA matrices, the drug release profile was studied by the application of EIS at different time slots. The first approximation was to build the equivalent circuit, which was the following combination: $(R_{sol}(Q_{dl}(R_{ct}Q_{film}))$, where the R_{sol} was correlated with the concentration of PA released into the saliva and compared with the concentration calculated using DPV in which it was used a BPP electrode as a sensing element. It was observed that the release profile also was divided into two linear regions which appears before and after 200 minutes. The results were comparable with the results obtained at the DPV concentration analysis. Therefore, these time slots were reported from all the polymeric matrices regardless of the pH value.

Moreover, from the R_{sol} values, three different mathematical models were built, which were zero-order, Higuchi, and Korsmeyer–Peppas. The selection of the most appropriate model was via the comparison of the adj-R^2. Thus, for all the matrices, the zero-order model described better the release of the PA into the saliva in both time slots (before and after 200 minutes), and the values of adj-R^2 were closer to 1 in comparison with the other two mathematical model. Therefore, all the results demonstrated that the release of the PA into the saliva occurred by diffusion control.

Overall, all the experiments and the characterization demonstrated that the prepared polymeric films have the potential to be used in therapeutic applications because the matrix can control the release of the PA in the saliva, reducing inflammatory pain and improving the patient's mood, emphasizing the efficiency of the treatment attached to the implant prostheses.

Furthermore, the EIS method has the potential to replace the UV-Vis method, which is currently the most used for this purpose. Because the EIS is a non-destructive technique

that is simple to handle and inexpensive. Consequently, this technique can give comprehensive details regarding material characteristics. The results obtained through the EIS method facilitate its successful application as an investigative methodology for conducting polymer-based delivery systems.

Likewise, with the new approach in building micro-potentiostats and wearable electrochemical devices, the proposed PEDOT-PA/Ti or PEDOT-2PA/Ti polymeric film can be incorporated together with the potentiostat into the dental implants. Thus, alternative biocompatible and appropriately designed films utilizing conducting polymers infused with antimicrobials and antibiotics warrant exploration to create carriers for the release of bioactive agents with beneficial uses in prosthetic or implant therapies.

In future work, it is necessary to perform wearable devices in which miniaturized potentiostat can be included. These devices should be able to perform EIS measurements continuously to measure the release of the drug into the human body. Moreover, it is also necessary to study if the results can be replicated into other human body fluids such as blood plasma, digestive fluids, to increase the uses of the DDS. Finally, it is necessary to study the interaction of the PEDOT with other drugs. This can increase the usability of the PEDOT into the construction of more advance's devices for example in the treatment of cancer.

3.2. Anticorrosive protection

3.2.1. Objective General

- To analyze different methodologies to produce highly effective corrosion protection elements in metallic electrodes exposed to corrosive environments.

3.2.2. Specific Objectives

- To produce a polymer coating composed of poly(methyl methacrylate)–expired ibuprofen composite film to protect Ti–6Al–4V metal plates exposed to a saline environment.
- To produce different plant extracts from Ecuador that can be used to protect mild steel plates from rusting in a variety of corrosive environments.
- To analyze the functional groups that act as anticorrosive agents using chemical characterization of the components.
- To establish the effect of the corrosion on the loss of the metal characteristics employing mechanical and surface characterization.

- To investigate the accelerated corrosion through the study the principal variables obtained from the linear polarization, OCP, and EIS measurements.
- To explore the mechanism of interaction between the metal plate and the anticorrosive agent by studying the Tafel and thermodynamic plots.

3.2.3. Polymeric Coatings

3.2.3.1. Reagents

To produce the polymeric coating the following chemicals were used: poly(methyl methacrylate) (PMMA, $[CH_2C(CH_3)(CO_2CH_3)]_n$; average Mw ~ 350000 by GPC, from Sigma-Aldrich), tetrahydrofuran (THF, C_4H_8O, 99% purity, from Sigma-Aldrich), ibuprofen (IBU, $C_{13}H_{18}O_2$, from Sun Pharma, Cluj-Napoca, Romania, purity not reported). While, for the preparation of the saline solution it was used 3.50% of sodium chloride (NaCl, 99%, from Sigma-Aldrich) and distillated water. Moreover, to clean the electrodes it was used alumina powder of 300 µM (Al_2O_3, 99% purity, from Buher). The reported chemicals have analytical purity, and they were used as it were received from the supplier without the application of any purification process.

3.2.3.2. Equipment

To prepare the polymeric coating it was used an automated dip coating system (KSV NIMA Dip Coaters, BioLin Scientific, Sweden). Moreover, to analyze the mechanical characteristics of the samples it was used a universal testing device SHIMADZU AGS–X (model Shimadzu A65–C equipped with a sensor of 5000 N). Likewise, to analyze the chemical structure of the polymeric coating it was used a Nicolet 6700 FTIR Spectrometer.

Furthermore, the morphological characteristics of the prepared polymeric films were evaluated by two different methods. The first method was optical microscopy (OM) using a SU8230 optical microscope (Hitachi, Japan). While the second method was atomic force microscopy (AFM) investigations, they were performed with a JEOL Scanning Probe Microscope JSMP 4210 (Jeol, Akashima, Japan).

Also, the electrochemical characterization experiments were carried out by using a controlled AutoLab potentiostat (PGSTAT302N EcoChemie, Utrecht, Netherlands) operated by GPES 4.70 and FRA 2.10. Hence, a conventional three cell configuration (equipped with a working electrode of Ti–6Al–4V metallic plate electrode, an Ag/AgCl, KCl_{sat} reference electrode, and a platinum wire auxiliary electrode).

3.2.3.3. Methodology

The present research was divided into five parts which were (a) preparation of the polymeric film, (b) fixation of the polymeric film at the Ti–6Al–4V metal plates by deep coating technique, (c) chemical characterization of the polymeric film, (d) morphological and mechanical analysis of the Ti–6Al–4V metal plates after the exposition to the corrosive saline environment, (e) evaluation of the effectiveness of the polymeric film by using accelerated corrosion test such as open circuit potential measurements (OCP), linear polarization (LP), potentiodynamic polarization (PDP), and EIS measurements. The mentioned parts will be discussed in detail in the bellow sections.

3.2.3.3.1. Preparation of the polymer

It was prepared 100 mL of polymeric solution by adding to a beaker the following components: 1 M of PMMA – 0.3 M of THF, and x-M of IBU (where x was equal to 0.20, 0.40 and 1 mM depending on the experimental conditions). Then, the solution was stirred and heated to 30 ºC. The process remained until the solution was a viscous colorless liquid. Every solution was prepared in triplicate to ensure the reproducibility of the prepared coating.

It was chosen THF as a solvent due to its high affinity with the PMMA and the IBU. The affinity of the THF towards the PMMA was calculated by the application of the Hansen solubility parameter (HSP), thus the value of the dispersion forces, polar interactions, and H-bond formation obtained results above 90 for all these measurements, so the THF is a good solvent to prepare solutions of PMMA [110]. In the same way, THF is a good solvent for the IBU (solubility equal to 0.88 g/L [111]), thus this solvent is proper for the preparation of the PMMA-IBU polymeric solution.

3.2.3.3.2. Titanium plates preparation

Before the coating step, three Ti plate samples (Ti–6Al–4V) having 7 cm length, 5 cm width, and 1 mm thickness and a composition of C:0.01 %, Al:6.26 %, V:4.05 %, O: 0.16 %, N: 8×10^{-3} %, Fe: 0.20 %, Ti: 89.32 % were purchased from TSM (USA). Then, they were mechanically polished using sandpaper (2000 to 100 grit) containing alumina powder of 300 μm (from Buehler) until the plates presented a homogenous color and structure, thus, to avoid the passive layer formation, a characteristic process of the Ti electrodes, which can affect the measurements. Then, the metallic plates were immersed in an ultrasonic bath containing ethanol (95 %, from Sigma-Aldrich) for 5 min for each

cleaning step. After that, the plates were well rinsed with distilled water and dried at room temperature.

3.2.3.3.3. Preparation of the Ti- polymeric coating samples

The preparation of the coating was performed by using a deep coating machine (KSV NIMA Dip Coaters, BioLin Scientific, Sweden). Therefore, the clean Ti–6Al–4V electrodes were immersed at a constant speed, varying from 5, 10, and 15 $cm \cdot min^{-1}$, in a beaker which contains the 1 M of PMMA – 0.3 M of THF, and x-M of IBU solution at 30 ºC until it reaches the middle of the beaker (approximately 5 cm of the Ti plates were covered by the solution).

Then, the Ti plates remained in the solution for 1 minute. Subsequently, the plates were withdrawn for the polymeric sample at 3 $cm \cdot s^{-1}$ and stayed out of the solution for 3 minutes. The same procedure was repeated 5 times for each metallic plate. After all, the metallic coating plates were stored at room temperature for 24 hours. The chosen displacement speed was 5 $cm \cdot s^{-1}$ because at this speed the coating was homogenous, compact, and crack-free.

Finally, before testing the prepared coatings, 10 cm^2 of the metallic plates were isolated using a Teflon band. Therefore, this procedure was repeated for all the prepared metallic plates. Hence, in total, 9 metallic plates were prepared by the same procedure to repeat each formulation 3 times to ensure the reproducibility and reduce the experimental error of the proposed coating technology.

3.2.3.3.4. Chemical characterization of the polymeric film

The chemical characterization of the prepared polymeric films was carried out by using a Nicolet 6700 FTIR Spectrometer. Thus, the different polymeric films (1 M of PMMA – 0.30 M of THF, and x-M of IBU (where x was equal to 0.20, 0.40, and 1 mM) were prepared according with the section 3.2.3.3, then, the coating was grazed from the metallic surface and the obtained film was introduced into the cantilever of the FTIR machine and the experiment was performed.

3.2.3.3.5. Morphological and mechanical characterization

The morphology of the prepared electrodes was studied by optical and AFM microscopy techniques. The first one was carried out by employing a SU8230 optical microscope (Hitachi, Japan), thus the different coating metallic plates were introduced

into the cantilever of the microscopy and the surface of the electrode was investigated. While the second characterization was carried out by using a JEOL Scanning Probe Microscope JSMP 4210 (Jeol, Akashima, Japan).

The samples were also tested with NSC 15 hard cantilevers made by the MikroMasch Company in Sofia, Bulgaria. These have a resonant frequency of 325 kHz and a force constant of 40 N/m. Each sample underwent scanning over an area measuring 5 μm × 5 μm, with three distinct macroscopic zones being analyzed. The acquired topographic images underwent additional analysis using JEOL WinSPM 2.00 processing soft (Jeol, Akashima, Japan).

Bi- and tri-dimensional profiles were recorded, and surface roughness was evaluated by measuring the R_a and R_q parameters. R_a denotes the arithmetic average of the profile height, as defined by equation 10, while R_q represents the root mean square of the profile height, as outlined in equation 11 [106]. In Equations 10 and 11, the limits of integration are 0 and l_r, with the value 0 positioned outside the integral symbol [199].

$$R_a = \frac{1}{l_\tau}\int_0^{l_\tau} |z(x)|dx \quad (10)$$

$$R_q = \sqrt{\frac{1}{l_\tau}\int_0^{l_\tau} |z(x)^2|dx} \quad (11)$$

where l_r is the profile length and z is the height at x point.

A universal testing machine SHIMADZU AGS–X (model Shimadzu A65–C equipped with a 5000 N sensor) was also used to measure the coating's mechanical properties. Hence, three grazed polymeric films of each formulation (xIBU–PMMA (where x = 0, 0.20, 0.40, and 1 mM IBU) were cut into rectangles, then they were introduced into the clamps of the machine, and the experiments were carried out by using a speed of 5 mm per minute, and the machines stopped when the sample broke.

At the breaking point, the final length of the samples was measured, and from these values, the nominal stress (s, according to equation 12), and the nominal strain (e, according to equation 13) were calculated. Also, it was determined the thickness of the film by using an Elco–A456CN1S coating thickness gage connected to an Elcometer A456 (model T) instrument.

$$s = \frac{F}{A_o} \quad (12)$$

$$e = \frac{\Delta L}{L_o} \quad (13)$$

Where F is the tensile force (N), Ao is the cross-sectional area of the sample (m^2), L_0 is the initial gage length (mm), and ΔL is the change in gage length ($L - L_0$) (mm) [198].

3.2.3.3.6. Electrochemical characterization

Electrochemical characteristics of the samples were acquired by employing Linear polarization, potentiodynamic polarization and EIS measurements. The employed three cell configuration was described in section 3.2.3.2. Moreover, before each measurement an equilibrium time was stablished to achieve the steady-state OCP.

Thus, the linear polarization was measured in the Ti/PMMA-xIBU electrodes immersed in a 3.50 % saline solution. The measurements were carried out in an electrode potential range of ± 0.02 V vs. OCP at a scan rate of 0.50 mV/s. From them the inhibition efficiency was calculated by comparing the R_p obtained with and without (R_p^0) coating according to the equation 14 [198].

$$IER_P = \frac{R_p - {R_p}^0}{R_p} * 100 \quad (14)$$

The potentiodynamic polarization was measured in the PMMA-xIBU/ Ti–6Al–4V electrodes immersed in a 3.50 % saline solution. The measurements were carried out in an electrode potential range of ± 200 mV vs. OCP at a scan rate of 0.50 $mV \cdot s^{-1}$. These results were plotted as Tafel figures. From them, it was estimated the corrosion kinetic parameters such as corrosion potential (E_{corr}), corrosion current density (i_{corr}), anodic (b_a), and cathodic (b_c) Tafel slopes. The corrosion inhibition efficiency (IEp) was estimated using the following equation [200]:

$$IE_p = \frac{{i^o}_{corr} - i_{corr}}{{i^o}_{corr}} * 100 \quad (15)$$

where ${i^0}_{corr}$ and i_{corr} represents the corrosion current densities from the potentiodynamic polarization test in the absence and in the presence of ibuprofen in the coating film, respectively. Furthermore, EIS technique was executed at OCP in the frequency range of 10 mHz-10 kHz using an ac excitation signal of 5 mV amplitude. The results were obtained in form of Nyquist and Bode plots and the configuration of them was studied by comparing with an equivalent circuit obtained by using g ZSimp–Win

3.21 software. From this data, it was calculated the inhibition efficiency according to the following equation:

$$IER_{ct} = \frac{R_{ct} - R_{ct}^{0}}{R_{ct}} * 100 \quad (16)$$

where R^0_{ct} and R_{ct} represents the charge transfer resistant from the equivalent circuit simulation in the absence and in the presence of ibuprofen in the coating film, respectively.

In addition, all the tests were done at room temperature, and a new Ti–6Al–4V/xIBU–PMMA electrode that had been modified was used for each characterization technique test, and the results were compared with a polymeric coating which does not contain IBU labelled as Ti-6Al-4V/PMMA.

3.2.3.4. Results and discussion

3.2.3.4.1. Chemical characteristics

FTIR analysis allowed the interaction of the PMMA with the IBU to form the polymeric solution by analyzing the peak vibration of each prepared coating film. Thus, the results obtained were compared with the spectra of the PMMA and IBU to see if, after polymerization, the films reported the same features as the isolated compounds.

Consequently, the FTIR spectrum of PMMA, whether pure or mixed with varying amounts of IBU, displays characteristic peaks between 2800 and 3000 cm^{-1} due to methylene and methyl group vibrations (>CH_2 and –CH_3). A strong C=O stretching band appears at 1730 cm^{-1}. Additionally, vibrational modes from C–C–O bonds are observed at 1280 and 1247 cm^{-1}, while C–O–C bonds show peaks at 1193 and 1143 cm^{-1}. In the case of IBU, the FTIR spectrum reveals peaks at 2955, 1705, and 1231 cm^{-1}, which correspond to asymmetric –CH_3 stretching, C=O stretching, and C–O stretching, respectively (see Figure 10). Further, bands at 669 and 626 $cm^{-1}$are attributed to vibrations of the aromatic ring present in the ibuprofen structure.

All the characteristic peaks of IBU are also observed in the xIBU–PMMA mixture, confirming that IBU is incorporated within the composite matrix. Furthermore, in the xIBU–PMMA mixture, the increasing intensity of the carbonyl band at 1730 cm^{-1}, corresponding with higher IBU concentrations, demonstrates the successful integration of IBU into the PMMA polymer matrix coating [201].

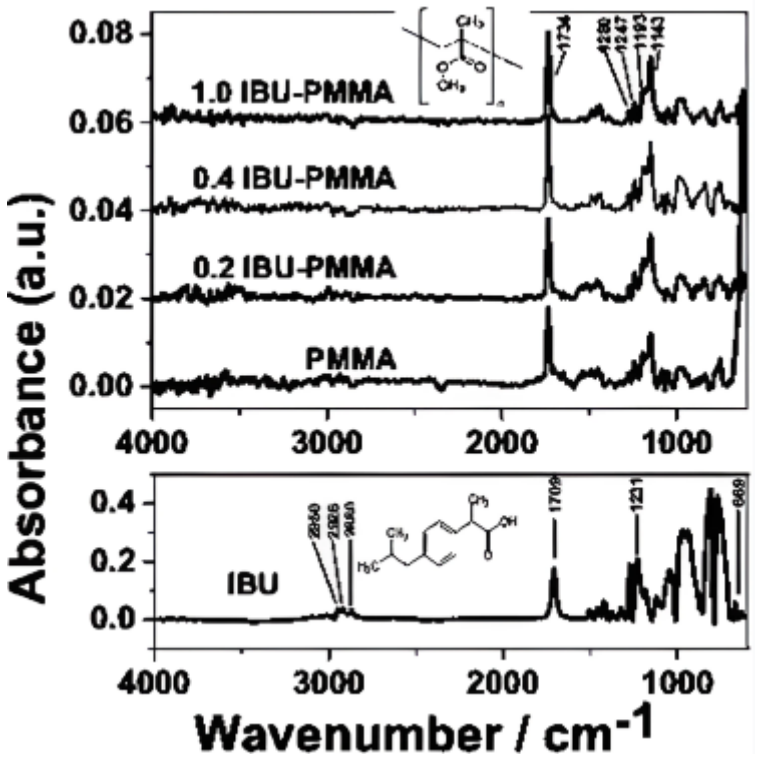

Figure 10. FTIR absorbance spectra recorded for ibuprofen, PMMA, and the mixtures 0.20 IBU−PMMA, 0.40 IBU−PMMA, and 1 IBU−PMMA
Source: [199]

3.2.3.4.2. Morphological and mechanical characterization

Microscopic images are fundamental to probing the effectiveness of a preparing coating in the inhibition of the corrosion because the images provide information about the thickness of the sample; thus, as the thickness increases, the resistance of the electron flow increases, and the corrosion reactions decrease [140]. Furthermore, the images provide information about the degree of coverage of the film above the metallic plates, which is fundamental to avoid free spaces where the corrosion process can be started and extended to all the metal surfaces.

Hence, in Figure 11A, it can be observed that the homogenous structure of the Ti–6Al–4V has some irregular grooves and height differences between peaks and valleys above all the surface because of the cleaning process. However, in Figures 11B, the elimination of the grooves and the formation of a homogenous structure above the film confirmed the adhesion of the polymer onto the metal surface.

In contrast, Figures 11C and 11D show a small group of particles clumped together in some areas of the metal structure. These particles are spread out randomly on the surface. These points appear because of the IBU presence, and as much as the IBU is added to the polymeric solution, there are more points fixed on the metal. Therefore, it can be deduced

that the good adhesion of the polymer to the metallic surface is because the surface looks homogenous, crack- and defect-free, and it covers all the studied surfaces, thus ensuring the good corrosion inhibition [108] that can be conferred using the PMMA-IBU film.

However, the optical pictures are not informative enough to inform about the film structure. In them, the thickness of the film or other micro- or nanoscale parameters cannot be observed, and they are important to see the effectiveness of the film to prevent corrosion; thus, the film was studied in more detail by employing an atomic force microscope (AFM) because it allows one to acquire information about the surface topography and roughness.

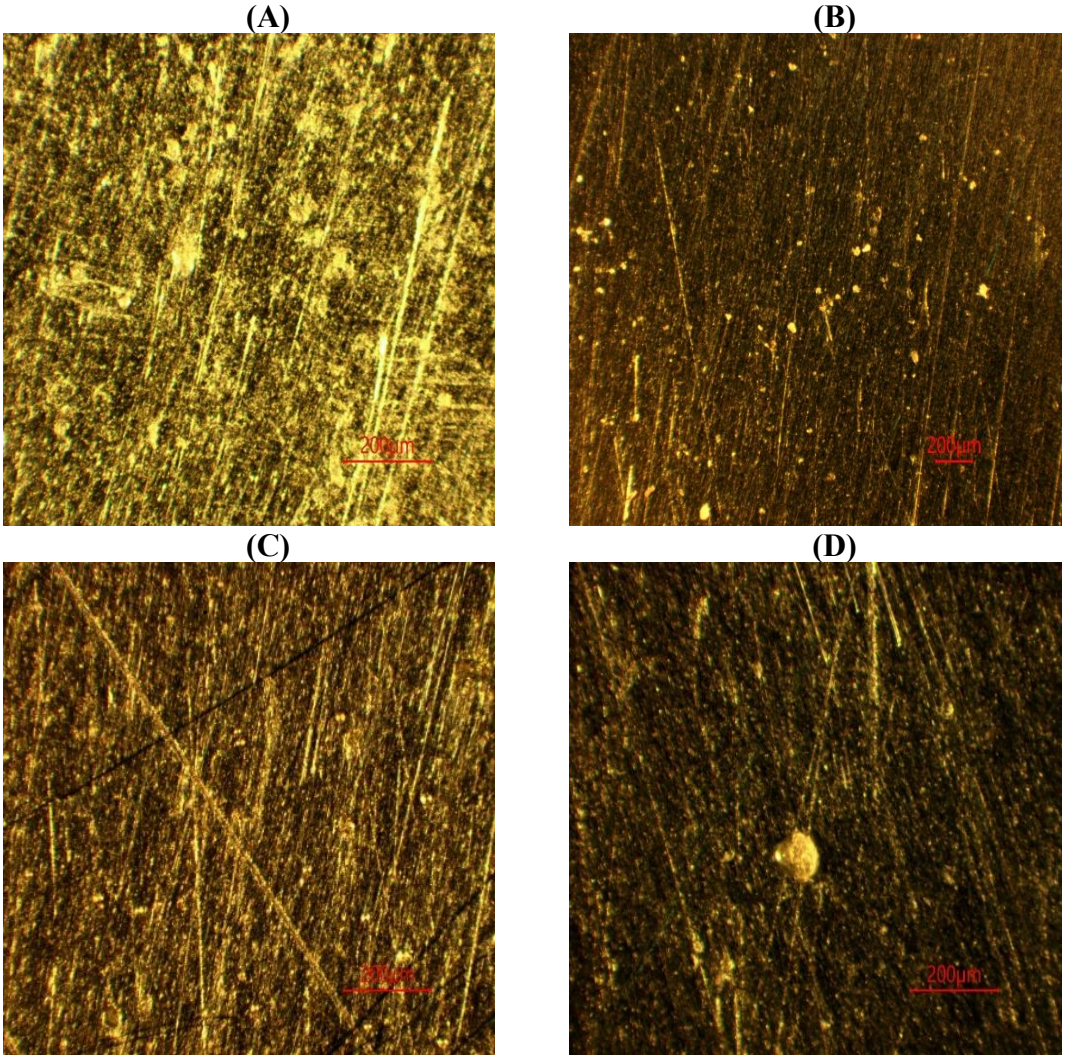

Figure 11. Optical microscopy images of the Ti–6Al–4V/ 0 IBU-PMMA (A), Ti–6Al–4V/0.20 IBU-PMMA (B), Ti–6Al–4V/0.40 IBU-PMMA (C) and Ti–6Al–4V/1 IBU-PMMA (D) coatings at scale equal to 200 µm and a magnification equal to 500x.

Source: [199]

Therefore, in Figure 12A, a relatively uniform and homogenous film formed under the Ti–6Al–4V plates for all the tested polymers can be observed. This film covers most of the metallic plate. Moreover, one can observe fine microstructural details that form during the solvent evaporation and drying of the polymeric films. Furthermore, several "windows" are presented in all the studied monolayers, including the outermost one; thus, it can be calculated that the monolayer film thickness can be calculated by the two-dimensional profile in Figure 12B.

Thus, from the monolayer film thickness, the thickness of the film can be calculated by multiplying with the number of monolayer films. Moreover, the three-dimensional profile reveals an island-like formation. This formation reveals that the PMMA is concentrated in a tumulus shape with a diameter of about 1 μm and local heights of about 161.33 ± 16.41 nm.

The effects of varying concentrations of ibuprofen incorporated into the PMMA structure are illustrated in the AFM images (Figure 12A, 12B, 12C, and 12D).

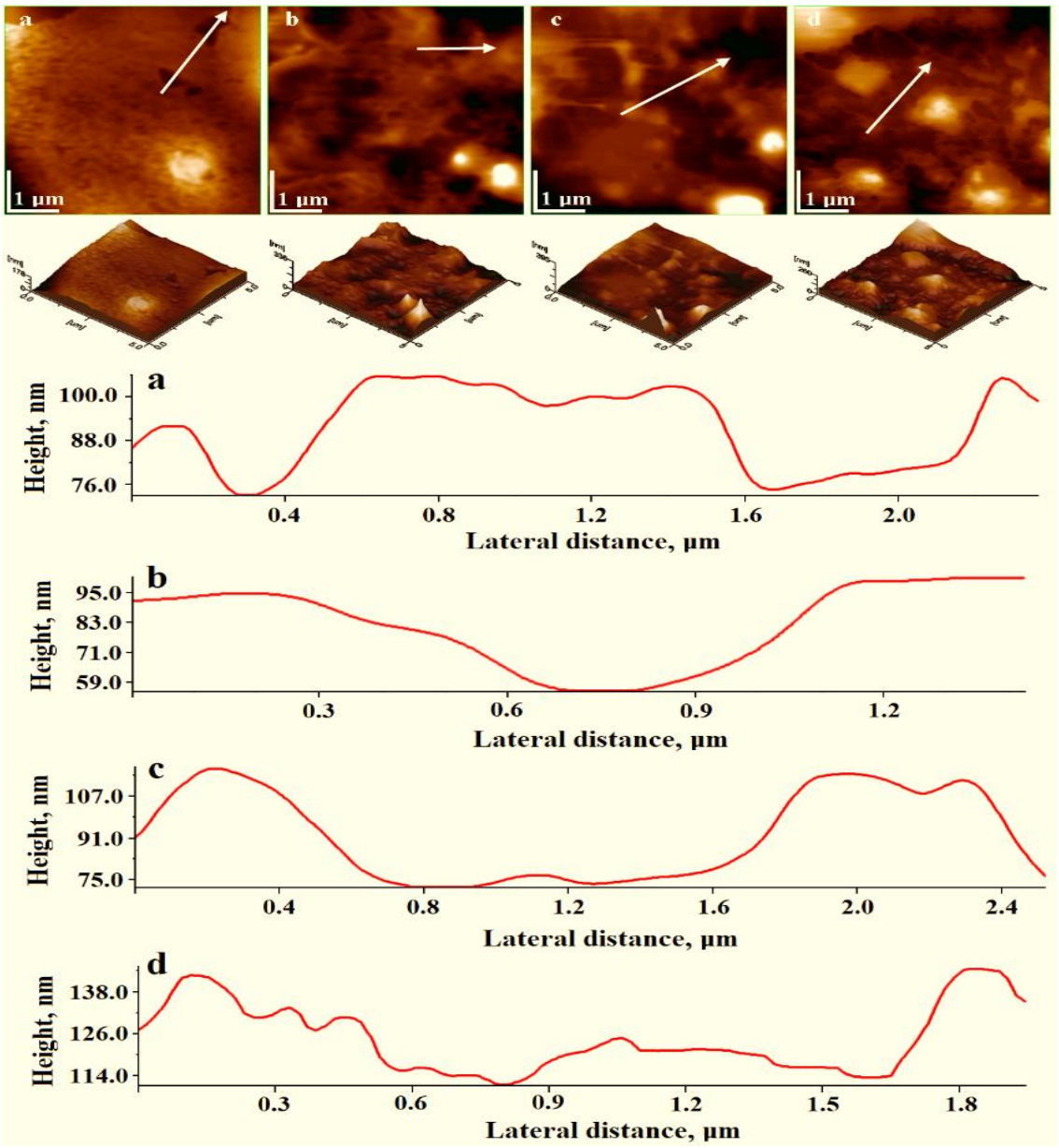

Figure 12. 2D (top panel) and 3D (bottom panel) topographical AFM images of tri-dimensional profiles and bi-dimensional profiles corresponding to the displayed white arrows for the Ti–6Al–4V/0 IBU-PMMA (a), Ti–6Al–4V/0.20 IBU-PMMA (b), Ti–6Al–4V/0.40 IBU-PMMA (c), Ti–6Al–4V/1 IBU-PMMA (d) dip–coated titanium alloys samples

Source: [199]

It is noticed that an increase in ibuprofen concentration inside the polymeric solution significantly alters the thickness and roughness of the polymer. Consequently, microstructural domains emerged during the formation of the IBU–PMMA network. This process generates surface imperfections and promotes the enlargement of tumulus dimensions, both in diameter and height, as seen by the incremental rise in ibuprofen concentration.

These changes are reported in Table 5; there, a clear tendency is reported. Thus, when the concentration of the IBU increases, the height of the film increases considerably, as do the R_s and R_q values. This indicates a successful crosslinking reaction between PMMA and IBU, allowing for an increase in film thickness.

Table 5. AFM estimated values for Ti–6Al–4V electrodes coating with PMMA + x IBU (where x is 0.20, 0.40, and 1)

Measurement	0 IBU–PMMA	0.2 IBU–PMMA	0.4 IBU–PMMA	1 IBU–PMMA
Height (nm)	161.33 ± 161.61	245.66 ± 51.68	378.00 ± 30.37	**326.66 ± 37.56**
R_a (nm)	11.41 ± 1.29	14.86 ± 2.25	22.96 ± 5.61	**26.03 ± 1.07**
R_q (nm)	15.06 ± 1.63	21.36 ± 3.46	33.23 ± 8.47	**36.27 ± 2.08**

Mean ± standard deviations of 3 measurements

Mechanical characteristics of the film are important when they are prepared to corrosion inhibition applications. Thus, they enable to understand what the real extent of the application is, and under which conditions the polymeric film can be applied without losing its performances. Thus, it is primordial to evaluate the force that the film can resist until it breaks, thus if the film is breaking the electron transfer is more favorable and the corrosion appears at certain points of the metal surface [60].

Under this premise, it was mandatory to evaluate the fracture stress and the fracture strain of the polymeric films. Therefore, Figure 13 evaluates the mechanical properties by applying a constant force to the samples. Thus, it is observed that all the samples behave in the same way. The samples exhibit the same behaviour as the thermoplastic PMMA.

So, when the load first starts, there is a linear deformation of the elastic part. This phase is followed by a deformation from the elastic to the plastic part, which is recorded at the highest stress resistances. If the load keeps going after this point, it breaks at a stress value (tensile strength) lower than the yield stress. When adding different levels of IBU, the strain-stress curves from the prepared polymer provide information about the changes in the mechanical properties.

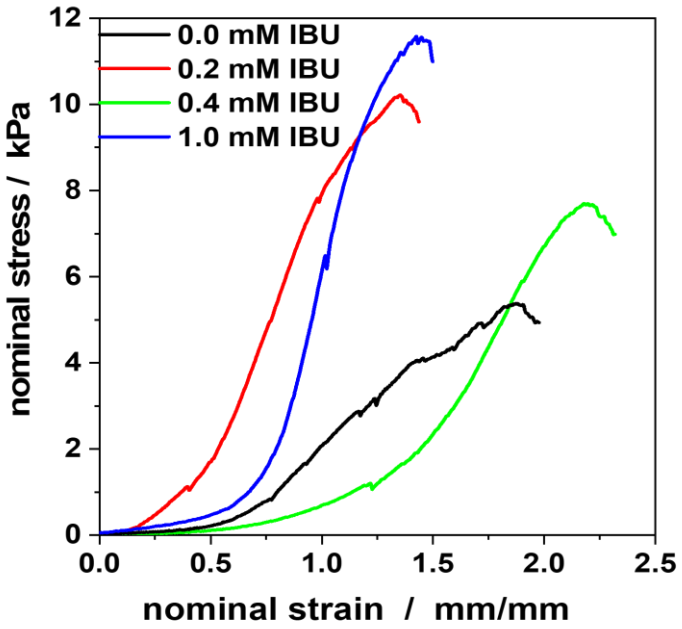

Figure 13. Stress-strain curves recorded at the polymeric films containing different concentrations of IBU (see inset)
Source: [106]

Therefore, Table S6 summarizes the results obtained in the fracture tensile test. It was found that the film made with 1 mM of IBU had the highest fracture stress, measuring 10.99 ± 0.01 kPa. On the other hand, the films that did not contain IBU had the highest fracture strain, measuring 1.98 ± 0.03 mm/mm. Moreover, the 1 IBU-PMMA polymeric films reported the highest Young's modulus, reporting values equal to 9.30 ± 0.12 kPa.

Furthermore, the film thickness was evaluated; thus, the highest film thickness was reported by the films prepared with 1 IBU, which reported values equal to 12.86 ± 1.14 µm. The trend in film thickness was as follows: 0 IBU–PMMA < 0.2 IBU–PMMA < 0.4 IBU–PMMA < 1 IBU–PMMA, thus confirming the calculated thickness reported by the AFM technique and proving the high level of interaction between the PMMA and the IBU during the polymerization.

Overall, the good performances in the mechanical test are indicative of a good level of interaction between the polymer and the IBU. This feat is due to the good control of the nucleation and grain growth processes, which both depend on the bulk concentration of the precursors. The more IBU that is added, the more resistant the polymeric film is to mechanical stress, which is a beneficial feature when the films are applied as corrosive coatings. However, this film has limitations as the Young's modulus is between 7 and 11 kPa; if the mechanical load goes beyond these limits, it could damage the polymer

coating, which becomes useless as an anticorrosion protective film from metallic plates that are exposed to high-stress loads.

3.2.3.4.3. Electrochemical characterization

The electrochemical techniques give information about the corrosion process and how efficient is the prepared polymer to be used as a coating agent over Ti–6Al–4V metal plates. Hence, the first approach was to measure the open circuit potential (OCP) to check the process between the electrolyte-electrode interface until reach the equilibrium state.

Therefore, it is observed in Figure 18-A that the OCP of the different prepared coatings follows the same tendency. Hence, until 250 seconds, the OCP of all samples increases, and then it remains constant until 3600 seconds. Thus, there is a notable reduction in the OCP as the concentration of the IBU increases, and the tendency follows the same patter: −258 mV vs. Ag/AgCl, KCl_{sat} (for Ti–6Al–4 V) < -202 mV vs. Ag/AgCl, KCl_{sat} (for 1 IBU–PMMA/Ti–6Al–4 V) < −180 mV vs. Ag/AgCl, KCl_{sat} (for 0.40 IBU–PMMA/Ti–6Al–4 V) < −16 mV vs. Ag/AgCl, KCl_{sat} (for 0.20 IBU–PMMA/Ti–6Al–4 V) < 9 mV vs. Ag/AgCl, KCl_{sat} (for 0 IBU–PMMA/Ti–6Al–4 V).

When more IBU is added to the polymeric matrix, the voltage drops, which shows that the cathodic protection is working. Moreover, the IBU tends to stop the cathodic reactions; this is understood by the adsorption of the IBU on the Ti–6Al–4 V [203], which enables it to be used in the preparation of inhibitors of corrosion. Therefore, the OCP does not establish a broad panorama of the mechanism of inhibition, so it is necessary to study the inhibition mechanism by the application of other electrochemical techniques, as will be covered in the next paragraph.

Potentiodynamic polarization (PDP) (anodic and cathodic Tafel) curves for Ti–6Al–4V with and without the coating were prepared by using 3.50 % NaCl as an electrolyte. The curves are presented as linear polarization resistance curves and Tafel curves, and several electrochemical parameters derived from the extrapolation of the linear segment of the Tafel curve were obtained to calculate the inhibition mechanism and the inhibition efficiency.

Therefore, as a first approximation, the Tafel curve shows a tendency in the potential to move into the cathodic range while the IBU concentration increases in the polymeric matrix. The current density of corrosion (i_{corr}), which significantly decreases as the IBU concentration increases, also reflects this tendency. Thus, the i_{corr} for the 1 IBU–PMMA/ Ti–6Al–4 V electrode is equal to $1.07\times10^{-8} \pm 0.06\times10^{-8}$ A/cm^2 which is almost 10 times

lower than the uncoated Ti–6Al–4 V electrode (i_{corr} = 9.79×10^{-8} ± 0.19×10^{-8} A/cm^2) and the tendency is represented by Ti–6Al–4 V electrode > 0 IBU–PMMA/ Ti–6Al–4 V > 0.20 IBU–PMMA/ Ti–6Al–4 V > 0.40 IBU–PMMA/ Ti–6Al–4 V > 1 IBU–PMMA/ Ti–6Al–4 V.

This tendency indicates that the polymer reduces apparition of free anions or cations because it limits the electrode/electrolyte interaction, thus reducing the corrosion rate [204]. Moreover, from the Tafel curve, the shift in the corrosion potential (E) can be noticed, which started from 10 ± 1.41×10^{-2} mV vs. Ag/AgCl when the polymer does not contain IBU; they tend to move to the left side as the concentration increases. So, it decreases from 9.50 ± 1.41×10^{-3} mV vs. Ag/AgCl, KCl_{sat} when IBU was not added to the polymer to -204 ± 2 mV vs. Ag/AgCl, KCl_{sat} when 1 mM of IBU was added to the polymer.

These results show that IBU is a cathodic type of inhibitor. This is because a compound is either an anodic or cathodic type [118] if the change in E_{corr} value between the inhibited solution and the uninhibited solution is greater than 85 mV (see Figure 14).

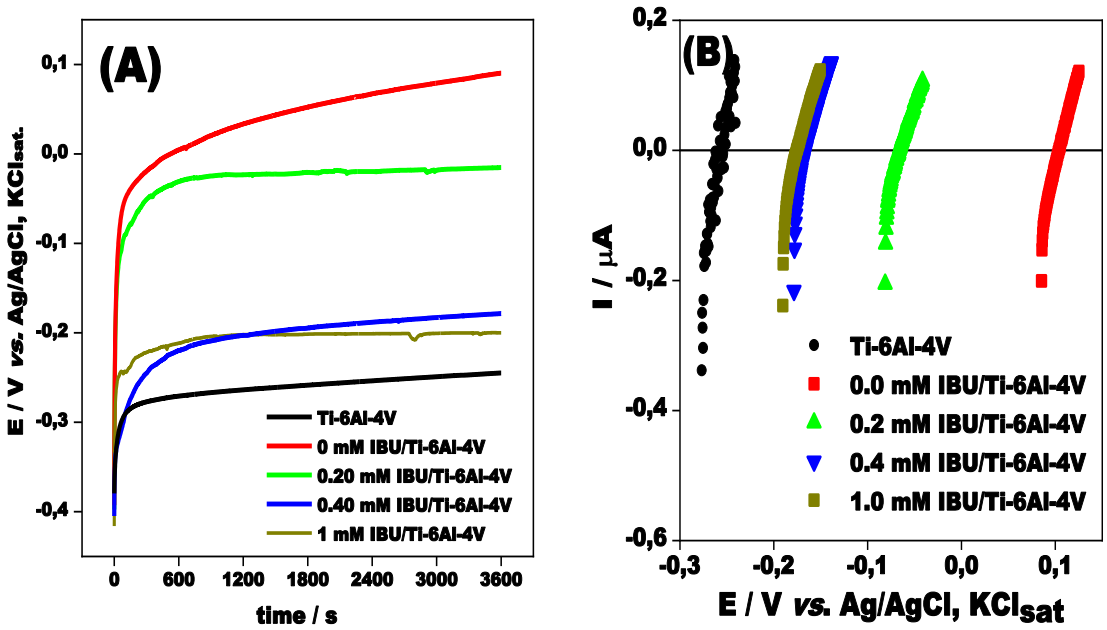

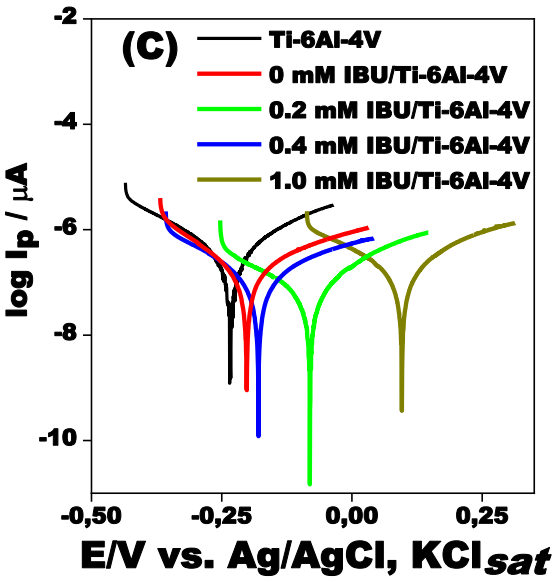

Figure 14. Open circuit potential (A), linear polarization resistance (B), and Tafel representation (C) recorded at the bare Ti 6Al–4 V (black) and coated Ti–6Al–4 V/x IBU− PMMA specimens, where x = 0 (red, ■), 0.20 mM (green, ▲), 0.40 mM (blue, ▼), and 1 mM (dark brown, ■) IBU. Experimental conditions: electrolyte, 3.50 % NaCl; scan rate, 0.50 mV/s; starting potential − 0.40 V vs. Ag/AgCl, KCl_{sat} (A), ± 20 mV vs. OCP (B), ± 200 mV vs. OCP (C).

Also, it was investigated whether the accelerated corrosion rate was investigated after one year of exposition of the sample to the corrosion solution. In this case, the 0.40 mM IBU–PMMA/Ti–6Al–4 V reported the lowest values for this measurement, with a corrosion rate equal to $2.41\times10^{-4} \pm 0.05\times10^{-4}$ mm/year, which was five times lower than the accelerated corrosion that can occur in the Ti–6Al–4 V without the coating which reported a corrosion rate equal to $1.20\times10^{-3} \pm 0.35\times10^{-5}$ mm/year.

The obtained data enable to calculate the efficiency of the corrosion protection when it was added the coating to the metallic samples. In this context, the highest corrosion inhibition efficiency calculated by the change in the i_{corr} was obtained when it was added 0.40 mM of IBU to the polymeric solution (69.02 % ± 0.76 %), while the lowest inhibition efficiency was reported when it was added 1 mM of IBU to the polymer (67.17 % ± 0.58 %) as it is reported at Table S8.

The reported results by the LP and the Tafel process does not report a detailed information about the coating/electrolyte interface, so, it was necessary to studied this by using EIS impedance, to obtained detailed data of the process and to stablish the

conclusions about the efficiency of the protection obtaining by the application of the PMMA – IBU coating.

In this context, the EIS results were plotted as Nyquist and Bode graphs (Figures 14A and 14B). The first step was determining the equivalent circuit, which was $R_s(Q_fR_f)(Q_{dl}R_{ct})$, and it was composed of two-time constants, a solution resistance (R_s), a charge transfer resistance (R_{ct}), film resistance (R_f), and two constant phase elements (Q_f and Q_{dl}). The proposed equivalent circuit was reported by the author Daia et al. (2022) [204] when analyzing the corrosion behavior of selective laser melted Ti-6Al-4V alloy in an NaCl solution. Also, bode plots (Figure S6B) indicate that the total |Z| impedance values at the lowest frequency of 0.01 Hz range from 889 to 1466.90 × 10^3 ohm·cm^2, regardless of the presence or absence of IBU in the polymeric coating. The slope of |Z| versus frequency dependencies in the 0.01–10 Hz range is approximately −0.6, decreasing slightly to −0.45 in the 10 – 10000 Hz range, regardless of the presence or absence of IBU. The same behavior is noted for the phase angle, which exhibits values of 55 – 65 ° in the 0.01–10 Hz frequency range and 35 – 45 ° in the 10–10000 Hz frequency range.

Therefore, it is necessary to compare the numerical values to conclude the inhibition process. As the first approach, the R_f values were compared; the highest values were obtained for the 0.4 IBU–PMMA/Ti–6Al–4V coating film; the R_f was equal to 3776 ± 2.89 ohm·cm^2, which approximated two times higher than the results reported for the IBU–PMMA/Ti–6Al–4V (R_f= 1734 ± 1.82 ohm·cm^2). Moreover, it was clear that the R_f reflects the resistance value of the film formed on the metal surface because the R_f values are similar between IBU–PMMA/Ti–6Al–4V and PMMA/Ti–6Al–4V, but in the last, the R_f reported an insignificant increase because of the ability of the titanium alloys to form an oxide film [204]. Moreover, it was evaluated the results obtained to the R_{ct} which reported the following tendency 0 IBU/Ti–6Al–4 V electrode < 1 IBU–PMMA/ Ti–6Al–4 V < 0.20 IBU–PMMA/ Ti–6Al–4 V < Ti–6Al–4 V < 0.40 IBU–PMMA/ Ti–6Al–4 V, in which the R_{ct} when it was added 0.40 IBU reported the highest value (R_{ct}= 23.41 ± 5.41 ohm·cm^2) which reflects the capacity of the IBU + PMMA to decrease the electron transfer between the Ti–6Al–4 V and the NaCl, and this is related to the reduction of the corrosion reaction resulting in a considerable inhibition against the corrosion (see Table S9).

Furthermore, the Q_f and Q_{dl} results were evaluated and thus reported a decrease when the concentration of IBU increased; therefore, it is an indication of the protective barrier formed by the polymeric matrix against the corrosion process. The module of impedances

(|Z|) showed the same trend as Rct and Rf: when 0.40 mM of IBU was added, it was reported the highest |Z| which reported a value equal to 1466.90 ohm·cm^2 (see Table S9).

Finally, the inhibition efficiency was calculated by using the obtained R_{ct}. In this sense, the highest inhibition efficiency was obtained when 0.40 mM IBU was added to the polymeric film with an IER_p equal to 89.53 ± 1.37 % as it is indicated in the Figure 15, which was significantly superior to the other polymeric coatings. The results reported by the EIS are compared with the Tafel results. Therefore, the good inhibition reported by the PMMA – IBU polymeric is related to the good synergy between the PMMA and the IBU, which allows the crosslinking of the polymer to form a mechanically resistant and stable coating. The PMMA-IBU is a promising material to coat materials which are exposed to saline medium with special regards with the Ti-6Al-4V metallic surface which are widely used in the aircraft, car, or medicine field.

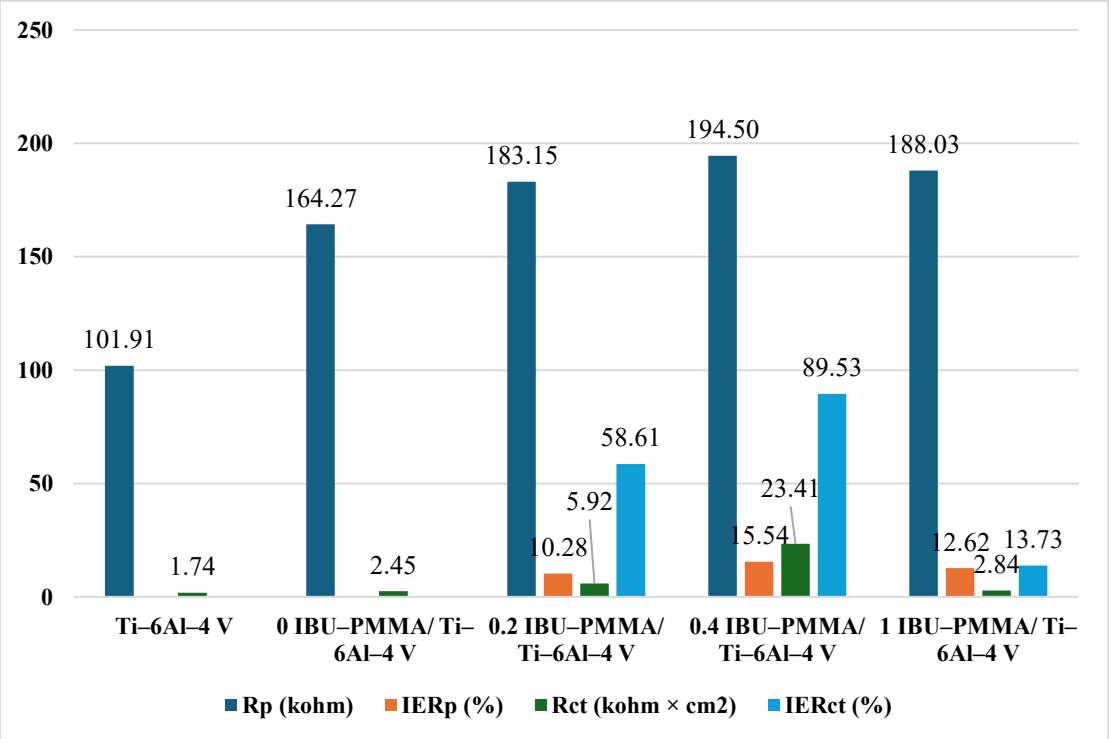

Figure 15. Polarization resistances (blue), inhibition efficiency obtained by DPD (orange), charge transfer resistances obtained by equivalent circuit fit (green) and inhibition efficiency obtained by EIS technique (sky-blue) at different polymeric coatings (see inset). Experimental conditions: electrolyte, 3.50 % NaCl.

3.2.3.4.4. ANOVA test

The ANOVA (analysis of the variance) test was used to study the effect of the addition of the IBU into the polymeric coating by studying the efficiency of inhibition calculated

by EIS techniques as variable response. 6 measurements were performed for every concentration of IBU (0.20 mM, 0.60 mM, and 1 mM) added to the polymeric solution. Moreover, the ANOVA test was performed at 99 % confident interval and the interactions were evaluated by Duncan Test. This was performed in InfoStat software. Moreover, the following hypothesis were stablished:

H_0: The level of IBU (0.2 mM, 0.4 mM, and 1 mM) incorporated into the PMMA coating layer has no effect on the efficiency of corrosion protection evaluated at Ti-6Al-4V samples immersed in 3.50% NaCl solution.

H_1: The level of IBU incorporated into the PMMA coating layer (0.20 mM, 0.40 mM, and 1 mM) significantly influences on the efficiency of corrosion protection evaluated at Ti-6Al-4V samples immersed in 3.50% NaCl solution.

The null hypothesis (H_0) is not accepted because the p-value is lower to 0.01 (see Table 6), therefore it can be concluded that the level of IBU incorporated into the PMMA coating layer (0.2 mM, 0.4 mM, and 1 mM) significantly influences on the efficiency of corrosion protection evaluated at Ti-6Al-4V samples immersed in 3.50% NaCl solution. This is consistent with the results obtained in the mechanical, chemical, and accelerated corrosion analysis. Moreover, it can be concluded that the best formulation to produce PMMA polymeric coating should included 0.40 mM of IBU, because this formulation reported the highest efficiency in the corrosion protection.

Table 6. ANOVA test of the inhibition efficiency as effect of the IBU concentration in the polymeric coating

Source of Variation	**SS**	**DF**	**MS**	**F**	**p-value**
Model	2425.50	2	1212.75	23882.46	$< 1\times10^{-3}$
Ibuprofen concentration	2425.50	2	1212.75	23882.46	$< 1\times10^{-3}$
Experimental Error	0.76	15	0.05		
Total	2426.26	17			

SS: Sum of Squares, DF: Degree of freedom, MS: Mean Square

3.2.4. Green Inhibitors

3.2.4.1. Reagents

To produce the plant green inhibitor extracts the following chemicals were used: ethyl alcohol (CH_3CH_2OH, form Sigma-Aldrich, 92% purity), nitric acid (HNO_3, from Merck, 99% purity), and alumina powder (Al_2O_3, from Buher, 98% purity), *Caelsaspinia Spinosa*

(Tara Powder, produced by Ecuadorean local producers (production procedure reported at section 3.2.4.3.1), purity not reported), *Guayusa Ilex* (Guayusa, harvest from Ecuadorean jungle, purity not reported). The reported chemicals have analytical purity, and they were used as they were received from the supplier without the application of any purification process, while the plant material was washed only with distillated water before the production of the extract. Moreover, all the solutions were made using ultra pure water.

3.2.4.2. Equipment

To prepare the plant extract it was used a Soxhlet equipment. Moreover, to analyze the mechanical characteristics of the mild steel samples it was used a universal automatic tensile testing machine (model H001B, equipped with a sensor of 1000 kN, from MATEST). Likewise, to analyze the chemical structure of the produced plant extracts it was used a FTIR spectrometer (type Vector 22, from Bruker), in the wavelength range of 4000−700 cm^{-1}.

Furthermore, the morphological characteristics of the mild steel exposed to the corrosion environment with and without inhibitor were evaluated by using an emission scanning electron microscope (SEM, type JSM-IT800 Schottky Field, from Jeol) equipped with an energy-dispersive X-ray spectrometer (EDX, from Jeol). Also, the electrochemical characterization experiments were carried out by using a computer-controlled Autolab potentiostat (PGSTAT101 EcoChemie and PGSTAT 12 EcoChemie, Utrecht, Netherlands) operated by NOVA 2.1. and connected to a standard three-electrode cell. The cell was equipped with a working electrode, a reference electrode of Ag/AgCl, KCl_{sat} (from Radiometer, Germany), and an auxiliary electrode made of platinum wire.

3.2.4.3. Methodology

The present research was divided into six parts which were (a) preparation of the plant extracts; (b) preparation of the mild steel samples; (c) chemical characterization of the plant extract; (d) morphological and mechanical analysis of the mild steel plates before and after the exposition to the corrosive acid environment (10 % nitric acid); (e) evaluation of the effectiveness of the green extract inhibition by using accelerated corrosion test such as linear polarization (LP), weight loss, and EIS measurements; (f) evaluation of the mechanism of the protection by thermodynamic studies. The mentioned parts will be discussed in detail in the bellow sections.

3.2.4.3.1. Preparation of the plant extract

In the case of the Tara plant extract, the extraction was performed by using the hot-liquid extraction method (Soxhlet) and the cold solid-liquid extraction method (Maceration), while to obtain Guayusa extract, only the Soxhlet technique was used under the same conditions reported for the obtaining of the Tara extract. This was performed to analyze the influences of the extraction method on the final characteristics of the plant extracts.

Therefore, in the case of the Tara extract preparation, Tara powder was used, which was produced by a local producer in Chimborazo-Ecuador. In brief, they collected the brown Tara pods; the brown color indicates that the pods are ready to harvest, and then they manually cleaned the pods with water. Subsequently, they manually cracked the pods to obtain the seeds, which are going to be used in the production of the powder.

Then, they dried the seeds in a dark room at 16ºC for 24 hours. The dried seed was ground into a powder using a ball mill (ALPA IBM1830, USA). After, they mechanically sieved the powder, and they introduced the powder in a bread mill (Moulinex, France) to reduce its size; finally, they sieved the powder again, and they stored the final product in a dark place to sell for further uses.

To produce the Soxhlet extract, it was following this procedure: 100 g of Tara powder was introduced in a cellulose thimble and closed by putting cotton in the top; then, the distillation flask was filled with 500 mL of ethanol (diluted to 60%); subsequently, the thimble was introduced in the chamber of the Soxhlet extractor. The next step involved assembling and turning on the cooling and heating systems. The system controls that the temperature is 60 ºC. The Soxhlet extraction process lasted 24 hours.

As the time elapsed, the cellulose thimble was dried and weighed for further calculations. The Tara extract-ethanol mixture in the distillation flask was put in a rotary evaporator for one hour. The rotary evaporator was set to 100 ºC and 20 kPa of vacuum pressure. After one hour, the ethanol was separated and saved for another Soxhlet extraction, while the extract was weighed (0.14 g), labeled as Tara-SE, and put in a desiccator for later use.

On the other hand, the maceration process was easier. Thus, 1 kg of Tara powder was placed in a bottle of 3 liters, which contained a 2-liters concentrated ethanol-water mixture (60:40 w/w); then, the bottle was closed, and the mixture remained for 3 days in

a dark and dry place. Thereafter, the solution was taken off and filtered by using filter paper to eliminate the solid residues of the Tara powder.

Afterwards, the Tara-ethanol-water solution was introduced in a rotary evaporator machine, set up at the same conditions for the Tara-SE purification, and run for 1 hour. When time elapsed, the ethanol water was reused in other extraction processes, while the extract, labeled Tara-ME, was stored in a desiccator for later use.

For the Guayusa extraction process, the Soxhlet extraction used to obtain Tara-SE, as described in previous paragraphs, was followed, because this extraction method reported higher corrosion protection as it is described in the following sections. The only changes that were applied were (a) instead of Tara powder, it was used fresh Guayusa leaves (obtained from local producers in Puyo, Ecuador), and (b) the ethanol concentration was 96 % without dissolution because when it was used with diluted alcohol, it could not be obtained a good quantity of extract. Therefore, the Guayusa Soxhlet extract received the label Guayusa-SE.

3.2.4.3.2. Mild steel samples preparation

Before the corrosion process, 100 units of mild steel cylinder (type ASTM A706, grade 60) having 3 cm diameter, and 3 mm thickness and a composition of C: 0.25 %, Si: 0.56 %, Mn: 1.51 %, and Fe: 97.68 %, were cut from construction rods produced by Adelca, Ecuador. The samples were mechanically polished using sandpaper (6000 to 1000 grit) containing alumina powder of 300 µm (from Buehler) until the plates presented a homogenous color and structure. Then, the metallic cylinders were introduced in a degreased solution (CCl_4) for 20 minutes and rinsed with distillated water. Finally, the cylinders were dried with filter paper and stored in a desiccator for later uses.

3.2.4.3.3. Chemical characterization of the plant extracts

The chemical characterization of the prepared plant extracts (Tara-SE, Tara-ME, and Guayusa-SE) was carried out by using the Vector 22 (from Bruker, Germany) FTIR Spectrometer in the wavelength range of 4000−700 cm^{-1}. Thus, extracts of the prepared dried extract were introduced into the cantilever of the FTIR machine, and the experiment was performed.

Moreover, the polyphenolic content, polyphenols are the chemical groups that act as corrosion inhibitors, was evaluated in all the samples. For this, the Folin-Ciocalteu assay [205] was followed. Thus, 0.50 mg of each plant extract was placed in a test tube and

combined with 2.50 ml of a 10-fold diluted Folin-Ciocalteu reagent and 2 ml of 7.50 % sodium carbonate. The tubes were sealed with parafilm and left them to rest for 30 minutes at ambient temperature. The absorbance was measured spectrometrically at 760 nm (model C10082CA, Hamamatsu) using Gallic acid as a reference, with concentrations of 0.01, 0.02, 0.03, 0.04, and 0.05 mg/mL in methanol.

Furthermore, the qualitative content of alkaloids was determined only in the Guayusa-SE extract. Thus, DragenDorff, Wagner, and Mayer's reactions were employed in the determination of these functional groups [206, 207].

Moreover, the chemical characterization also included the determination of the humidity content of all the plant material. For this, the oven-drying ISO 18134-3 standard method was followed [208]. Finally, the yield of extraction (mass of extract/mass of dry matter) was calculated to be used as an indicator of the extraction efficiency. Thus, it was calculated according to the following equation:

$$\text{Yield of extraction} = \frac{m_{ex}}{m_{dp}} \times 100 \quad (17)$$

Where m_{ex} is the extract mass in grams, m_{dp} is the dried material mass in grams, and the yield of extraction is given in % (g dry extract/100 g dry weight of plant material). Also, it was investigated the solubility of the prepared extract in different solvents. This was executed by visual inspection of the turbidity after dissolving a small amount of powder extract in 10 mL of distilled water, ethanol, HNO_3 or acetic acid, and stirring at 1000 rpm with a magnetic stirrer, at 20 °C [209].

3.2.4.3.4. Morphological and mechanical mild steel characterization

The morphology of the prepared electrodes was studied by emission scanning electron microscope (SEM, type JSM-IT800 Schottky Field, from Jeol) equipped with an energy-dispersive X-ray spectrometer (EDX, from Jeol); thus, 10 different metallic cylinder samples were prepared as follows: (i) 1 sample was prepared by immersing it in a 10 % nitric acid solution for 2 weeks, (ii) 3 samples were prepared by immersing it in a 10 % nitric acid + 200 ppm Tara-SE, Tara-ME, or Guayusa-SE for 2 weeks, (iii) 3 samples were prepared by immersing it in a 10 % nitric acid + 600 ppm Tara-SE, Tara-ME, or Guayusa-SE for two weeks, (iv) 3 samples were prepared by immersing them in 10 % nitric acid + 1000 ppm Tara-SE, Tara-ME, or Guayusa-SE. Once the time passed, the samples were taken off, rinsed with distilled water, and dried for 2 hours at room

temperature. The dried samples were introduced into the cantilever of the microscopy, and the surface of the electrode was investigated. This methodology was used to ensure a prolongated contact of the mild steel samples with the medium and to demonstrate the effect of the addition of the extracts onto the medium.

A universal testing machine (model H001B, equipped with a sensor of 1000 kN, from MATEST) was also used to measure the mild steel sample's properties before and after the immersion in the corrosion solution. Hence, eight mild steel samples, prepared according to the procedure described in the previous paragraph, were introduced into the clamps of the machine, and the experiments were carried out by using a speed of 5 mm per minute, and the machines stopped when the metallic sample broke.

At the breaking point, the final length of the samples was measured, and from these values, the nominal stress (s, according to equation 12), and the nominal strain (e, according to equation 13), and Young's modulus (according to the equation 18) were calculated.

$$E = \frac{S}{e} \quad (18)$$

Where E is the Young's modulus, e is the engineering strain (m), and s is the tensile force (in MPa) [115].

3.2.4.3.5. Weight loss measurement

The prepared mild steel samples (see section 3.2.4.3.2) were introduced in a controlled atmosphere by using a corrosion chamber, and the weight loss measurement proceeded as for the morphological characterization (see section 3.2.4.3.4), but in triplicate. Therefore, the weight loss of the corroded samples was calculated according to the following equation [210]:

$$CR = \frac{W_o - W_{ex}}{S \times t \times d} \times k \quad (19)$$

where: CR is the corrosion rate expressed (in mm·year^{-1}); k = 87600 is a constant so that CR is in mm year^{-1}; W_o and W_{ex} are the average weight of specimens before and after exposure (in g); S is the surface area of specimens (in cm^2); d is the density of iron (7.87 g·cm^{-3}); and t is the exposure time (in h). The obtained data was used to calculate the inhibition efficiency according to the following equation [211, 212]:

$$IE = \frac{CR_o - CR_{ex}}{CR_o} \times 100 \quad (20)$$

where: CR_0 is the corrosion rate in the absence of the inhibitor and CR_{ex} is the corrosion rate in the presence of the inhibitor.

3.2.4.3.6. Electrochemical characterization

Electrochemical characteristics of the samples were acquired by employing Linear polarization, potentiodynamic polarization and EIS measurements. The employed three cell distributed as follow: (a) mild steel cylinders as working electrode, (b) Ag/AgCl, KCl_{sat} as references electrode, (c) platinum wire as counter electrode, and (d) 10 % nitric acid without and with x concentration of plant extract (x= 200, 600, 1000 ppm Tara-SE, Tara-ME, and Guayusa-SE) as electrolyte.

Thus, the linear polarization measurements were carried out in an electrode potential range of ± 20 mV vs. OCP (60 minutes) at a scan rate of 0.50 mV/s. From them the inhibition efficiency was calculated by comparing the R_p obtained with and without (R_p^0) coating according to the equation 14.

The potentiodynamic polarization was measurements were carried out in an electrode potential range of ± 200 mV vs. OCP (60 minutes) at a scan rate of 0.50 $mV \cdot s^{-1}$. These results were plotted as Tafel plots. From them, it was estimated the corrosion kinetic parameters such as corrosion potential (E_{corr}), corrosion current density (i_{corr}), anodic (b_a), and cathodic (b_c) Tafel slopes. The corrosion inhibition efficiency (IEp) was estimated using the equation 15.

Furthermore, EIS technique was executed at the same conditions of the polymeric coating EIS experiments. From Bode and Nyquist plots, it was calculated the inhibition efficiency according to the equation 16.

In addition, each test was repeated three times, using a newly prepared solution and WE. The test solutions were not exposed to the surrounding atmosphere, and the temperature was regulated using a thermostat at 298 K.

3.2.4.3.7. Thermodynamics studies

The thermodynamic studies were conducted by calculating the energy of activation (E_a) which was calculated from the slope of the log (CR) versus 1/T plot in an experiment where the variation of the temperature of the acid and inhibitor solutions is performed, and the corrosion rate (CR), calculated according to the methodology described in weight lost measurement section, was evaluated after a certain time (2 to 7 hours), following the equation (21) [211].

$$\log CR = \log A - \frac{E_a}{2.30RT} \quad (21)$$

where: R is the molar gas constant (8.31 J·mol^{-1}K^{-1}), T is the absolute temperature (in K), and A is the pre-exponential or Arrhenius factor. Also, it was calculated the entropy from the intercept of the plot $\log\frac{CR}{T}$ vs. $\frac{1}{T}$, giving by the Eyring transition-state equation in its logarithmic form (check equation 22)

$$\log\frac{\mathrm{CR}}{\mathrm{T}} = \left[\log(\frac{\mathrm{R}}{\mathrm{Nh}}) - (\frac{\Delta\mathrm{S}}{2.303\mathrm{R}})\right] - \frac{\Delta\mathrm{H}}{2.303\mathrm{R}}(\frac{1}{\mathrm{T}}) \quad (22)$$

where: h is Planck's constant (6.63×10^{-34} J·s), N is the Avogadro's number (6.02×10^{23} mol^{-1}), ΔS is the activation entropy (in J·mol^{-1}·K^{-1}), ΔH is the activation enthalpy (in J·mol^{-1}), T is the absolute temperature (in K), and R is the universal gas constant (8.31 J·mol^{-1}·K^{-1}).

To study the mechanism of adsorption of the active principle of the inhibitor (polyphenols in the case of the Tara extracts and alkaloids in the case of Guayusa extract) on the metal surface, it is necessary to establish the relation between the corrosion rate (calculated according to the procedure described in the weight loss measurement section) and the surface coverage of the inhibitor. This interaction allows us to understand if the interaction between the metal and the inhibitor is greater than the interaction of the metal and water-adsorbed molecules at equilibrium [213]. If this is true, then the inhibitor molecules are adsorbed and the water molecules are displaced. Thus, a wide number of mathematical models are established to study these interactions; however, the most used are the models that give a physical meaning of the adsorption process [214]. These thermodynamic models are (a) Langmuir: this model assumes that the adsorption/desorption process is reversible, the surface is homogeneous with no lateral interactions, and the system operates under isothermal conditions [215]. From these assumptions, it is obtained the linearized mathematical equation of the model is used to calculate the equilibrium constant of adsorption (see equation 22); (b) Freundlich: this semi-empirical model describes the adsorption as a non-linear process occurred on rough and multi adsorption site surface. Therefore, this model provides information about (a) the heterogeneous nature of the metal – solution interaction and (b) the exponential distribution of active sites and their energies [216]. Thus, the equilibrium constant of adsorption is calculated by the equation 23; (c) Temkin: this semi-empirical model describes the adsorbate–adsorbate interaction by assuming a liner decrease in the

adsorption heat as a function of the surface coverage. This decrease is caused by the repulsion of adsorbate–adsorbate occurring during a multilayer process [216]. Hence, the equilibrium constant is calculated according to equation 24; (d) Flory Huggins model: this model described a lattice-based substitutional adsorption process that occurs between the adsorbed molecules and the displaced water molecules. So, the model assumes a multilayer adsorption process in a heterogenous surface in which the water molecules are displace by the adsorbed molecules by using the surface coverage value [216]. The equilibrium constant of adsorption is calculated by the equation 25; (e) El Awady model: this model adopts a combined kinetic-thermodynamic framework in which the number of active sites n is included. The equilibrium constant is calculated according to equation 24. Before the application of the mentioned mathematical models, the following assumption were stablished: (a) the surface coverage was calculated as the ratio IE (%)/100, where IE (%) is the reciprocal of the corrosion inhibition efficiency calculated according to equation 19 (weight loss measurement section); (ii) the initial concentration of the inhibitor is equal to its concentration at equilibrium; (iii) the surface of the mild steel samples remains constant during the time of the corrosion evaluation experiments (3 hours). By this assumption, the applied equations were [216]:

Langmuir $\frac{c_{ex}}{\theta} = \frac{1}{\theta_m K_{ads}} + \frac{c_{ex}}{\theta}$ (23),

Freundlich $log\ \theta = log\ K_{ads} + \frac{1}{n} log\ c_{ex}$ (24),

Temkin $\theta = \frac{RT}{b} log\ K_{ads} + \frac{RT}{b} log\ c_{ex}$ (25),

Flory Huggins $log \frac{\theta}{c_{ex}} = log\ K_{ads} + n\ log(1-\theta)$ (26),

El Awady $log(\frac{\theta}{1-\theta}) = log\ K_{ads} + n\ log\ c_{ex}$ (27);

where: CR is the corrosion rate, K_{ads} is the equilibrium constant of the adsorption process, θ is the degree of surface coverage [216], n is a measure of the number of adsorbed water molecules substituted by a given inhibitor molecule [216].

From this data it was calculated the adsorption's Gibb's free energy (ΔG_{ads}), using the equation 37.

$\Delta G_{ads} = -2.303RT \times \log(55.50 \times K_{ads})$ (28)

where: K_{ads} is the adsorption equilibrium constant obtained from the isotherm, and the number 55.50 is the molar concentration of water in aqueous solution [218]

3.2.4.4. Results and discussion

3.2.4.4.1. Chemical characterization

The inhibition capacity of a plant extract is related to the heterocyclic atoms that conform to the plant structure because these atoms could be adsorbed at the metal structure and reduce the corrosion reactions by increasing the charge transfer resistance or by decreasing the apparition of free hydroxyl groups or cations, which can accelerate the corrosion [219].

Therefore, it was necessary to characterize the functional groups in the prepared extracts. Firstly, we analyzed the Tara extracts using the IR spectrum, which spans from 4000 to 500 cm^{-1} (see Figure 16). At first sight, it can be observed that the type of extraction does not affect the vibration bands; however, the vibration intensity is higher in the Tara-SE, but it is not a significant change between both extracts. This is explained by the fact that the concentration of the functional groups is related to the vibration peaks obtained in the FTIR determination. Thus, as a first approach, the Tara-SE has more quantity of functional groups in comparison to the Tara-ME [220].

Thus, the FTIR spectra of the Tara extract, regardless of the extraction method, reported a stretching at 3480 cm^{-1}, which is related to the –OH stretching. This deviation is a significant sign of the presence of polyphenols [208]. Then, a C=O stretching is seen in the area between 1722 and 1702 cm^{-1}. This is because of hydrolysable tannins, especially tannins made from gallic acid [208]. Subsequently, it appears the C=C– aromatic region in the range of 1600 to 1500 cm^{-1}. C–H bending appears at the region 1450–1320 cm^{-1}. Moreover, at the region between 1300 and 1100, it is reported C–O stretching vibrations; this appeared in the Tara extract, which confirms the presence of hydrolysable polyphenols. Moreover, at the low infrared region between 1100 and 950 cm^{-1}, there appear complicated and overlapped stretching and bending vibrations because of C–O stretching of methoxy groups with C–C, C–OH, and C–H of sugar fractions. It is the most frequently fingerprinted spectra obtained when the extract has high quantities of polyphenols [221].

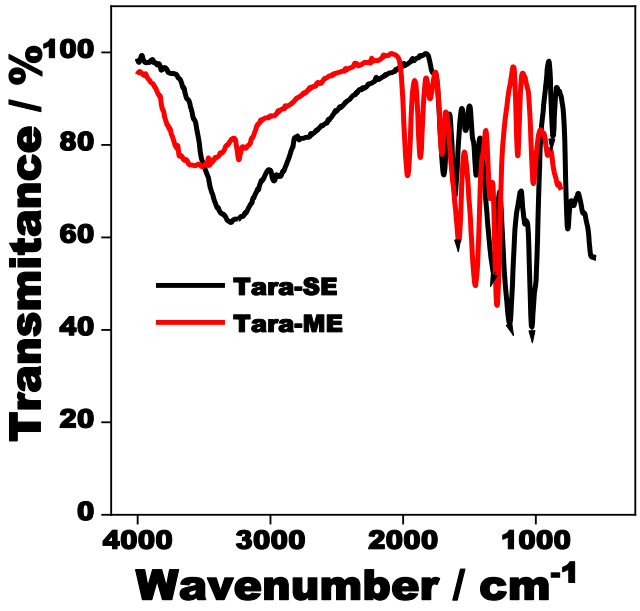

Figure 16. FTIR spectra for Tara-SE (black line) and Tara-ME (red line).

On the other hand, the Guayusa-SE presented a significantly different IR spectrum (see Figure S6). An -OH vibration band stands out at position 3490 cm^{-1}. Then, it is reported that a -C-H stretching at 3100 cm^{-1}; this confirms the presence of flavonoid compounds. Then, at the region between 2000 and 1500 cm^{-1}, a high-intensity stretching is reported, which confirms the presence of $C \equiv N$ functional groups [222]. Also, the strong band at 1500 cm^{-1} showed that there were C=C and C=N stretching, as well as imine or oxime, amide or ε-lactum C=O stretching and amine N-H bending. These are the main vibrational features that show that alkaloids are present. At 1350 cm^{-1}, an O-H bending is reported, and the strong peak at 1336 cm^{-1} is caused by alcohol, phenol, gem dimethyl, or aldehyde C-H bending [222]. At 1110 cm^{-1}, an adsorption band appears, which is caused by the C-O stretching of aromatic ethers, tertiary alcohols, esters, and the C-N stretching of amines. Finally, at 860 cm^{-1}, a band appears because of the presence of alkenes (C=C band) [123].

Overall, from the FTIR, the following can be confirmed: (a) the composition of the Tara vibrational peaks confirms the presence of hydrolysable and condensed tannins, the main components of the polyphenolic compounds; and (b) the composition of the Guayusa vibrational peaks confirms the presence of alkaloids.

Therefore, the qualitative analysis of the plant extracts was confirmed by the quantitative analysis of the composition of the extracts. In this sense, the extract obtained from the Tara by Soxhlet extraction reported a polyphenol content equal to 0.36 ± 0.03

g/kg of extract, the Tara maceration extract reported a polyphenolic content equal to 0.19 ± 0.07 g/kg of extract, while the Guayusa extract reported a polyphenol content equal to 0.05 ± 0.07 g/kg of extract.

On the other hand, both Tara-SE and Tara-ME did not report positive results to the different alkaloid determination methods (Mayer's test, Dragendorff's test, or Wagner's test), while the Guayusa-SE reported positive values for all the alkaloid group determination mentioned tests. In this sense, Tara does not present alkaloids, while Guayusa reported alkaloids of different types.

Furthermore, the moisture content of the plant materials was evaluated; it follows the increased tendency: Tara-SE < Tara-ME < Guayusa-SE. Also, the yield of extraction was calculated, which increased according to Guayusa-SE < Tara-ME < Tara-SE. It was also tested to see how well the extract dissolved in different solvents. As shown in Table 7, all the extracts were soluble in water, ethanol, nitric acid, and acetic acid.

Overall, from the chemical analysis of the plant material, it can be concluded that: (a) both Tara extracts reported adequate polyphenolic content, thus, it is a clear sign of the presences of heterocyclic atom which can be potentially adsorbed on the metallic surface forming a protective layer, while in the Guayusa, the content of alkaloids can be accomplish the same principle; (b) the high solubility of the extracts in different solvents it is crucial, because the extracts are going to be in contact with the metal surface, thus decreasing the rate of corrosion reactions; (c) the yield of extraction of the plant extracts is favorable, so the production process can be viable.

Table 7. Chemical characteristics of the obtained plant extracts

Property	**Tara-SE**	**Tara-ME**	**Guayusa-SE**
Polyphenolic Content, g/kg of extract	0.36 ± 0.03	0.19 ± 0.07	0.05 ± 0.01
Yield of extraction, %	10.59 ± 0.06	13.89 ± 0.09	18.25 ± 0.03
Moisture Content, %	22.43 ± 0.07	22.38 ± 0.14	33.78 ± 0.26
Solubility in distilled water/ethanol/ HNO_3/ acetic acid	Soluble/soluble/soluble /soluble	Soluble/soluble/soluble /soluble	Soluble/soluble/soluble /soluble
Mayer's test	-	-	+

Dragendorff's test	-	-	+
Wagner's test	-	-	+

Mean ± standard deviations of 3 measurements.

3.2.4.5. Morphological and mechanical characterization

SEM imagines are used as first approximation to see the corrosion effect of the metal surfaces when it is exposed to the corrosive medium, and the effect of the addition of the inhibitors of corrosion in maintain as much as possible the crystal structure of the metal and to reduce the apparition of cracks on the metal surface, which be propagated from all the crystal structure [224].

Hence, Fig 17A shows the crystal structure of the mild steel plate which was not immersed in the corrosive medium. In this, it can be observed a smooth homogenous surface with little scratches because of the grinding process. On the other hand, when the metal plate was exposed to 0.10 M HNO_3, it can be observed a destruction of the surface (check Figure 17B), and the apparition of holes at a scale equal to 200 μm and a magnification equal to 800x.

It indicates the high degree of corrosion suffered by the metallic plate after two weeks in an acid medium. This is also confirmed by the EDS spectra, which in the case of the metallic plate in room conditions, presented Fe, C, and Mn (the main components of the alloy), while the EDS mild steel, which was immersed in an acid solution, reported only the presence of Fe because of the destruction of the metallic crystal phase and the apparition of oxides, which indicates a high degree of corrosion propagated for all the metallic structure [224].

The analysis of the pictures obtained by the addition of the plant extracts in the acid medium showed a reduction in the destruction of the metallic surface according to the type of extract added. Hence, when 1000 ppm of Tara-SE extract (Figure 17C) was added, the propagation of the corrosion was not extended to all the metal surfaces. It can be observed that holes (the destruction of the crystal structure) appear only at certain points.

While the addition of 1000 ppm of Tara-ME does not control the propagation of corrosion with the same effectiveness reported by Tara-SE, the pictures (see figure 17D) showed the apparition of holes expanded in all the surfaces; thus, the crystal structure lost its properties, and the apparition of rust in the crystal composition is a clear sign of the presence of corrosion. However, in some way, the crystal structure maintained its

properties in comparison to the crystal structure after the exposition of the corrosive medium without plant extracts.

Furthermore, the addition of 1000 ppm of Guayusa-SE also ensures the maintenance of the crystal structure, as you can see in Figure 17I. However, for a deeper understanding of this, the EDS confirmed this, as can be observed in Figures 17E, 17F, and 17G; the content of Fe changes according to the apparition of cracks in the structure; thus, it is a sign of the production of corrosion in the interlayer of the metal surface because it means that the Fe is dissolved into the acid medium and this is correlated to the extension of the corrosion process. The corrosion process is described by equation 18. Of course, these values are lower in comparison to the samples without the addition of inhibitors, thus they can be a sign of the efficacy of the produced extracts.

(A) **(B)**

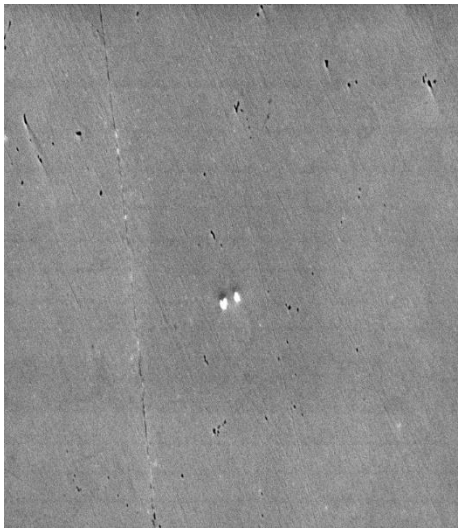

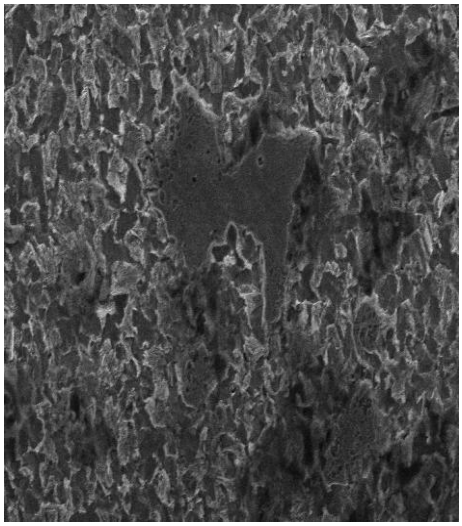

(C) **(D)**

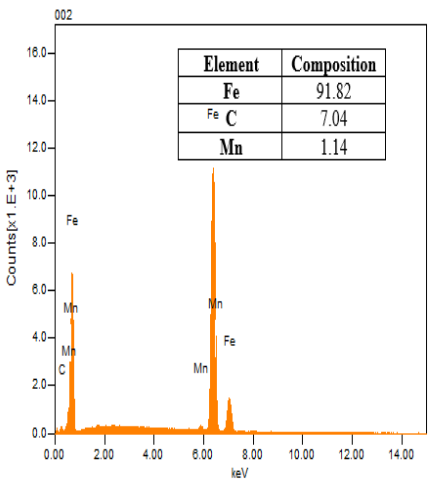

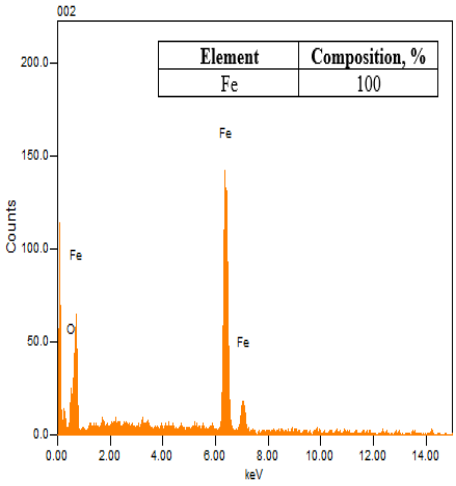

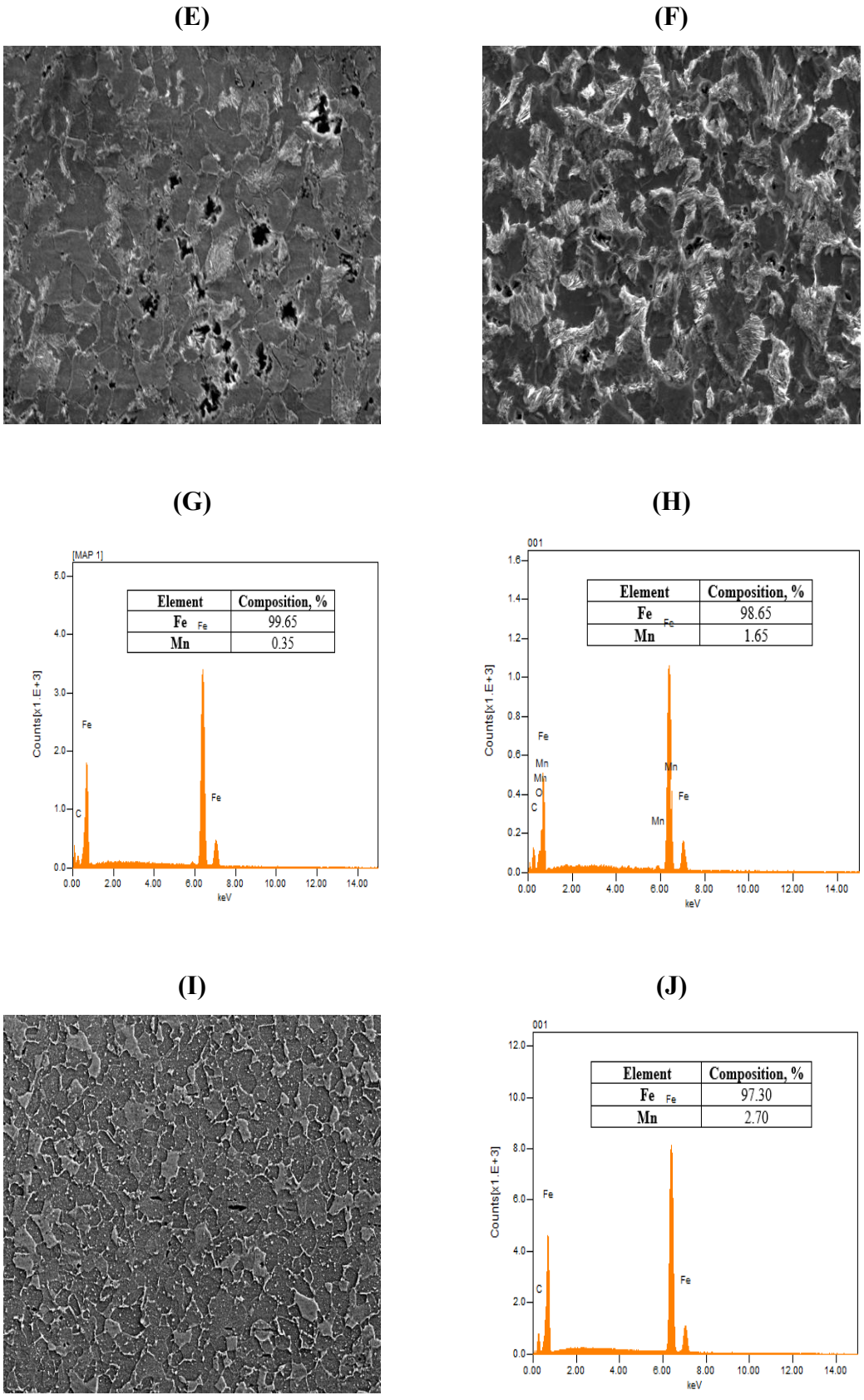

Figure 17. SEM images (A, B, E, F,I) and the corresponding EDS graphs (C, D, G, H,J) for mild still before the immersion in the 0.10 M HNO_3 (A,C) and after the immersion in

0.10 M HNO_3 solution without (B,D) and with Tara extract obtained via hot solid-liquid extraction (E, G, Tara-SE extraction), and cold solid-liquid extraction (F, H, Tara-ME extraction), and Guayusa hot solid-liquid extraction (I, J, Guayusa-SE) at a scale equal to 200 μm and a magnification equal to 800x.

To probe the maintenance of the properties of the mild steel, the SEM images were accompanied by the measurement of the mechanical resistances of the mild steel samples immersed in an acid environment with and without the addition of plant extract corrosion inhibitors, and these results were compared with the values obtained by the mild steel samples stored at room conditions. Therefore, Figure 18 shows the behavior of the mild steel samples when a force it is applied. It can be observed for all samples an elastic deformation accompanied by an inelastic deformation until the metallic sample is broken. As it is observed in the figure at the metallic sample which was not in contact with acid medium (black line) this process takes longer in comparison with the other samples.

Adding 1000 ppm of Tara-SE to the corrosive medium caused the Young's modulus to decrease less, with a value of 189.56 ± 13.06 GPa. On the other hand, mild steel that was exposed to acid conditions without an inhibitor caused the largest decrease, with a value of 175.14 ± 25.69 GPa. Thus, after two weeks of immersion without an inhibitor, the mild steel suffers a considerable loss in its mechanical properties because of the apparition of pits, which enable their propagation into the metallic structure, as indicated in Table S10.

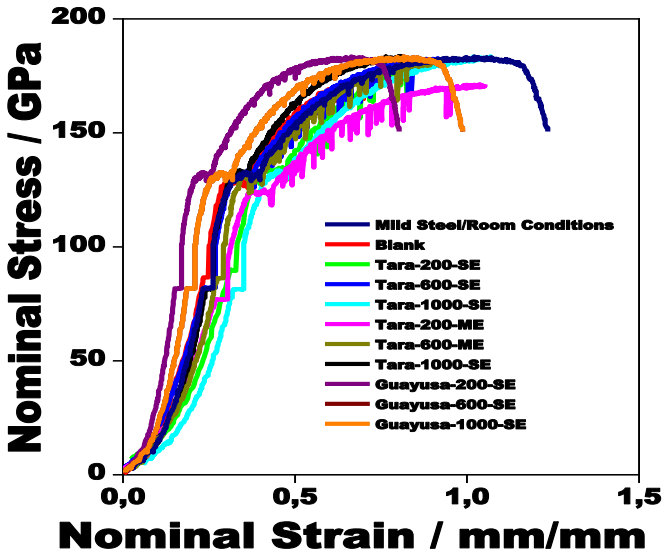

Figure 18. Stress−strain curves obtained at mild steel immersed in 0.10 M HNO_3 in the absence and presence of Tara-x-SE, Tara-x-ME, and Guayusa-SE extracts at different concentrations (where x = 200, 600, 1000 ppm)

3.2.4.6. Weight loss measurements

The weight loss measurements are the simplest method to analyze the apparition of the corrosion in a metallic piece. As the corrosion process consist in the dilution of the metal ions into the corrosive medium, by this method it can be analyzed how much is lost due to the cited process. On the mild steel the dilution process is accompanied by the hydrogen evolution according to the following process:

$Fe\ (s) \rightarrow Fe^{2+}\ (aq) + 2e;\ 2H^{+}\ (aq) + 2e^{-} \rightarrow 2H_{ads} + H_2\ (g)$ (28) [225],

so, the weight loss gives information about the extend of the corrosion reaction by correlated the weight loss.

In this sense, Table 8 collected the weight loss measurements of the samples after 2 weeks of exposition to the corrosive medium with and without the addition of 1000 ppm of the different plant extracts. From the weight loss, the inhibition efficiency was calculated. Hence, the maximum inhibition efficiency was reported by the Tara-SE with a value equal to 95.90 % ± 1.41 %.

Moreover, an increased tendency was observed in the inhibition efficiency while there was more plant extract. As for a view, it can be deduced that the functional groups of the prepared extracts, polyphenols in the case of the Tara and alkaloids in the case of the Guayusa, are protecting the metallic plates by reduction of the corrosion reactions or by adsorption into the metal surface; that is why the more extract is added, the better the corrosion protection.

In a more profound analysis, it can be discussed that (a) the heterocyclic atoms are adsorbed onto the metallic surface and hinder the availability of free electrons to produce corrosion reactions [225], (b) the heterocyclic atoms and the π-orbitals in the aromatic ring from plant extract inhibitor are able to form chemical bonds with the iron atoms (d) orbital [129].

Both phenomena are covered in the later sections; thus, electrochemical measurements allow one to see what the mechanism of protection created by the addition of the plant extracts is, and by thermodynamic studies, it can be seen if the substances are chemically or physically adsorbed into the metallic structure; however, as a preliminary study, the weight loss measurements help to see the good applicability of the plant extracts as a corrosion inhibition.

Table 8. Weight loss results for mild steel immersed in 0.10 M HNO_3 acid solution in the absence and presence of different concentrations of Tara-x-SE, Tara-x-ME, and Guayusa-x-SE extracts (where x = 200, 600, 1000 ppm)

Extract	Mass of the sample (g)	Corrosion Rate ($mm \cdot year^{-1}$)	Inibhition Efficiency (%)
Initial weight	5.19 ± 0.49	-	-
Blank	3.55 ± 0.70	1.50 ± 0.27	-
Tara-200-SE	4.10 ± 0.11	0.96 ± 0.10	35.83 ± 4.54
Tara-600-SE	4.70 ± 0.22	$0.40 \pm 1\times10^{-3}$	76.97 ± 2.75
Tara-1000-SE	5.12 ± 0.16	$0.07 \pm 2\times10^{-3}$	95.93 ± 1.41
Tara-200-ME	3.94 ± 0.34	1.11 ± 0.06	27.5 ± 3.83
Tara-600-ME	4.37 ± 0.16	0.71 ± 0.15	51.18 ± 1.86
Tara-1000-ME	4.95 ± 0.14	0.22 ± 0.13	85.31 ± 4.24
Guayusa-200-SE	4.72 ± 0.45	1.36 ± 0.25	9.30 ± 0.05
Guayusa-600-SE	3.85 ± 0.14	0.62 ± 0.13	58.67 ± 1.10
Guayusa-1000-SE	4.24 ± 0.03	0.56 ± 0.22	62.70 ± 0.25

Values are expressed as mean ± standard deviations of 3 measurements

3.2.4.7. Electrochemical Characterization

OCP measurements were studied for all concentrations of the different plant extracts, Tara-SE, Tara-ME, and Guayusa-SE, to see how the addition of the prepared extract prevents the apparition of a corrosion potential [129]. Furthermore, it enables checking if the process is fast or slow until it reaches the equilibrium. The OCP was measured for 60 minutes, at that time all the samples achieved the equilibrium, thus the OCP reported constant values as it is reported in Figure 19A.

Figure 19B indicates that in all the samples prepared, the potential tends to increase. However, this data does not indicate the presence of any kinetic parameters in the system [226]. So, it was necessary to study it by employing potentiodynamic polarization (PDP) to understand what the mechanism of protection is generated by the addition of the different plant extracts, and from them it can be subtracted important information about the corrosion inhibition process.

Therefore, the PDP analysis was extrapolated and draw as Tafel graphs (Figure 20B), and from the Tafel value, there were subtracted the potential of corrosion (E_{corr}), the current of corrosion (i_c), the cathodic Tafel slope (b_c), the anodic Tafel slope (b_a), and from this data it was calculated the corrosion inhibition efficiency for the different extracts. All the information is summarised in Table S11.

Hence, the E_{corr} for most of the prepared samples decrease in both densities of anodic and cathodic current. This change was >85 mV; thus, the inhibitors behave as mixed-type inhibitors (cathodic and anodic protection) according to the criteria proposed by the authors Jianhong Tan et. al. (2020) [227]. This indicates that the prepared extracts can reduce both the anodic metal dissolution and cathodic reduction reactions simultaneously. This is a normal behavior in the inhibitors obtained from plant extracts because they content heteroatom-rich functional groups such as polyphenols and alkaloids [227]. Also, the data showed a decrease in the corrosion current density when a larger quantity of inhibitors was added to the acid. Thus, the passage of the current is decreased by the presence of the inhibitor in the metallic surface, which creates a stable medium [227].

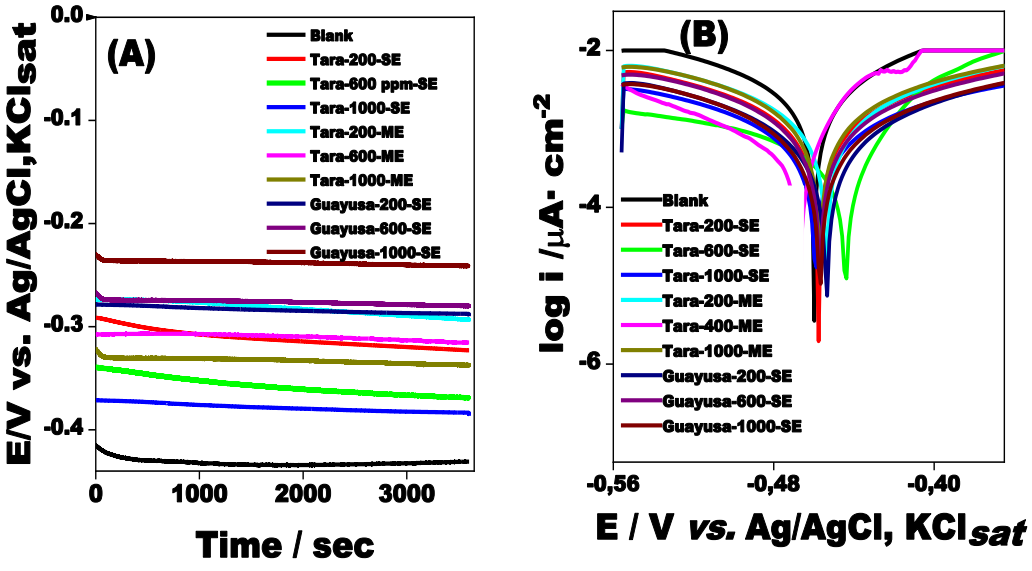

Figure 19. Open circuit potential (A), and Tafel representation (B) recorded at the bare mild steel in the absence (blank) and in the presence of different concentrations of Tara

extracts (Tara-x-SE and Tara-x-ME, (where: x = 200, 600, 1000 ppm) and Guayusa extract (Guayusa-x-SE (where: x = 200, 600, 1000 ppm)). Experimental conditions: electrolyte, 0.10 M HNO_3; scan rate, 0.5 mV s^{-1}; potential range, ± 200 mV vs. OCP at 60 min.

From the obtained data, the inhibition efficiency was calculated; therefore, the increased tendency followed this pattern: Guayusa-200-SE < Tara-200-ME < Tara-200-SE < Guayusa-600-ME < Guayusa-1000 < Tara-600-ME < Tara-400-SE < Tara-1000-ME < Tara-1000-SE. Hence, the maximum inhibition efficiency was equal to 97.38 ± 2.04 % (see Figure 20). The inhibition efficiency depends on both the concentration and the type of extract, as it is indicated; the Guayusa reported the lowest rates of inhibition compared with the other two extracts. In this sense, the polyphenol content in the Tara-SE is almost doubled in comparison to the Tara-ME and almost 7 times higher to the Guayusa-SE, that means there are more heterocycle compounds rich in electrons which can interact with the metallic surface; thus, the formed protective layer is thicker. When, the protective layer is thicker the dissolution reactions are less probable to occur, and this increases the corrosion resistance of the material and as result the efficiency in the corrosion protection increase.

The inhibition efficiency reported by the Tara extract, indifferent to the type of extraction, is comparable with other plant materials used to protect the metals exposed to acid condition. For example, the author Haiquin Ren, et al., [228] prepared an environmentally friendly corrosion inhibitor by using Pumpkin leaf extract (PLE) crop waste for copper in 0.50 M H_2SO_4. The results reported that the inhibition efficiency of the PLE against copper reached 89.98% when the concentration of the PLE reached 800 mg/L. Also, the author Bouchan Tan, et al., [229] prepared an environmentally friendly corrosion inhibitor by using Pyracantha fortuneana alcohol extracts (PFAE) for copper in sulfuric acid. The principal outcomes of the study demonstrated an inhibition efficiency upper of 95 % when it was added 600 mg/L of PFAE.

Therefore, plant extract with a high content of functional groups reported a high degree of corrosion protection when the metal was exposed to acid condition. In the present case, the polyphenol compounds, present by the Tara-ME and Tara-SE, play a fundamental role in corrosion protection. The inhibition is related to the presence of oxygen atoms, which could be adsorbed in the metal surface [229].

Another process produced by the addition of polyphenols is the stabilization of the medium, due to the high content of π electrons, which can move freely into the anode and

cathode, thus preventing the hydrogen evolution; hence, the potential at the electrolyte/metal surface is maintained stable, and the occurrences of corrosion reactions is slowed down because of the formation of a protective layer, which hinders the electronic transfer.

EIS characterization enables the study of both the corrosion process in the metal surface and the adsorption of the plant extract into the metal surface because of the analysis of the electrolyte/metal interface. Changes in resistances and capacitances in the double layer allow for the study of the process. Moreover, the main advantage of using the EIS in the corrosion analysis is the controlled rate of the process, which allows control of the kinetics of the reactions.

Moreover, from the Nyquist plot, it can be observed two well-defined sections; at the medium-high frequency, it can be observed a capacitive loop, which has a semicircle shape; this indicates a transfer-controlled corrosion mechanism, and at low frequencies, a low inductive loop is observed because of the dispersion of the frequency. So, the diameter of the semicircle portion is attributed to the roughness and inhomogeneous surface coverage of the inhibitor over the metallic surface [134]. In this context, the semicircle can be studied at the beginning stage of the corrosion process; thus, it can be seen if there is the apparition of pitting corrosion by NO_3^- ions [230].

Therefore, an increase in the semicircle diameter is observed when the concentration of the corrosion inhibitor is increased, so the corrosion protection is increased by the formation of a protective layer on the metallic surface, which denies the passage of electrons in the acid medium. This high efficiency of the corrosion protection is attributed to the reduction of the free atoms by the adsorption of the molecules of the plant extract [230]. Therefore, the EIS were interpreted as Nyquist and Bode plots (see Figures 20A, and 20B) and the values of the resistances and the capacitances were calculated by the equivalent circuit model. In the present case, all the experiments were simulated by using the simple Randles circuit R_s(CPE R_{ct}) [133], in which R_s is the solution resistances, CPE is constant phase element, and the R_{ct} is the charge transfer resistance. The polarization resistance Rp value includes the Rct and the resistance of solution (R_s).

In addition, Figure 19B reported the bode diagrams of the samples exposed to the corrosive environment with and without the addition of different times of inhibitors (Tara-SE, Tara-ME, Guayusa-SE). In the plots, it can be observed at the low frequency region an increase in two or three magnitude orders in the impedance's modulus (|Z|) because of

the decrease in the capacitances [231] caused by the adsorption of the polyphenols into the metal structure.

On the other hand, in the high impedance region, the modulus of impedance's modulus (|Z|) decreased in a two or three magnitude order because of the increase in the resistance of the system, attributed to the reduction in the transfer of free electrons at the electrolyte/metal interface [136]. Both phenomena are required to increase the corrosion protection of metals soaked in an acidic environment.

Moreover, the phase angle vs. log f reported a constant value at both the high and the low frequency region. In the middle region, we observe a notable increase in the phase angle as the inhibitor concentration rises. This effect is attributed to the formation of two-time constants; the first one is attributed to the electric double layer capacitance (C_{dl}) at the metal/solution interface. Another cause of the relaxation process is due to the adsorption and desorption of the inhibitor at the mild steel/solution interface [232].

Therefore, the data plotted as Bode figures demonstrate unambiguously the formation of a new layer because of the adsorption of the functional groups of the plant extract, which are fixed on the metal surface. This is desirable when it is prepared as an inhibitor extract because the adsorption slows down the corrosion process and increases the charge transfer between the metal and the medium.

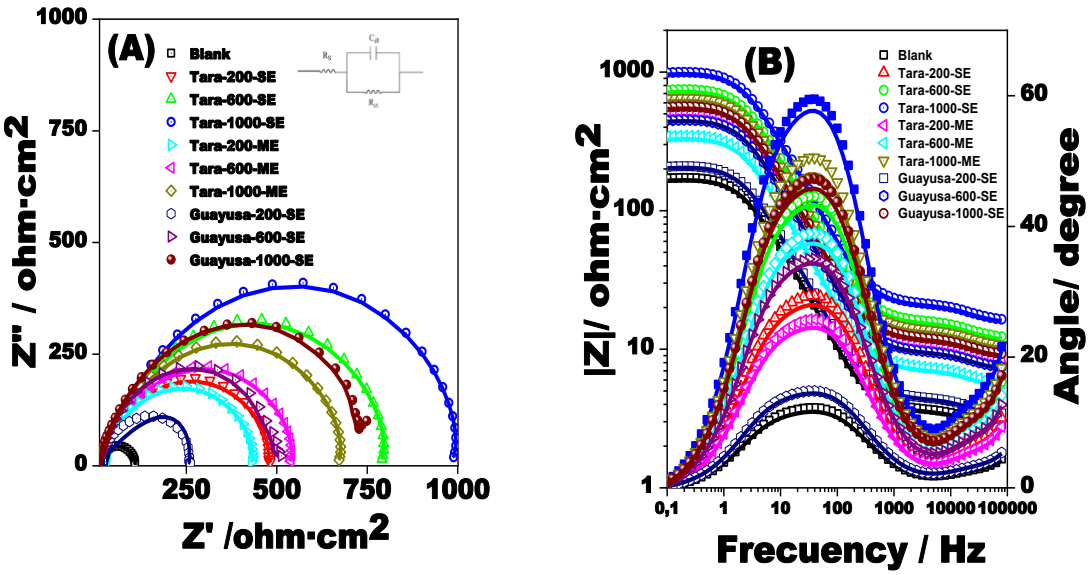

Figure 20. Nyquist (A) and Bode (B) plots of impedance spectra recorded at mild steel in 0.10 M HNO_3 in the absence and presence of Tara-x-SE, Tara-x-ME, and Guayusa-x-SE extracts, where: x = 200, 600, 1000 ppm (see inset), and the corresponding equivalent circuit (see inset). Experimental conditions: electrolyte, 0.10 M HNO_3; frequency range, 10 mHz to 10 kHz.

The equivalent circuit fitted perfectly the shape of the Nyquist plots ($\chi^2 > 0.99$). According to the circuit, it was calculated the different parameters of the system (according to equations 29 and 30), thus:

$C_{dl} = (R_p{}^{1-n} \times CPE)^{\frac{1}{n}}$ (29), and

$\tau = C_{dl} \times R_p$ (30)

where CPE is the constant phase element, C_{dl} is the double layer capacitance, n is measurement of the surface roughness (from 0 – 1), and τ is the relaxation time.

The numerical results of the EIS parameters are specified in Table S11, there, it can be seen undoubtedly the increase of R_{ct} as the concentration of the inhibitor increases, and the decrease in the C_{dl} which is linked to the increase of the R_p. Therefore, the highest R_{ct} was reported when Tara-1000-SE was added, which reported values equal to 1027 ± 10.27 ohm·cm^2, and the lowest values were reported when there was no addition of any type of inhibitor; these reported values equal 95.23 ± 3.42 ohm·cm^2.

On the other hand, the highest values of the C_{dl} were obtained when there was no addition of inhibitor, which reported values equal to 14.61 ± 0.85 μF·cm^{-2}, and the lowest results were reported by the Tara-1000-SE with a C_{dl} equal to 3.41 ± 0.02 μF·cm^{-2}. Moreover, the relaxation time (the estimated time required to reach the equilibrium of the charge distribution after an electrical perturbation) reported the highest values when Tara-400-ME was added, with values equal to 6.57 ± 0.04 mS, and the lowest values were reported at the metallic samples without an inhibitor; with values equal to 1.69 ± 0.05 mS. Also, the n value changed, because of the concentration of the added inhibitor, hence, the highest n values were reported when it was added 1000-Tara-SE (n = 0.88), while the lowest n values were reported when it was not addition of plant extracts (n = 0.73).

The inhibition efficiency was calculated based on the data obtained. Therefore, the highest inhibition efficiency was obtained when Tara-1000-SE was added, which reported values equal to 90.73 % ± 0.03 %, while the lowest inhibition efficiency was reported when Guayusa-200-SE was added, which reported values equal to 13.04 % ± 0.21 %. The inhibition efficiency trend is as follows: Guayusa-200-SE < Tara-200-ME < Tara-200-SE < Guayusa-400-ME < Tara-400-ME < Tara-600-SE < Guayusa-1000-SE < Tara-1000-ME < Tara-1000-SE as is reported in Figure 21. Therefore, the tendency is maintained in relation to the values obtained by the Tafel analysis; thus, it can be discussed that the inhibition efficiency for the present study is related to the type of

extraction method, the type of plant extract, and the concentration of the green inhibitor added to the corrosion environment.

Overall, from the Nyquist plot, the presence statements are found for the present research: (a) the increases in the R_{ct} values highly depend on the amount of the inhibitor added to the solution, because of the formation of a protective layer over the metal surface which restricts the corrosion reactions, (b) the C_{dl} decreases as function of the increased of the R_p, which indicates a decrease in the local dielectric constant and/or rise in the thickness of the electrical double layer, because of the major presences of the inhibitor molecules adsorbed in the metal surface and the high dielectric water at the interface being replaced by some substances that is larger in molecular size, (c) the increases in the n value denotes a reduction of the destruction of the metal surface, thus the reaction of corrosion are controlled, and (d) the increases in the relaxation time is attributed to the time taken to form the protective layer because of the adsorption of the extract molecules into the metal surface. All these results denote the good performance of the prepared plan extract to inhibit the corrosion of the mild steel exposed to acid conditions.

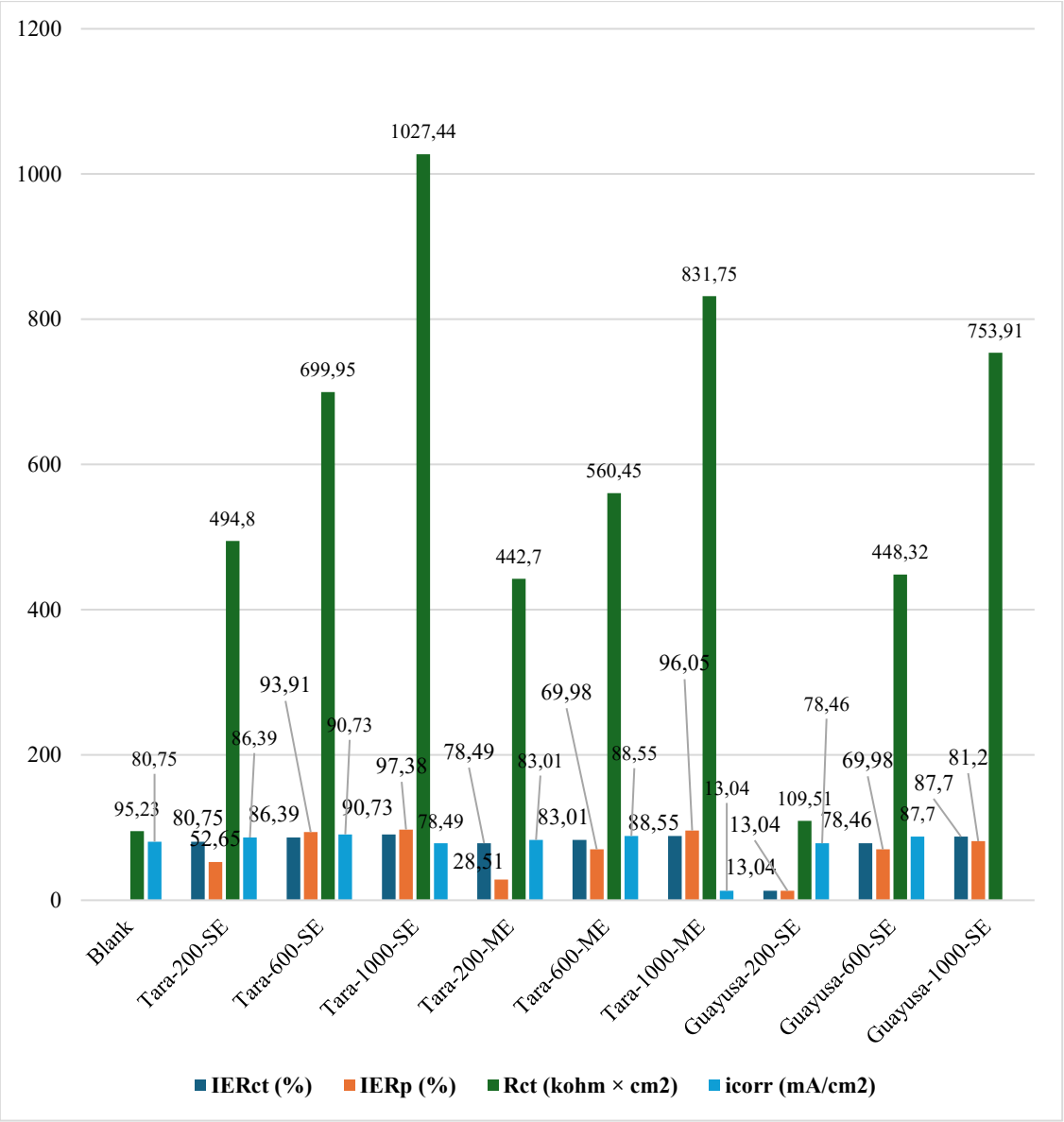

Figure 21. Corrosion current (sky-blue), inhibition efficiency obtained by DPD (blue), charge transfer resistances obtained by equivalent circuit fit (green) and inhibition efficiency obtained by EIS (orange) at plant extract (see inset). Experimental conditions: electrolyte, 3.50 % NaCl.

3.2.4.7.1. ANOVA test

The ANOVA test was used to study the effect of the extraction technique (Soxhlet or Maceration extraction) and the added concentration of the different inhibitors (Tara or Guayusa) into the corrosion protection of the mild steel samples immersed in 0.10 M of nitric acid by studying the efficiency of inhibition calculated by EIS techniques as variable response. 6 measurements were performed for every treatment. Thus, it was first studied the effect of the type of the extraction technique, then, it was studied the effect of

the plant extract into the corrosion protection. This was evaluated in the mild steel samples exposed to 0.10 M nitric acid solution plus 1000 ppm of each type of extract (Tara-SE, Tara-ME, or Guayusa-SE). Furthermore, the test was performed in the same condition reported for the IBU studies (section 3.2.3.4.4). This was performed in InfoStat software. Moreover, the following hypothesis were stablished:

H_0: The type of extraction technique (Soxhlet or Maceration) has no effect on the efficiency of corrosion protection evaluated at mild steel samples immersed in 0.10 M of nitric acid solution which contains 1000 ppm of plant extract.

H_1: The type of extraction technique (Soxhlet or Maceration) significantly influences on the efficiency of corrosion protection evaluated at mild steel samples immersed in 0.10 M nitric acid solution which contains 1000 ppm of plant extract.

The null hypothesis (H_0) is not accepted because the p-value is lower to 0.01 (see Table 9), therefore it can be concluded that the type of extraction technique significantly influences on the efficiency of corrosion protection evaluated at mild steel samples immersed in 0.10 M nitric acid solution which contains 1000 ppm of Tara plant extract. This is consistent with the results obtained in the FTIR and polyphenolic test. Thus, the Tara-SE reported a higher concentration of polyphenols, therefore there is more electron rich functional groups that can interact with the mild steel surface forming a thicker protective layer.

Table 9. ANOVA test of the inhibition efficiency as effect of the type of extraction technique

Source of Variation	**SS**	**DF**	**MS**	**F**	**p-value**
Model	14.28	1	14.28	40.55	$< 1\times10^{-3}$
Type of extraction technique	14.28	1	14.28	40.55	$< 1\times10^{-3}$
Experimental Error	3.52	10	0.35		
Total	17.80	11			

SS: Sum of Squares, DF: Degree of freedom, MS: Mean Square

H_{0*}: The type of plant material (Tara or Guayusa) has no effect on the efficiency of corrosion protection evaluated at mild steel samples immersed in 0.10 M of nitric acid solution which contains 1000 ppm of plant extract.

H_{1*}: The type of plant material (Tara or Guayusa) significantly influences on the efficiency of corrosion protection evaluated at mild steel samples immersed in 0.10 M nitric acid solution which contains 1000 ppm of plant extract.

The null hypothesis (H_{0*}) is not accepted because the p-value is lower to 0.01 (see Table 10), therefore it can be concluded that significantly influences on the efficiency of corrosion protection evaluated at mild steel samples immersed in 0.10 M nitric acid solution which contains 1000 ppm of Tara plant extract. This is consistent with the results obtained in the mechanical test, weight loss measurements, LP, and PDP characterization techniques. Thus, the Tara-SE reported the highest corrosion protection for mild steel samples exposed to acid corrosive environment.

Table 10. ANOVA test of the inhibition efficiency as effect of the type of extraction technique

Source of Variation	**SS**	**DF**	**MS**	**F**	**p-value**
Model	271.32	1	271.32	821.10	$< 1\times10^{-3}$
Type of plant material	271.32	1	271.32	821.10	$< 1\times10^{-3}$
Experimental Error	3.30	10	0.33		
Total	274.62	11			

SS: Sum of Squares, DF: Degree of freedom, MS: Mean Square

3.2.4.8. Thermodynamics studies

The adsorption process is divided into two groups: (a) chemical adsorption, this involves the transfer of lone pair of heteroatoms and the formation of coordination bonds with the metal unoccupied orbitals according to the following reaction [233]:

$$Inhibitor_{sol} + xH_2O\ (ads) \leftrightarrow\ Inhibitor_{ads} + xH_2O_{sol} \quad (29),$$

where $H_2O_{(ads)}$ represents the water molecule adsorption onto the metal surface, $inhibitor_{(ads)}$ represents the corrosion inhibitor molecule adsorption onto the metal surface, x represents the size/ratio, which indicates the number of H_2O molecules replaced by an organic molecule [233], and (b) physical adsorption, this accomplishes by electrostatic interaction between the charged corrosion inhibitor and the charged metal [232]. Therefore, it is fundamental to stablish the mechanism of the adsorption, to understand better the inhibition process.

Therefore, by analyzing the EIS results, the adsorption of the compounds presented in the different plant extracts is the controlled step to protect the metallic plates against the

corrosion. However, it is necessary to establish which type of adsorption occurred in the metal structure; thus, it is necessary to perform the thermodynamic studies to establish which type of adsorption occurred and what the interaction is between both elements.

To study the mechanism of adsorption, firstly, the inhibition efficiency was established as a function of the immersion time, the temperature, and the concentration of inhibitor. Thus, the immersion time varied from 3 to 7 hours, the temperature varied from 305 to 345 K, while the concentration varied from 200 to 1000 ppm for the three obtained plant extracts. Figure S8 showed a loss of efficiency in the corrosion protection when the temperature of the medium increased; thus, at 345 K, the lowest corrosion inhibition was obtained for all the samples, as evidence of the desorption occurred at higher temperatures. This temperature effect reflects the exothermic nature of physisorption processes commonly observed in corrosion inhibition systems, where the weakening of adsorptive forces between inhibitor molecules and active surface sites occurs as thermal energy increases. The phenomenon demonstrates that the energy released during adsorption is insufficient to maintain stable surface complexes at elevated temperatures, ultimately favoring the entropy-driven desorption process [234].

Moreover, the time dependency followed the same patter, thus, as the time of immersion increased, the reduction of the corrosion inhibition was notable for all the tested concentrations. As it is indicated in Figure S7, when the metallic pieces are immersed in the solution after 5 hours, the decreased in the corrosion protection is notable. This occurred for all the temperatures. This is explained by the apparition of more spaces available to the acid attack as the evolution of hydrogen gas occurred when the time passes [235], thus the coverage surface covering capacity of the inhibitor decreased.

The second step to understand the adsorption process was the calculation of the energy of activation (E_a), the enthalpy of adsorption (ΔH_a), and the entropy of adsorption (ΔS_a) by plotting the logarithm of the inverses of the corrosion inhibition (1/CR) against the inversed of the temperature (1/T), see Figure S9. The data was acquired by using the Arrhenius equation (equation 20) and the transition state equation (equation 21).

Thus, Table 8 gathered the results of the E_a, $\Delta H_{a,\ and}$ ΔS_a as a function of the concentration of the plant extract. It is observed that for all the concentration, the E_a reported higher values when they are compared to the E_a of the blank solution (without the addition of inhibitor, E_a= 16.83 ± 1.10 kJ·mol^{-1}). Moreover, the highest E_a was obtained when 1000-SE was added with values equal to 30.52 ± 1.14 kJ·mol^{-1}. Hence, it

is a positive indicator of the protection properties of the prepared inhibitors because the higher the E_a, the slower the corrosion process becomes and the more difficult it is to occur by increased energy barrier. This incident also confirms the formation of a complex compound between the inhibitor and mild steel [235].

Also, from the data, an increase in the enthalpy of adsorption was observed for all the concentrations of the different plant extracts. For example, the ΔH_a increased from 12.45±0.45 kJ·mol^{-1} when it was not added an inhibitor to 22.17 ± 0.22 kJ·mol^{-1} when it was added 1000 ppm of Tara-SE (see Table 11). This result indicates that the process of dissolution of the metallic ions is restricted by the inhibitor, and the corrosion reactions are less favorable when the inhibitor is adsorbed into the metal structure [233].

Table 11. Activation calculated parameters for mild steel in the presence of different concentrations of prepared Tara, and Guayusa green inhibitors, at 3 hours of immersion.

Inhibitor	**E_a (kJ·mol^{-1})**	**R/n**	**ΔH_a (kJ·mol^{-1})**	**ΔS_a (kJ·mol^{-1} K^{-1})**
Blank	16.83± 1.10	0.7597 /5	12.45± 0.45	-8.47±0.03
Tara-200-SE	20.54± 1.12	0.9515/5	20.91± 0.50	-11.80± 0.11
Tara-600-SE	20.56± 2.18	0.9755/5	21.98± 0.32	-12.02± 0.21
Tara-1000-SE	30.52± 1.14	0.9934/5	22.17± 0.22	-43.17± 0.17
Tara-200-ME	14.93± 1.28	0.9316/5	18.95±0.70	-12.52± 0.08
Tara-600-ME	20.55± 2.08	0.9543/5	20.87±0.70	-15.42± 0.14
Tara-1000-ME	19.42± 2.35	0.9785/5	21.52±0.57	-29.25± 0.17
Guayusa-200-SE	18.51 ±1.21	0.8454/5	13.70± 0.50	-9.32± 0.03
Guayusa-600-SE	16.75± 1.70	0.9054/5	17.01± 0.57	-12.57± 0.11
Guayusa-1000-SE	18.42± 1.86	0.9547/5	18.71± 0.63	-13.82± 0.13

Values are expressed as mean ± standard deviations of 3 measurements

In the same direction, the entropy of adsorption went to more negative values for all the concentrations of the prepared inhibitors. As an example, starting from -8.47±0.03 kJ·mol^{-1}, when no inhibitor was added, the ΔS_a changed to -43.17 ± 0.17 kJ·mol^{-1}, when it was added 1000 ppm-SE. This is explained by the high order between the molecules, because of the formation of a protective layer, which consists in the high ordered heteroatoms of the components of the plant extract.

Also, the more negative values of the ΔS_a are a clear sign of the adsorption of organic molecules from the prepared plant extracts. This process necessitates water desorption, and the competition between these opposing processes results in specific disturbances at the electrolyte-metal interface. Furthermore, the larger negative ΔS_a values observed at elevated inhibitor concentrations indicated an increase in the entropy of the solvent. This is likely attributable to the desorption of a substantial quantity of water molecules previously adsorbed on the metallic surface, along with the presence of small, disordered inhibitor molecules adsorbed on the mild steel surface [224].

The previous studies demonstrated the favorable adsorption process between the components of the plant extract and the metal surface; however, this approximation should be deeper understood to have a clear picture of the process in the interlayer of the metal surface and the electrolyte. For that it was studied the adsorption process by calculating the equilibrium constant (K_{ads}) by different mathematical models as it was described in the section 3.2.4.3.7 (see Figure 22).

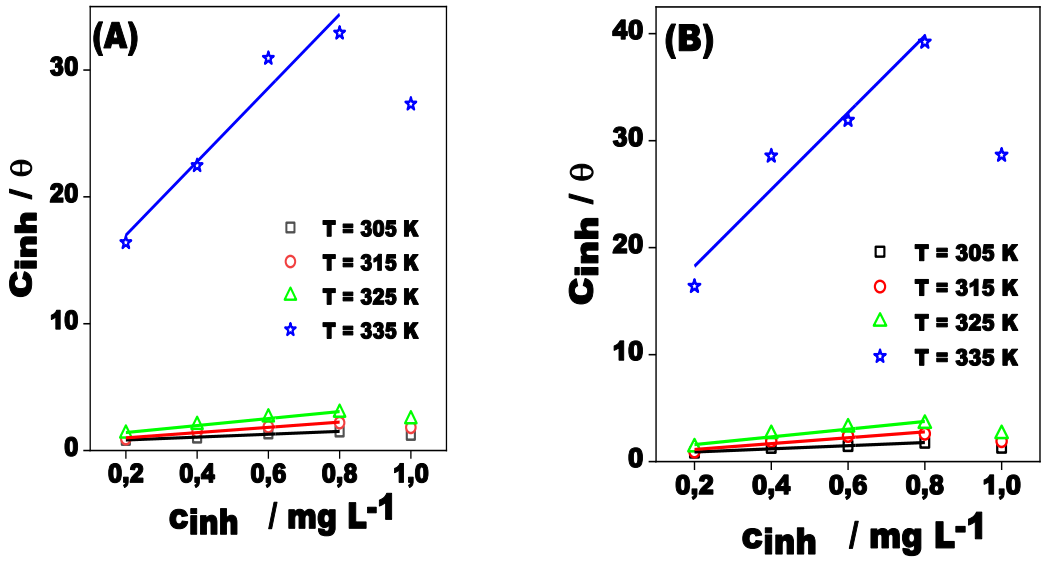

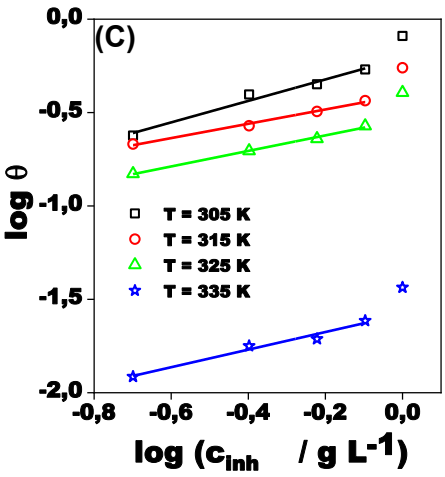
(C)
log θ
T = 305 K
T = 315 K
T = 325 K
T = 335 K
log (c_inh / g L-1)

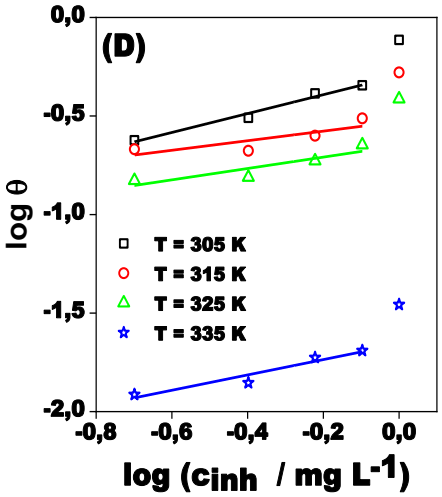
(D)
log θ
T = 305 K
T = 315 K
T = 325 K
T = 335 K
log (cinh / mg L-1)

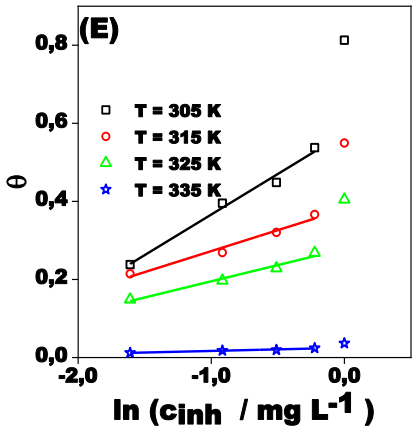
(E)
θ
T = 305 K
T = 315 K
T = 325 K
T = 335 K
ln (cinh / mg L-1)

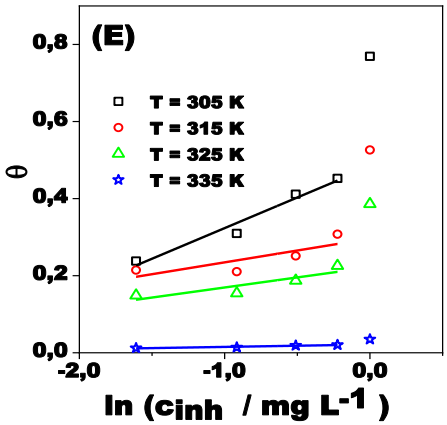
(E)
θ
T = 305 K
T = 315 K
T = 325 K
T = 335 K
ln (cinh / mg L-1)

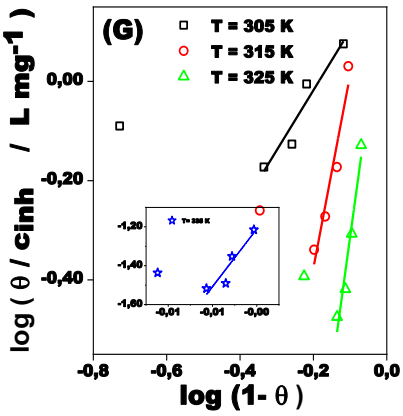
(G)
T = 305 K
T = 315 K
T = 325 K
log (θ / cinh / L mg-1)
log (1- θ)

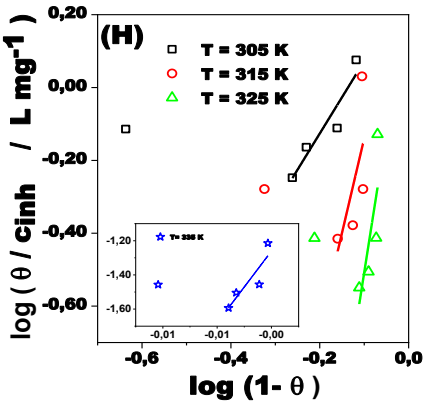
(H)
T = 305 K
T = 315 K
T = 325 K
log (θ / cinh / L mg-1)
log (1- θ)

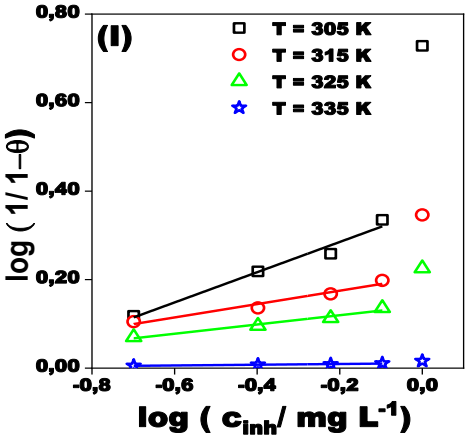
(I)
T = 305 K
T = 315 K
T = 325 K
T = 335 K
log (1/ 1–θ)
log (c_inh/ mg L-1)

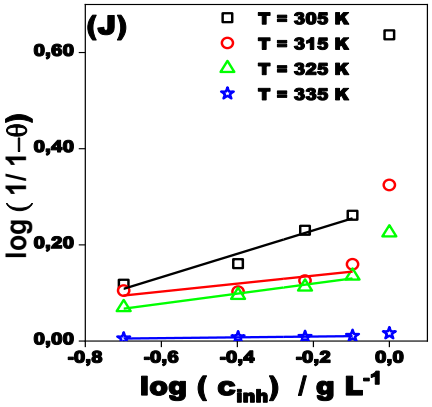
(J)
T = 305 K
T = 315 K
T = 325 K
T = 335 K
log (1/ 1–θ)
log (c_inh) / g L-1

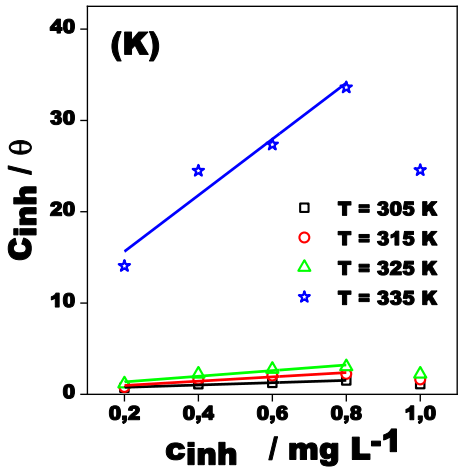
(K)
T = 305 K
T = 315 K
T = 325 K
T = 335 K
Cinh / θ
cinh / mg L-1

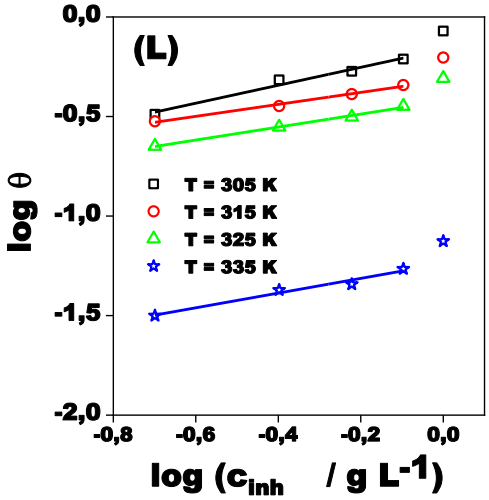
(L)
T = 305 K
T = 315 K
T = 325 K
T = 335 K
log θ
log (c_inh / g L-1)

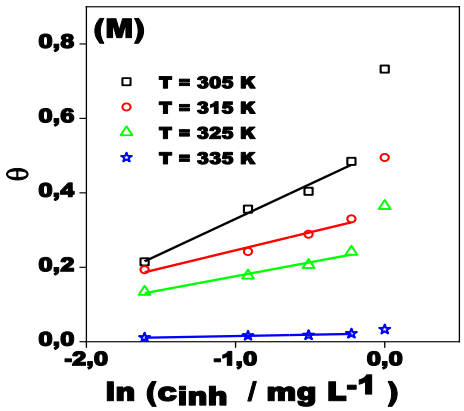
(M)
T = 305 K
T = 315 K
T = 325 K
T = 335 K
θ
ln (cinh / mg L-1)

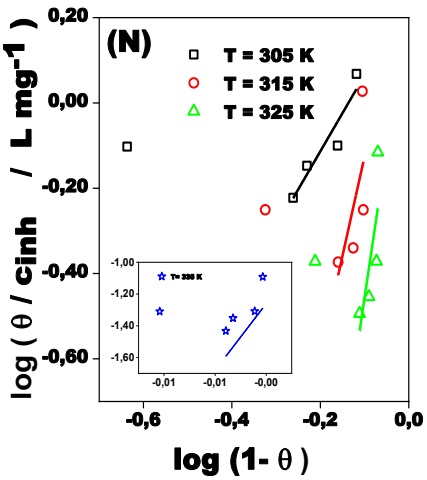
(N)
T = 305 K
T = 315 K
T = 325 K
log (θ / cinh / L mg-1)
log (1- θ)

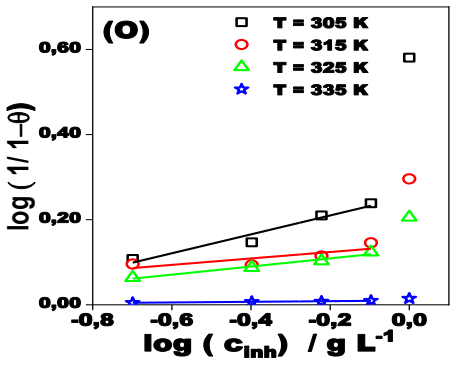

Figure 22. Plot of Langmuir (A, B, K), Freundlich (C, D, L), Tempkin (E, F, M), Flory Huggins (G, H, N) and El-Awary (I, J, O) isotherm models in mild steel samples in 0.10 M HNO_3 in the presence of Tara-SE extract (A, C, E, G, I), Tara-ME extract (B, D, F, H, J), and Guayusa-SE extract (K, L, M, N, O) at different temperatures (see inset), after 3 hours of immersion.

Moreover, two statistically parameters, the coefficient of correlation (R) and the reduced Chi-square (red-chi^2), were calculated to a better adjust of the thermodynamic model.

Therefore, Table S12 and Table S13 collected the statical parameters of the different modes. From this, it can be studied from the simultaneous perspective of obtaining an R-value close to 1, as well as a reduced Chi-square value of less than 1×10^{-3}. Therefore, for the Langmuir and Freundlich model are far away from 1, so both parameters are unnameable to explain the adsorption of the green inhibitor into the metal surface, and these models should discard from the present analysis.

Moreover, for the Temkin, Flory Huggins, and El-Awady isotherm models, both the R and the reduced Chi-square were very close to 1 in all the temperatures studied for the Tara extract, regardless of the extraction technique, except for the Tara-ME at 315 K, probably due to some experimental errors. While the R for the Guayusa-SE was far away from the desired value (1), the Chi-square reported similar values in comparison to the other extracts; thus, these mathematical models can also be applied to the Guayusa extract.

Therefore, the inhibition adsorption of the prepared extracts is better described by the Freundlich or El Awady models, which consider the number of molecules adsorbed into the metal surface; this parameter is represented by 1/n [233]. Thus, values of 1/n less than one imply the formation of a multi-layer of the inhibitor on the metal surface, while the value of n greater than one means that a given inhibitor occupies more than one active site [233]. As it is observed in Table 19, all the extracts reported values of 1/n lower than

one, so it indicated that a multilayer composed of the polyphenols, in the case of the Tara, and alkaloids, in the case of Guayusa, is adsorbed into the metal surface and thus reduces the rate of corrosion.

From Temkin, Flory Huggins, and El-Awady isotherm models, the K_{ads} were calculated. The results showed an increase in this parameter when it was studied at 305 K, while this tendency started to change; the K_{ads} decreased when the temperature increased. Therefore, the adsorption process is not favorable when the temperature increases because of the desorption of the molecules, as was explained by Figure S7. However, at 305 K, the increase in K_{ads} is a clear sign of corrosion protection because of the strong electric contact between the adsorbed species and the double layer; hence, at this temperature, the replacement of the adsorbed water molecules by the molecules of the inhibitor is favorable [234].

Finally, from the obtained results, the Gibbs free energy of adsorption (ΔG_{ads}) was calculated according to the equation 29. By analyzing the numbers, it can be appreciated that all the values were negative, so they consistently indicated the spontaneous reaction process. Therefore, the adsorption process and the stability of the adsorbed layer on the mild steel surface are favorable. Furthermore, all the ΔG_{ads} were higher than -40 $kJ \cdot mol^{-1}$; it can be concluded that the inhibitor is physically adsorbed onto the metallic surface. So, the adsorption is controlled by the electrostatic interactions between the metal and the charged molecules that come from the extract's functional groups [234].

Overall, from the thermodynamic studies, the presence statements for all the prepared plant extracts (Tara-ME, Tara-SE, and Guayusa-SE) are found for the present research: (a) the inhibition process is hugely influences by the time and the temperature, thus, when the time of immersion is higher than 3 hours and the temperature is higher than 305 K, the prepared extracts loss their performances; (b) the E_a, ΔH_a, and ΔS_a calculated values demonstrate the protection given by the addition of the prepared extracts, thus the corrosion reactions are less favorable in the presences of the inhibitor; (c) the Temkin, Flory Huggins, and El-Awady isotherm models described better the adsorption process of the inhibitor; (d) the reported ΔG_{ads} values indicated that the inhibitor is physically adsorbed in the metal surfaces, this means that a given inhibitor occupies more than one active site in the metal, this occurred by the electrostatic interactions between the functional groups (polyphenols in case of the Tara, and alkaloids in the case of the Guayusa) and the metal surface, which enables to replace the adsorbed water molecules and considerable reducing the corrosion.

3.2.5. Partial conclusions

A novel polymer coating to protect Ti–6Al–4V exposed to a saline corrosive environment and different plant extracts, used as green inhibitors, to protect mild steel exposed to acid corrosive environments were developed. The first technology was produced by an in-situ polymerization of PMMA plus different levels of IBU (0.20, 0.40, and 1 mM) using THF as a solvent due to its high affinity with both components. Hence, Ti–6Al–4V was covered with the polymeric solution by applying a speed-controlled dip coating process. Therefore, the produced technology was evaluated from different perspectives. One perspective consisted of the chemical characterization of the polymeric solution, another perspective consisted of the mechanical characterization of the polymeric coating, and the other perspective was the study of the inhibition effectiveness by using electrochemical methods.

Consequently, the chemical characterization of the prepared polymers was performed by using FTIR technique to analyze the principal vibrational bands, which indicate the degree of interaction between the PMMA and the IBU. In this context, the reported stretching vibration, adsorption band, and bending bands for all the prepared polymers (PMMA-xIBU) were comparable to the peaks obtained at the pure PMMA and IBU compounds. However, the only differences between all the spectra were the intensity of the vibrations. Thus, when more IBU was added to the polymeric matrices, the specific vibrations for the IBU increases. The findings confirmed the cross-linked polymerization caused by the addition of the IBU to the PMMA.

Therefore, at first glance, the interaction between the IBU and the PMMA occurred, but it was necessary to study the mechanical characteristics of the prepared polymer matrices to see if the addition of the IBU was positive. Hence, the mechanical properties were evaluated by means of the universal tensile strength test. The data show that all the prepared films had a linear deformation of the elastic part, along with a deformation from the elastic to the plastic part when the stress was high. So, the polymeric matrices were stronger when more amount of IBU were added. This was demonstrated by the highest stress being reported when 1 mM of IBU was added with a strain stress equal to $10.99 \pm 4\times10^{-3}$ kPa. The same tendency was also reported for film thickness; thus, the highest values were reported when 1 mM IBU was added; it reported values equal to 12.86 ± 1.14 kPa. On the other hand, the addition of IBU decreased the fracture strain; thus, the lowest values were reported by the PMMA-1mM-IBU, and the strain was equal to 1.50 ± 0.02

mm/mm. So, from the mechanical resistances, it was discussed that the prepared coating technology is viable when the Ti–6Al–4V is not exposed to high stress loads.

Then, it was necessary to evaluate the morphological characteristics of the coatings because the corrosion protection by coating is highly dependent on the homogeneity of the polymeric surface. Therefore, optical microscopy revealed a well-distributed film on the metal surface, and the addition of IBU led to the appearance of some agglomerates. However, this information was not clear enough, so more detailed information on the polymeric film was obtained by using AFM. Thus, it was observed that there was a change in the roughness and homogeneity of the polymeric film when more content of IBU was added. Consequently, microstructural domains emerged during the creation of the IBU–PMMA network. This process generates surface imperfections and promotes the enlargement of tumulus dimensions, both in diameter and height, as seen by the incremental rise in ibuprofen concentration.

The excellent mechanical properties were the first approach to the effectiveness of polymerization. However, the electrochemical measurements yielded deeper information. Therefore, we divided them into two parts. We looked at the OCP, the linear polarization, and the potentiodynamic polarization (shown as Tafel plots) in the first part. Consequently, from the OCP, it was the first approach that the coating acts as a cathodic type because of the dropping OCP values. The Tafel results clearly demonstrated this. It was clearly observed that the shift in the corrosion potential tends to move to the left side as the concentration of IBU increases. So, it went from 95 ± 0.14 mV vs. Ag/AgCl, KCl_{sat} when IBU wasn't on the polymer to -204 ± 2.02 mV vs. Ag/AgCl, KClsat when 1 mM of IBU was added to the PMMA. These results indicate that IBU is a cathodic type of inhibitor (the change exceeded 85 mV). Moreover, from the data it was calculated the inhibition efficiency. In this context, the highest inhibition efficiency was obtained when 0.40 mM of IBU was added to the polymeric solution (69.02 % ± 0.76 %), while the lowest inhibition efficiency was reported when 1 mM of IBU was added to the polymer (67.17 % ± 0.58 %).

The second part of the electrochemical measurements consisted of the EIS technique. It explained the interaction between the coating and the corrosive solution, and from these interactions, the inhibition efficiency was calculated. So, the interface interactions were plotted as Nyquist and Bode graphs. From them, it was established the equivalent circuit; for all the polymeric films, the equivalent circuit was $R_s(Q_fR_f)(Q_{dl}R_{ct})$. This circuit was composed of two-time constants, a solution resistance (R_s), a charge transfer resistance

(R_{ct}), film resistance (R_f), and two constant phase elements (Q_f and Q_{dl}). The principal insights detailed an increase in the R_{ct} as follows: 0 IBU/Ti–6Al–4 V electrode < 1 IBU–PMMA/ Ti–6Al–4 V < 0.20 IBU–PMMA/ Ti–6Al–4 V < 0.40 IBU–PMMA/ Ti–6Al–4 V, in which the R_{ct} when it was added 0.40 IBU reported the highest value (R_{ct}= 23.41 ± 5.41 ohm·cm^2), which reflects the capacity of the IBU + PMMA to decrease the electron transfer between the Ti–6Al–4 V and the NaCl, thus reporting a considerable inhibition against the corrosion. Moreover, the highest inhibition efficiency was reported when 0.40 mM was added to the polymeric solution with an efficiency equal to 89.53 % ± 1.37 %.

Then in the second part of the experiments, different Ecuadorian plants (Tara and Guayusa) were studied for the first time to produce a green corrosion inhibitor for mild steel exposed to acid conditions (0.10 M of HNO_3). Therefore, the first step was to obtain the plant extract from the powder, in the case of the Tara, and the leaves, in the case of the Guayusa. Thus, the influences of the extraction method were studied. Therefore, in the case of the Tara, a hot-liquid extraction method was performed (Soxhlet), achieving a yield of extraction equal to 10.59 % ± 0.06 %, and a cold solid-liquid extraction method (Maceration), achieving a yield of extraction equal to 13.89 % ± 0.09 %, while, in the case of the Guayusa, only the Soxhlet extraction was studied because of the higher performance of this technique reported in the Tara extraction.

After the preparation of the plant extracts, the chemical characteristics of them were studied to check if they have the potential to be used as corrosion inhibitors. In this sense, the principal functional groups were studied by employing the FTIR characterization technique. So, the main parts of the extracts were polyphenols (hydrolysable and condensed tannins), as shown by the stretching vibration, adsorption band, and bending bands found in the Tara-SE and Tara-ME. The Guayusa-SE showed a specific spectrum of the alkaloids. After the qualitative analysis, the quantitative content of the functional groups in the Tara and Guayusa extracts was studied. Hence, the content of polyphenols varied according to the type of extraction method (0.36 ± 0.03 g/kg of extract, 0.19 ± 0.07 g/kg of extract, and 0.05 ± 0.01 g/kg of extract for Tara-SE, Tara-ME, and Guayusa-SE). While only the Guayusa reported positive values to the alkaloids content, evaluated by using the Mayer's test, Dragendorff's test, and Wagner's test. So, as a first approach, it was observed that both the polyphenols and the alkaloids have heteroatoms (O, N, etc.) that can be used to reduce the extent of corrosion reactions.

Therefore, it was necessary to study if the functional groups in Tara and Guayusa could be applicable as corrosion inhibitors. To prove this, the mechanical and morphological

characteristics of the mild steel exposed to a corrosive acid environment were studied without and with the addition of different concentrations (200, 600, and 1000 ppm) of the prepared extract. Then, the effectiveness of the inhibition protection was tested by using accelerated tests of corrosion (PDP and EIS), and finally, the mechanism of protection was studied by applying thermodynamic studies.

Consequently, for the morphological characterization of the mild steel, SEM, tensile strength, and weight loss techniques were employed. First, the mild steel was immersed in 0.10 M HNO_3 without and with the addition of 1000 ppm extracts, and after this time the characterization was carried out. So, when the mild steel samples were exposed to the acid conditions without the inhibitor, the surface of the metal was highly affected by the corrosion reactions. The apparition of pits and the rupture of the structure were observed all over the surface. However, when extracts were added, the destruction process was slowed down, and only in certain places did a pit appear. This was also proved by the EDS spectra; thus, when the destruction of the metal appeared, the composition of the samples changed drastically. The destruction of the samples was also proved by the loss of the mechanical properties of the mild steel. Hence, the mild steel samples, which were not exposed to the acid medium, reported a fracture stress equal to 193.98 ± 2.40 GPa, while the mild steel samples soaked in nitric acid reported a fracture stress equal to 183.91 ± 2.95 GPa, and the samples soaked in nitric acid + 1000-Tara-SE reported a fracture stress equal to 191.65 ± 1.68 GPa. Furthermore, weight loss also reported the same tendency; thus, the calculated rate of corrosion, when no inhibitor was added, reported a calculated corrosion rate equal to 1.50 ± 0.27 $mm \cdot year^{-1}$, while with the addition of 1000 ppm of Tara-SE, the corrosion rate was equal to 0.07 ± 2×10^{-3} $mm \cdot year^{-1}$, achieving an inhibition efficiency equal to 95.90 % ± 1.41 %.

These results were supported by the results obtained from electrochemical characterization. First, the mechanism of protection was evaluated by using PDP; thus, the principal electrochemical parameters were extrapolated from the Tafel curve. Hence, the E_{corr} for most of the prepared samples moved to the cathodic part, but this change was >100 mV; thus, the inhibitors behave as mixed-type inhibitors (cathodic and anodic protection). Moreover, it was reported that there was a decrease in the current density (i_{corr}) because of the presence of the inhibitor. From these values, the inhibition efficiency was calculated, which achieves the highest results when 1000 ppm of Tara-SE was added, with IE values equal to 97.38 % ± 2.04 %. Moreover, the behavior of the metal/inhibitor/electrolyte interface was also studied by employing EIS measurements.

The EIS results were plotted as Nyquist and Bode graphs. The first was composed of two well-defined parts. The high-intensity region was presented as a semicircle, and the lowest region frequency was reported as an inductive loop because of the frequency dispersion. So, the diameter of the semicircle grows when the inhibitor concentration increases, as a function of the more resistivity of the system. On the other hand, the Bode graph reported an increase in two or three magnitude orders in the impedance's modulus (|Z|) because of the decrease in the capacitances caused by the adsorption of the polyphenols into the metal structure and a decrease in the impedances' modulus (|Z|) in a two or three magnitude order because of the increase in the resistance of the system, attributed to the reduction in the transfer of free electrons at the electrolyte/metal interface.

The graphs were analyzed using the Randles equivalent circuit (R_s(CPE R_{ct})), in which R_s is the solution resistance, CPE is the constant phase element, and the R_{ct} is the charge transfer resistance. From the calculated values, it was observed that the increases in the R_{ct} values highly depend on the amount of the inhibitor added to the solution; the C_{dl} decreases as a function of the increase in the $R_{p;}$ the increases in the n value, which represents the homogeneity of the surface, depend on the concentration of the inhibitor, and the increases in the relaxation time are attributed to the time taken to form the protective layer because of the adsorption of the extract molecules into the metal surface. From the R_{ct} values it was calculated the inhibition efficiency, which follows this trend: Guayusa-200-SE < Tara-200-ME < Tara-200-SE < Guayusa-400-ME < Tara-400-ME < Tara-600-SE < Guayusa-1000-SE < Tara-1000-ME < Tara-1000-SE. The highest inhibition efficiency was equal to 90.73 % ± 0.03 %.

The good performance of the prepared inhibitors reported inhibition efficiency higher than 90% for the 1000-Tara-SE, this efficiency reported similar results for the weight loss, the DPD, and the EIS measurements. Hence, the performance of the prepared inhibitor was comparable to other reported inhibitors. After proving the performances of the inhibitor, it was necessary to describe the adsorption mechanism of the extracts in the mild steel surface.

This was accomplished by utilizing thermodynamic studies. From the thermodynamic graphs (time of immersion vs. IE vs. inhibitor concentration; log CR vs. 1/T) it was build the mathematical adsorption models. Therefore, the principal results obtained to these studies were: (a) loss of efficiency in the corrosion protection when the temperature of the medium increased, (b) loss of efficiency in the corrosion protection when the

immersion time goes over the 3 hours; (c) increased of the activation energy as function of the increased of inhibitor concentration, which denotes the formation of a protective layer; (d) the increases in the ΔH_a and the decreases in the ΔH_s as function of the inhibitor concentration indicates the favorable reactions between the inhibitor and the metal surface; (e) Temkin, Flory Huggins, and El-Awady isotherm models described better the adsorption process, because of the R and reduced Chi-square were closed to 1; (f) the increased in the K_{ads} at 305 K is a clear sign of corrosion protection because of the strong electric contact between the adsorbed species and the double layer; and (g) inhibitor is physically adsorbed onto the metallic surface ($\Delta G_{ads} > -40$ kJ·mol^{-1}).

Overall, it can be concluded that both technologies prepared in the present chapter accomplish their functionality, so the corrosion protection for different metals (Ti–6Al–4V and mild steel) exposed to corrosive environments can be accomplished either using polymer coating or using plant extract inhibitors. They reported a high degree of inhibition protection, so they can be scaled up to produce in an industrial way. So, in the first case, the polymeric coating can be applied to the protection of prosthesis, and in the second case, the green extract can be applied to the oil, petroleum, and construction industry.

3.3. Modified electrodes for sodium diclofenac detection

3.3.1. Objective General

To chemically modified a glassy carbon electrode to produce sensing electrodes matrix for the sensitive detection of sodium diclofenac (DS).

3.3.2. Specific Objectives

- To investigate the electrochemical behaviour of the diclofenac sodium by using cyclic voltammetry and square wave voltammetry techniques.
- To obtain information about the redox reactions that occur in the GCE modified electrodes surface in the presence of DS.
- To study the effect of the addition of different nanomaterials to the GCE surface in the analytical parameters.
- To optimize the square wave conditions to achieve the maximum performances of the modified electrodes in sensing DS.
- To analyze the specificity, reproducibility, limit of detection, and sensitivity of the modified GC electrodes.

- To compare the obtained concentration of sodium diclofenac in tablets and wastewater with the results obtained by the standard UPLC-MS/MS method.

3.3.3. Reagents

To produce the chemically modified GC electrodes, the following chemicals were used: 2-[(2,6-dichlorophenyl) amino] benzeneacetic acid sodium salt (DS, $C_{14}H_{10}Cl_2NNaO_2$, 98.50 % purity, from Sigma-Aldrich), titanium(IV) isopropoxide (TIP, $Ti[OCH(CH_3)_2]_4$, 97 % purity, from Sigma-Aldrich), monopotassium phosphate (KH_2PO_4, 99 % purity, from Sigma-Aldrich), di-sodium hydrogen phosphate dihydrate ($Na_2HPO_4 \cdot 2H_2O$, 98 % purity, from Sigma-Aldrich), orthophosphoric acid (H_3PO_4, 99.99 % purity, from Merck), caustic soda (NaOH, 97 % purity, from Merck), nitric acid (HNO_3, 70 %, from Sigma-Aldrich), deacetylated chitin, poly(D-glucosamine), know as chitosan (chit), $((C_6H_{11}O_4N)_n$, from shrimp shells, ≥ 75 % (deacetylated), from Sigma-Aldrich), acetic acid (CH_3CO_2H, 30 % purity, from Merck), glucose monohydrate ($C_6H_{12}O_6 \cdot H_2O$, 98 % purity, from Sigma-Aldrich), IBU ($C_{13}H_{18}O_2$, from Sum Pharma/Romania, commercial tablets), D-(−)-fructose, D-levulose ($C_6H_{12}O_6$, 99 % purity, from Merck), PA ($CH_3CONHC_6H_4OH$, Sum Pharma/Romania, commercial tablets), citric acid ($HOC(COOH)(CH_2COOH)_2$, 99.50 % purity, from Merck), dopamine hydrochloride ($(HO)_2C_6H_3CH_2CH_2NH_2 \cdot HCl$, 98 % purity, from Merck), DS tablet (from Sum Pharma/Romania, commercial tablets), potassium ferricyanide ($K_3[Fe(CN)_6]$, 99 % purity from Sigma-Aldrich), potassium ferrocyanide ($K_4[Fe(CN)_6] \cdot 3H_2O$, 99.50 % purity, from Sigma-Aldrich), potassium chloride (KCl, 99 % purity, from Merck), ethyl alcohol (CH_3CH_2OH, 99 % purity, from Merck), titanium (IV) oxide anatase (TiO_2, 99.80 % purity, from Sigma-Aldrich), HEPES ($C_8H_{18}N_2O_4S$, 99.80 % purity, from Sigma-Aldrich), multiwalled carbon nanotubes (MWCNTs, 98 % purity, 6–13 nm diameter and 2.50–20 mm length, from Sigma-Aldrich), sulfuric acid (H_2SO_4, 99 % purity, from Merck). The reported chemicals have analytical purity, and they were used as they were received from the supplier without the application of any purification process. Moreover, all the solutions were made using ultra pure water.

3.3.4. Equipment

To produce the nanomaterial the following equipment were used: Samdri—PVT-3D dryer (Tousimis Res. Corp., USA), Carbolite furnace, T4-DNA ligation kit (Thermo Scientific), plasmid purification kit (Viogene), plasmid DNA purificator (ThermoFisher).

Furthermore, morphological characterization of both the nanomaterials and the modified electrodes were performed by using the following equipment: XRD analysis of TiO_2 aerogel powder was realized by using a PANanalytical X'pert diffractometer (Almelo, Netherlands) (40 kV, 40 mA) with Cu-Ka radiation (λ =0.15 nm), N_2 adsorption/desorption evaluation was carried out on the TiO_2AG-NPs powder using a Sorptomatic 1990, Thermo Electron S.p.A., UK gas sorption system, structural characterization of the bioF was carried out by using FTIR spectroscopy using a Varian 2000 – Scimitar Series machine, and the morphological characterization of the modified electrodes were carried out by using scanning electron microscope (VEGAS 3 SBU, Tescan, Brno-Kohoutovice, Czech Republic) with energy-dispersive X-ray spectroscopy (EDX) spectra.

Moreover, the electrochemical characterization of the modified electrodes was carried out by using a computer-controlled AutoLab potentiostat (PGSTAT302N and PGSTAT 12, EcoChemie, Utrecht, The Netherlands) for cyclic voltammetry (CV), square-wave voltammetry (SWV), and electrochemical impedance spectroscopy (EIS) measurements. Finally, the wastewater characterization was carried out by using ultra-high performance liquid chromatography-mass spectrometry/mass spectrometry (UPLC-MS/MS), using a Shimadzu GCMS-TQ8050 NX apparatus.

3.3.5. Methodology

3.3.5.1. Preparation of the nanomaterials

The preparation of the TiO_2AG-NPs was carried out by the method reported by the authors Fort, et al. [236]. In brief, the nanoparticles were prepared by the sol-gel method in acid catalysis. Therefore, a solution of 5 mL TIP in 5 % ethanol was prepared and labeled as solution 1. Then, a second solution was prepared; it contained 1.12 mL doubly distilled water, 85 µL nitric acid (70 %) and 10 mL absolute ethanol. Subsequently, guanidine-HCl (GD) and urea (UR) were added to the first solution and let to reflux at 60 ºC for 4 hours. Afterwards, the reflux solution was slowly added to the second solution under vigorous stirring. After this process, a gel was obtained, which was matured for 3 weeks at room conditions. After this time, the ethanol was removed from the gel by using a supercritical CO_2 drying. The product obtained after the dried process was introduced in a furnace; it was set at 530 ºC in air and operated at a heat rate equal to 60 ºC/min. This process took 2 hours. Finally, the NPs were stored for further characterizations.

The preparation of the f-MWCTs was carried out by the method reported by the authors Pifferi, L. et. at. [237]. In brief, a solution which contained 150 g of MWCTNs, 12 mL of HNO_3 (3 N), was prepared and stirred for 24 hours. Then, the obtained solid was filtered on a polyvinylidene fluoride membrane, washed with distillated water until the pH of the solution was equal to 7. Subsequently, the filtrated solid was dried for 24 hours at 100 ºC.

The preparation of the bioF was carried out using the method reported by Jankovics et al. [238]. In brief, the first step was design. So, it was selected as a flagellin-based protein in which the D3 domain of Salmonella typhimurium flagellin was replaced by oligo peptides which interact with the DS. The experiment was performed using the pKOT-based vector, which contains the gene of the D3-deficient flagellin protein. Then, the protein expression and purification were done using the electroporated SJW2536 Salmonella strain that doesn't have flagellin and they were added plasmids that code for different types of flagellin (FliC-ArsR6, FliC-ArsR9, and FliC-ArsR10). The only adaptation step during the process in comparison with the flagellin produced for arsenic detection [142] was the polymer formation. Instead, it was performed in 20 mM HEPES, 150 mM NaCl, and pH 7 buffer, via the addition of ammonium sulfate in a final concentration of 0.60 M.

Therefore, the three prepared nanoparticles, TiO_2, TiO_2AG, and f-MWCNTs, were stored in room conditions in a dark place. While the bioF solution was stored in the fridge at 4 ºC to avoid the lose of its characteristics. The nanoparticles were then used according to the process described in the next sections.

3.3.5.2. Buffer and stock solution preparation

A 25 mM phosphate buffer solution (PB) was prepared by dissolving the precise mass of monopotassium phosphate and di-sodium hydrogen phosphate dihydrate in distilled water plus 0.10 M KCl. Thus, the pH of the buffer solutions was adjusted using H_3PO_4 and NaOH solutions. Moreover, a stock solution of DS at a concentration of 10 µM was prepared in a 25 mM PB buffer solution with a pH of 7 and stored in a refrigerator at 4ºC between measurements.

3.3.5.3. Electrode preparation

The GC (ALS Co., Tokyo, Japan, inner diameter of 3 mm) electrode was first sonicated by introducing it in an Erlenmeyer together with ethanol in an ultrasound bath for 30

minutes. Then, the surface of the GC was washed with distilled water. Subsequently, the surface was polished by using alumina (from Buher), which was poured into sandpaper (2000 mm). Afterward, the GC was rinsed with abundant distilled water and let dry at room temperature for 40 minutes for further use. This procedure was repeated each time before modification. Furthermore, for each electrochemical characterization technique, 3 cleaned GCs were prepared according to the previous detailed procedure.

3.3.5.4. Electrode modification

The modification of the electrode surface was carried out by the following steps: (a) chitosan solution preparation; (b) chitosan plus bioF solution preparation; (c) chitosan + bioF + nanoparticle solution preparation; (d) drop casting and solvent evaporation. In some of the electrode modifications, step b was omitted to prove the recognition characteristics of the bioF solution, so in these cases the solution consisted only of the addition of chitosan and the nanoparticles. However, each step will be described in the following paragraphs.

- Chitosan solution preparation (Chit): In a volumetric flask of 10 mL, 0.06 mL of acetic acid was poured, and the flask was filled with distilled water to produce a 0.10 M acetic acid solution. This solution was labeled as solution A. Then, in a volumetric flask of 5 mL, 5 mg of chitosan was introduced, and it was filled with solution A. The solution was sonicated in an ultrasound for 3 hours and labeled as solution B. Finally, 0.50 mL of solution A and 0.50 mL of solution B were introduced in an Eppendorf, and it was sonicated for 2 hours.
- Chitosan-bioF solution preparation: 1 mL of chitosan and x-bioF solution (where x is equal to 0, 1, 1.50, and 2 mg/L) were mixed in an Eppendorf. The solution was sonicated for 2 hours, then, it was labelled as Chit-x-bioF and stored in the fridge at 4 ºC.
- Chitosan-bioF-NPs preparation: 1 mL of the chitosan – 1 mg/L-bioF solution was mixed with x-nanoparticles (where x= 1, 2, and 3 mg/L). The solution was sonicated in ultrasound, then, it was labeled according to the type and concentration of the nanoparticle and stored in the fridge for further uses.
- Drop casting and solvent evaporation: 3 µL of the prepared chitosan, chitosan-bioF, and chitosan-bioF-NPs solutions were dropped-casted by using a micropipette into the cleaned surface of the pristine GC electrode. To specify, each solution was dropped in separately to study the effect of the addition of chitosan, bioF, and the NPs into the

electrode. Then, the electrode remained in a vertical position in a shaded area at room temperature for 2 hours to evaporate the solvent. Additionally, the changed electrodes were given names such as Chit/GCE, Chit+bioF/GCE, Chit+bioF+NPs/GCE (NPs can be TiO_2, TiO_2AG, or f-MWCNTs), and NPs+Chit/GCE.

3.3.5.5. Nanomaterials characterization

TiO_2 aerogel powder was characterized by means of XRD examination. This was conducted utilizing a PANalytical X'pert diffractometer (Almelo, Netherlands) operating at 40 kV and 40 mA with Cu-Kα radiation (λ = 0.15 nm). Diffraction patterns were acquired for 10 ˚ – 80 ˚ (2θ) by step scanning with a step increment of 0.02 ˚. The Scherrer equation was employed to calculate the average size of the crystallites. The evaluation of N_2 adsorption/desorption was conducted on the TiO_2AG powder utilizing a Sorptomatic 1990 gas sorption system from Thermo Electron S.p.A., UK. The sample was initially degassed and heated to 120 ˚C to eliminate any moisture. The Brunauer-Emmett-Teller (BET) method was employed to assess the specific surface area of TiO_2AG. The porosity was assessed using the Barrett-Joyner-Halenda (BJH) method.

Bioengineering flagellin (bioF) characterization was carried out by using FTIR spectroscopy using a Varian 2000 – Scimitar Series machine. Thus, 1 mL of the bioF suspension was introduced in the cantilever of the equipment, and the determination was run for 40 minutes. After that time, it was obtained the characteristic spectra.

The MWCNTs were not characterized in the present research because the characteristics of them were reported in [140], and it was not necessary to make further analysis. Finally, the TiO_2 also was not characterized because it was a commercial type of nanomaterial, so all the characteristics were reported by the produced (Sigma-Aldrich).

3.3.5.6. Electrode characterization

The morphological characteristics of the modified electrodes were carried out by using a VEGAS 3 SBU - SEM equipped with energy-dispersive X-ray spectroscopy (EDX) spectra. Thus, Chit/GCE, Chit+bioF/GCE, Chit+bioF+NPs/GCE (NPs can be TiO_2, TiO_2AG, or f-MWCNTs), and Chit+NPs/GCE electrodes were introduced in the cantilever of the equipment and pictures accompanied with EDS spectra were acquired.

Electrochemical characteristics of the samples were acquired by employing cyclic voltammetry, EIS, and square-wave voltammetry measurements. The employed three cell configuration distributed as follow: (a) pristine GCE or chemically modified GCE

(according to the section 3.3.2.4) as working electrode, (b) Ag/AgCl, KCl_{sat} as references electrode, (c) platinum wire as counter electrode, and (d) PB, stock solution or $K_3[Fe(CN)_6]/K_4[Fe(CN)_6]$ solution as electrolyte.

Thus, the CV measurements were carried out in an electrode potential range of -1 to 1 vs. Ag/AgCL, KCl_{sat}. In this context, the scan rate depends on the measurements, hence, for the determination of the redox process it was utilized a rate equal to 50 $mV \cdot s^{-1}$. While, for the effective area and controlled process calculation the scan rate varied from 10 to 500 $mV \cdot s^{-1}$.

Furthermore, EIS technique was performed at OCP, time interval of 15 min, in the frequency range of 10 mHz-10 kHz using an ac excitation signal of 5 mV amplitude. The results were obtained in form of Nyquist and Bode plots and the configuration of them was studied by comparing with an equivalent circuit obtained by using g ZSimp–Win 3.21 software.

Moreover, for the SWV techniques, the first step was to optimize the step potential, the frequency, the modulation amplitude, and the deposition potential (see section 3.3.6.5). Then, with the optimal parameters, different SWV voltammetry curves were prepared to build the calibration curve; this curve was built by the standard addition method. They were prepared by varying the volume of the standard solution with 10 mL of 25 mM PB electrolyte. The same methodology was used to determine the concentration of the tablets and the wastewater (without any purification), with the only difference being that the first addition was the tablet or the wastewater, respectively. Finally, the results obtained were compared with a UPLC - MS/MS analysis. Shimadzu (Japan) LCMS8060 instruments were used for the experiment. They had an ESI source and a Kinetex C18 LC column (100˚A, 150 × 2.10 mm, 2.60 µm particle size) with a flow rate of 0.20 mL/min. This study was conducted on wastewater samples at the Laboratory of the Department of Soil and Water Sciences (Soós Ernő Water Technology Research and Development Center, Nagykanizsa, Hungary). In addition, each SWV was repeated three times, using a newly chemically modified GCE.

3.3.6. Results and discussion

3.3.6.1. Nanomaterial characterization

The analysis of the crystal structure is fundamental in the preparation of TiO_2 aerogel nanomaterials, because it described the structural properties in the materials, which is necessary to be the most crystalline possible for better catalytic activity of the

nanoparticles, and it reported the morphology of the prepared material [239]. Moreover, the analysis structure detailed the formation of mesoporous ordered layers with a specific pore topology [240].

Consequently, Figure 23A illustrates the XRD measurements conducted to analyze the crystal structure of the synthesized nanomaterials. The pattern exhibited pronounced Bragg peaks, so affirming the extremely crystalline characteristics of the synthesized material. The recognized diffraction peaks were indexed as (101), (112), (200), (105), (211), (204), (116), (220), and (215), indicating the presence of the TiO_2AG anatase phase with tetragonal crystal lattice [140]. Furthermore, utilizing the equation:

$$t = \frac{k\gamma}{B\cos\theta} \quad (30),$$

where t represents the average crystallite dimension, k denotes a shape factor constant (assumed to be 1 for spherical particles), B signifies the full width at half maximum (FWHM), λ indicates the wavelength, and θ is the incident angle of the X-rays, the mean crystallite size was calculated to be approximately 14 nm.

Also, the adsorption/desorption isotherm of the TiO_2 nanoparticles was investigated (see Figure 23B). It shows IV type adsorption/desorption isotherms with H_4 hysteresis loop, which indicated that the samples were not have agglomerated particles with slit-like pores [241]. From the data, it can be observed the TiO_2AG matrix exhibits a monomodal pore distribution, with 63% of the pores measuring around 47 Å in diameter (Figure 21B inset). The usual values for mesopores are as follows: a radius of 5.30 nm, a pore volume of 0.42 cm^3/g, and a specific surface area (SBET) of 132 m^2/g. The particular surface area and total pore volume of the electrode matrix significantly influence its electroactive performance, as it relies on a surface electrode process, therefore the prepared TiO_2 aerogel nanoparticles (TiO_2AG) are good candidate to modified GCE to be used as a platform from detecting DS [242].

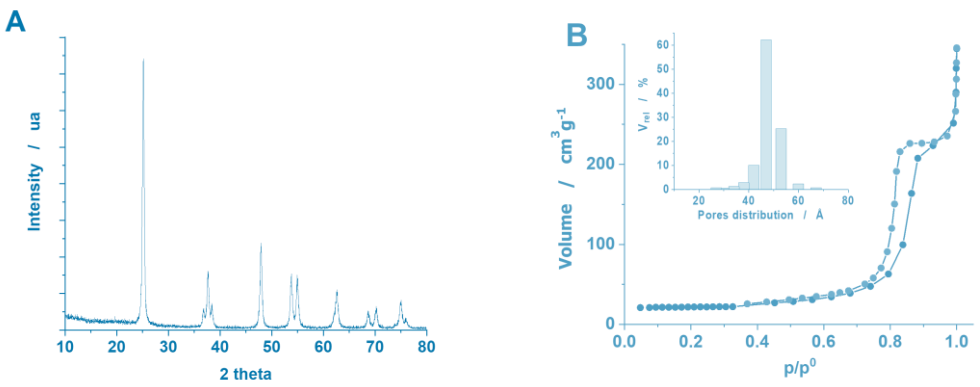

Figure 23. XRD spectra of TiO_2AG (A), and N_2 adsorption-desorption isotherm of TiO_2AG-NPs (B)

Source: [239]

Furthermore, the produced nanoengineering filaments were characterized by using FTIR measurements in the middle spectra (4000–500 cm^{-1}) because in this region it is possible all molecules possess characteristic absorbance frequencies and primary molecular vibrations in this range [243], and this principle allows the identification of the principal functional groups that compose the flagellin nanostructure. Figure 24 clearly divides the spectrum into five portions, as it is described below.

(i) at the position 4000-3500 cm^{-1} corresponds to the fatty acid region. This is described as a broad band made up of -OH groups (3489 cm^{-1}) and NH stretching modes (amide A around 3200 cm^{-1} and amide B around 3030 cm^{-1}) [244].

(ii) a region composed by stretching vibration between 3100 and 2800 cm^{-1}. In this region, it can be observed that C-H stretching vibrations of CH_3 and $=CH_2$ functional groups (spectra at 3050 cm^{-1} and 2850 cm^{-1}, respectively). These vibrations show the main parts of the fatty acid chains that make up the different membrane amphiphiles (phospholipids) and unsaturated fatty acid chains that are locked into the cell membrane's phospholipid structure [244].

(iii) At 1500-1200 cm^{-1}, this area is marked by the appearance of mixed stretching vibrations. These are made up of fatty acid bending vibrations, proteins, and compounds that carry phosphate. In this way, a vibrational stretching can be seen at 1600 cm^{-1}, which is caused by the -C=O (ester groups in lipids), and at 1490 cm^{-1}, a vibrational stretching can be seen that is caused by the nucleic acids (-C=O, -C=N, and -C=C) stretching of the DNA or RNA heterocyclic base structures [245]. Furthermore, at position 1490 cm^{-1}, the stretching vibration resulted from the presence of the tyrosine band [246]. It is important

to highlight that this portion is the most energetic because of the presence of conformation-sensitive amide I and amide II bands, which are the most intensive bands in the spectra of nearly all flagellin samples [247].

(iv) At 1200 to 900 cm^{-1}, this region corresponds to the presence of carbohydrates in microbial cell walls. This area had a complicated adsorption profile, with peaks mostly caused by the C-O-C and C-O-P stretching vibrations of different oligosaccharides and polysaccharides [248]. The peaks were mostly caused by the symmetric stretching vibration of PO_2 groups in nucleic acids. Hence, at position 1100 cm^{-1} is reported a P=O symmetric stretching, and at position 910 cm^{-1}, a stretching vibration group is observed in C-O-C groups.

(v) At 900 and 700 cm^{-1}, this region corresponds to the fingerprint of the molecule. It is by aromatic ring vibrations, in particular, amino acids and nucleotides. They are weak but unique absorbance that are characteristic of specific filaments [248]. Overall, the spectra shows that the properties of the prepared filaments were maintained during the production process; thus, the next sections will cover how these filaments contribute to the properties of the DS sensing platform.

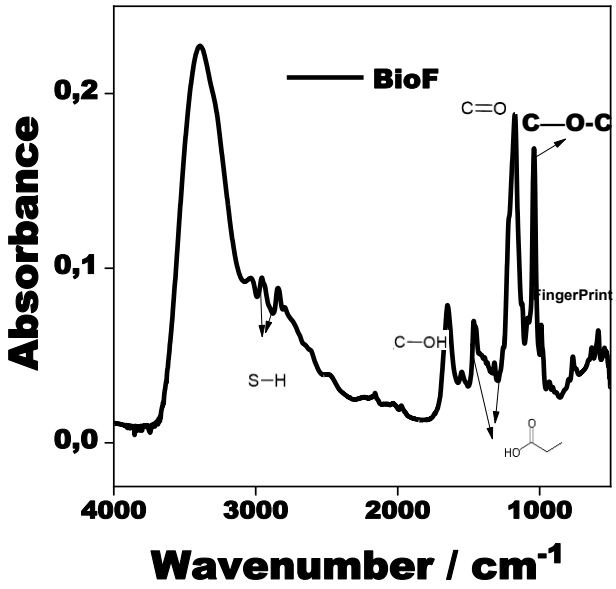

Figure 24. FTIR spectra for the nanoengineering filaments (bioF)

3.3.6.2. Modified electrodes morphological characterization

3.3.6.2.1. Glassy carbon electrode

Electrochemical techniques are basically interface techniques that measure how electrode and electrolyte interact with each other [249, 250]. This means that the shape of the chemically modified GC electrodes studied can tell you a lot about their properties,

since it's important to look at how uniform and thick they are to guess how well they will work in electrochemistry and catalysis, which then can be confirmed by electrochemical measurements.

Therefore, the morphological characterization was studied by means of SEM images. Figure 25A reports a non-homogeneous surface corresponding to the GCE electrode. It can be observed that some mountains and fractures appear all over the surface, with only certain homogenous spaces between the whole structure. On the contrary, at the chitosan/GCE, a homogenous surface can be observed in which no defects appear on the surface. Thus, the addition of chitosan allowed the improvement of the surface characteristics. Furthermore, when the GCE and chit/GCE EDS spectrum (Figures 23A and 23B, respectively) are compared, it is observed that there is a reduction in the carbon content when the chit is fixed on the surface (see Figure 23C and 23D). Furthermore, the chit/GCE reported a nitrogen content equal to 29.44 %, so it confirms the immobilization of the chitosan into the GCE surface.

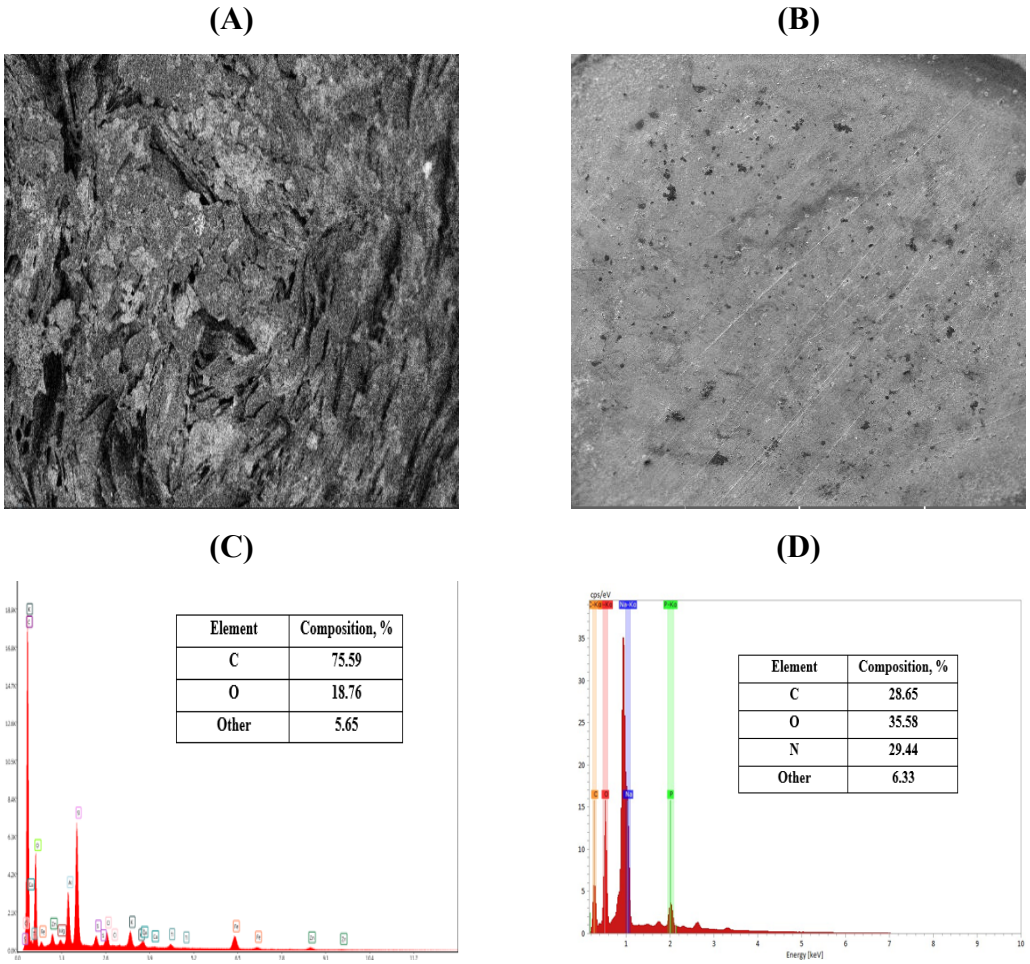

Figure 25. SEM pictures of the pristine GCE (A), Chit/GCE (B) matrix at amplitude 20 µm and magnification 800x, and the corresponding EDX spectra (C, D)

3.3.6.2.2. Glassy carbon electrode modified with bioF and TiO_2NPs

Moreover, when it is compared the modification of the electrodes by using the different nanomaterials prepared in the research, a notable change can be observed. Therefore, when it is added the bioF (Figure 26A), the surface of the electrode remains homogenous, but it appears a small conglomerate distributed all over the surface. These conglomerates appeared in a circular shape, and are randomly distributed all over the electrode surface, thus, the composition is optimal, because there will be more available stops in which the filaments can recognize the DS and perform the redox process [252].

While, when it is compared to the TiO_2 and TiO_2AG modified surfaces, it can be observed that both surfaces are homogenous and present a small round microstructure distributed randomly all over the surface. The main difference that can be observed in both electrodes is that in the case of the TiO_2 anatase, these microstructures formed a circular shape, and the radius of them is quite large, while in the case of the TiO_2, the size of these agglomerates is lower, and they presented a flat shape. Thus, the TiO_2 nanoparticles are better distributed into the electrode surface because of their crystalline structure and their small size in comparison to the commercial TiO_2 nanoparticles (Figures 26B and 26C). In this context, when the EDS spectra of both TiO_2 and TiO_2AG electrodes are analyzed, it is observed that the TiO_2 concentration increases in the case of the TiO_2AG because, of their small size, they can be fixed better onto the electrode surface. This enables the apparition of more active spaces, which will catalyze the redox reactions onto the electrode better. The inherent properties of the TiO_2AG nanoparticles enable them to improve the sensitivity and the selectivity of the modified surfaces in comparison to commercial anatase TiO_2 [253], and as a first approach, it can be seen by SEM and EDS images that they are better immobilized onto the surface structure.

(A) **(B)**

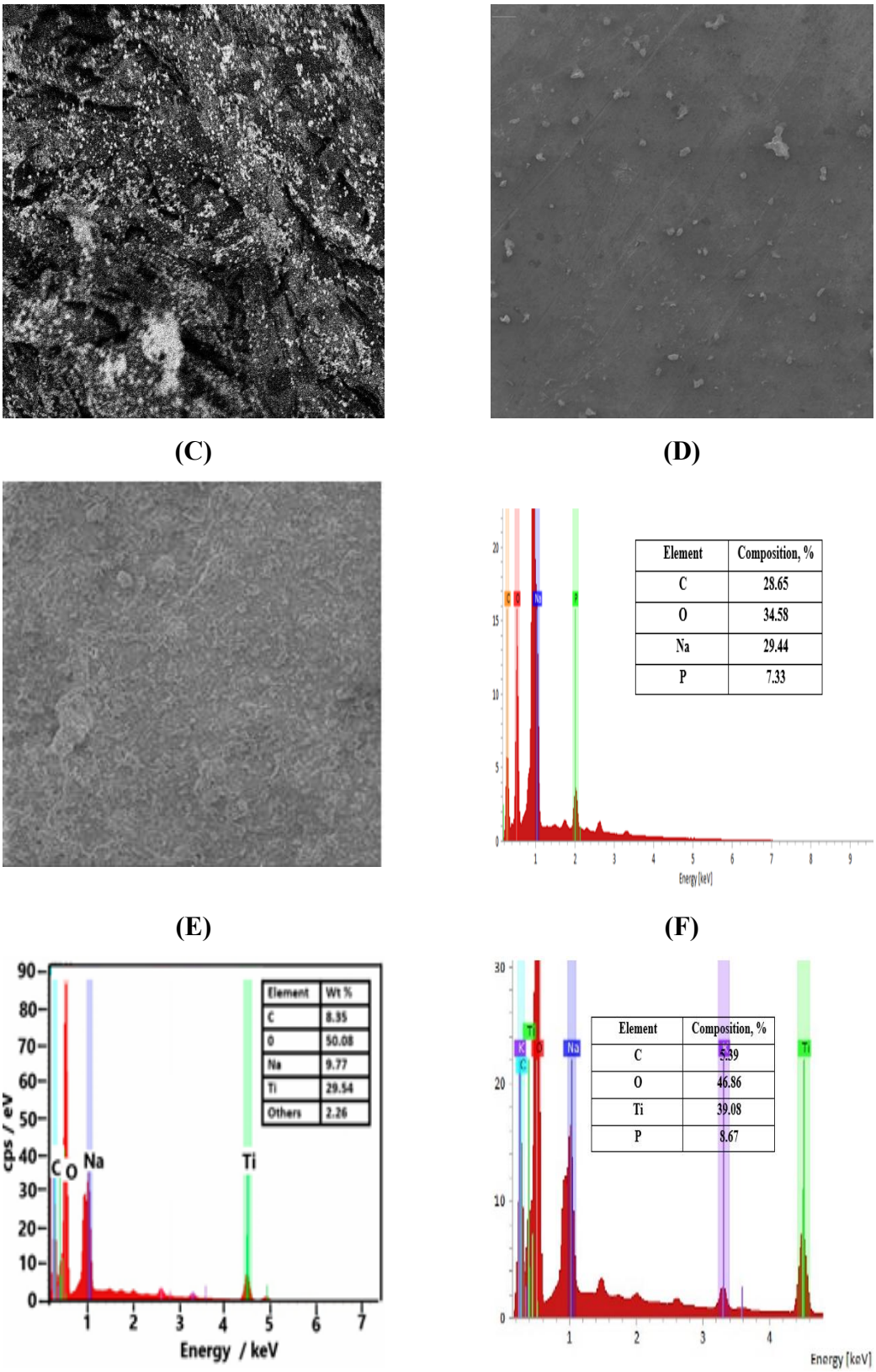

Figure 26. SEM pictures of the bioF+Chit/GCE (A), bioF+Chit+TiO_2 (B), and bioF+Chit+TiO_2AG-NPs/GCE (C) at amplitude 20 µm and magnification 800x, and the corresponding EDS spectra (D, E, F)

3.3.6.2.3. Glassy carbon electrode modified with bioF and f-MWCNTs

In addition, Figure 27A, which shows the change made by adding f-MWCNTs, showed a very different structure from the other electrodes. This reveals that the electrode surfaces have a tubular structure on them. This tubular structure is the normal shape of the MWCNT [254]. The image also shows that the nanotubes are evenly distributed onto the surface; thus, the porous structure and high surface-to-volume ratio of the f-MWCNT allows better modification. This is confirmed by the EDS spectrum (Figure 23B), which reported a carbon content equal to 80.45 %, which is highly superior to the other electrodes because the f-MWCNTs are basically carbon structures. Both the SEM and the EDS images demonstrated the homogenous distribution and coverage of the electrode by the addition of the f-MWCNTs.

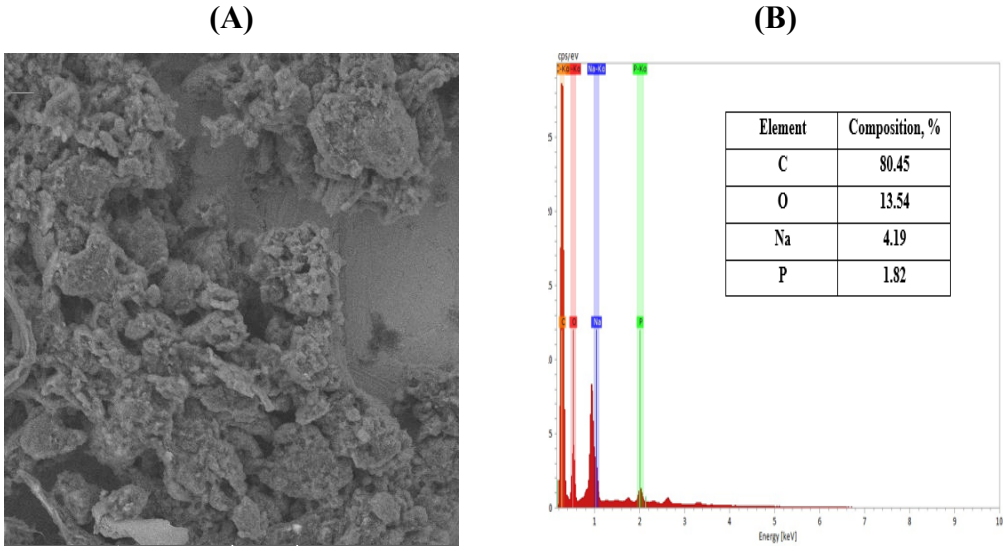

Figure 27. SEM pictures of the bioF+Chit+f-MWCNTs (A) matrix at amplitude 20 µm and magnification 800x, and the corresponding EDS spectra (B)

From the SEM and EDS images, it can be discussed (a) the surface in all the cases, except the GCE, is homogenous with the nanomaterial distributed all over the electrode surface; (b) the nanoengineering filaments (bioF) are placed randomly onto the electrode surface; however, in the case of the addition of other nanoparticles, they cannot be observed. This is confirmed by the EDS, which in all cases is dominated by the nanoparticle and not the filament; (c) the TiO_2AG nanoparticles are better distributed onto the surface in comparison to the TiO_2 anatase nanoparticles; thus, the better area-to-ratio, crystallinity, and sizes of the former nanoparticles enable their better distribution onto the surface; and (d) the f-MWCNTs are fixed all over the surface of the electrode; thus, the

area of the electrode appears to be covered by a tubular-shaped structure; anyways, the nanoengineering filaments cannot be appreciated in the image, but they are included. The last can be observed by the EDS spectra, which reported a small content of P and Na, which are former elements of the filaments.

Overall, the SEM picture shows that the electrode was changed by adding different nanoparticles (bioF, TiO_2, f-MWCNTs). These nanoparticles were stuck to the GC structure with chitosan. Therefore, the next sections are going to describe if the addition of each nanoparticle improves the behavior of the electrode to better detect the DS, with special regard to the analytical performances of the DS sensing platform.

3.3.6.3. Optimization of the bioF content

A primordial step prior to the electrochemical characterization of the modified electrodes was the optimization of the content of the nanoparticle. Thus, it was necessary first to study the effect of the bioF content. In this context, four different concentrations of bioF were added to the electrode surface, and the peak potential was measured in a solution that contains 10 µM DS. Figure 28 reported the peak intensities obtained by the addition of different levels of the nanoengineering filament solution (bioF). It is denoted that when there was no addition of bioF, no peak was reported, while the highest intensity peak was reported when 1 g/L of bioF solution was added, it reported an intensity peak equal to 6.75 µA vs. Ag/AgCl, KCl*sat*. Thus, this concentration was chosen to perform the rest of the optimization experiments.

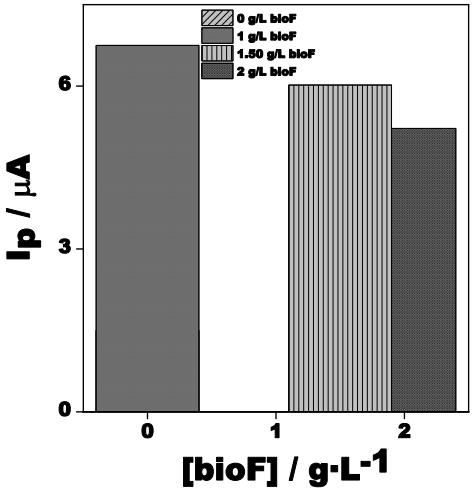

Figure 28. The dependency of the peak current registered at different compositions of the bioF. Experimental conditions: electrolyte, 25 mM PB (pH 4.6) plus 10 μM DS; scan rate, 50 mV/s; starting potential, −1 V *vs*. Ag/AgCl, KCl_{sat}.

3.3.6.4. Optimization of the nanoparticles content

Afterwards, the concentration of the nanoparticles was optimized onto the modifier solution. This process involved varying the concentration of nanoparticles (TiO_2, TiO_2AG, and f-MWCTNs) from 0 to 3 g/L. Therefore, for all cases, the lowest peak was obtained when there was no addition of nanoparticles, and the highest peaks were obtained when 2 g/L of NPs were added to the modifier solution. Moreover, it was reported that there was an increased tendency as the concentration of NPs increases, which was reversed when it was added NPs beyond 2 g/L. This increased peak current tendency was repeated for all the NPs as follows: 0 g/LNPs < 1 g/LNPs < 3 g/LNPs < 2 g/LNPs.

From the reported results, it can be discussed that the addition of the NPs increases the catalytic properties of the electrode; thus, the NPs can catalyze reactions due to their exceptional surface properties, which are transferred to the electrode; however, at high concentrations of NPs, these properties are not observed anymore; thus, the peak intensity decreased considerably. At first look, the nanoparticles tend to agglomerate or block the electrode surface, which increases the charge transfer resistances in the system.

Furthermore, another phenomenon that occurs when a larger quantity of nanoparticles is added is the hindering of the bioF. Thus, as it is observed in the SEM image, the bioF is accommodated into the NPs structure, but if there is more quantity of the NPs, the bioF

is hindered in their structure, and fewer filaments are available to sense the DS. So, it is recommendable to use 2 g/L of NPs to take advantage of both the filament and the NPs towards the DS. Therefore, for further analysis the sensor will be modified by a solution containing the optimal quantity of bioF and NPs, as it was obtained in the optimization analysis (see Figure 29).

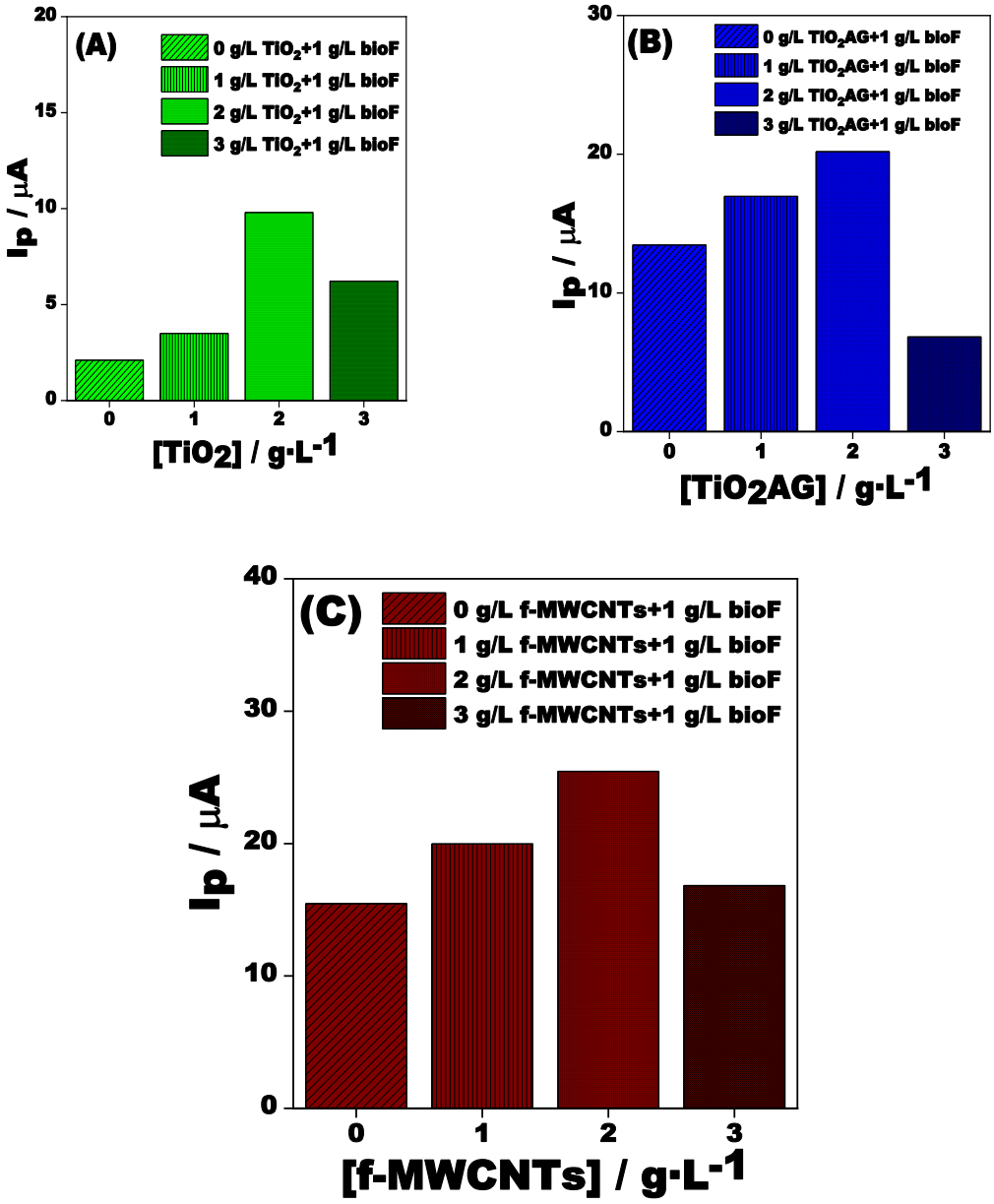

Figure 29. The dependency of the peak current registered at different compositions of TiO_2 (A), TiO_2AG and f-MWCNTs (C) in combination with 1 g/L of bioF. Experimental conditions: electrolyte, 25 mM PB (pH 4.6) plus 10 µM DS; scan rate, 50 mV/s; starting potential, −1 V vs. Ag/AgCl, KCl_{sat}.

3.3.6.5. Electrochemical Characterization

3.3.6.5.1. Electrochemical characterization at glassy carbon electrode modified with bioF and TiO_2NPs

After the morphological and structural characterization of the prepared modified electrodes, the key step in the preparation of the DS sensing platform was to study the electrochemical behavior of the chemically prepared electrodes by means of CV and EIS techniques performed in the presence and in the absence of DS to understand the route that the DS oxidation follows and to understand the insights of the electrode/electrolyte interface.

Firstly, it was necessary to see if the buffer solution reported any oxidation peak; thus, Figure 30A shows the cyclic voltammetry results of the different modified electrodes in the presences of 25 mM of PB at pH 4.6. Hence, all the modified electrodes did not report any apparent peak in the whole range of analysis; the information suggested that there is no interaction between the buffer solution and the modified electrode; thus, the PB is optimal to be used in this case because it did not create any interferences in the determination.

Moreover, Figure 30B reported the CV experiments when 10 µM of DS was added to the electrolyte solution. Thus, the voltammograms are clearly divided into two groups; the first group is composed of the GCE and the Chit. In this group, the voltammograms did not report any peaks, indicating the absence of redox reactions on the electrode surface. Therefore, both electrodes are not suitable for DS detection. In this sense, it can be understood that the GCE by itself is unable to detect DS, and the chit is only used as a membrane to physically or chemically entrap the bioF and the NPs; it does not do anything during the sensing process.

In the second group, the voltammograms of the bioF, TiO_2, and TiO_2AG can be distinguished in the presence of the DS. From them, it can be discussed that the presence of an oxidation peak at cathodic position +0.70 V vs. Ag/AgCl, KClsat at Chit+bioF/GCE, is shifted to +0.74 V vs. Ag/AgCl, KClsat, when the different TiO_2NPs were added. This peak only appeared at the cathodic section of the Figure 28, while at the reverse cycle there is no peak, which confirms that the redox process is irreversible [255].

In depth, the advantages of using NPs together with bioF are demonstrated by the increase in the peak current intensity, which follows this pattern: 4.74 µA (at Chit+bioF/GCE) < 7.75 µA (at Chit+ TiO_2/GCE) < 9.15 µA (at chit+TiO_2AG) < 15.19 µA (at Chit bioF+TiO_2+Ch/GCE) < 20.05 µ (at Chit+bioF+TiO_2AG/GCE). The synergetic effect of the TiO_2NPs and the bioF is demonstrated by the graph; however, it

is worth noticing that the peak tendency is highly dominated by the type of the added nanoparticles; thus, as was seen in the SEM images, the addition of TiO_2 reported a more homogenous surface, which at the same time increased the electron transfer kinetics; moreover, the addition of TiO_2AG also acted as an electron acceptor, allowing the collection of electrons generated from the redox reaction [256].

Therefore, Chit+bioF/GCE, Chit+TiO_2/GCE, Chit+TiO_2AG/GCE, Chit+bioF+TiO_2/GCE, and Chit+bioF+TiO_2AG/GCE voltammograms described the following two step reaction mechanism: the first step involves the transfer of one electron to the DS, and the second step occurred because the DS molecule losses one electron and one proton, so, the nitrogen resonates between the formation of a double bond and formation of a radical, which may be able to react with the medium thus producing the irreversible DS rupture into two products: a) 2,6 dichloroaniline and b) 2-(2-hydroxy prop-2-enyl) phenol. Therefore, the process involves a 1 e^- transfer, and it confirmed the irreversible process in which both intermediates are formed [255].

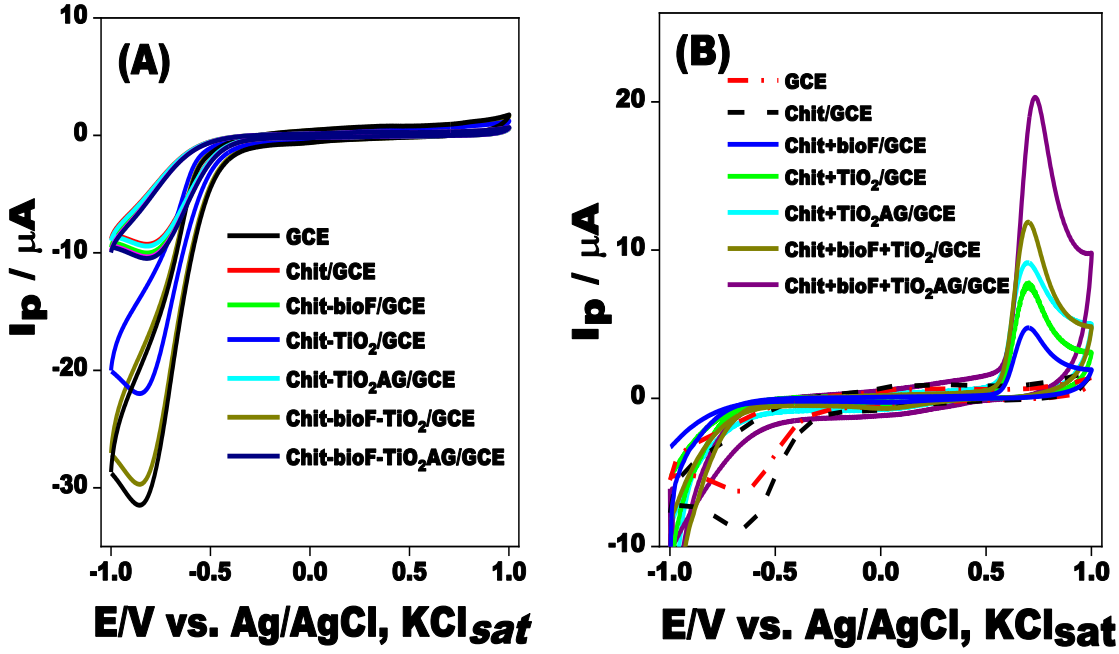

Figure 30. CVs recorded in the absence (A) and in the presence of 10 µM DS (B) at different electrodes (i.e., GCE, Chit/GCE, Chit+TiO_2/GCE, Chit+TiO_2AG/GCE, Chit+bioF+TiO_2/GCE, Chit+bioF+TiO_2AG/GCE, and Chit+bioF+TiO_2AG/GCE, see inset). Experimental conditions: electrolyte, 25 mM PB (pH 4.6); scan rate, 50 mV/s; starting potential, −1 V vs. Ag/AgCl, KCl_{sat}.

3.3.6.5.2. Electrochemical characterization at glassy carbon electrode modified with bioF and f-MWCNTs

Figure 31A shows the cyclic voltammetry results of the different modified electrodes in the presences of 25 mM of PB at pH 4.60 for the modified electrodes by using f-MWCNTs alone or in combination with bioF. There are no observed oxidation or reduction peaks, thus there are no reactions without the presence of DS. On the other hand, Figure 31B reported the CV obtained at chemically modified electrodes by using f-MWCNTs alone or in combination with bioF. Thus, in these voltammograms it can be seen the apparition of two quasi-irreversible peaks at the forward and reverse scan. The peaks appeared at +0.46 V and +0.74 V vs. $Ag/AgCl/KCl_{sat}$ in the anodic branch, and at +0.11 V and +0.38 V vs. $Ag/AgCl/KCl_{sat}$ in the cathodic branch irrespectively of the modifier. Moreover, at the Chit+bioF+f-MWCNTs/GCE modified electrode, the peak-to-peak separation potential ($\Delta Ep = Epa - Epc$) is 0.35 V for the peak I and 0.36 V for the peak II, and the ratio Ipa/Ipc is 2.39 for the peak I and 5.30 for the peak II, proving the quasi-reversible DS redox process occurring at this electrode interface. The anodic peak current intensities increase in the subsequent order: 19.50 µA (at Chit+f-MWCNTs/GCE) < 24.26 µA (at Chit+bioF+f-MWCNTs/GCE).

Chit+bioF+f-MWCNTs/GCE, and Chit+bioF+f-MWCNTs/GCE voltammograms described the following multistep mechanism: (1) initial step appears to involve an electron abstraction, which leads to a nitrogen centered radical cation (2) The radical cation undergoes rearrangement and deprotonation leading to a carbon centered radical para to the amino group, (3) the radical then undergoes a second electron abstraction leading to a carbocation (4) which reacts with water and by aromatization of the intermediate, 5-OH diclofenac (5) is formed and (6) by a reversible process of $2e^-$, $2H^+$ and it is obtained at the final the formation of diclofenac-2,5-quinone imine. This process is reported by other sensors prepared using MWCNTs [255, 256], thus, the bioF helped only in the enhance of higher electron transfer but the redox process is controlled by the MWCNTs.

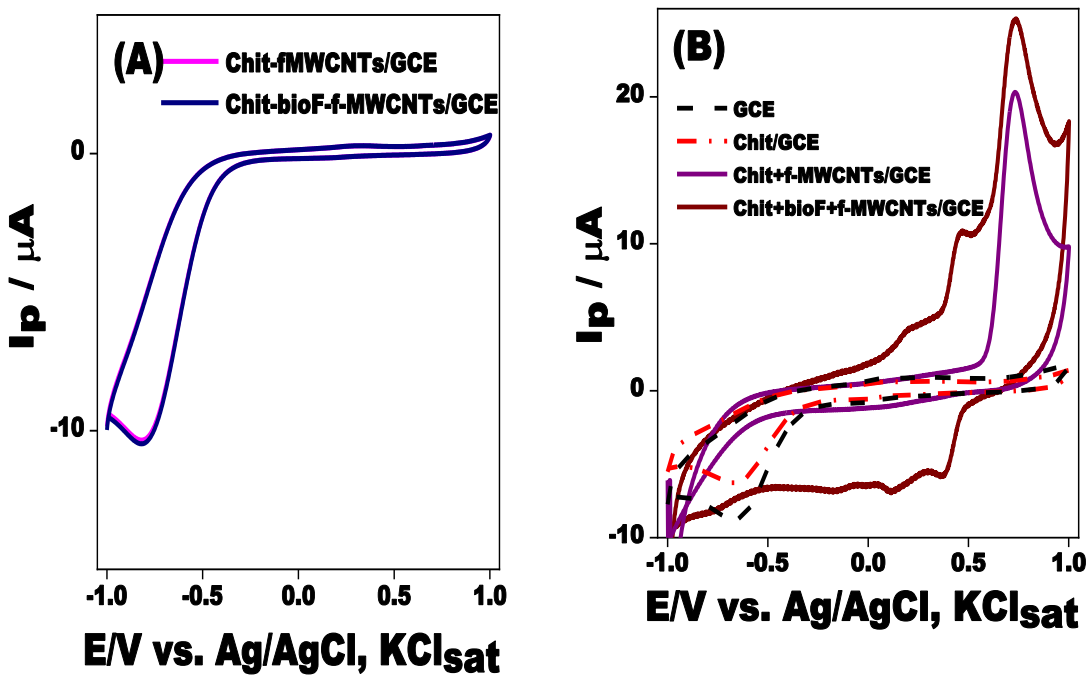

Figure 31. CVs recorded in the absence (A) and in the presence of 10 µM DS (B) at different electrodes (i.e., GCE, Chit/GCE, Chit+f-MWCNTs/GCE, and Chit+bioF + f-MWCNTs/GCE, see inset). Experimental conditions: electrolyte, 25 mM PB (pH 4.6); scan rate, 50 mV/s; starting potential, −1 V vs. Ag/AgCl, KCl_{sat}.

Therefore, it is clearly observed that, irrespective of the mechanism of reaction, the addition of the NPS together with the bioF reported satisfactory results at DS sensing; this responds to the high efficiency of the NPs in catalyzing reactions, as well as the recognition properties of the nanoengineering filaments when DS appears in the solution. Also, the processes are enhanced by the combination of adsorption and catalysis of the intermediates of the reaction, which should be studied as it is described in the following paragraphs.

3.3.6.6. EIS characterization

A key step to understanding the modification of the electrode surface is the EIS in the ferry/ferrocyanide redox probe, which enables understanding the degree of modification and the effectiveness of the modification in terms of current resistance, current charge capacity of the double layer, and catalytic efficiency of the modifier because of both variables (current and capacitances). This process is simple; because of that, it is well established for the characterization of chemically modified working electrodes.

In this context, the EIS spectrum was studied for all the modified electrodes, and the results were plotted as Nyquist diagrams (see Figure 32). The diagram showed a common two-section structure for all the tested electrodes. Thus, it consisted of (i) a semicircular portion at high frequencies and (ii) a straight line with a 45º slope, which corresponds to the Warburg mass-transfer process (diffusion process) [259].

Therefore, the plot was fitted with the equivalent circuit ($R_{el}(Q(R_{ct}W))$) which is composed of an uncompensated solution resistance (Rs), a charge transfer resistance (R_{ct}), which appears during electrolyte passage through the membrane, an interface non-ideal capacitor composed of a constant phase element of film (CPE film) and the double layer constant phase element (CPE_{dl}), and Warburg impedance (W) that estimates the mass-transport. It indicates the diffusion of the electroactive species through the film matrix [260]; this equivalent circuit was the best fit for the present data (χ^2).

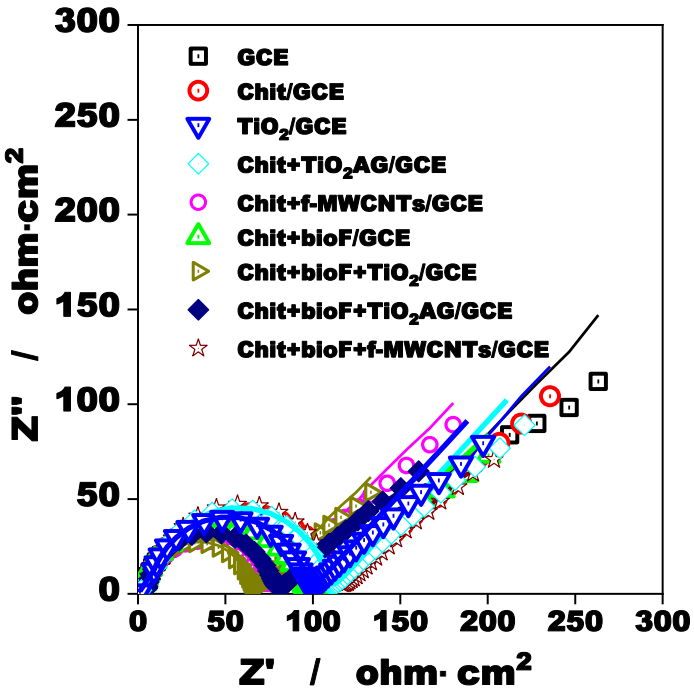

Figure 32. Nyquist diagram recorded at bare GCE (□), Chit/GCE (⊙), Chit+TiO_2/GCE (◊), Chit+TiO_2AG/GCE (◊), Chit+f-MWCNTs/GCE (⊙), Chit+bioF+TiO_2/GCE (◊), Chit+bioF+TiO_2AG/GCE (◆), and Chit+bioF+f-MWCNTs/GCE (★) modified electrodes. Experimental conditions: supporting electrolyte, 0.10 M KCl containing 5 mM $[Fe(CN)_6]^{3-/4-}$; frequency interval, 0.10–10^4 Hz (A).

Consequently, the parameters of the fitted data were compared to establish the principal changes that occurred as a function of the inclusion of the different chitosan

nanoparticles and nano-engineering filaments. The first approach that can be seen in the data is the dramatic change in the charge transfer resistances, which is correlated with the facility of interchange electrons, which in the case of electrochemical platforms this value should be the lowest possible to ensure the proper extension of the redox reactions.

Table S14 described the equivalent circuit parameters obtained for all the modified electrodes. It can be observed that in terms of charge transfer resistances (R_{ct}) the lowest value was obtained when it was added TiO_2AG with a resistance equal to 67.81 ± 0.78 ohm·cm^2, while the highest R_{ct} was reported by the electrode modified with chitosan, resistance charge equals to 128.20 ± 0.67 ohm·cm^2. Moreover, the decreased tendency reported for the charge transfer resistance follows the same pattern: Chit/GCE < GCE < Chit+bioF/GCE < Chit+TiO_2/GCE < Chit+bioF+TiO_2/GCE < Chit+TiO_2AG/GCE < Chit+f-MWCNTs/GCE < Chit+bioF+MWCNTs/GCE < Chit+bioF+TiO_2AG/GCE. Therefore, it can be observed that the addition of the chitosan increases the resistances of the current, because of the insulator properties of this polymeric. However, when it is added bioF to the electrode structure does not increase considerable the resistances in all the cases. Moreover, the addition of the NPs decreases considerably the charge transfer resistance, because TiO_2, TiO_2AG, and MWCNTs are good conductors, and the surface-area allows to create more active spaces along the electrode surface [247, 254].

On the other hand, the capacitances (C) presented the opposite trend, thus, Chit/GCE > GCE > Chit+TiO_2/GCE > Chit+bioF+TiO_2/GCE > Chit+TiO_2/GCE > Chit+bioF/GCE > Chit+TiO_2/GCE > Chit+bioF+TiO_2AG/GCE > Chit+f-MWCNTs/GCE > Chit+bioF+MWCNTs/GCE > Chit+bioF+TiO_2AG/GCE, therefore the inclusion of the nanoparticles increase the diffusion-limited processes, thus the ions are able to be diffused into the polymeric structure and the redox process are more favorable to occurs. On the other hand, the Warburg remains almost constant for all the modified electrode, this shows that this element is not affected by the addition of the NPs, the chitosan and the filaments.

Another interesting results, is the increases of the charge transfer rate (k_s) which from a value equal to 4.15×10^{-4} cm/s, reported at Chit/GCE electrode, increases to 7.94×10^{-4} cm/s when it was studied the Chit+bioF+TiO_2AG/GCE, thus confirming the optimal addition of the NPs in improving the sensors performances. In the sense of charge transfer rate, as faster is the process, the higher peak current intensity in voltammetric measurements. Therefore, the sensitivity and the limit of detection will increase due to the rapid transfer between the electroactive species and the electrode surface.

Consequently, the EIS analysis of the various modified electrodes highlights the following points: (i) The inclusion of the chitosan increases the charge transfer resistances because of the poor conductivity of the polymer, which acts as an insulator; (b) the inclusion of the engineering filaments does not change considerably the EIS parameters; (c) the inclusion of the NPs decreases the charge transfer resistance; thus, the lowest R_{ct} is obtained by the inclusion of TiO_2 which was expected because of the excellent properties of these nanoparticles reported by the XRD and SEM images; (d) the capacitances of the electrodes behave contrary to the $R_{ct;}$ thus, the increases in the capacitances caused the increase in the diffusion-limited processes; (e) k_s increases as the NPs are included into the GC surface; thus, the kinetic processes are accelerated by the NPs, and this enables achieving better analytical parameters of the prepared platform.

However, the EIS parameters are a first approach to the behavior of the electrodes; therefore, it is necessary to study other electrochemical properties of the system and to study the analytical properties of the electrodes to have a deeper understanding of the DS sensing capacity of the modified GC electrodes.

3.3.6.7. Studies of the pH influences

3.3.6.7.1. Studies of the pH influences at glassy carbon electrode modified with bioF and TiO_2 NPs

In terms of electrochemical characterization of the system, it was necessary to study the influences of the pH into the capacity of the modified electrodes to detect DS, because the pH of the supporting electrolyte affects the oxidation peak potential of diclofenac [255]. In this sense, the voltammetric oxidation was examined by using a solution containing 10 µM DS in 25 mM PB buffer solution (see Figure 33A). Hence, the pH of the solution change for 4 to 9, and the scan rate of the CV method was kept constant at 50 $mV{\cdot}s^{-1}$.

Figure 31A reported the behaviour of the peak potential when the pH is changed. Thus, the peak potential vs. pH reported a linear tendency for all the modified electrodes. In this sense, the equations reported for the prepared electrodes were:

Ep (pH 4−9) = [1050 ± 2.78 -53.57 ± 0.41 pH] mV vs. Ag/AgCl, KCl_{sat} (R = 0.9892/6) (31);

Ep (pH 4−9) = [992.02 ± 4.60 - 39.03 ± 0.68 pH] mV vs. Ag/AgCl, KCl_{sat} (R = 0.9993/6) (32);

Ep (pH 4−9) = [1035.28 ± 31.22 - 50.20 ± 4.65 pH] mV vs. Ag/AgCl, KCl_{sat} (R = 0.9838/6) (33);

For the Chit+bioF/GCE, Chit+bioF+TiO_2/GCE, Chit+bioF+TiO_2AG/GCE.

From the data, it can be deduced that the slope of the pH vs. cell potential (E) reported by Chit+bioF/GCE and the Chit+bioF+TiO_2AG/GCE proved a slight sub-Nernstian electrochemical behavior of the redox reaction; this little deviation from the Nernstian value (-59 mV). This lower value with respect to the theoretical one was generated because of the DS protonation states or the coordination of water molecules with the target molecules [263]. This conclusion confirms the two-step mechanism of reaction in the case of Chit+bioF/GCE and Chit+bioF+TiO_2AG/GCE [255].

Moreover, it also studied the influences of the pH with respect to the peak intensity. Therefore, Figure 33B reported that the optimal pH working condition for all the electrodes is a pH value equal to 4.60, because at this pH value the peak intensity was the highest in all the studied cases. This can be understood by two facts: the first is related to the pKa value of the chitosan ($pK_a \approx 6.50$, [164]), thus, to use chitosan is preferable to work at acid conditions, because at acid pH values there are larger amounts of protonated -NH_2 groups, which enable the interaction of the bioF and the NPs with the analyte [265]. The second fact pertains to the behavior of DS at lower pH values. The pKa value is 4.20, meaning DS tends to be ionized in acidic conditions, increasing its chances of participating in redox reactions [266]. The data analyzed led to the selection of pH 4.60 for all subsequent experiments performed with Chit+bioF+TiO_2/GCE or Chit+bioF+TiO_2AG/GCE.

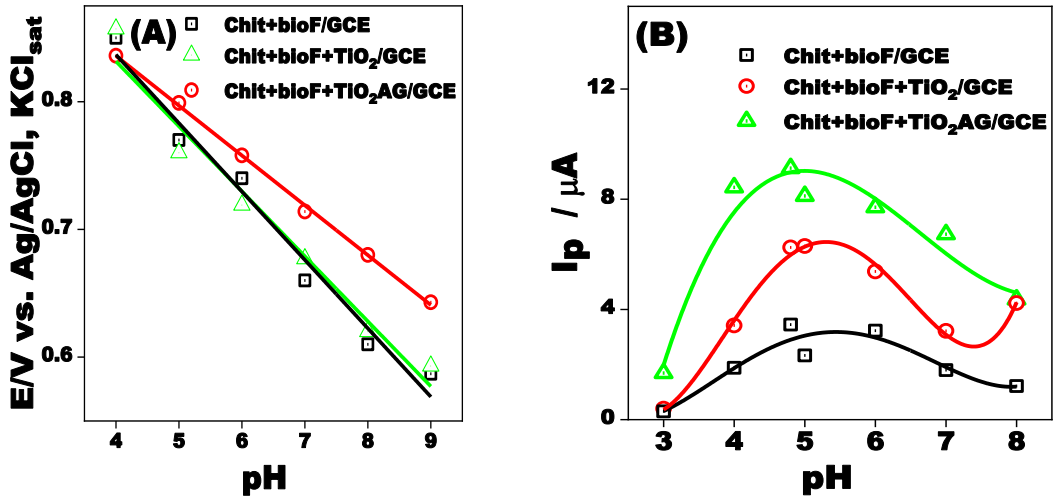

Figure 33. Influence of pH's solution values on the peak potential (A), and the peak intensity current (B) in the presence of 10 µM DS at different modified electrodes (see

inset). Experimental conditions: electrolyte, 25 mM PB; scan rate, 50 mV/s; starting potential, −1 V vs. Ag/AgCl, KCl_{sat}.

3.3.6.7.2. Studies of the pH influences at glassy carbon electrode modified with bioF and f-MWCNTs

At the same conditions reported above the pH influences in the electrode modified with bioF and f-MWCNTs (see Figure 33A) reported the following equation:

Ep (pH 4−9) = [1035.28±31.22 - 59.10 ± 4.65 pH] mV vs. Ag/AgCl, KCl_{sat} (R = 0.9838/6) for the Chit+bioF/GCE as indicates Figure 34A. Moreover, the slope of the slope of the pH vs. cell potential (E) plot reported a value equal to -59.10 mV which represents a Nernstian behavior. This confirms that the addition of the MWCNTs prevents the protonation of water molecules near to the electrode surface. Also, this confirmed that the same number of electrons and protons are involved in the redox process. This confirms the multistep mechanism [256].

Moreover, it also studied the influences of the pH with respect to the peak intensity. Therefore, Figure 34B reported that the optimal pH working condition for all the electrodes is a pH value equal to 5, because at this pH value the peak intensity was the highest in all the studied cases. Contrary to the TiO_2, the optimal pH is more positive, this is explained by the fact that f-MWCNTs, particularly those with carboxylic acid groups, are sensitive to pH changes, impacting their electrochemical behavior and, consequently, the accuracy of DS measurements [256]. Therefore, pH equal to 5 was chosen for the rest of the experiments performed with Chit+bioF+f-MWCNTs/GCE modified electrode.

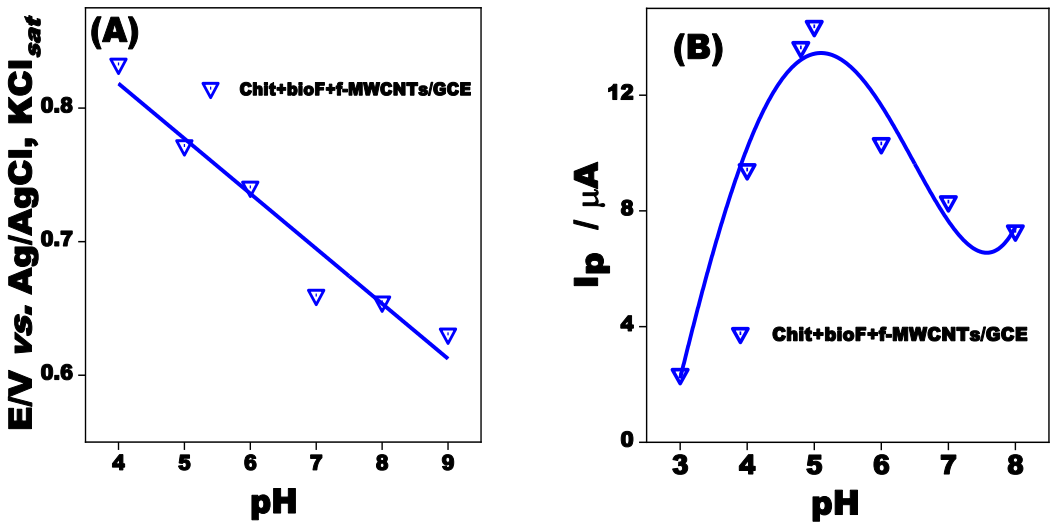

Figure 34. Influence of pH's solution values on the peak potential (A), and the peak intensity current (B) in the presence of 10 μM DS at Chit+bioF+f-MWCNTs/GCE. Experimental conditions: electrolyte, 25 mM PB; scan rate, 50 mV/s; starting potential, −1 V *vs*. Ag/AgCl, KCl_{sat}.

3.3.6.8. Controlled process studies and electrochemical active surface area calculation

3.3.6.8.1. Controlled process studies electrochemical active surface area calculation at glassy carbon electrode modified with bioF and TiO_2 NPs

The controlled process and the effective area calculation of the prepared sensors were studied by varying the scan rate of the cyclic voltammetry in different media (10 μM of DS in 25 mM PB and 5 mM $[Fe(CN)_6]^{3-/4-}$, respectively). Thus, from the controlled process, the slope of the tendency between log scan rate vs. log I_p indicates what is the process that is dominant in the redox reaction process of the DS over the electrode surface.

Therefore, Figure 35A described the above-mentioned relation the modified electrodes. Hence, the log I/A - log v/(V s^{-1}) dependencies have the following equations:

$\log I_p/A = (-6.53 \pm 0.22) + (0.62 \pm 0.01) \times \log v/(V/s)$ (33), R/no. points = 0.9550/6, for Chit+bioF/GCE;

$\log I_p/A = (-5.76 \pm 0.10) + (0.45 \pm 0.01) \times \log v/(V/s)$ (34), R/no. points = 0.9799/6, for Chit+bioF+TiO_2/GCE;

$\log I_p/A = (3.56 \pm 0.01) + (0.52 \pm 0.01) \times \log v/(V/s)$ (35), R/no. experimental points = 0.9921/6 at Chit+bioF+TiO_2AG/GCE.

Based on the data, all the electrodes had a slope close to 0.50. This means that the electrochemical redox reaction is controlled by a diffusion process [257]. Thus, the DS can diffuse into the electrode surface, which enables the redox process occurrence because there is more available analyte to perform the redox reactions; this facilitates the sensing mechanism of the analyte [267].

Moreover, from the slope of the relation between the square of the scan rate (v in $V \cdot s^{-1}$) against the peak intensity (I_p) presented in Figure 35B, the electrochemical active surface area (ECSA) was calculated according to the Randles–Sevcik Equation for irreversible processes at 25 °C [268]:

$$I_p = (2.69 \cdot 10^{5}) \times n^{\frac{3}{2}} \times A \times D_o \times v^{\frac{1}{2}} \times \alpha \times C_o^{*} \quad (36)$$

where I_p is the intensity of the peak in Amperes, n is the number of electrons (according to the mechanism of reaction 1 e^-), A is the geometric area in cm^2, v is the scan rate in $V \cdot s^{-1}$, D_0^* is the diffusion coefficient (7.72×10^{-6} $cm^2 \cdot s^{-1}$, for a solution of 5 mM $[Fe(CN)_6]^{3-/4-}$; [268]), α is the transfer coefficient (0.5 for the present case), and C_0* is the concentration of $[Fe(CN)_6]^{3-/4-}$ solution in M. By applying the formula, the following ECSA were calculated:

Chit+bioF/GCE: 0.07 cm^2, Chit+TiO_2/GCE: 0.05 cm^2; Chit+bioF+TiO_2: 0.08 cm^2; Chit+TiO_2AG/GCE: 0.09 cm^2; Chit+TiO_2AG/GCE: 0.14 cm^2. As it was expected, when is included the TiO_2 NPs irrespective of the type, the effective surface area increases. Also, from the data, it can be observed that the filament does not change considerable the active surface area. This was observed in the SEM imagines, that the filaments are attached to the nanoparticles, so there are no influences on the ECSA.

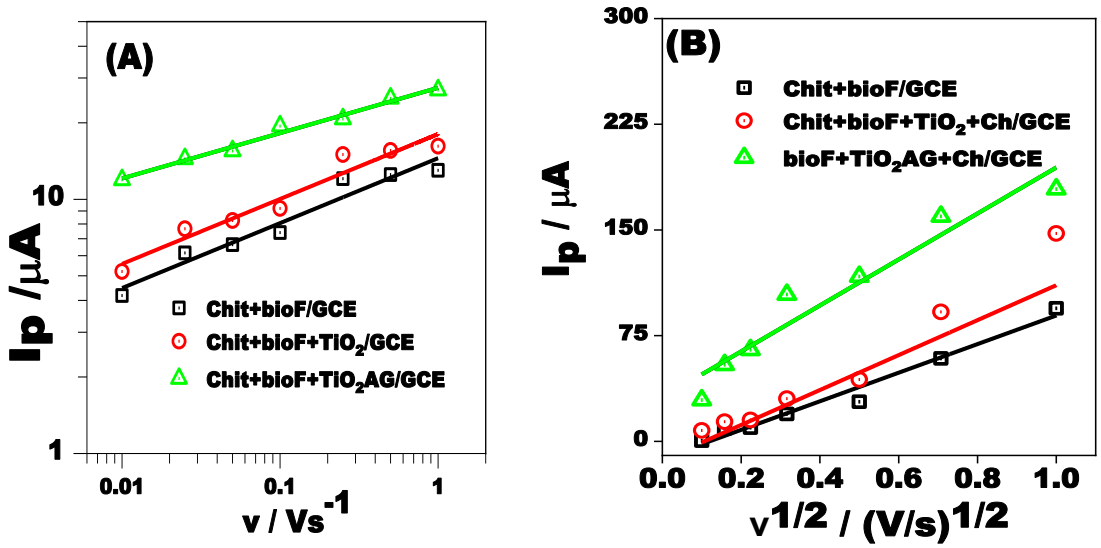

Figure 35. log I versus log scan rate (A), and I_p versus $v^{1/2}$ (B) dependencies recorded at Chit+bioF/GCE (□), Chit+bioF+TiO_2/GCE (⊙), and Chit+bioF+TiO_2AG/GCE (△). (A) Experimental conditions: electrolyte, 25 mM PB (pH 4.60); starting potential, -1 V vs. Ag/AgCl, KCl_{sat}. (B) Experimental conditions: supporting electrolyte, 0.1 M KCl containing 5 mM $[Fe(CN)_6]^{3-/4-}$; starting potential, -1 V vs. Ag/AgCl,KCl_{sat} (B)

3.3.6.8.2. Controlled process studies electrochemical active surface area calculation at glassy carbon electrode modified with bioF and f-MWCNTs

The controlled process and the ECSA were studied in f-MWCNTs with and without the addition of bioF at the condition reported in the above section. Thus, Figure 36A shows the tendency between log scan rate vs. log I_p. From there, the controlled process equations were:

$\log I_p /A = (-4.36 \pm 0.05) + (0.52 \pm 0.04) \times \log v/(V/s)$ (37), R/no. experimental points = 0.9870/7 at Chit+f-MWCNTs/GCE; and

$\log I_p /A = (-4.10 \pm 0.03) + (0.62 \pm 0.02) \times \log v/(V/s)$ (38), R/no. experimental points = 0.9975/7 at Chit+bioF+f-MWCNTs/GCE.

From the data, it can be observed that as the scan rate increases, the anodic peak current (peak II) grows. Additionally, both the IIa anodic peak and the IIc cathodic peak shift to more negative potentials, indicating the redox process of DS molecules at the modified electrode interface exhibits quasi-reversible behavior [269]. Moreover, the log I_p vs. log v reported a slope close to 0.5. This demonstrates, according to the Randles–Sevcik equation, that the electrochemical reaction is governed by diffusion control. Moreover,

the ECSA, calculated by the equation 42, were equal to 0.13 cm^2, 0.16 cm^2 Chit+f-MWCNTs/GCE and Chit+bioF+f-MWCNTs/GCE respectively, see Figure 36B.

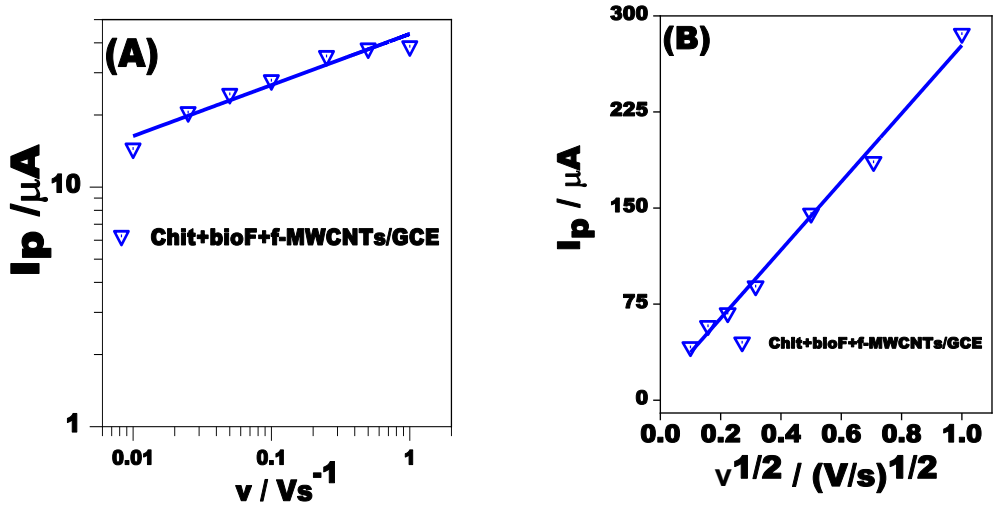

Figure 36. log I versus log scan rate (A), and I_p versus $v^{1/2}$ (B) dependencies recorded at Chit+bioF+f-MWCNTs/GCE (Δ) modified electrode. (A) Experimental conditions: electrolyte, 25 mM PB (pH 5); starting potential, -1 V vs. Ag/AgCl, KCl_{sat}. (B) Experimental conditions: supporting electrolyte, 0.1 M KCl containing 5 mM $[Fe(CN)_6]^{3-/4-}$; starting potential, -1 V vs. Ag/AgCl,KCl_{sat} (B)

Overall, the comparison of the pH influences, the controlled process, and the ECSA are described in Table 12. In this sense, the studies on the variation of the scan rate highlight the following key points: (i) The diffusion-controlled process was reported for all the chemically modified electrodes; thus, the DS diffuses onto the electrode surface, and there the redox process takes place; (ii) the inclusion of the nanoparticles increases the effective area of the electrode achieving the highest value at the Chit+bioF+f-MWCNTs/GCE with a ECSA equal to 0.16 cm^3; thus, the modification effectively covers the whole electrode surface and allows the active sites in which the DS can be oxidized, and it can be detected by the electrode. Overall, the electrochemical properties of the modified electrodes were optimal; as an example, the R_{ct} decreases, the effective area increases, and the k_s increases by the inclusion of the NPs onto the electrode surface, with better results reported by the TiO_2AG nanoparticles. This is as an effect of the high crystallinity of the TiO_2A.G., which effectively controlled the analytical performance of the chemically modified electrodes. It is widely recognized that the size, crystallinity,

and dispersion of nanoparticles are key factors influencing the conductivity and electrocatalytic performance of a nanomaterial [256].

Table 12. Electrochemical parameters obtained at the different modified electrodes

Type of electrode	Slope of E vs. pH / mV	Slope of log I_p vs. log scan rate / V/s	ECSA / cm^2
Chit+bioF/GCE	53.57	0.62	0.07
Chit+bioF+TiO_2/GCE	39.03	0.45	0.08
Chit+bioF+TiO_2AG/GCE	50.20	0.52	0.14
Chit+bioF+f-MWCNTs/GCE	59.10	0.62	0.16

3.3.6.9. Analytical characterization

3.3.6.9.1. Optimization of the square wave voltammetry operational parameters

Prior to the execution of the calibration curves of the different modified electrodes, it was necessary to find the best parameters for the SWV analysis. Thus, the influences of the step potential, step amplitude, and frequency were studied. The parameters were optimized on the Chit+bioF/GCE by analyzing a solution that contained 2 µM of DS dissolved in 25 mM of PB buffer solution. There were three measurements for each studied variable. The sequence of the optimization was: first, it optimized the step potential; then, with this optimized parameter, it optimized the step amplitude; finally, with both optimized parameters, it optimized the frequency.

Hence, for the optimization of the step potential, it was chosen two values which were 5 and 10 mV vs. Ag/AgCl, KCl_{sat}. The values were chosen according to the specification of the GPES software, which for this parameter cannot go below 5, and values higher than 10 did not report any peak. So, the highest peak intensity was reported at 10 mv vs. Ag/AgCl, KCl_{sat}, with an intensity peak equal to 0.72 µA (check Figure 37A), so this step potential was chosen for the next experiments.

Afterwards, it was optimizing the amplitude potential. For it, the amplitude potential varies from 5 to 75 mV vs. Ag/AgCl, $KCl_{sat,}$ as it is indicated in Figure 37B. The study found that 75 mV (0.81 µA) had the highest peak potential. However, there was a lot of variation between measurements, and the results could not be repeated in other experiments, so this step amplitude was not right. On the other hand, at a step potential

equal to 10 mV vs. Ag/AgCl, it obtained the second highest results, and the results were consistent between measurements, thus obtaining good reproduction; hence, this value was chosen at the optimal point to validate the SWV experiments.

Ultimately, the frequency underwent optimization. Thus, the frequency varied from 10 to 120 Hz; these values were the minimum and the maximum values allowed by the GPS software. In this context, Figure 37C reported that a frequency equal to 10 Hz yielded the best results. Because the reproducibility was the highest across all frequencies, regardless of peak intensity. These results were reproducible across different modified electrodes, which ensures the applicability of the electrode in the sensing of DS. When it was studied with different electrodes, the other frequencies could not be reproduced. Because of this, these frequencies are not good for this study. So, the bioF is too sensitive and can't recognize the DS well at high frequencies. This condition is also shown when the step amplitude is high; the performance of the bioF is reduced. Therefore, the best parameters for the SWV in the present research were: 10 mV vs. Ag/AgCl, KCl_{sat} step potential; 10 mV vs. Ag/AgCl, KCl_{sat} step amplitude, and 10 Hz frequency. These values were utilized for all the square wave measurements (construction of the calibration curve, study of the interferences, study of the reproducibility, study of the stability, and real sample studies) for the different modified electrodes.

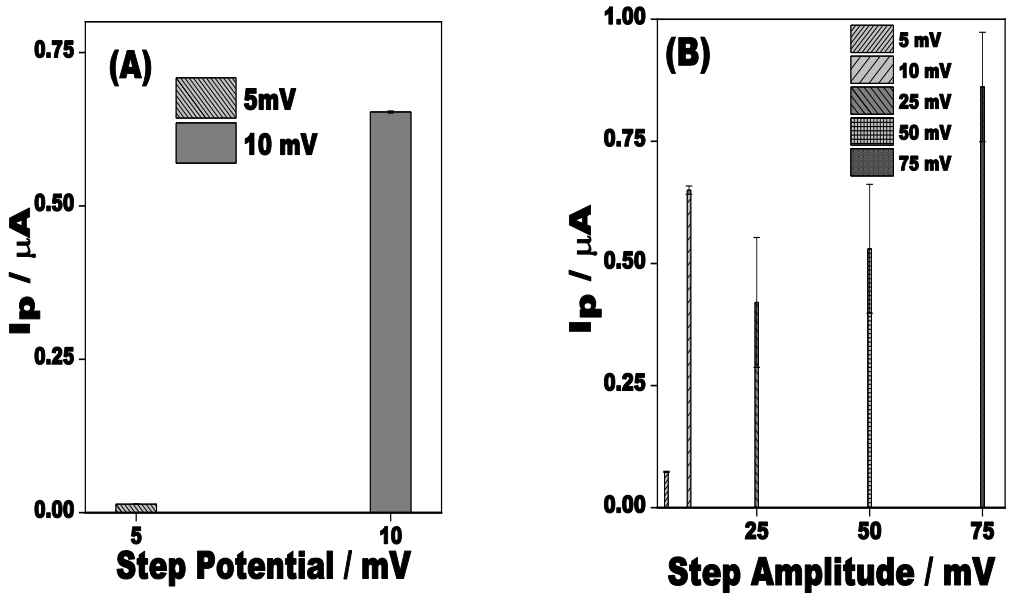

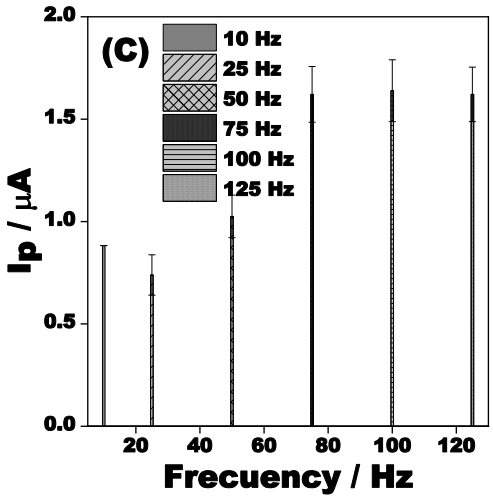

Figure 37. Optimization of the SWVs operational parameters recorded at Chit+bioF/GCE. Study of the step potential (A), study of the step amplitude (B) and study of the frequency (C). Experimental conditions: electrolyte, 25 mM PB (pH 4.60) plus 2 μM of DS; frequency, see inset; step potential, see inset; amplitude, see inset; starting potential, 0.60 V vs. Ag/AgCl, KCl_{sat}.

3.3.6.9.2. Calibration curve at glassy carbon electrode modified with bioF and TiO_2 NPs

The ability of the prepared modified electrodes to recognized DS in the buffer solution was performed by using the standard addition method which consisted in adding different volumes of the DS in 25 mM PB at pH 4.60, and after the addition the peak intensity, which was obtained by SWV, was measured for each addition, finally the voltammograms were plotted all together, to see their change as function of the DS added volume (check Figures 38A, 38B, and 38C).

Moreover, In Figure 38 (D, and E), the peak intensity (Ip) was calculated and plotted against the concentration of DS in the container. Hence, the linear tendency reported for the electrodes was:

$I_p/A = (-3.60 \pm 0.97) \times 10^{-8} + (0.31 \pm 0.01)$ [DS]/M (39), R = 0.9968, n = 10 points for the Chit+bioF/GCE;

$I_p/A = (1.13 \pm 0.04) \times 10^{-7} + (0.15 \pm 4\times10^{-3})$ [DS]/M (40), R = 0.9976, n = 10 points for the Chit+TiO_2/GCE;

$I_p/A = (1.29 \pm 0.02) \times 10^{-7} + (0.25 \pm 3\times10^{-3})$ [DS]/M (41), R = 0.9997, n = 10 points for the Chit+bioF+TiO_2/GCE;

$I_p/A = (6.05 \pm 0.22) \times 10^{-9} + (0.02\cdot \pm 2.904\times10^{-4})$ [DS]/M (42), R=0.9981, n =10 points for the Chit+TiO_2AG/GCE;

$I_p/A = (1.62 \pm 0.24) \times 10^{-8} + (0.41 \pm 1 \times 10^{-3})$ [DS]/M (43), R =0.9998; n =10 for the Chit+bioF+TiO_2AG/GCE.

From the above equations, the limit of detection (LOD; 3sb/m) and the limit of quantification (LOQ, 10sb/m), where sb is the standard deviation blank analyte signal and m is the slope of the calibration equation [169], were calculated for the different modified electrodes. Therefore, the calculated values of the LOD as follows: 90 nM for the Chit+bioF/GCE; 66 nM for the Chit+TiO2/GCE, 33 nM for the Chit+bioF+TiO2/GCE; 31 nM for the Chit+TiO2AG/GCE; 17 nM for the Chit+bioF+TiO2AG/GCE.

While the calculated LOQ for the different modified electrodes were as follows: 630 nM for the Chit+bioF/GCE; 250 nM for the Chit+TiO2/GCE; 111 nM for the Chit+bioF+TiO_2/GCE; 104 nM for the Chit+TiO2AG/GCE; 58 nM for the Chit+bioF+TiO2AG/GCE; 166.5 nM for the Chit+f-MWCNTs/GCE; and 310 nM for the Chit+bioF+f-MWCNTs/GCE.

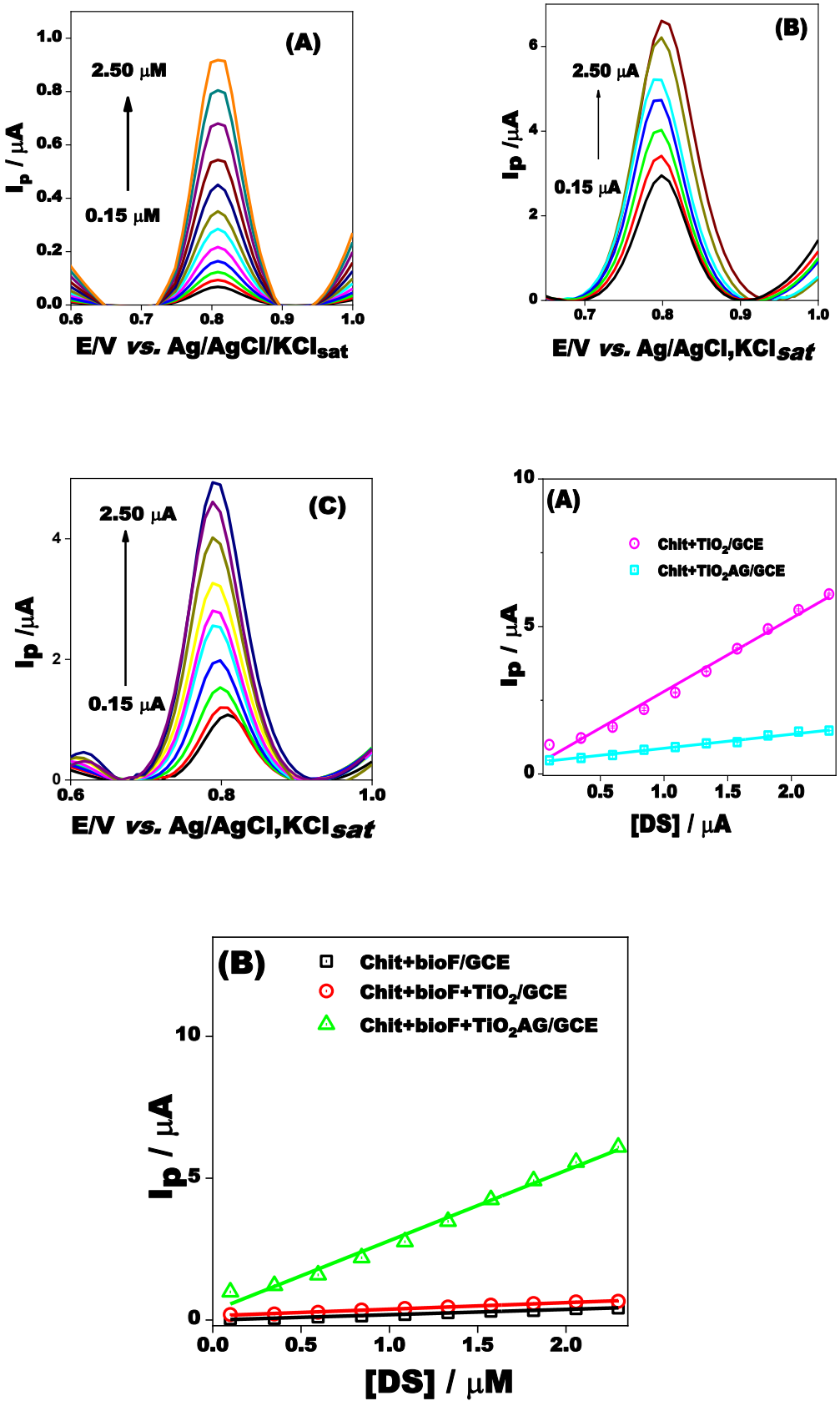

Figure 38. SWV recorded at Chit+bioF/GCE (A), Chit+bioF+TiO_2/GCE (B), and Chit+bioF+TiO_2AG/GCE (C) and the corresponding calibration curves. Experimental

conditions: electrolyte, 25 mM PB (pH 4.60); frequency, 10 Hz; step potential, 0.01 V; amplitude, 0.01 V; starting potential, 0.60 V vs. Ag/AgCl, KCl_{sat}.

3.3.6.9.3. Calibration curve at glassy carbon electrode modified with bioF and f-MWCNTs

To evaluate the analytical parameters of the fMWCNTs+4HIS+Chit/GCE modified electrode for detecting DS, the SWV method was employed. This technique is considered among the most advanced, versatile, and sensitive pulsed voltammetry approaches because it effectively minimizes the impact of background current. Therefore, the modified working electrodes by using f-MWCNTs exhibited a linear domain in the concentration range between 0.10 to 2.50 µM DS (Figure 39A). The linear regression equations of the calibration curves are:

I_p /A = (2.08 ± 0.04) × 10^{-6} + (2.36 ± 0.02) [DS]/M, R = 0.9998 (44), n = 10 points for the Chit+f-MWCNTs/GCE; and

I_p /A = (1.52 ± 0.10) × 10^{-6} + (1.63 ± 0.12) [DS]/ M (45), R = 0.9686, n = 10 points for the Chit+bioF+f-MWCNTs/GCE, as it is reported in Figure 39B.

The LOD, calculated according to the above section, was equal to 190 nM for the Chit+f-MWCNTs/GCE; and 50 nM for the Chit+bioF+f-MWCNTs/GCE. While the LOQ was equal to 166.5 nM for the Chit+f-MWCNTs/GCE; and 310 nM for the Chit+bioF+f-MWCNTs/GCE.

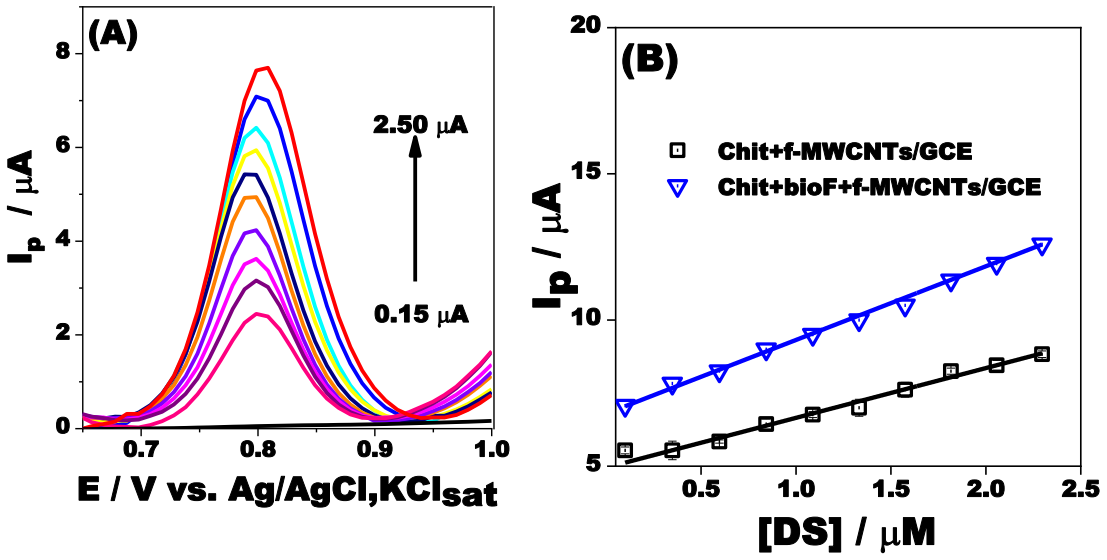

Figure 39. SWV recorded at Chit+f-MWCNTs/GCE (A), and Chit+bioF+f-MWCNTs/GCE (B) Experimental conditions: electrolyte, 25 mM PB (pH 5); frequency,

10 Hz; step potential, 0.01 V; amplitude, 0.01 V; starting potential, 0.60 V vs. Ag/AgCl, KCl_{sat}.

Therefore, we observed that the NPs significantly increased the LOD and LOQ in the DS determination. In this sense, the lowest LOD was reported by the Chit+bioF+TiO_2AG/GCE, with an LOD equal to 17 nM, while the highest LOD was reported by the Chit+f-MWCNTs/GCE, with an LOD equal to 166.50 nM. The results indicated that the effect of the addition of the nanoengineering filaments conferred a high performance on the sense ability of the electrode towards the DS and confirmed the synergetic effect between the chit, the filaments, and the NPs to enhance better analytical characteristics.

Moreover, the analytical performances of the prepared electrodes were in most cases superior or equal to other electrodes produced to detect DS in different samples. Table 13 gathers the principally developed electrochemical platforms for DS detection. As an example, when the author [273] used MWCNTs in combination with ionic liquids, they reported an LOD equal to 400, which is almost 10 times higher than the reported value in the present research. In the same way, the author [270] reported an LOD equal to 170 nM by using a modified pencil electrode with MWCNTs. In contrast, when the present research was added to MWCNTs + nanoengineering filaments, the LOD of detection was approximately 10 times lower in comparison with the author [273] and 3 times lower in comparison to the author [270].

Table 13. Analytical parameters reported for chemically modified electrodes used as sensing platform for DS determination

Electrode	LOD (nM)	Sensitivity (M/A)	Linear range (µM)	Real sample	References
GO-COOH/GCE	90	0.53	1.20 - 400	Tablets	[268]
Cu NPs/ rGO/GCE	8	20	0.02 – 1.50	Tablets	[269]
edge-plane pyrolytic graphite electrode	6.23	0.30	0.01 - 1	Tablets	[255]
ZIF-67/g-C_3N_4/ GCE	71	-	0.20 – 2.20	Human Urine	[270]

MWCNTs/$Cu(OH)_2$-NP/IL-GCE	400	0.02	0.18 – 19	Tablets	[271]
f-MWCNT/NC/GCE	120	0.19	2 – 250	Tablets	[272]
IL/MWCNTs paste electrode	900	0.13	350 - 750	Human Urine and tablets	[273]
MWCNTs/PG	170	0.77	0.05 – 12.95	Human Urine	[274]
PVC-Fe	130	57.71	0.001 - 0.15	Wastewater	[275]
IL/GCE	290	53.34	0.18 - 320	Water	[276]
PDMS	110	-	0.001 - 0.1	Wastewater	[277]
COOH-MWCNTs/SPE	170	0.01	0.05 – 12.95	Water	[278]
Chit+bioF	90	0.31	0.25 - 2.50	Wastewater, Tablets	This research
Chit+TiO_2/GCE	66	0.15	0.25 - 2.50	Wastewater, Tablets	This research
Chit+bioF+TiO_2/GCE	33	0.25	0.25 - 2.50	Wastewater, Tablets	This research
Chit+TiO_2AG/GCE	31	0.02	0.25 – 2.50	Wastewater, Tablets	This research
Chit+f-MWCNTs/GCE	190	2.36	0.25 – 2.50	Wastewater, Tablets	This research
Chit+bioF+TiO_2AG/GCE	17	0.41	0.25 – 2.50	Wastewater, Tablets	This research
Chit+bioF+f-MWCNTs /GCE	50	1.60	0.25 – 2.50	Wastewater, Tablets	This research

GO-COOH/GCE=carboxyl-functionalized graphene oxide, SWCNTs: Single walled carbon nanotubes, CuNPs: Copper nanoparticles, r-GO: reduced graphene oxide, ZIF-67/g-C_3N_4/ GCE: zeolite imidazolate framework-67/graphitic carbon nitride, IL: Ionic Liquid, Pencil Graphite, PDMS: poly(dimethylsi loxane), SPE: Screen Printed Electrodes, COOH: carboxyl

Furthermore, it is important to address that in the literature there were only a few works reported using the electrochemical electrodes to sense DS in water as an effect of the difficulty of the matrix due to the presence of a huge number of different analytes. In this context, the author Fard et al. [275] prepared a membrane composed of PVC-Fe. This

configuration reported an LOD equal to 130 nM, while the author Brennan et al. [276] modified a GCE by using IL and reported an LOD equal to 290 nM, which are 2 or 3 times higher than our report. Another important feature of the prepared electrodes in our research is that they comply with the quality standard imposed by the European policy regulation, which in the case of the DS, the Scientific Committee on Health, Environmental, and Emerging Risks (SCHEER, [277]) establishes an environmental quality standard (MAC-QS_{fw-eco}) of 250 nM, which is accomplished by all the modified electrodes, and it is a clear sign of the potential of using this platform for real water measurements.

3.3.6.9.4. ANOVA test

The ANOVA test was used to study the effect of the nanomaterial (bioF, TiO_2, TiO_2AG, and f-MWCNTs) and the synergistic effect of the bioF and the nanoparticles (bioF+ TiO_2, bioF+ TiO_2AG, and bioF+f-MWCNTs) into the modification of the GC electrodes to detect DS by analyzing the LOD obtained at the calibration curve. 6 calibration curves were performed for every treatment. Thus, it was first studied the effect of the nanomaterial in the modification of the electrode, then, it was studied the synergetic effect between the bioF and the NPs. Furthermore, the ANOVA test was performed in the same condition reported for the IBU studies (section 3.2.3.4.4). Moreover, the following hypothesis were stablished:

H_0: The type of nanomaterial (bioF, TiO_2, TiO_2AG, and f-MWCNTs) has no effect on the LOD for the determination of DS.

H_1: The type of nanomaterial (bioF, TiO_2, TiO_2AG, and f-MWCNTs) significantly influences the LOD for the determination of DS.

The null hypothesis (H_0) is not accepted because the p-value is lower to 0.01 (see Table 14), therefore it can be concluded that the type of nanomaterial highly influences the LOD to detect DS. This is consistent with the EIS and the ECSA calculated parameters. Thus, the Chit+TiO_2AG/GCE reported the highest LOD of the detection. This is explained by the excellent properties (high porosity, high crystallinity) which enables more active sites into the modified electrode surface and more chances to catalyze the redox reactions which increases the analytical parameters of the modified electrode.

Table 14. ANOVA test of the effect of the nanomaterial in the LOD for a chemical modified electrode used to detect DS

Source of Variation	SS	DF	MS	F	p-value
Model	83908.50	3	27969.50	1136.97	$< 1\times10^{-3}$
Type of nanomaterial	83908.50	3	27969.50	1136.97	$< 1\times10^{-3}$
Experimental Error	492	20	24.60		
Total	84400.50	23			

SS: Sum of Squares, DF: Degree of freedom, MS: Mean Square

Also, for the study of the synergy between the NPs and the bioF, the following hypothesis were stablished:

H_0: The synergy between the bioF and the NPs (TiO_2, TiO_2AG, and f-MWCNTs) has no effect on the LOD for the determination of DS.

H_1 The synergy between the bioF and the NPs (TiO_2, TiO_2AG, and f-MWCNTs) significantly influences the LOD for the determination of DS.

The null hypothesis (H_0) is not accepted because the p-value is lower to 0.01 (see Table 15), therefore it can be concluded that the nanoparticles have a proper synergy with the bioF. This is observed at the SEM pictures. At the modified electrode surface, the nanoparticles cover the surface of the electrode and the bioF occupies the inner spaces of the NPs, which enables both more active sites in the electrode surface and the chance for the bioF to interact with the DS increasing the analytical performance of the prepared electrodes. Overall, the properties of the nanoparticles play a crucial role in the analytical performance of the DS determination when they are combined with the bioengineering flagellin (bioF). Additionally, incorporating TiO_2 semiconductor nanoparticles or functionalized MWCNTs alongside with bioF results in an increased limit of detection (LOD) for the modified electrodes. This improvement is attributed to the synergistic effects between bioF and the nanoparticles, which enhance conductivity and expand the active surface area. At very low (nanomolar) concentrations, achieving both a high LOD and strong sensitivity requires balancing the need to reliably detect minute amounts of DS with the need for a distinct, easily recognizable electrochemical signal that stands out from background noise, even when the signal is very weak.

Table 15. ANOVA test of the effect of the synergy between the bioF and NPs in the LOD for a chemical modified electrode used to detect DS

Source of Variation	SS	DF	MS	F	p-value
Model	13720.50	3	4573.50	653.36	$< 1\times10^{-3}$
Type of modifier solution	13720.50	3	4573.50	653.36	$< 1\times10^{-3}$
Experimental Error	140	20	7		
Total	13860.50	23			

SS: Sum of Squares, DF: Degree of freedom, MS: Mean Square

3.3.6.9.5. Interferences studies

Water matrices are usually complex because they contain many different analytes. These different analytes can get in the way of figuring out the DS because they behave similarly to the analyte being studied. Thus, citric acid, lactose, sucrose, urea, ascorbic acid, ibuprofen, paracetamol, etc., are potential interferences that can coexist with the DS [270]. Thus, it was necessary to study the effect on the intensity peak when the modern solution is present on these cited contaminants.

Hence, the above-mentioned was studied by means of the SWV in the presence of DS and the interferent. In this sense, the intensity peak was measured when the electrolyte contained 1×10^{-5} M DS (Ip_{DS}); then another measurement was performed; but at the second measurement, 1×10^{-3} M of the interferent was added ($Ip_{DS+Interferences}$). Both peaks were compared, and the degree of interference was calculated by comparing the peak intensity with and without interferences, and the percentage was obtained according to $\%Deviation = \frac{Ip_{DS+interferences} - Ip_{DS}}{Ip_{DS}} \times 100$ (50).

Figures 40A, 40B, 40C, and 40D gathered the study of the intensity peak deviation when the different interferents were added to the solution. Thus, it can be observed that for all the interferences, the degree of variation was lower than 5 % in all the cases studied, which is a positive result. Moreover, it can be observed that when the nanofilaments were added to all the electrodes, the percentage of deviation was lower in comparison to the electrodes that were prepared only by the addition of the NPs. These results were expected, because, as was planned, the filaments are selective for the DS; thus, the addition of other substances does not interfere with their sensing ability.

Additionally, it can be observed that the biggest degree of deviation was reported when the glucose was added to the matrix. However, the change in the peak signals was not significant, so the interference with glucose is not a considerable problem in the determination. Moreover, no other peak was observed in the whole range of analysis when all the analytes were studied; it probed the high affinity of the electrodes towards the DS and gave potential evidence of the potential use of the prepared electrode in the determination of DS in real samples.

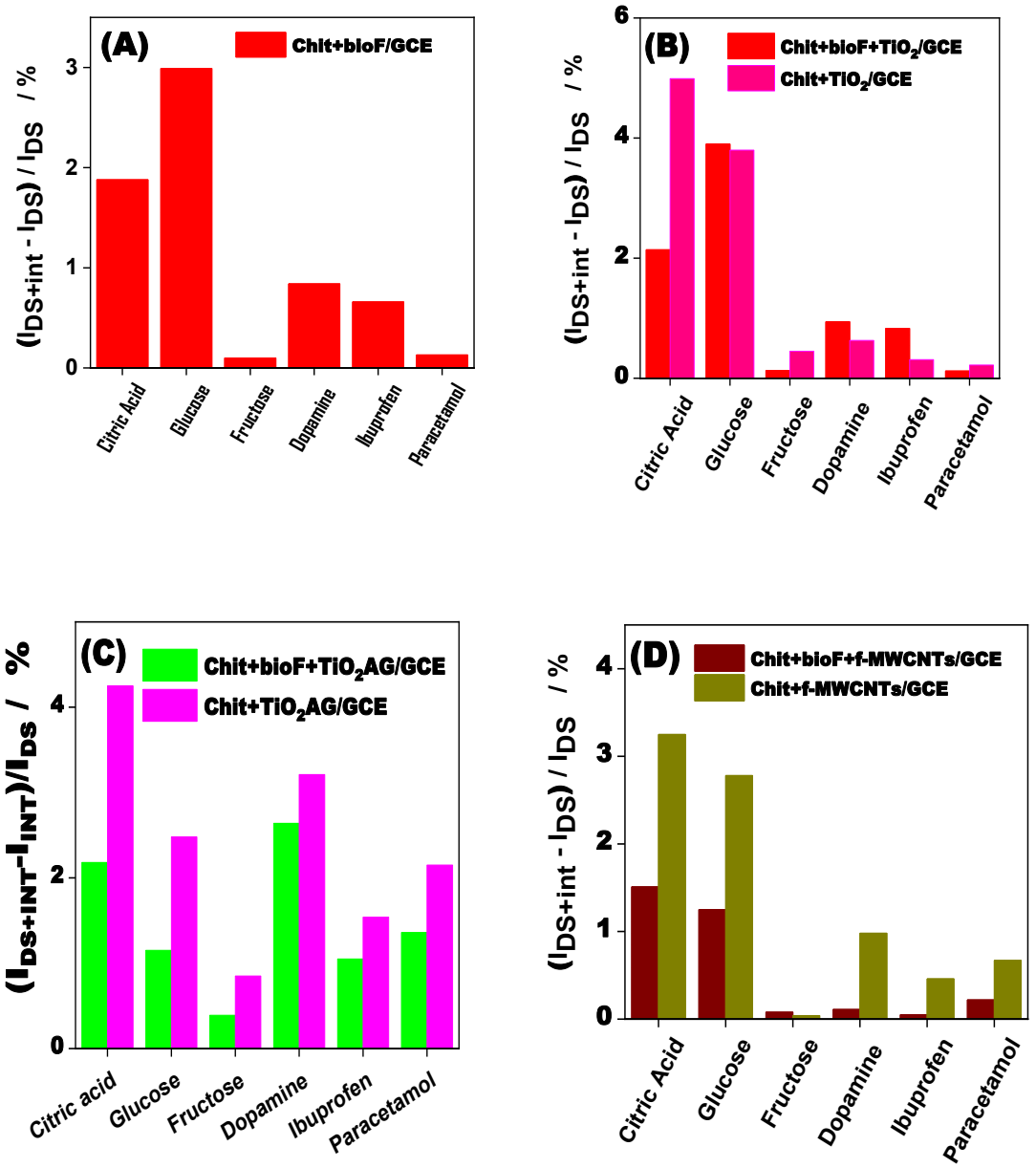

Figure 40. Interference studies at Chit+bioF/GCE (A), Chit+TiO_2/GCE or Chit+bioF+TiO_2/GCE (B), Chit+TiO_2AG or Chit+bioF+TiO_2/GCE (C), and Chit+f-MWCNTs/GCE or Chit+bioF+f-MWCNTs/GCE (D) modified electrodes in the presence

of 1×10^{-5} M DS and 1×10^{-3} M different interferences. Experimental conditions: electrolyte, 25 mM PB (pH 4.60); frequency, 10 Hz; step potential, 0.01 V; amplitude, 0.01 V; starting potential, 0.60 V vs. Ag/AgCl, KCl_{sat}.

3.3.6.9.6. Reproducibility, reusability and stability of the modified electrodes

The electrode's repeatability was evaluated utilizing the SWV analytical approach in the presence of 0.1 mM DS in 25 mM PB (pH 4.60 and in the case of Chit+bioF+MWCNTs/GCE the pH was equal to 5). Six modified electrodes (e.g., 6 Chit+bioF+f-MWCNTs/GCE) were employed under uniform testing conditions. The maximum intensity was recorded for each measurement, and the relative standard deviation was computed. The results were 2.25 % (Chit+bioF/GCE), 3.50 % (Chit+TiO_2/GCE), 2.78 % (Chit+bioF+TiO_2/GCE), 4.15 % (Chit+TiO_2AG/GCE), 3.25 % (Chit+TiO_2AG/GCE), 3 % (Chit+f-MWCNTs/GCE), and 4.50 % (Chit+bioF+f-MWCNTs+4HIS+Chit/GCE) modified electrodes, respectively. The results indicate that the modified electrode demonstrates robust repeatability and consistency in peak intensity levels.

The consistency of six measurements in a 0.10 mM DS solution in a 25 mM PB (pH 4.60, and 5 in the case of Chit+bioF+f-MWCNTs/GCE), conducted using the same modified electrode, was evaluated using the SWV method. The relative standard deviation (RSD) values for peak intensity were 1.87 % (Chit+bioF/GCE), 4.30 % (Chit+TiO_2/GCE), 2.75 % (Chit+bioF+TiO_2/GCE), 3.80 % (Chit+TiO_2AG/GCE), 4.25 % (Chit+bioF+TiO_2AG/GCE), 2.98 % (Chit+f-MWCNTs/GCE), and 3.43 % (Chit+bioF+f-MWCNTs/GCE) modified electrodes, respectively.

All the calibrated sensors demonstrated acceptable repeatability. The stability of the modified electrodes was evaluated by keeping them at room temperature for two weeks and evaluating them using the SWV method. After two weeks, the peak current diminished by only 5 % of its starting value, indicating the electrodes' remarkable stability at ambient temperature throughout this period. The modified electrodes that were made are very durable and easy to replicate, which makes them useful for real-sample analysis. For example, they can be used to study complex water, groundwater, or wastewater matrices.

3.3.6.9.7. Real sample assay

All the evaluated analytical parameters demonstrated the high performance of the chemically modified electrodes in DS sensing. However, the real applicability of the electrodes was tested in pharmaceutical and water samples, and the found concentration was compared with a standard method (UPLC/MS-MS). Additionally, the samples were not pretreated until the determination; thus, in the case of the tablets, they were crushed and dissolved in the PB, while in the case of the wastewater, they were directly added to the PB buffer solution.

Thus, the determination of the concentration of both real samples was executed by a standard addition method, in which 25 uL of the real sample was introduced in 25 mM PB and the peak intensity signal was recorded. Subsequently, 25 µL of the 10 µM DS solution was added, and the intensity peaks were registered. In this context, the linear dependencies were obtained as follows:

$I_p/A = (2.20 \pm 0.21) \times 10^{-7} + (0.16 \pm 0.03)\ c_{DS}/M$ (46), R/no. points = 0.9499/6 points for the Chit+bioF/GCE;

$I_p/A = (1.31 \pm 0.17) \times 10^{-7} + (0.66 \pm 0.04)\ c_{DS}/M$ (47), R/no. points = 0.9957/6 points for the Chit+bioF+TiO_2/GCE

$I_p/A = (4.82 \pm 0.72) \times 10^{-7} + (0.106 \pm 0.01)\ c_{DS}/M$ (48), R/no. points =0.9306/5 for the Chit+bioF+TiO_2AG/GCE; and

$I_p/A = (3.75 \pm 0.07) \times 10^{-6} + (2.5 \pm 0.11)\ c_{DS}\ /M$ (49), R/no. points = 0.9962/6 for the Chit+bioF+f-MWCNTs/GCE.

While the concentration of DS in wastewater the linear equation was as follows:

$I_p/A = (1.76 \pm 0.02) \times 10^{-8} + (0.02 \pm 5\times10^{-4})\ c_{DS}/M$ (50), R/no. points = 0.9980/6 points for the Chit+bioF/GCE;

$I_p/A = (2.20 \pm 0.16) \times 10^{-7} + (0.31 \pm 0.02)\ c_{DS}/M$ (51), R/no. points = 0.9499/6 points for the Chit+bioF+TiO_2/GCE

$I_p/A = (14.60\pm0.54) \times 10^{-8} + (0.80 \pm0.03)\ c_{DS}/M$ (52), R/no. points =0.9932/5 for the Chit+bioF+TiO_2AG/GCE; and

$I_p/A = (3.00 \pm 0.06) \times 10^{-6} + (2.41 \pm 0.23)\ c_{DS}\ /M$ (53), R/no. points = 0.9872/6 for the Chit+bioF+f-MWCNTs/GCE.

From the calibration curve, the unknown concentration was calculated and compared to the LC/MS-MS method. Therefore, Table 16 reports the calculated percentage of

apparent recovery. In the case of pharmaceutical tablets, all the prepared electrodes reported a percentage of recovery higher than 95 %; thus, the electrode is suitable for the analysis of DS in commercial tablets. On the other hand, for the wastewater samples, the Chit+bioF/GCE electrode reported a percentage of recovery equal to 80.17 %, which is not suitable for precise determination; thus, this electrode cannot be used in water samples. The other three electrodes reported a recovery percentage higher than 95 %. These results make the electrodes suitable for determining the DS content in different water samples.

Table 16. Results for DS determination in real water samples (number of experiments: 3).

Type of electrode	**Pharmaceutical tablets**		**Apparent recovery */ %**	**R / no. of points**
	***c*(DS)$_{added, SWV}$ /µM**	***c*(DS)$_{found, SWV}$ /µM**		
Chit+bioF/GCE	1.57	1.55 ± 0.63	98.72 ± 0.58	0.9964/ 6
Chit+bioF+TiO_2/GCE	1.57	1.51 ± 0.77	96.18 ± 0.47	0.9991/ 6
Chit+bioF+TiO_2AG/GCE	1.50	1.51± 0.77	99.34 ± 0.23	0.9736/ 5
Chit+bioF+f-MWCNTs/GCE	1.50	1.51 ± 0.02	100.60 ± 0.78	0.9962/ 6
	Wastewater sample		**Apparent recovery*/ %**	**RSD/ %**
	***C*(DS)$_{SWV}$ /µM**	***C*(DS)$_{UPLC-MS/MS}$ /µM**		
Chit+bioF/GCE	0.24 ± 0.03	0.19 ± 4.12×10^{-3}	80.17	3.53
Chit+bioF+TiO_2/GCE	0.20 ± 0.09		95.00	1.25
Chit+bioF+TiO_2AG/GCE	0.19 ± 0.04		103.15	0.39
Chit+bioF+f-MWCNTs/GCE	1.29 ± 0.06	1.30 ± 2×10^{-3}	100.77	1.25

3.3.7. Partial Conclusions

It was prepared different chemically modified glassy carbon electrodes to be used as a sensing platform for DS determination. A simple drop casting method was used to produce the GC modification. The different polymeric solutions included chitosan, nanoengineering filaments, and different nanoparticles (TiO_2, TiO_2AG, and f-MWCTNs). Thus, the produced electrodes were characterized using SEM imaging, cyclic voltammetry (CV), and electrochemical impedance spectroscopy (EIS). In this context, the SEM images showed a first look at the inclusion of the produced biofilms on the GCE surface. The images reported a homogeneous surface in which some agglomerations can be observed randomly distributed onto the surface; this indicates the addition of the nanoparticles to the surface. Also, in the images, the nanoengineering filaments cannot be observed because they are presumably entrapped in the NP structure. This finding was confirmed by the EDS spectra, which in all the cases reported the presence of nitrogen, sodium, and other compounds that formed the filament structure in combination with C, Ti and O content for the different electrodes. So, at first look, the immobilization of the nanoparticles and the filaments was successful in all the prepared electrodes.

Prior to the electrochemical characterization of the prepared electrodes, it was necessary to optimize the quantity of the filaments and NPs to increase their performances. First, we tested the optimal filament concentration in this context. Based on the peak intensities (I_p) values, we selected a filament concentration of 1 g/L for further experiments. Then, the optimal concentration of the three nanoparticles was studied. Again, from the peak intensity (I_p) values obtained by CV, the optimal concentration was chosen. The highest Ip was obtained when 2 g/L of NPs was added, indifferent to the type. Thus, the modified solution was prepared by the addition of 3 µL of a solution that contains chitosan, 1 mg/L of filament, and 2 mg of nanoparticles.

With the optimal parameters for the preparation of the modifier solution, the next step was to analyze the redox processes occurring on the electrode surface in the absence and presence of 10 µM of DS in a 25 mM PB buffer solution. Therefore, when there was no DS in the buffer solution, any peak was reported in all the tested electrodes; hence, there was no interaction between the components of the buffer solution and the modified electrodes. On the other hand, when it was added 10 µM of DS, it was reported to have an irreversible oxidation peak at the cathodic position (+0.75 V vs. Ag/AgCl, KClsat) at Chit+bioF/GCE, while it was shifted to 0.70 V vs. Ag/AgCl, KClsat, when the different TiO_2NPs were added. And in the case of the addition of MWCNTs and bioF+MWCNTs,

it was reported that two quasi-irreversible peaks appeared at the forward and reverse scans. The peaks appeared at +0.46 and +0.74 V vs. Ag/AgCl/KCl_{sat} in the anodic branch and at +0.11 V and +0.38 V vs. Ag/AgCl/KCl_{sat} in the cathodic branch. These results suggested that the mechanism of oxidation follows two different paths. Thus, in the case of the addition of bioF, TiO_2, and TiO_2AG, it follows a two-step mechanism, while when f-MWCNTs are added, the reaction follows a multistep mechanism. The literature reported information that supported the data.

Afterwards, the surface characteristics of the pristine and modified electrodes were studied by means of EIS measurement. In this context, the obtained results were fitted by the ((R_{el}(Q(R_{ct}W))) equivalent circuit ($\chi^2 \approx 0.99$). The principal outcomes were (a) the charge transfer (R_{ct}) decreases when the nanoparticles are added to the electrode surface; this enables a better redox process by the easiness in the electron flow; (b) the capacitances increase as the R_{ct} decreases, thus the diffusion-limited process is limited, which enables a better interaction between the analyte/electrode surface; (c) the charge transfer (k_s) increases when the NPs are added; and (d) the inclusion of the nanoengineering filaments did not considerably affect the surface properties of the surface film. Overall, in terms of R_{ct}, capacitances, and k_s, the Chit+TiO_2AG/GCE reported the best performances.

The effect of the pH on the DS detection was studied by changing it between 4 and 9. First, we obtained the relation between the pH value and the peak position vs. Ag/AgCl, KCl_{sat}. For the linear relation, the slope of the curve was calculated and compared with the Nernstian slope value (-59 mV). The results from Chit+bioF/GCE and Chit+bioF+TiO_2AG/GCE showed a slightly sub-Nernstian electrochemical behavior of the redox reaction. However, at Chit+bioF+f-MWCNTs/GCE, the slope value was similar to the Nernstian value. Both obtained results indicated that the oxidation of DS involves an equal number of protons and electrons, which was in accordance with the mechanism reactions reported in the bibliography. Moreover, the optimal pH value in which the CV reported the highest intensity peaks was studied. The results suggested that the optimal pH value was equal to 4.60 for the Chit+bioF/GCE, Chit+bioF+TiO_2AG/GCE and Chit+bioF+TiO_2AG/GCE, while the optimal pH was equal to 5 at Chit+bioF+f-MWCNTs/GCE

Likewise, the controlled process and the active surface area were studied by means of the variation of the scan rate of the CV performed in 10 µM DS in the first case and in 5 mM $[Fe(CN)_6]^{3-/4-}$ solution in the second case. Hence, for all the electrodes, the process

was controlled by a diffusion process because the slopes of log I/A vs. log v ($V\ s^{-1}$) were closer to 0.50. In the second case, the surface area calculation reported the following results: 0.07 cm^2 for the Chit+bioF/GCE, 0.09 cm^2 for the Chit+TiO_2/GCE, 0.14 cm^2 for the Chit+bioF+TiO_2, 0.05 cm^2 for the Chit+TiO_2AG/GCE, 0.07 cm^2 for the Chit+TiO_2AG/GCE, 0.13 cm^2 for the Chit+f-MWCNTs/GCE, and 0.16 cm^2 for the Chit+bioF+f-MWCNTs/GCE. Thus, it can be added that the inclusion of the nanoparticles enables the better diffusion of the DS into the electrode surface by increasing the surface area.

The analysis of the electrode's sensing capacity was evaluated by employing a SWV technique. Prior, it was necessary to optimize the parameters, which were 10 mV vs. Ag/AgCl, KCl_{sat} step potential, 10 mV vs. Ag/AgCl, KCl_{sat} step amplitude, and 10 Hz frequency. With these parameters, it was prepared different SWV analysis, and it was constructed a calibration curve which correlates the DS concentration vs. I_p. From the data, the LOD, LOQ, and the sensitivity were calculated in a linear range of 0.10 - 2.50 µM. Therefore, the LOD reported the following results: 90 nM for the Chit+bioF/GCE; 66 nM for the Chit+TiO_2/GCE, 33 nM for the Chit+bioF+TiO_2/GCE; 31 nM for the Chit+TiO_2AG/GCE; 17 nM for the Chit+bioF+TiO_2AG/GCE; 190 nM for the Chit+f-MWCNTs/GCE; and 50 nM for the Chit+bioF+f-MWCNTs/GCE; and the LOQ reported the following data: 630 nM for the Chit+bioF/GCE; 250 nM for the Chit+TiO_2/GCE; 111 nM for the Chit+bioF+TiO_2/GCE; 104 nM for the Chit+TiO_2AG/GCE; 58 nM for the Chit+bioF+TiO_2AG/GCE; 166.5 nM for the Chit+f-MWCNTs/GCE; and 310 nM for the Chit+bioF+f-MWCNTs/GCE. These results showed the optimal analyte performances of the NPs in combination with the engineering filaments towards the DS.

Moreover, the selectivity of the prepared electrodes was analyzed by adding interferents that are present together with the DS in pharmaceutical or water samples, as well as the reproducibility, reusability, stability, and repeatability of the prepared sensors. For all electrodes, the presence of interferents did not affect the measurements; thus, the percentage of variability was lower than 5 % for all the electrodes in the presence of all interferents. Moreover, all the modified sensors demonstrated acceptable repeatability and reproducibility; thus, the standard deviation (SD) and the relative standard deviation (RSD) were lower than 5 % in all the modified electrodes. Also, in terms of stability, the modified electrodes reported a dismissal lower than 5 % after two weeks, and they can be used 25 times without losing their effectiveness. All the parameters studied indicate the

excellent performance of the modified platform because of the excellent synergy between the chitosan, the filaments, and the NPs.

Analyzing the modified electrodes' applicability in real sample analysis proved their good performance. Because of this, the concentration of DS found in tablets and wastewater was studied, and the results were compared with the concentration of DS found using UPLC/MS-MS. To sum up, the percentage of recovery and differences between the electrodes and the standard method for all of them when the tablets were tested showed a recovery rate of more than 95 %. However, the Chit+bioF/GCE electrode only showed an 80.17 % recovery rate when it came to figuring out DS concentration in wastewater, which is too low for accurate determination and means it can't be used on water samples. The other three electrodes reported a recovery percentage higher than 95 %, which enables their use in wastewater or real pharmaceutical samples.

Overall, the low LOD and LOQ, which is below the European requirements; the high selectivity, reported at low deviation in the presence of interferents; the high reproducibility and repeatability (RSD $\leq$ 95 %); the high stability, above 25 measurements per modification; the low cost; and the high percentage of recovery for both commercial tablets and wastewater samples enable the use of the prepared electrode in DS determination and enable the miniaturization of these electrodes to be prepared on lab chips to analyze online the content of DS in different samples.

In future research, it is necessary to miniaturize the prepared modified electrodes for the determination of DS online in real samples. Thus, it is necessary to investigate the behavior of the electrodes in daily measurements. Also, it could be a good idea to connect the modified electrodes to boats to enable the monitoring of DS in lakes or rivers. If this is possible, also, it can be a good idea to create a database to analyze the environmental presences of DS in different points of Europe. From this monitoring, the data can be compared with the permissible limit and if the values exceed this limit, there is the necessity to mitigate the contamination.

4. General Conclusions

For this dissertation we successfully prepared electrochemical devices that have environmental, industrial, and health applications. We divided my experimental research into three different chapters, which were as follows: (A) Drug delivery systems (DDS), we prepared a drug delivery system by electropolymerizing 3,4-ethylenedioxythiophene (EDOT) in combination with different concentrations of paracetamol (PA) onto a

titanium metallic plate. The approach enables the construction of a device that responds to the electric impulses by delivering the paracetamol into the saliva. The novelty of this work relies on the application, for the first time, of an EIS methodology to determine the amount of paracetamol released onto the saliva solution. So, to optimize the performance of the prepared devices, it was analyzed for different variables such as pH, concentration of paracetamol, and the scan rate ratio of the cyclic voltammetry, the technique used to produce the PEDOT–Paracetamol membrane. Hence, I electropolymerize the EDOT monomer in-situ with different concentrations of PA (1 and 2 mM) by employing a cyclic voltammetry technique in which the voltage cycle went from -1 to 1 vs. Ag/AgCl, KCl_{sat} for 10 cycles, and we studied the influences of the scan rate by varying its values from 5 to 10 $mV \cdot s^{-1}$. The idea of this method was to dope the EDOT with the PA, and in that way, the PA can be introduced into the polymer structure, forming a nanocomposite. This approach was proved by the study of the FTIR spectrum, which reported the characteristic vibrational and stretching peaks of both the PEDOT and the PA. With the confirmation of the copolymerization of the PEDOT and PA, we studied the morphological structure of the polymer. At first look, we examined the SEM images after the polymerization; it shows the typical flower-like structure of the PEDOT, which was homogenously distributed on the metal surface, and when the PA was added, some clustered particles appeared, located randomly in the polymeric structure, confirming the addition of the PA in the polymeric structure. After the confirmation of these facts, we studied the profile of the delivery of the PA into the saliva solution by function of time. This measurement was made by EIS characterizations for 6 hours. After that time, the results were obtained in the form of Nyquist plots, and it was necessary to build an equivalent circuit to interpret the obtained results. The chosen equivalent circuit was $R_{sol}(Qdl(R_{ct}Q_{film}))$, and by the change of the solution resistance (R_{sol}), we obtained a correlation between the R_{sol} and the concentration delivered into the saliva. The correlated data was confirmed using a prepared electrochemical platform by using a BDD electrode for the detection of PA. Both results were in accordance, so the studied premise was verified. Subsequently, it was necessary to build the drug release mathematical model. For that, we chose three empirical models (zero-order, Higuchi, and Korsmeyer–Peppas), and I compared the adj-R^2 to decide the model that is best adjusted to my system. In this sense, the drug release profile was reported as a division into two time slots (before and after 200 minutes), and the zero-order model described better the release of the PA (adj-$R^2 = 1$). Therefore, with all the obtained data, I demonstrated the applicability of the EIS technique to determine

the drug release profile of the membranes in saliva. Thus, the main advantage of the EIS method is the ease of determination and the non-destructive nature of the analyzed membrane. Therefore, the built devices can be used in drug delivery devices, replacing the UV-Vis method, which is currently the most used for this purpose. Likewise, with the new approach to building micro-potentiostats and wearable electrochemical devices, the proposed PEDOT-PA/Ti or PEDOT-2PA/Ti polymeric film can be incorporated together with the potentiostat into the dental implants. Thus, alternative biocompatible and appropriately designed films utilizing conducting polymers infused with antimicrobials and antibiotics warrant exploration to create carriers for the release of bioactive agents with beneficial uses in prosthetic or implant therapies.

(B) Anticorrosive materials: In the same field, biomedical applications, I prepared a polymeric film to protect Ti–6Al–4V plates, which are highly used in the production of dental or other types of body implants, against the corrosion caused by the exposition to corrosive environments. So, I decided to add expired ibuprofen (IBU), which, in the case of not having alternative uses, should be treated before its disposal to the environment, into polymethyl methacrylate (PMMA), which is a low-cost, high-resistance polymer. Therefore, expired tablets of IBU were crushed, and the different concentrations (0.20, 0.40, and 1 mM) of the obtained powder were added to a solution that contains methyl methacrylate dissolved into THF. So, the solution was vigorously agitated and heated at 30 ºC; after two hours, a transparent solution was obtained. That solution was coated under the Ti–6Al–4V plates by applying a speed-controlled dip coating process, and the obtained coated plates were evaluated to investigate the effectiveness of the protection. Hence, the evaluation of the coating consisted of different steps, which were as follows: (i) Chemical evaluation: by means of FTIR, the inclusion of the IBU into the PMMA matrices was demonstrated, because the films reported the characteristic vibrational peaks of both the PMMA and the IBU, and the intensity of the peaks varied according to the concentration of IBU. (ii) Mechanical evaluation: it was necessary to check if the addition of the IBU changed the mechanical properties of the polymer film. In this sense, when different concentrations of IBU were added, the films were stronger, demonstrated by the increase in the highest stress being reported when 1 mM of IBU was added with a strain stress equal to $10.99 \pm 4\times10^{-3}$ kPa. Moreover, the other important mechanical properties were changed when IBU was added; for example, the film thickness increases as the IBU concentration increases, so the highest polymer thickness was reported when 1 mM of IBU was added; the thickness was equal to 12.86 ± 1.14 kPa. On the other hand, the

addition of IBU decreased the fracture strain; thus, the lowest values were reported by the PMMA-1mM-IBU, and the strain was equal to 1.50 ± 0.02 mm/mm. (iii) Morphological characterization involved evaluating the film structure using optical microscopy (OP) and atomic force microscopy (AFM). The OP image revealed a well-distributed film on the metal surface, and the addition of IBU led to the appearance of some aggregations randomly distributed onto the metallic surface. Conversely, AFM imaging demonstrated a shift in the polymeric film's roughness and homogeneity as the IBU content increased. (iv) Electrochemical test: it was performed accelerate corrosion tests such as OCP, linear polarization, potentiodynamic polarization, and EIS techniques, to understand the mechanism of protection and to calculate the effectiveness of protection. Consequently, from the OCP, it was the first approach that the coating acts as a cathodic type because of the dropping OCP values. The Tafel results clearly demonstrated this. As the concentration of IBU increases, the corrosion potential shifts clearly to the left. Furthermore, we calculated the inhibition efficiency based on the data. The best inhibition performance was seen when 0.40 mM of IBU was added to the polymeric solution (69.02 % ± 0.76 %), while the worst inhibition performance was seen when 1 mM of IBU was added to the polymer (67.17 % ± 0.58 %). Also, from EIS techniques, the principal insights detailed an increase in the R_{ct} as follows: The concentration of IBU increases, but the increase stops when the IBU concentration is bigger than 0.40 mM, which reflects the capacity of the IBU + PMMA to decrease the electron transfer between the Ti–6Al–4 V and the NaCl, thus reporting a considerable inhibition against the corrosion. Moreover, the highest inhibition efficiency was reported when 0.4 mM was added to the polymeric solution with an efficiency equal to 89.53 % ± 1.22 %. Overall, the polymeric film prepared by PMMA and 0.40 mM of expired IBU reported good protection against the corrosion of titanium alloys, and because of the biocompatibility of the ingredients of the film, this can be used in medical applications. It solved two problems at once: the corrosion of the implants, which is a big problem for the patient's finances, and the pollution caused by the thrown-away expired IBU. Thus, expired ibuprofen can be used alone or with polymers to effectively stop corrosion. Furthermore, for the corrosion protection, I prepared different plant extracts to be used as a green inhibitor on the mild steel exposed to acid conditions. The plants were Tara and Guayusa, Ecuadorean plants that are not industrialized, and two extraction techniques were performed: a hot-liquid extraction method (Soxhlet), achieving a yield of extraction equal to 10.59 % ± 0.06 %, and a cold solid-liquid extraction method (maceration), achieving a yield of extraction

equal to 13.89 % ± 0.09 % for the Tara extract production and only Soxhlet extraction in the case of the Guayusa. It is important to note that the chosen solvents were water and ethanol, which are Generally Recognized as Safe (GRAS) solvents; thus, the extraction method was green. The efficiency of the extract to be used as an inhibitor of corrosion was tested by immersing different metallic samples in acid without and with different concentrations of the inhibitor (200, 400, and 1000 ppm) for two weeks, and after it, the metallic plates were evaluated, and the following results were obtained: (i) morphological characterization: SEM imaging shows the apparition of pitting points as consequences of the corrosion when the inhibitor was not added, while the addition of the inhibitor decreased the pitting. (ii) mechanical characterization: the fracture stress of the metallic plates soaked in acid suffered a notable decrease in comparison to the metallic plates saved at room conditions, which reported a strain stress equal to 193.98 ± 2.40 GPa, while the tensile stress was not appreciable changed when the samples were immersed in acid which contains 1000 ppm of Tara-SE, which reported a fracture stress equal to 191.65 ± 1.68 GPa; (iii) weight loss measurements: from the measurement of the weight before and after the immersion, I can approximate the corrosion rate, which in the case of no addition of inhibitor was equal to 1.50 ± 0.27 $mm \cdot year^{-1}$, while with the addition of 1000 ppm of Tara-SE, the corrosion rate was equal to 0.07 ± 0.02 $mm \cdot year^{-1}$, achieving an inhibition efficiency equal to 95.90 % ± 1.41%; (iv) electrochemical measurements: from the Potentiodynamic measurements, I can explain that the inhibitor behave as mixed-type, which means it confers a cathodic and anodic protection, while from the i_{corr}, I calculated the inhibition efficiency, the highest inhibition was obtained when it was added 1000 ppm Tara-SE, it was equal to 97.38 % ± 2.04%. Moreover, EIS characterization also allows to calculate the inhibition efficiency, which was equal to 90.73 % ± 0.03% when it was added 1000 ppm Tara-SE, so the weight loss, the PDP and the EIS reported similar results to the corrosion inhibition efficiency, (v) thermodynamic studies: from this the principal outcomes that were obtained were: (1) the inhibitor loss their efficiency when the time and the temperature goes beyond 315 K and 3 hours respectively, (2) the activation of energy (E_a), the enthalpy (ΔH_a) and the entropy (ΔH_s) increases as function of the inhibitor concentration, (3) Temkin, Flory Huggins, and El-Awady isotherm models described better the adsorption process, (4) the inhibitor is physically adsorbed onto the metallic surface (ΔG_{ads} >-40 $kJ \cdot mol^{-1}$). Therefore, from the second chapter, I analyzed the viability of producing new methods to prevent the corrosion of different materials. Thus, the use of expired drugs and plant inhibitors is

suitable because, in the first case, the reduction of the contamination is notable; thus, the expired drugs can have other applications instead of being finally disposed of, and in the second case, Ecuadorian plants can be industrialized, and the local producers can obtain better economic benefits because the green extract can be applied to the oil, petroleum, and construction industries.

(C) Chemically modified electrodes: In terms of environmental protection, I produce different chemically modified electrodes to be used as sensing platforms for the determination of DS in wastewater. The idea was to produce a simple device that can replace expensive analytical methods such as UPLC, UPLC-MS/MS, etc. Thus, the glassy carbon electrode (GC) was modified using a novel bioengineering filament combined with different nanoparticles, such as anatase TiO_2, aerogel TiO_2, and functionalized multiwalled carbon nanotubes. Therefore, the immobilization of both the filaments and the NPs was accomplished using chitosan. In this context, I optimized a modifier solution, and this was simply drop-casted onto the GC, and the evaluation of the performances of the modified electrodes was evaluated first by analyzing the morphological characteristics of the electrode surface, secondly by analyzing the electrochemical characteristics, thirdly by analyzing the analytical characteristics, and fourthly by analyzing their use in the determination of sodium diclofenac (DS) in real samples. So, the following were obtained: (1) Morphological structure: in the SEM image, a homogenous surface with some small clusters formed randomly onto the GC surface was reported; (2) electrochemical characterization: the redox reactions of DS were studied by cyclic voltammetry. The voltammograms reported a cathodic irreversible peak in the case of bioF, bioF+TiO_2, and bioF+TiO_2AG and two quasi-irreversible peaks in the case of bioF+f-MWCNTs when 10 μM of DS was used as electrolyte. The peaks appeared at +0.46 and +0.74 V vs. Ag/AgCl, KClsat in the anodic branch and at +0.11 V and +0.38 V vs. Ag/AgCl, KClsat in the cathodic branch. These results suggested that the mechanism of oxidation follows two different paths. Thus, in the case of the addition of bioF, TiO_2, and TiO_2AG, it follows a two-step mechanism, while when f-MWCNTs are added, the reaction follows a multistep mechanism. Furthermore, from the electrochemical studies, the optimal pH to perform the DS determination was obtained; moreover, the controlled process, which in all the cases was a diffusion process, was studied, and the surface area was calculated, and the results were as follows: 0.07 cm^2 for the Chit+bioF/GCE, 0.09 cm^2 for the Chit+TiO_2/GCE, 0.14 cm^2 for the Chit+bioF+TiO_2, 0.05 cm^2 for the Chit+TiO_2AG/GCE, 0.08 cm^2 for the

Chit+TiO_2AG/GCE, 0.12 cm^2 for the Chit+f-MWCNTs/GCE, and 0.16 cm^2 for the Chit+bioF+f-MWCNTs; (3) analytical parameters: From the calibration curve, Ip vs. [DS], the following results were obtained: a LOD of detection equal to 90 nM for the Chit+bioF/GCE; 66 nM for the Chit+TiO_2/GCE; 33 nM for the Chit+bioF+TiO_2/GCE; 31 nM for the Chit+TiO_2AG/GCE; 17 nM for the Chit+bioF+TiO_2AG/GCE; 190 nM for the Chit+f-MWCNTs/GCE; and 50 nM for the Chit+bioF+f-MWCNTs/GCE; and a LOQ equal to 630 nM for the Chit+bioF/GCE; 250 nM for the Chit+TiO_2/GCE; 111 nM for the Chit+bioF+TiO2/GCE; 104 nM for the Chit+TiO_2AG/GCE; 58 nM for the Chit+bioF+TiO_2AG/GCE; 166.5 nM for the Chit+f-MWCNTs/GCE; and 310 nM for the Chit+bioF+f-MWCNTs/GCE. Moreover, in terms of selectivity, the presence of interferents did not affect the measurements; thus, the percentage of variability was lower than 5 % for all the electrodes in the presence of all interferents. In terms of repeatability, the standard deviation (SD) and the relative standard deviation (RSD) were lower than 5 % in all the modified electrodes. In terms of stability, the modified electrodes reported a dismissal lower than 5% after two weeks, and they can be used 25 times without losing their effectiveness. (4) Real sample analysis: the found concentration of DS in tablets and wastewater was compared with the concentration of DS found using UPLC-MS/MS. To sum up, the percentage of recovery and differences between the electrodes and the standard method for all of them when the tablets were tested showed a recovery rate of more than 95 %. However, the Chit+bioF/GCE electrode only showed an 80.17 % recovery rate when it came to figuring out DS concentration in wastewater, which is too low for accurate determination and means it can't be used on water samples. The other three electrodes reported a recovery percentage of ≤ 95 %, which enables their use in wastewater or real pharmaceutical samples. Overall, the performed modified electrodes reported a low LOD and LOQ, which is below the European requirements; a high selectivity; a high reproducibility and repeatability (RSD ≤ 95 %); a high stability; a simple method of preparation; and a low-cost production. A high percentage of recovery for both commercial tablets and wastewater samples enables the use of the prepared electrode in DS determination and enables the miniaturization of these electrodes to be prepared on lab chips to analyze online the content of DS in different samples.

5. References

[1] Y. D. Gamburg., 2023. The Fundamentals of Electrochemistry, Cambridge Scholars Publishing, ISBN (13): 978-1-5275-0164-5

[2] Chaudhuri, A., Sandha, K. K., Agrawal, A. K., & Gupta, P. N. (2023). Introduction to smart polymers and their application. In Smart Polymeric Nano-Constructs in Drug Delivery (pp. 1–46). Elsevier. https://doi.org/10.1016/B978-0-323-91248-8.00002-7

[3] Krukiewicz, K., Gniazdowska, B., Jarosz, T., Herman, A. P., Boncel, S., & Turczyn, R. (2019). Effect of immobilization and release of ciprofloxacin and quercetin on electrochemical properties of poly(3,4-ethylenedioxypyrrole) matrix. *Synthetic Metals*, *249*, 52–62. https://doi.org/10.1016/j.synthmet.2019.02.001

[4] Krukiewicz, K., Cichy, M., Ruszkowski, P., Turczyn, R., Jarosz, T., Zak, J. K., Lapkowski, M., & Bednarczyk-Cwynar, B. (2017). Betulin-loaded PEDOT films for regional chemotherapy. *Materials Science and Engineering: C*, *73*, 611–615. https://doi.org/10.1016/j.msec.2016.12.115

[5] Ma, H., Yu, J., Liu, L., & Fan, Y. (2021). An optimized preparation of nanofiber hydrogels derived from natural carbohydrate polymers and their drug release capacity under different pH surroundings. *Carbohydrate Polymers*, *265*, 118008. https://doi.org/10.1016/j.carbpol.2021.118008

[6] García-Uriostegui, L., Meléndez-Ortíz, H. I., Camacho-Villegas, T. A., Lugo-Fabres, P. H., & Toriz, G. (2022). Synthesis and characterization of mesoporous silica-g-poly(hydroxyethylmethacrylate) nanohybrid particles as a drug delivery system. *Materials Chemistry and Physics*, *283*, 126048. https://doi.org/10.1016/j.matchemphys.2022.126048

[7] D'Agostino, A., Colella, M., de Rosa, M., de Rosa, A., Lanza, A., & Schiraldi, C. (2009). Chemico-physical characterization of hybrid composites based on hydroxyethyl methacrylate and nanosilica. *Journal of Polymer Research*, *16*(5), 561–567. https://doi.org/10.1007/s10965-008-9260-9

[8] Yarali, E., Baniasadi, M., Zolfagharian, A., Chavoshi, M., Arefi, F., Hossain, M., Bastola, A., Ansari, M., Foyouzat, A., Dabbagh, A., Ebrahimi, M., Mirzaali, M. J., & Bodaghi, M. (2022). Magneto-/ electro-responsive polymers toward manufacturing, characterization, and biomedical/ soft robotic applications. *Applied Materials Today*, *26*, 101306. https://doi.org/10.1016/j.apmt.2021.101306

[9] Goudu, S. R., Yasa, I. C., Hu, X., Ceylan, H., Hu, W., & Sitti, M. (2020). Biodegradable Untethered Magnetic Hydrogel Milli-Grippers. *Advanced Functional Materials*, *30*(50). https://doi.org/10.1002/adfm.202004975

[10] *Electrical Conductivity in Polymer-Based Composites: Experiments, Modelling and Applications*. (2019). Elsevier. https://doi.org/10.1016/C2016-0-03699-9

[11] Ge, D., Qi, R., Mu, J., Ru, X., Hong, S., Ji, S., Linkov, V., & Shi, W. (2010). A self-powered and thermally-responsive drug delivery system based on conducting polymers. *Electrochemistry Communications*, *12*(8), 1087–1090. https://doi.org/10.1016/j.elecom.2010.05.035

[12] Marchesi, L. F., Jacumasso, S. C., Quintanilha, R. C., Winnischofer, H., & Vidotti, M. (2015). The electrochemical impedance spectroscopy behavior of poly(aniline) nanocomposite electrodes modified by Layer-by-Layer deposition. *Electrochimica Acta*, *174*, 864–870. https://doi.org/10.1016/j.electacta.2015.05.077

[13] Pasqual, J. A. R., Freisleben, L. C., Colpo, J. C., Egea, J. R. J., dos Santos, L. A. L., & de Sousa, V. C. (2021). In situ drug release measuring in α-TCP cement by electrochemical impedance spectroscopy. *Journal of Materials Science: Materials in Medicine*, *32*(4), 38. https://doi.org/10.1007/s10856-021-06507-9

[14] Krukiewicz, K., Zawisza, P., Herman, A. P., Turczyn, R., Boncel, S., & Zak, J. K. (2016). An electrically controlled drug delivery system based on conducting poly(3,4-ethylenedioxypyrrole) matrix. *Bioelectrochemistry*, *108*, 13–20. https://doi.org/10.1016/j.bioelechem.2015.11.002

[15] Krukiewicz, K., Jarosz, T., Zak, J. K., Lapkowski, M., Ruszkowski, P., Bobkiewicz-Kozlowska, T., & Bednarczyk-Cwynar, B. (2015). Advancing the delivery of anticancer drugs: Conjugated polymer/triterpenoid composite. *Acta Biomaterialia*, *19*, 158–165. https://doi.org/10.1016/j.actbio.2015.03.006

[16] Sakunpongpitiporn, P., Morarad, R., Naeowong, W., Niamlang, S., & Sirivat, A. (2024). Poly(3,4-ethylenedioxythiophene):polystyrene sulfonate (PEDOT:PSS) as an insulin carrier in silk fibroin hydrogels for transdermal delivery *via* iontophoresis. *RSC Advances*, *14*(3), 1549–1562. https://doi.org/10.1039/D3RA06857A

[17] *Advances in Smart Coatings and Thin Films for Future Industrial and Biomedical Engineering Applications*. (2020). Elsevier. https://doi.org/10.1016/C2016-0-02150-2

[18] Zehra, S., Mobin, M., & Aslam, R. (2022). Corrosion prevention and protection methods. In *Eco-Friendly Corrosion Inhibitors* (pp. 13–26). Elsevier. https://doi.org/10.1016/B978-0-323-91176-4.00023-4

[19] Jafari, H., Rezaeivala, M., Mokhtarian, N., Berisha, A., & Ameri, E. (2022). Corrosion Inhibition of Carbon Steel in 0.5 M H2SO4 by New Reduced Schiff Base Ligand. *Journal of Bio- and Tribo-Corrosion*, *8*(3), 81. https://doi.org/10.1007/s40735-022-00679-9

[20] Maya-Visuet, E., Gao, T., Soucek, M., & Castaneda, H. (2015). The effect of TiO 2 as a pigment in a polyurethane/polysiloxane hybrid coating/aluminum interface based on damage evolution. *Progress in Organic Coatings*, *83*, 36–46. https://doi.org/10.1016/j.porgcoat.2015.02.001

[21] Devakumar, J., Jaya Santhi, R., Amaladass, P., & Ramesh, V. (2021). Anticorrosion activities of polymethacrylic acid and grafted/modified polymethacrylic acid on pure aluminium in acid medium. *Materials Today: Proceedings*, *42*, 1184–1194. https://doi.org/10.1016/j.matpr.2020.12.537

[22] Nassier, L. F., & Shinen, M. H. (2022). Study of the optical properties of poly (methyl methacrylate) (PMMA) by using spin coating method. *Materials Today: Proceedings*, *60*, 1660–1664. https://doi.org/10.1016/j.matpr.2021.12.213

[23] Shang, Z., & Zhu, J. (2021). Overview on plant extracts as green corrosion inhibitors in the oil and gas fields. *Journal of Materials Research and Technology*, *15*, 5078–5094. https://doi.org/10.1016/j.jmrt.2021.10.095

[24] Al-Amiery, A., Wan Isahak, W. N. R., & Al-Azzawi, W. K. (2024). Sustainable corrosion Inhibitors: A key step towards environmentally responsible corrosion control. *Ain Shams Engineering Journal*, *15*(5), 102672. https://doi.org/10.1016/j.asej.2024.102672

[25] Sajid, M., Nazal, M. K., Mansha, M., Alsharaa, A., Jillani, S. M. S., & Basheer, C. (2016). Chemically modified electrodes for electrochemical detection of dopamine in the presence of uric acid and ascorbic acid: A review. *TrAC Trends in Analytical Chemistry*, *76*, 15–29. https://doi.org/10.1016/j.trac.2015.09.006

[26] Wu, D., Hu, Y., & Liu, Y. (2022). A Review of Detection Techniques for Chemical Oxygen Demand in Wastewater. *American Journal of Biochemistry and Biotechnology*, *18*(1), 23–32. https://doi.org/10.3844/ajbbsp.2022.23.32

[27] Yilmaz, B. (2010). GC–MS Determination of Diclofenac in Human Plasma. *Chromatographia*, *71*(5–6), 549–551. https://doi.org/10.1365/s10337-010-1479-z

[28] Roškar, R., & Kmetec, V. (2003). Liquid chromatographic determination of diclofenac in human synovial fluid. *Journal of Chromatography B*, *788*(1), 57–64. https://doi.org/10.1016/S1570-0232(02)01015-2

[29] Postolović, K., & Stanić, Z. (2023). Chitosan/TiO2 nanoparticles modified carbon paste electrode as a sensitive voltammetric sensor for the determination of diclofenac sodium as an anti-inflammatory drug. *Materials Today Communications*, *37*, 107416. https://doi.org/10.1016/j.mtcomm.2023.107416

[30] Lonappan, L., Brar, S. K., Das, R. K., Verma, M., & Surampalli, R. Y. (2016). Diclofenac and its transformation products: Environmental occurrence and toxicity - A review. *Environment International*, *96*, 127–138. https://doi.org/10.1016/j.envint.2016.09.014

[31] Sathishkumar, P., Meena, R. A. A., Palanisami, T., Ashokkumar, V., Palvannan, T., & Gu, F. L. (2020). Occurrence, interactive effects and ecological risk of diclofenac in environmental compartments and biota - a review. *Science of The Total Environment*, *698*, 134057. https://doi.org/10.1016/j.scitotenv.2019.134057

[32] Hashida, M. (2020). Role of pharmacokinetic consideration for the development of drug delivery systems: A historical overview. *Advanced Drug Delivery Reviews*, *157*, 71–82. https://doi.org/10.1016/j.addr.2020.06.015

[33] Walker, M. 2014. Methods in Molecular Biology: Drug Delivery Systems, Springer., 1 ed, 45-90, New York, doi: 10.1007/978-1-4939-0363-4

[34] Cassano, R., Mellace, S., & Trombino, S. (2018). Responsive polymer-biomacromolecule conjugates for drug delivery. In *Stimuli Responsive Polymeric Nanocarriers for Drug Delivery Applications, Volume 1* (pp. 433–452). Elsevier. https://doi.org/10.1016/B978-0-08-101997-9.00020-5

[35] Reza Rezaie, H., Esnaashary, M., Aref arjmand, A., & Öchsner, A. (2018). *Classification of Drug Delivery Systems* (pp. 9–25). https://doi.org/10.1007/978-981-10-0503-9_2

[36] Das, D., & Pal, S. (2015). Modified biopolymer-dextrin based crosslinked hydrogels: application in controlled drug delivery. *RSC Advances*, *5*(32), 25014–25050. https://doi.org/10.1039/C4RA16103C

[37] Webster John G (2006) Encyclopedia of medical devices and instrumentation, 2nd edn. Wiley, Hoboken, NJ, USA

[38] Agrawal, S., Giri, T. K., Tripathi, D. K., . A., & Alexander, A. (2012). A Review on Novel Therapeutic Strategies for the Enhancement of Solubility for Hydrophobic Drugs through Lipid and Surfactant Based Self Micro Emulsifying Drug Delivery System: A Novel Approach. *American Journal of Drug Discovery and Development*, *2*(4), 143–183. https://doi.org/10.3923/ajdd.2012.143.183

[39] Sultana, A., Zare, M., Thomas, V., Kumar, T. S. S., & Ramakrishna, S. (2022). Nano-based drug delivery systems: Conventional drug delivery routes, recent developments and future prospects. *Medicine in Drug Discovery*, *15*, 100134. https://doi.org/10.1016/j.medidd.2022.100134

[40] Bari, E., Perteghella, S., & Torre, M. L. (Eds.). (2020). *Silk-based Drug Delivery Systems*. The Royal Society of Chemistry. https://doi.org/10.1039/9781839162664

[41] Sonawane, S. H., Bhanvase, B. A., Sivakumar, M., & Potdar, S. B. (2020). Current overview of encapsulation. In *Encapsulation of Active Molecules and Their Delivery System* (pp. 1–8). Elsevier. https://doi.org/10.1016/B978-0-12-819363-1.00001-6

[42] Martínez Rivas, C. J., Tarhini, M., Badri, W., Miladi, K., Greige-Gerges, H., Nazari, Q. A., Galindo Rodríguez, S. A., Román, R. Á., Fessi, H., & Elaissari, A. (2017). Nanoprecipitation process: From encapsulation to drug delivery. *International Journal of Pharmaceutics*, *532*(1), 66–81. https://doi.org/10.1016/j.ijpharm.2017.08.064

[43] Ye, W., Zhang, G., Liu, X., Ren, Q., Huang, F., & Yan, Y. (2022). Fabrication of polysaccharide-stabilized zein nanoparticles by flash nanoprecipitation for doxorubicin sustained release. *Journal of Drug Delivery Science and Technology*, *70*, 103183. https://doi.org/10.1016/j.jddst.2022.103183

[44] Ahmed Bhutto, R., Fu, Z., Wang, M., Yu, J., Zhao, F., Khanal, S., Halepoto, A., Wang, J., Cohen Stuart, M. A., & Guo, X. (2021). Facile controlling internal structure of β-carotene-loaded protein nanoparticles by Flash Nanoprecipitation. *Materials Letters*, *304*, 130523. https://doi.org/10.1016/j.matlet.2021.130523

[45] Roshan, Z., Haddadi-Asl, V., Ahmadi, H., & Moussaei, M. (2024). Curcumin-Encapsulated Poly(lactic- *co* -glycolic acid) Nanoparticles: A Comparison of Drug Release Kinetics from Particles Prepared via Electrospray and Nanoprecipitation. *Macromolecular Materials and Engineering*, *309*(7). https://doi.org/10.1002/mame.202400040

[46] Hasankhan, S., Tabibiazar, M., Hosseini, S. M., Ehsani, A., & Ghorbani, M. (2020). Fabrication of curcumin-zein-ethyl cellulose composite nanoparticles using antisolvent co-precipitation method. *International Journal of Biological Macromolecules*, *163*, 1538–1545. https://doi.org/10.1016/j.ijbiomac.2020.08.045

[47] Bidone, J., Schuh, R. S., Farinon, M., Poletto, É., Pasqualim, G., de Oliveira, P. G., Fraga, M., Xavier, R. M., Baldo, G., Teixeira, H. F., & Matte, U. (2018). Intra-articular nonviral gene therapy in mucopolysaccharidosis I mice. *International Journal of Pharmaceutics*, *548*(1), 151–158. https://doi.org/10.1016/j.ijpharm.2018.06.049

[48] Shende, P., Patil, A., & Prabhakar, B. (2020). Layer-by-layer technique for enhancing physicochemical properties of actives. *Journal of Drug Delivery Science and Technology*, *56*, 101519. https://doi.org/10.1016/j.jddst.2020.101519

[49] Xiao, F.-X., Pagliaro, M., Xu, Y.-J., & Liu, B. (2016). Layer-by-layer assembly of versatile nanoarchitectures with diverse dimensionality: a new perspective for rational construction of multilayer assemblies. *Chemical Society Reviews*, *45*(11), 3088–3121. https://doi.org/10.1039/C5CS00781J

[50] Kurapati, R., Groth, T. W., & Raichur, A. M. (2019). Recent Developments in Layer-by-Layer Technique for Drug Delivery Applications. *ACS Applied Bio Materials*, *2*(12), 5512–5527. https://doi.org/10.1021/acsabm.9b00703

[51] Mofazali, P., Atapour, M., Nakamura, M., Galati, M., & Saboori, A. (2024). Evaluation of layer-by-layer assembly systems for drug delivery and antimicrobial properties in orthopaedic application. *International Journal of Pharmaceutics*, *657*, 124148. https://doi.org/10.1016/j.ijpharm.2024.124148

[52] P. A. Ferreira, M., Martins, J. P., Hirvonen, J., & Santos, H. A. (2020). Spray-drying for the formulation of oral drug delivery systems. In *Nanotechnology for Oral Drug Delivery* (pp. 253–284). Elsevier. https://doi.org/10.1016/B978-0-12-818038-9.00007-7

[53] Szczepanowicz, K., Bzowska, M., Kruk, T., Karabasz, A., Bereta, J., & Warszynski, P. (2016). Pegylated polyelectrolyte nanoparticles containing paclitaxel as a promising candidate for drug carriers for passive targeting. *Colloids and Surfaces B: Biointerfaces*, *143*, 463–471. https://doi.org/10.1016/j.colsurfb.2016.03.064

[54] P. A. Ferreira, M., Martins, J. P., Hirvonen, J., & Santos, H. A. (2020). Spray-drying for the formulation of oral drug delivery systems. In *Nanotechnology for Oral Drug Delivery* (pp. 253–284). [55] Elsevier. https://doi.org/10.1016/B978-0-12-818038-9.00007-7

Shi, N.-Q., Zhou, J., Walker, J., Li, L., Hong, J. K. Y., Olsen, K. F., Tang, J., Ackermann, R., Wang, [56] Y., Qin, B., Schwendeman, A., & Schwendeman, S. P. (2020). Microencapsulation of luteinizing hormone-releasing hormone agonist in poly (lactic-co-glycolic acid) microspheres by spray-drying. *Journal of Controlled Release*, *321*, 756–772. https://doi.org/10.1016/j.jconrel.2020.01.023

al Khatib, A. O., Yousfan, A., Abed, A., El-Tanani, M., & Al-Obaidi, H. (2025). Development of pimozide spray dried lipid nanoparticles with enhanced targeting of non-small cell lung cancer. *Journal of Drug Delivery Science and Technology*, *109*, 106969. https://doi.org/10.1016/j.jddst.2025.106969

[57] Ngwuluka, N. (2010). Application of In Situ Polymerization for Design and Development of Oral Drug Delivery Systems. *AAPS PharmSciTech*, *11*(4), 1603–1611. https://doi.org/10.1208/s12249-010-9535-4

[58] Mahkam, M. (2009). New terpolymers as hydrogels for oral protein delivery application. *Journal of Drug Targeting*, *17*(1), 29–35. https://doi.org/10.1080/10611860802438728

[59] Ramanan, R. M. K., Chellamuthu, P., Tang, L., & Nguyen, K. T. (2006). Development of a Temperature-Sensitive Composite Hydrogel for Drug Delivery Applications. *Biotechnology Progress*, *22*(1), 118–125. https://doi.org/10.1021/bp0501367

[60] Escobar, K., Carrera, I., Naveas, N., Pulido, R., Manso, M., Guarnieri, J. P. de O., Lancellotti, M., Cotta, M. A., Corrales-Ureña, Y. R., Rischka, K., & Hernandez-Montelongo, J. (2023). Functionalization of breast implants by cyclodextrin in-situ polymerization: a local drug delivery system for augmentation mammaplasty. *Frontiers in Bioengineering and Biotechnology*, *11*. https://doi.org/10.3389/fbioe.2023.1254299

[61] Attia, M. F., Montaser, A. S., Arifuzzaman, M., Pitz, M., Jlassi, K., Alexander-Bryant, A., Kelly, S. S., Alexis, F., & Whitehead, D. C. (2021). In Situ Photopolymerization of Acrylamide Hydrogel to Coat Cellulose Acetate Nanofibers for Drug Delivery System. *Polymers*, *13*(11), 1863. https://doi.org/10.3390/polym13111863

[62] Fang, H., Chen, L., Deng, Z., Gao, Y., Yang, Y., Chen, Q., & Liu, Z. (2023). *In Situ* Polymerization of Zwitterions on Therapeutic Proteins to Enable Their Effective Oral Delivery. *ACS Nano*, *17*(2), 1128–1143. https://doi.org/10.1021/acsnano.2c08434

[63] Vasant, V., Mannfred, A., Hollinger, A. 2004. Drug delivery systems, CRC. Press., New York, 1 ed., 40-47

[64] Hazelton, P., Mengguang, Y., Xianfeng, C. 2023. Introduction to Conducting Polymers. ACS. Omega., 1 ed., 15, 20-22

[65] Bert, L., Groenendaal, F., Freitag, D., Pielartzik, H., Reynolds, J. 2000. Poly(3,4-ethylenedioxythiophene) and Its Derivatives: Past, Present, and Future. Adv. Mater. 2000, 12, 7, doi: 0935-9648/00/0704-0482

[66] Boz, E. B., Fritz, M., Forner-Cuenca, A. 2023. Electropolymerized Poly(3,4-ethylenedioxythiophene) Coatings on Porous Carbon Electrodes for Electrochemical Separation of Metals. Advanced. Materials. Interfaces., 10(9), 2202497, doi: https://doi.org/10.1002/admi.202202497

[67] Titanium. (2016). In *Meyler's Side Effects of Drugs* (pp. 21–25). Elsevier. https://doi.org/10.1016/B978-0-444-53717-1.01560-2

[68] Fakhr Nabavi, H., & Aliofkhazraei, M. (2019). Morphology, composition and electrochemical properties of bioactive-TiO2/HA on CP-Ti and Ti6Al4V substrates

fabricated by alkali treatment of hybrid plasma electrolytic oxidation process (estimation of porosity from EIS results). *Surface and Coatings Technology*, *375*, 266–291. https://doi.org/10.1016/j.surfcoat.2019.07.032

[69] Liu, S., & Shin, Y. C. (2019). Additive manufacturing of Ti6Al4V alloy: A review. *Materials & Design*, *164*, 107552. https://doi.org/10.1016/j.matdes.2018.107552

[70] Hendriks, J. G. E., van Horn, J. R., van der Mei, H. C., & Busscher, H. J. (2004). Backgrounds of antibiotic-loaded bone cement and prosthesis-related infection. *Biomaterials*, *25*(3), 545–556. https://doi.org/10.1016/S0142-9612(03)00554-4

[71] Zhang, L., & Chen, L. (2019). A Review on Biomedical Titanium Alloys: Recent Progress and Prospect. *Advanced Engineering Materials*, *21*(4). https://doi.org/10.1002/adem.201801215

[72] Losic, D., Aw, M. S., Santos, A., Gulati, K., & Bariana, M. (2015). Titania nanotube arrays for local drug delivery: recent advances and perspectives. *Expert Opinion on Drug Delivery*, *12*(1), 103–127. https://doi.org/10.1517/17425247.2014.945418

[73] Rajesh, K., Ghosh, S., Islam, A., Rangaswamy, M. K., Haldar, S., Roy, P., Keshri, A. K., & Lahiri, D. (2022). Multilayered porous hydroxyapatite coating on Ti6Al4V implant with enhanced drug delivery and antimicrobial properties. *Journal of Drug Delivery Science and Technology*, *70*, 103155. https://doi.org/10.1016/j.jddst.2022.103155

[74] Wang, M., Wang, C., Zhang, Y., & Lin, Y. (2021). Controlled release of dopamine coatings on titanium bidirectionally regulate osteoclastic and osteogenic response behaviors. *Materials Science and Engineering: C*, *129*, 112376. https://doi.org/10.1016/j.msec.2021.112376

[76] Lyndon, J. A., Boyd, B. J., & Birbilis, N. (2014). Metallic implant drug/device combinations for controlled drug release in orthopaedic applications. *Journal of Controlled Release*, *179*, 63–75. https://doi.org/10.1016/j.jconrel.2014.01.026

[77] Ayoub, S. S. (2021). Paracetamol (acetaminophen): A familiar drug with an unexplained mechanism of action. *Temperature*, *8*(4), 351–371. https://doi.org/10.1080/23328940.2021.1886392

[78] Hider-Mlynarz, K., Cavalié, P., & Maison, P. (2018). Trends in analgesic consumption in France over the last 10 years and comparison of patterns across Europe. *British Journal of Clinical Pharmacology*, *84*(6), 1324–1334. https://doi.org/10.1111/bcp.13564

[79] Goscianska, J., Olejnik, A., Ejsmont, A., Galarda, A., & Wuttke, S. (2021). Overcoming the paracetamol dose challenge with wrinkled mesoporous carbon spheres. *Journal of Colloid and Interface Science*, *586*, 673–682. https://doi.org/10.1016/j.jcis.2020.10.137

[80] Pishnamazi, M., Hafizi, H., Shirazian, S., Culebras, M., Walker, G., & Collins, M. (2019). Design of Controlled Release System for Paracetamol Based on Modified Lignin. *Polymers*, *11*(6), 1059. https://doi.org/10.3390/polym11061059

[81] Goscianska, J., Olejnik, A., Ejsmont, A., Galarda, A., & Wuttke, S. (2021). Overcoming the paracetamol dose challenge with wrinkled mesoporous carbon spheres. *Journal of Colloid and Interface Science*, *586*, 673–682. https://doi.org/10.1016/j.jcis.2020.10.137

[82] Gautam, S., Singhal, J., Lee, H. K., & Chae, K. H. (2022). Drug delivery of paracetamol by metal-organic frameworks (HKUST-1): improvised synthesis and investigations. *Materials Today Chemistry*, *23*, 100647. https://doi.org/10.1016/j.mtchem.2021.100647

[83] Adhikary, S., al Hoque, A., Ray, M., Paul, S., Hossain, A., Goswami, S., & Dey, R. (2023). Investigation of Paracetamol Entrapped Nanoporous Silica Nanoparticles in Transdermal Drug Delivery System. *Applied Biochemistry and Biotechnology*, *195*(8), 4712–4727. https://doi.org/10.1007/s12010-023-04576-w

Asci, H., Savran, M., Cengiz Callıoglu, F., Sahin, S., Hasseyid, N., Kaynak, M., Izat, N., & Kesici [84] Guler, H. (2022). Supralingual administration of paracetamol embedded in polyvinyl alcohol nanofibers: A pharmacokinetic study. *Journal of Drug Delivery Science and Technology*, *67*, 102948. https://doi.org/10.1016/j.jddst.2021.102948

[85] Laracuente, M.-L., Yu, M. H., & McHugh, K. J. (2020). Zero-order drug delivery: State of the art and future prospects. *Journal of Controlled Release*, *327*, 834–856. https://doi.org/10.1016/j.jconrel.2020.09.020

[86] Talevi, A., & Ruiz, M. E. (2022). Zero-Order Drug Release. In *The ADME Encyclopedia* (pp. 1195–1200). Springer International Publishing. https://doi.org/10.1007/978-3-030-84860-6_33

[87] Mathematical models of drug release. (2015). In *Strategies to Modify the Drug Release from Pharmaceutical Systems* (pp. 63–86). Elsevier. https://doi.org/10.1016/B978-0-08-100092-2.00005-9

[88] Strategies to control drug release rates from degradable polymers toward zero order profiles, in: J. Siepmann, R.A. Siegel, M.J. Rathbone (Eds.), Fundam. Appl. Control. Release Drug Deliv. Springer, 2012, pp. 211–212

[89] Zaki, A. 2006. Principles of Corrosion Engineering and Corrosion Control. Elsevier Science. Technology., 1 ed, 45-87

[90] Part I: General Aspects of Corrosion, Corrosion Control, and Corrosion Prevention. (2022). In *Corrosion Atlas Case Studies* (pp. xxv–xlii). Elsevier. https://doi.org/10.1016/B978-0-323-85849-6.02002-3

[91] Qasim, A., Khan, M. S., Lal, B., & Shariff, A. M. (2019). A perspective on dual purpose gas hydrate and corrosion inhibitors for flow assurance. *Journal of Petroleum Science and Engineering*, *183*, 106418. https://doi.org/10.1016/j.petrol.2019.106418

[92] Makhlouf, A. S. H., & Botello, M. A. (2018). Failure of the metallic structures due to microbiologically induced corrosion and the techniques for protection. In *Handbook of Materials Failure Analysis* (pp. 1–18). Elsevier. https://doi.org/10.1016/B978-0-08-101928-3.00001-X

[93] Ahmad, Z. (2006). SELECTION OF MATERIALS FOR CORROSIVE ENVIRONMENT. In *Principles of Corrosion Engineering and Corrosion Control* (pp. 479–549). Elsevier. https://doi.org/10.1016/B978-075065924-6/50010-6

[94] Agrawal, A. K. (2001). Corrosion Monitoring. In *Encyclopedia of Materials: Science and Technology* (pp. 1698–1701). Elsevier. https://doi.org/10.1016/B0-08-043152-6/00302-8

[95] Papavinasam, S. (2021). Electrochemical polarization techniques for corrosion monitoring. In *Techniques for Corrosion Monitoring* (pp. 45–77). Elsevier. https://doi.org/10.1016/B978-0-08-103003-5.00003-5

[96] Chi, D., Xu, Z., & Liu, H. (2024). Detection and Imaging of Corrosion Defects in Steel Structures Based on Ultrasonic Digital Image Processing. *Metals*, *14*(4), 390. https://doi.org/10.3390/met14040390

[97] Farin, M., Moulin, E., Chehami, L., Benmeddour, F., Nicard, C., Campistron, P., Bréhault, O., & Dupont, L. (2022). Monitoring saltwater corrosion of steel using ultrasonic coda wave interferometry with temperature control. *Ultrasonics*, *124*, 106753. https://doi.org/10.1016/j.ultras.2022.106753

[98] Chhipa, M., Sharma, S., Bagha, K. 2024. Recent development in polymer coating to prevent corrosion in metals: A review. Materials Today: Proceedings., doi: https://doi.org/10.1016/j.matpr.2024.09.001

[99] Harper, Charles A., Handbook of Plastic Processes, John Wiley & Sons, 2005

[100] Vaszilcsin, N., Kellenberger, A., Dan, ML., Duca, DA., Ordodi, VL. 2023. Efficiency of Expired Drugs Used as Corrosion Inhibitors: A Review. Materials., 16(16), 5555, doi: https://doi.org/10.3390/ma16165555

[101] BASF, 2018. Technical Information Ibuprofen

[102] Abdullah, D. 2011. A review: plant extracts and oils as corrosion inhibitors in aggressive media. Industrial. Lubrication. Tribology., 277-233, doi: 10.1108/00368791111140431

[103] Ren, H., Liu, Y., Gong, Z., Tan, B., Deng, H., Xiong, J., Shao, P., Dai, Q., Cao, J., & Marzouki, R. (2024). Pumpkin Leaf Extract Crop Waste as a New Degradable and Environmentally Friendly Corrosion Inhibitor. *Langmuir*, *40*(11), 5738–5752. https://doi.org/10.1021/acs.langmuir.3c03399

[104] Tan, B., Liu, Y., Gong, Z., Zhang, X., Chen, J., Guo, L., Xiong, J., Liu, J., Marzouki, R., & Li, W. (2024). Pyracantha fortuneana alcohol extracts as biodegradable corrosion inhibitors for copper in H2SO4 media. *Journal of Molecular Liquids*, *397*, 124117. https://doi.org/10.1016/j.molliq.2024.124117

Shahmoradi, A. R., Talebibahmanbigloo, N., Nickhil, C., Nisha, R., Javidparvar, A. A., Ghahremani, [105] P., Bahlakeh, G., & Ramezanzadeh, B. (2022). Molecular-MD/atomic-DFT theoretical and experimental studies on the quince seed extract corrosion inhibition performance on the acidic-solution attack of mild-steel. *Journal of Molecular Liquids*, *346*, 117921. https://doi.org/10.1016/j.molliq.2021.117921

[106] Rizi, A., Sedik, A., Acidi, A., Rachedi, K. O., Ferkous, H., Berredjem, M., Delimi, A., Abdennouri, A., ALAM, M., Ernst, B., & Benguerba, Y. (2023). Sustainable and Green Corrosion Inhibition of Mild Steel: Insights from Electrochemical and Computational Approaches. *ACS Omega*, *8*(49), 47224–47238. https://doi.org/10.1021/acsomega.3c06548

[107] Tan, B., Ren, H., Liu, Y., Li, X., Wang, R., Sun, J., Cao, X., Dai, Q., Guo, L., Liu, H., & Al-Sadoon, M. K. (2024). Insight into the anti-corrosion performance of crop waste as a degradable corrosion inhibitor for copper in sulfuric acid medium. *Industrial Crops and Products*, *222*, 119654. https://doi.org/10.1016/j.indcrop.2024.119654

[108] Al-Moghrabi, R. S., Abdel-Gaber, A. M., & Rahal, H. T. (2019). Corrosion Inhibition of Mild Steel in Hydrochloric and Nitric Acid Solutions Using Willow Leaf Extract. *Protection of Metals and Physical Chemistry of Surfaces*, *55*(3), 603–607. https://doi.org/10.1134/S2070205119030031

[109] Salem, Aya. M., & Al-Sharif, M. S. (2024). Eco-Friendly *Piper cubeba* Official Extract Corrosion Inhibition of C-Steel in 1 M Sulfamic Acid. *ACS Omega*, *9*(4), 5024–5037. https://doi.org/10.1021/acsomega.3c09334

[110] Zhang, X., Li, W., Yu, G., Zuo, X., Luo, W., Zhang, J., Tan, B., Fu, A., & Zhang, S. (2020). Evaluation of Idesia polycarpa Maxim fruits extract as a natural green corrosion inhibitor for copper in 0.5 M sulfuric acid solution. *Journal of Molecular Liquids*, *318*, 114080. https://doi.org/10.1016/j.molliq.2020.114080

[111] Pourmohseni, M., Rashidi, A., & Karimkhani, M. (2024). Preparation of corrosion inhibitor from natural plant for mild stil immersed in an acidic environmental: experimental and theoretical study. *Scientific Reports*, *14*(1), 7937. https://doi.org/10.1038/s41598-024-58637-z

[112] Manh, T. D., Huynh, T. L., Thi, B. V., Lee, S., Yi, J., & Nguyen Dang, N. (2022). Corrosion Inhibition of Mild Steel in Hydrochloric Acid Environments Containing *Sonneratia caseolaris* Leaf Extract. *ACS Omega*, *7*(10), 8874–8886. https://doi.org/10.1021/acsomega.1c07237

[113] Behl, T., Rana, T., Sehgal, A., Sharma, N., Albarrati, A., Albratty, M., Makeen, H. A., Najmi, A., Verma, R., & Bungau, S. G. (2023). Exploring the multifocal role of phytoconstituents as antidepressants. *Progress in Neuro-Psychopharmacology and Biological Psychiatry*, *123*, 110693. https://doi.org/10.1016/j.pnpbp.2022.110693

[114] Mounim Lebrini, M. 2023. Alkaloids from Plant Extracts as Corrosion Inhibitors for Metal Alloys. Intech. 1 ed., 25, 78-80

[115] Grant A. Edwards, Adam Johan Bergren, Marc D. Porter, 2007. Chemically Modified Electrodes. Handbook of Electrochemistry. Elsevier., 295-327, doi: https://doi.org/10.1016/B978-044451958-0.50021-5

[116] Edwards, G. A., Bergren, A. J., & Porter, M. D. (2007). Chemically Modified Electrodes. In *Handbook of Electrochemistry* (pp. 295–327). Elsevier. https://doi.org/10.1016/B978-044451958-0.50021-5

[117] Wang, L., Li, Y., Li, G., & Ye, B. (2015). A new strategy for enhancing electrochemical sensing from MWCNTs modified electrode with Langmuir-Blodgett film and used in determination of methylparaben. *Sensors and Actuators B: Chemical*, *211*, 332–338. https://doi.org/10.1016/j.snb.2015.01.056

[118] Liu, Y., Yang, R., Zhao, M., Guo, H., Liu, Y., Yan, H., & Liu, Z. (2024). Layer-by-layer self-assembled poly(diallyldimethylammonium chloride)/cyclodextrin composite materials for the electrochemical detection of paracetamol. *International*

Journal of Electrochemical Science, *19*(12), 100878. https://doi.org/10.1016/j.ijoes.2024.100878

[119] Bataglioli, R. A., Rocha Neto, J. B. M., Leão, B. S., Germiniani, L. G. L., Taketa, T. B., & Beppu, M. M. (2020). Interplay of the Assembly Conditions on Drug Transport Mechanisms in Polyelectrolyte Multilayer Films. *Langmuir*, *36*(42), 12532–12544. https://doi.org/10.1021/acs.langmuir.0c01980

[120] Wang, Z., Wu, S., Wang, J., Yu, A., & Wei, G. (2019). Carbon Nanofiber-Based Functional Nanomaterials for Sensor Applications. *Nanomaterials*, *9*(7), 1045. https://doi.org/10.3390/nano9071045

[121] Liu, Y., Yang, R., Zhao, M., Guo, H., Liu, Y., Yan, H., & Liu, Z. (2024). Layer-by-layer self-assembled poly(diallyldimethylammonium chloride)/cyclodextrin composite materials for the electrochemical detection of paracetamol. *International Journal of Electrochemical Science*, *19*(12), 100878. https://doi.org/10.1016/j.ijoes.2024.100878

[122] Qin, X., Zhang, J., Shao, W., Liu, X., Zhang, X., Chen, F., Qin, X., Wang, L., Luo, D., & Qiao, X. (2021). Modification of electrodes with self-assembled, close-packed AuNPs for improved signal reproducibility toward electrochemical detection of dopamine. *Electrochemistry Communications*, *133*, 107161. https://doi.org/10.1016/j.elecom.2021.107161

[123] Hefnawy, M. A., Medany, S. S., Fadlallah, S. A., El-Sherif, R. M., & Hassan, S. S. (2022). Novel Self-assembly Pd(II)-Schiff Base Complex Modified Glassy Carbon Electrode for Electrochemical Detection of Paracetamol. *Electrocatalysis*, *13*(5), 598–610. https://doi.org/10.1007/s12678-022-00741-7

[124] Pimpilova, M. (2024). A brief review on methods and materials for electrode modification: electroanalytical applications towards biologically relevant compounds. *Discover Electrochemistry*, *1*(1), 12. https://doi.org/10.1007/s44373-024-00012-8

[125] Li, S., & Ma, Q. (2022). Electrochemical nano-sensing interface for exosomes analysis and cancer diagnosis. *Biosensors and Bioelectronics*, *214*, 114554. https://doi.org/10.1016/j.bios.2022.114554

[126] Li, Y., Zhou, J., Song, J., Liang, X., Zhang, Z., Men, D., Wang, D., & Zhang, X.-E. (2019). Chemical nature of electrochemical activation of carbon electrodes. *Biosensors and Bioelectronics*, *144*, 111534. https://doi.org/10.1016/j.bios.2019.111534

[127] Yang, Z., Guo, H., Yu, Z., Wang, M., Wei, X., Lu, Z., Sun, L., Ren, H., & Yang, W. (2024). Ratiometric electrochemical biosensor based on Cu(II) modified covalent

organic framework for the ultra-sensitive and specific detection of glutathione. *Chemical Engineering Journal*, *492*, 152271. https://doi.org/10.1016/j.cej.2024.152271

[128] Rahi Algraittee, S. J., Hussein Bdair, B. W., Abass Sukir, F. A., Muslim Muhibes, R., Mudhafar, M., & Lahhob, Q. R. (2025). Screen printed graphite electrode modified with two-dimen-sional leaf-like zeolitic imidazolate framework-L (Zn) for efficient electrochemical sensing of sulphite. *Journal of Electrochemical Science and Engineering*, 2580. https://doi.org/10.5599/jese.2580

[129] Xiao, Y., Wu, N., Wang, L., & Chen, L. (2022). A Novel Paper-Based Electrochemical Biosensor Based on N,O-Rich Covalent Organic Frameworks for Carbaryl Detection. *Biosensors*, *12*(10), 899. https://doi.org/10.3390/bios12100899

[130] Zhang, T., Gao, C., Huang, W., Chen, Y., Wang, Y., & Wang, J. (2018). Covalent organic framework as a novel electrochemical platform for highly sensitive and stable detection of lead. *Talanta*, *188*, 578–583. https://doi.org/10.1016/j.talanta.2018.06.032

[131] Zittel, H. E., Miller, F. J., 1965. A Glassy-Carbon Electrode for Voltammetry. Anal. Chem., 37(2), 200–203. doi:10.1021/ac60221a006

[132] Dekanski, A., Stevanović, J., Stevanović, R., Nikolić, B. Ž., Jovanović, V. M., 2001. Glassy carbon electrodes. Carbon, 39(8), 1195–1205. doi:10.1016/s0008-6223(00)00228-1

[133] Uskokovic, V., 2021. A historical review of glassy carbon: Synthesis, structure, properties and applications. Carbon. Trends., 5, 100116, doi: https://doi.org/10.1016/j.cartre.2021.100116

[134] Serp, P., Reedijk, J., Poeppelmeier, K., 2013. Comprehensive inorganic chemistry II: From elements to applications. Elsevier. Oxford., 323–369

[135] Kishan, G., Ramawat, J. 2015. Polysaccharides. Springer. 1 ed., 2, 219-250, doi: 10.1007/978-3-319-16298-0

[136] Aranaz, I., Alcántara, AR., Civera, MC., Arias, C., Elorza, B., Heras Caballero, A., Acosta, N. 2021. Chitosan: An Overview of Its Properties and Applications. Polymers.,13(19), 3256, doi: https://doi.org/10.3390/polym13193256

[137] Yan, X., Chen, X. 2015. Titanium Dioxide Nanomaterials. Encyclopedia of Inorganic and Bioinorganic. Chemistry., 1–38, doi: 10.1002/9781119951438.eib

[138] Sungur, Ş. 2021. Titanium Dioxide Nanoparticles: Handbook of Nanomaterials and Nanocomposites for Energy and Environmental Applications. Springer. Cham., doi: https://doi.org/10.1007/978-3-030-36268-3_9

[139] Monthioux, M. 2007. Introduction to Carbon Nanotubes. In: Bhushan, B. (eds) Springer Handbook of Nanotechnology., Springer., 1 ed., 1, 25-40, doi: https://doi.org/10.1007/978-3-540-29857-1_3

[79] Schuhmacher, J.S., Thormann, K.M., Bange, G. 2015. How bacteria maintain location and number of flagella?. FEMS. Microbiol. Rev., 39, 812–822, doi: https://doi.org/10.1093/femsre/fuv034

[140] Beatson, S.A., Minamino, T., Pallen, M.J. 2006. Variation in bacterial flagellins: From sequence to structure. Trends Microbiol., 14, 151–155, doi: 10.1016/j.tim.2006.02.001

[142] Mimori, Y., Yamashita, I., Murata, K., Fujiyoshi, Y., Yonekura, K., Toyoshima, C., Namba, K. 1995. The structure of the R-type straight flagellar filament of Salmonella at 9 A resolution by electron cryomicroscopy. J. Mol. Biol. 249, 69–87, doi: https://doi.org/10.1006/jmbi.1995.0281

[143] Morgan, D.G., Owen, C., Melanson, L.A., DeRosier, D.J. 1995. Structure of bacterial flagellar filaments at 11 A resolution: Packing of the alpha-helices. J. Mol. Biol. 249, 88–110, doi: https://doi.org/10.1006/jmbi.1995.0282

[144] Tavazzi, S., Paracchini, B., Suurkuusk, G., Mariani, R., Loos, M., Ricci, M., Gawlik, B. 2020. Water Framework Directive Watch List Method: Analysis of diclofenac in water JRC., 25, 90, doi: 10.2788/19818

[145] Adeyeye, C. M., Li, P.-K. 1990. Diclofenac Sodium. Analytical. Profiles. of Drug. Substances., 123–144., doi:10.1016/s0099-5428(08)60366-4

[146] Directive 2013/39/EU of the European Parliament and of the Council of 12 August 2013 amending Directives 2000/60/EC and 2008/105/EC as regards priority substances in the field of water policy. Off. J. Eur. Union. 2013;L226:1–17

[147] Boumya, W., Taoufik, N., Achak, M., Bessbousse, H., Elhalil, A., & Barka, N. (2021). Electrochemical sensors and biosensors for the determination of diclofenac in pharmaceutical, biological and water samples. *Talanta Open*, *3*, 100026. https://doi.org/10.1016/j.talo.2020.100026

[148] Măghinici, A.-R., Bounegru, A.-V., & Apetrei, C. (2025). Electrochemical Detection of Diclofenac Using a Screen-Printed Electrode Modified with Graphene Oxide and Phenanthroline. *Chemosensors*, *13*(2), 55. https://doi.org/10.3390/chemosensors13020055

[149] Das, S., Chakravorty, A., Raj, A., Luktuke, S., Appu Mini, A., Awasthi, S., Sankar Sana, S., Kumar Pandey, S., & Raghavan, V. (2024). Graphene/MWCNT/copper-

nanoparticle fabricated printed electrode for diclofenac detection in milk and drinking water: Electrochemical and in-silico analysis. *Journal of Molecular Liquids*, *411*, 125750. https://doi.org/10.1016/j.molliq.2024.125750

[150] Tang, L., Huang, Y., Wang, Y., & Zhao, H. (2025). A Flexible Electrochemical Sensor for Simultaneous Detection of Acetaminophen and Diclofenac Sodium Using a Carbon Nanotube-Doped Hydrogel. *Journal of Electronic Materials*, *54*(8), 6218–6228. https://doi.org/10.1007/s11664-025-12056-6

[151] Elbalkiny, H. T., Yehia, A. M., Riad, S. M., & Elsaharty, Y. S. (2019). Potentiometric diclofenac detection in wastewater using functionalized nanoparticles. *Microchemical Journal*, *145*, 90–95. https://doi.org/10.1016/j.microc.2018.10.017

[152] Das, S., Chakravorty, A., Luktuke, S., Raj, A., Mini, A. A., Ramesh, K., Grace, A. N., Pandey, S. K., & Raghavan, V. (2023). Graphene/gadolinium oxide composite modified screen-printed electrochemical sensor for detection of diclofenac sodium. *Results in Chemistry*, *6*, 101189. https://doi.org/10.1016/j.rechem.2023.101189

[153] Honakeri, N. C., Malode, S. J., Kulkarni, R. M., & Shetti, N. P. (2020). Electrochemical behavior of diclofenac sodium at coreshell nanostructure modified electrode and its analysis in human urine and pharmaceutical samples. *Sensors International*, *1*, 100002. https://doi.org/10.1016/j.sintl.2020.100002

[154] Webb, J., & Holgate, J. H. (2003). MICROSCOPY | Scanning Electron Microscopy. In *Encyclopedia of Food Sciences and Nutrition* (pp. 3922–3928). Elsevier. https://doi.org/10.1016/B0-12-227055-X/00779-3

[155] Zhou, W., Apkarian, R., Wang, L., Joy, D. 1990. Fundamentals of Scanning Electron Microscopy. Springer. 1 ed, 2, 40-45.

[156] M.T. Postek, K.S. Howard, A.H. Johnson and K.L. McMichael, Scanning Electron Microscopy: A Student's Handbook Williston, VT., 1980)

[157] Phogat, P., Sharma, S., Jha, R., & Singh, S. (2024). *Microstructural Influence on Electrochemical Devices* (pp. 257–306). https://doi.org/10.1007/978-981-96-0527-9_7

[158] Greco, G., Tatchev, D., Hoell, A., Krumrey, M., Raoux, S., Hahn, R., & Elia, G. A. (2018). Influence of the electrode nano/microstructure on the electrochemical properties of graphite in aluminum batteries. *Journal of Materials Chemistry A*, *6*(45), 22673–22680. https://doi.org/10.1039/C8TA08319C

[159] Zhang, S., & Byrne, G. (2021). Characterization of transport mechanisms for controlled release polymer membranes using focused ion beam scanning electron

microscopy image-based modelling. *Journal of Drug Delivery Science and Technology*, *61*, 102136. https://doi.org/10.1016/j.jddst.2020.102136

[160] Faber, T., McConville, J. T., & Lamprecht, A. (2024). Focused ion beam-scanning electron microscopy provides novel insights of drug delivery phenomena. *Journal of Controlled Release*, *366*, 312–327. https://doi.org/10.1016/j.jconrel.2023.12.048

[161] Pessu, F. O., Saleem, E., Espejo, C., & Neville, A. (2022). Understanding the local pitting corrosion characteristics of carbon steel in CO2 corrosion environment using artificially machined pits. *Results in Engineering*, *16*, 100700. https://doi.org/10.1016/j.rineng.2022.100700

[162] Alam, Md. A., Jahan, A., Suzuki, E., & Yashiro, H. (2024). Surface morphology and corrosion behavior of pure aluminum and its alloys in aqueous sulfuric acid medium. *Engineering Reports*, *6*(4). https://doi.org/10.1002/eng2.12750

[163] Abdelaziz, S., Benamira, M., Messaadia, L., Boughoues, Y., Lahmar, H., & Boudjerda, A. (2021). Green corrosion inhibition of mild steel in HCl medium using leaves extract of Arbutus unedo L. plant: An experimental and computational approach. *Colloids and Surfaces A: Physicochemical and Engineering Aspects*, *619*, 126496. https://doi.org/10.1016/j.colsurfa.2021.126496

[164] Qin, R., Zhang, Y., Xu, H., & Nie, P. (2024). Gold Nanoparticle-Modified Electrodes for Electrochemical Sensing of Ammonia Nitrogen in Water. *ACS Applied Nano Materials*, *7*(1), 577–593. https://doi.org/10.1021/acsanm.3c04757

[165] Wong, A., Razzino, C. A., Silva, T. A., & Fatibello-Filho, O. (2016). Square-wave voltammetric determination of clindamycin using a glassy carbon electrode modified with graphene oxide and gold nanoparticles within a crosslinked chitosan film. *Sensors and Actuators B: Chemical*, *231*, 183–193. https://doi.org/10.1016/j.snb.2016.03.014

[166] Voigtländer, B. 2015. NanoScience and Technology: Atomic Force Microscopy. Springer. 2 ed., 50-60, 15, doi: https://doi.org/10.1007/978-3-030-13654-3

[167] Almalla, A., Ozcan, O., & Witt, J. (2022). In Situ Atomic Force Microscopy Analysis of the Corrosion Processes at the Buried Interface of an Epoxy-like Model Organic Film and AA2024-T3 Aluminum Alloy. *Advanced Engineering Materials*, *24*(6). https://doi.org/10.1002/adem.202101342

[168] Perry, J. M., Neville, A., & Hodgkiess, T. (2002). A Comparison of the Corrosion Behavior of WC-Co-Cr and WC-Co HVOF Thermally Sprayed Coatings by In Situ Atomic Force Microscopy (AFM). *Journal of Thermal Spray Technology*, *11*(4), 536–541. https://doi.org/10.1361/105996302770348673

[169] Man, Y. 2015. Instrumental Methods of Analysis and Laboratory. Springer, 1 ed., 14

[170] Stuart, B. 2004. Analytical Techniques in the Sciences: Infrared Spectroscopy: Fundamentals and Applications. Willey. 1 ed, 14, 20-30, ISBN0-470-85427-8

[171] Ardrey, E., 2004. Liquid chromatography mass spectrometry: An introduction. Willey. 1 ed., 45, 78-90, ISBN 0-471-49799-1

[172] Busch, K. L., Glish, G. L., McLuckey, S. A. 1988. Mass Spectrometry/Mass Spec trometry: Techniques and Applications of Tandem Mass Spectrometry, VCH., New York, 2 ed.

[173] Li. Antropov, Theoretical Electrochemistry, English Ed. Mir publishers, Moscow.

[174] Scholz, F., 2015. Voltammetric techniques of analysis: the essentials. ChemText., 1:17, 1 ed., doi: 10.1007/s40828-015-0016-y

[175] Mirceski, V., Komorsky-Lovric, A., Lovric, M., 2007. Square-wave voltammetry. In: Scholz F (ed) Monographs in electrochemistry. Springer, Berlin

[176] Kissinger, P., Heineman, W., 1983. Cyclic Voltammetry. J. Chem. Ed., 60, 9, 2 ed.

[177] Mirceski, V., Skrzypek, S., Stojanov, L., 2018. Square-wave voltammetry. ChemTexts., 4:17, doi: https://doi.org/10.1007/s40828-018-0073-0

[178] Molina, A., Gonzalez, J., Scholz, F. 2016. Pulse voltammetry in physical electrochemistry and electroanalysis: theory and applications. Springer., 1 ed, 270-25, New York

[179] Alexandros, Ch., Mamas I. 2023. Electrochemical Impedance Spectroscopy-A Tutorial. ACS Meas. Sci. Au., 3, 162−193, doi: https://doi.org/10.1021/acsmeasuresciau.2c00070

[180] Cheng, Y., Kunga, Ch., Choua, L., Vittala, R., Ho, K. 2014. Poly(3,4-ethylenedioxythiophene) (PEDOT) hollow microflowers and their application for nitrite sensing. Sensors and Actuators B. 192, 762– 768, doi: http://dx.doi.org/10.1016/j.snb.2013.10.126

[181] Trivedi, MK., Patil, S., Shettigar, H., Bairwa, K., Jana, S. 2015. Effect of Biofield Treatment on Spectral Properties of Paracetamol and Piroxicam, Chem. Sci. J., 6:3, doi: http://dx.doi.org/10.4172/2150-3494.100098

[182] Bashpa, P., Bijudas, K., Tom, A., Archana, P., Murshida, K., Banu, N., Amritha, K., Vimisha, R. 2015. Polymorphism of paracetamol: a comparative study on commercial paracetamol samples, Int. J. Chem. Stud., 1 (2015) 25–29

[183] Trivedi, M., Patil, S., Shettigar, H., Bairwa, K., Jana, S. 2015. Effect of biofield treatment on spectral properties of paracetamol and piroxicam, Chem. Sci. J., 6, 98–104, doi: https://doi.org/10.4172/2150-3494.100098

[184] Patra, S., Barai, K., Munichandraiah, N. 2008. Scanning electron microscopy studies of PEDOT prepared by various electrochemical routes, Synthetic Metals., 158, 430–435, doi: 10.1016/j.synthmet.2008.03.002

[185] Boz, B., Fritz, M., Forner-Cuenca, A. 2023. Electropolymerized Poly(3,4-ethylenedioxythiophene) Coatings on Porous Carbon Electrodes for Electrochemical Separation of Metals, Adv. Mater. Interfaces., 10, 2202497, doi: https://doi.org/10.1002/admi.202202497

[186] Krukiewicz, K., Zak, J. 2014. Conjugated polymers as robust carriers for controlled delivery of anti-inflammatory drugs, J. Mater. Sci., 49, 5738–5745, doi: 10.1007/s10853-014-8292-2

[187] Krukiewicz, K., Zawisza, P., Herman, A., Turczyn, R., Boncel, S., Zak, J. 2016. An electrically controlled drug delivery system based on conducting poly(3,4-ethylenedioxypyrrole) matrix, Bioelectrochemistry., 108, 13–20, doi: https://doi.org/10.1016/j.bioelechem.2015.11.002

[188] Tanji, H., Lima, F., Santos, S., Maia, G. 2012. Persistent Direct Electron Transfer between O_2 and Glucose Oxidase-Embedded in Polymyxin Supported on a Glassy Carbon Electrode, J. Phys. Chem. C., 116, 18857−18864, doi: dx.doi.org/10.1021/jp305633v

[189] Calborean, A., Murariu, T., & Morari, C. (2019). Determination of current homogeneity on the electrodes of lead-acid batteries through electrochemical impedance spectroscopy. *Electrochimica Acta*, *320*, 134636. https://doi.org/10.1016/j.electacta.2019.134636

[190] Rathore, P., & Schiffman, J. D. (2023). Effect of pH Value on the Electrical Properties of PEDOT:PSS-Based Fiber Mats. *ACS Engineering Au*, *3*(6), 527–536. https://doi.org/10.1021/acsengineeringau.3c00044

[191] Presa, M. J. R., Bandey, H. L., Tucceri, R. I., Florit, M. I., Posadas, D., & Hillman, A. R. (1999). Film thickness and electrolyte concentration effects on the EIS response of Poly-(o-toluidine) in the conducting state. *Electrochimica Acta*, *44*(12), 2073–2085. https://doi.org/10.1016/S0013-4686(98)00315-6

Inzelt, G. 2012. Conductive Polymers: A new era in electrochemistry, 2 nd ed., 2, 25, doi: 10.1007/978-3-642-27621-7

[192] Harlan J. Byker, J. 2001. Electrochromics and polymers, Electrochimica Acta., 46, 13–14, 2015-2022, doi: https://doi.org/10.1016/S0013-4686(01)00418-2

[193] Aubert, P., Argun, A., Cirpan, A., Tanner, D., Reynolds, R. 2004. Microporous Patterned Electrodes for Color-Matched Electrochromic Polymer Displays, Chem. Mater., 16, 2386-2393, doi: 10.1021/cm049951s

[194] Farkas, N., Marincaș, L., Barabas, R., Bizo, L., Ilea, L., Turdean, GL., Tosa, M., Cadar, O., Barbu-Tudoran, L. 2022. Preparation and characterization of doxycycline-loaded electrospun PLA/HAP nanofibers as a drug delivery system, Materials, 15, 1–16, doi: https://doi.org/10.3390/ma15062105

[195] Hidalgo, J., Cotolan, N., Barbu-Tudoran, L., Turdean, G. 2023. A paracetamol - poly(3,4-ethylenedioxythiophene) composite film for drug release studies. Materials Today Communications., 34, 105084, doi: https://doi.org/10.1016/j.mtcomm.2022.105084

[196] Peppas, N., Sahlin, J. 1989. A simple equation for the description of solute release. III. Coupling of diffusion and relaxation, Int. J. Pharm., 57, 169–172, doi: https:// doi.org/10.1016/0378-5173(89)90306-2

[197] Varma, M., Kaushal, M., Garg, S. 2005. Influence of micro-environmental pH on the gel layer behavior and release of a basic drug from various hydrophilic matrices, J. Control. Release., 103, 499–510, doi: https://doi.org/10.1016/j. jconrel.2004.12.015

[198] Davis JR (ed) (2004) Tensile testing, 2nd edition. Published by ASM International, pp 1–12

[199] Hidalgo, J., Cotolan, N., Lupan, A., Brânzanic, A., Turdean, GL. 2024. A poly(methyl methacrylate)–ibuprofen composite film as anticorrosive coating of Ti–6Al–4 V surface, Journal. Solid. State. Electrochemistry., 28, 479–494, doi: https://doi.org/10.1007/s10008-023-05681-w

[200] Singh, AK., Quraishi, MA. 2010. Effect of cefazolin on the corrosion of mild steel in HCl solution. Corros. Sci., 52, 152–160, doi: https://doi.org/10.1016/j.corsci.2009.08.050

[201] Khan, S., Khan, B., Khan, L., Kalsoom. B., Asiri, M. 2018. Fourier Transform Infrared Spectroscopy: Fundamentals and Application in Functional Groups and Nanomaterials Characterization, Springer International Publishing AG., 15, 2, doi: https://doi.org/10.1007/978-3-319-92955-2_9

[202] Pavithra, MK., Venkatesha, TV., Vathsala, K., Nayana, KO. 2010. Synergistic effect of halide ions on improving corrosion inhibition behavior of benzisothiozole–3–

piperizine hydrochloride on mild steel in 0.5 M H_2SO_4 medium, Corros. Sci., 52, 3811–3819, doi: https://doi.org/10.1016/j.corsci.2010.07.034

[203] Tasić, Z., B. Petrović., Mihajlović, A., Simonović, M., Radovanović, M., Antonijević, M. 2019. Ibuprofen as a corrosion inhibitor for copper in synthetic acid rain solution, Scientific Reports., 9, 14710, doi: https://doi.org/10.1038/s41598-019-51299-2

[204] Vermaa, M., Quraishib, I.B., Obotb, Eno E., Ebenso, E. 2019. Effect of substituent dependent molecular structure on anti-corrosive behavior of one-pot multicomponent synthesized pyrimido [2,1-B] benzothiazoles: Computer modelling supported experimental studies, Journal of Molecular Liquids., 287, 110972, doi: https://doi.org/10.1016/j.molliq.2019.110972

[205] Council of Europe. Determination of tannins in herbal drugs. In European Pharmacopoeia. 2006, 6th ed., European Directorate for the Quality of Medicines, Strasbourg, France

[206] Dar, A. 2011. A review: plant extracts and oils as corrosion inhibitors in aggressive media, Industrial Lubrication and Tribology., 63, 4, 227– 233, doi: 10.1108/00368791111140431

[207] Tondi, G., Petutschnigg, A. 2015. Middle infrared (ATR FT-MIR) characterization of industrial tannin extracts. Ind. Crops. Prod., 65, 422–428, doi: https://doi.org/10.1016/j.indcrop.2014.11.005

[208] Grasel, S., Flôres Ferrão, M., Wolf, C. 2015. Development of methodology for identification the nature of the polyphenolic extracts by FTIR associated with multivariate analysis, Spectrochimica Acta Part A: Molecular and Biomolecular Spectroscopy., 153, 94–101, doi: https://doi.org/10.1016/j.saa.2015.08.020

[209] Schwanninger, M., Rodrigues, J.C., Pereira, H., Hinterstoisser, B., 2004. Effects of short-time vibratory ball milling on the shape of FT-IR spectra of wood and cellulose, Vibrat. Spectrosc., 36 (1), 23–40, doi: https://doi.org/10.1016/j.vibspec.2004.02.003

[210] Nabin, K., Shova, N., Dipak, K., Anju, D., Sanjay, S., Gayatri, M., Yogesh, C., Amar, P. 2021. Berberine isolated from Mahonia nepalensis as an eco-friendly and thermally stable corrosion inhibitor for mild steel in acid medium. Arab. J. Chem., 14, 12, doi: https://doi.org/10.1016/j.arabjc.2021.103423

[211] Davilal, P., Srijana, S., Hari, B., Dilip, S., Deval, P., Arjun, P.T., Amar, Y. 2022. Comparative Study of Corrosion Inhibition Efficacy of Alkaloid Extract of Artemesia vulgaris and Solanum tuberosum in Mild Steel Samples in 1 M Sulphuric Acid, Electrochem., 3, 416–433, doi: https://doi.org/10.3390/electrochem3030029

[212] Bai, Z., Xiao, K., Dong, P., Dong, C., Weic, D., Lia, X. 2018. Effect of iron ion diffusion on the corrosion behavior of carbon steels in soil environment, RSC Adv., 8, 40544, doi: 10.1039/c8ra08032a

[213] Ghosal, P. S., & Gupta, A. K. (2017). Determination of thermodynamic parameters from Langmuir isotherm constant-revisited. *Journal of Molecular Liquids*, *225*, 137–146. https://doi.org/10.1016/j.molliq.2016.11.058

[214] Shahzad, K., Sliem, M. H., Shakoor, R. A., Radwan, A. B., Kahraman, R., Umer, M. A., Manzoor, U., & Abdullah, A. M. (2020). Electrochemical and thermodynamic study on the corrosion performance of API X120 steel in 3.5% NaCl solution. *Scientific Reports*, *10*(1), 4314. https://doi.org/10.1038/s41598-020-61139-3

[215] Ghosal, P. S., & Gupta, A. K. (2017). Determination of thermodynamic parameters from Langmuir isotherm constant-revisited. *Journal of Molecular Liquids*, *225*, 137–146. https://doi.org/10.1016/j.molliq.2016.11.058

[216] Kokalj, A. (2023). On the use of the Langmuir and other adsorption isotherms in corrosion inhibition. *Corrosion Science*, *217*, 111112. https://doi.org/10.1016/j.corsci.2023.111112

[217] Ayawei, N., Ebelegi, A. N., & Wankasi, D. (2017). Modelling and Interpretation of Adsorption Isotherms. *Journal of Chemistry*, *2017*, 1–11. https://doi.org/10.1155/2017/3039817

[218] Ren, H., Liu, Y., Gong, Z., Tan; B., Deng, H., Xiong, J., Shao, P., Dai, Q., Cao, J., Marzouki, R. 2024. Pumpkin Leaf Extract Crop Waste as a New Degradable and Environmentally Friendly Corrosion Inhibitor, Langmuir., 40 (11), 5738–5752, doi: https://doi.org/10.1021/acs.langmuir.3c03399

[219] Dar, A. 2011. A review: plant extracts and oils as corrosion inhibitors in aggressive media, Industrial Lubrication and Tribology., 63, 4, 227– 233, doi: 10.1108/00368791111140431

[220] Merriman, S., Chandra, D., Borowczak, M., Dhinojwala, A., & Benko, D. (2022). Simultaneous determination of additive concentration in rubber using ATR-FTIR spectroscopy. *Spectrochimica Acta Part A: Molecular and Biomolecular Spectroscopy*, *281*, 121614. https://doi.org/10.1016/j.saa.2022.121614

[221] Schwanninger, M., Rodrigues, J.C., Pereira, H., Hinterstoisser, B., 2004. Effects of short-time vibratory ball milling on the shape of FT-IR spectra of wood and cellulose, Vibrat. Spectrosc., 36 (1), 23–40, doi: https://doi.org/10.1016/j.vibspec.2004.02.003

[222] Nabin, K., Shova, N., Dipak, K., Anju, D., Sanjay, S., Gayatri, M., Yogesh, C., Amar, P. 2021. Berberine isolated from Mahonia nepalensis as an eco-friendly and thermally stable corrosion inhibitor for mild steel in acid medium. Arab. J. Chem., 14, 12, doi: https://doi.org/10.1016/j.arabjc.2021.103423

[223] Davilal, P., Srijana, S., Hari, B., Dilip, S., Deval, P., Arjun, P.T., Amar, Y. 2022. Comparative Study of Corrosion Inhibition Efficacy of Alkaloid Extract of Artemesia vulgaris and Solanum tuberosum in Mild Steel Samples in 1 M Sulphuric Acid, Electrochem., 3, 416–433, doi: https://doi.org/10.3390/electrochem3030029

[224] Bai, Z., Xiao, K., Dong, P., Dong, C., Weic, D., Lia, X. 2018. Effect of iron ion diffusion on the corrosion behavior of carbon steels in soil environment, RSC Adv., 8, 40544, doi: 10.1039/c8ra08032a

[225] Rahiman, AF., Sethumanickam, S. 2017. Corrosion inhibition, adsorption and thermodynamic properties of poly(vinyl alcohol-cysteine) in molar HCl, Arabian J. Chem., 2017, 10, 3358-3366, doi: https://doi.org/10.1016/j.arabjc.2014.01.016

[226] Norsworthy, R. 2014. Understanding corrosion in underground pipelines: Basic principles. In *Underground Pipeline Corrosion*, 1st ed.; Woodhead Publishing Series in Metals and Surface Engineering; Orazem, M.E., Ed.; Woodhead Publishing: Cambridge, UK, 2014; Chapter 1; pp. 3–34, doi: https://doi.org/10.1533/9780857099266.1.3

[227] Tan, J., Guo, D., Wu, S., Wang, S., Yu, R., Zhang, F., Kaya, S. 2020. Electrochemical and Computational Studies on the Corrosion Inhibition of Mild Steel by 1-Hexadecyl-3-methylimidazolium Bromide in HCl Medium, Int. J. Electrochem. Sci., 15, doi: https://doi.org/10.20964/2020.03.36

[228] Ren, H., Liu, Y., Gong, Z., Tan; B., Deng, H., Xiong, J., Shao, P., Dai, Q., Cao, J., Marzouki, R. 2024. Pumpkin Leaf Extract Crop Waste as a New Degradable and Environmentally Friendly Corrosion Inhibitor, Langmuir., 40 (11), 5738–5752, doi: https://doi.org/10.1021/acs.langmuir.3c03399

[229] Bochuan, T., Yan, L., Zhili, G., Xiru, Z., Jie, C., Lei, G., Junle, X., Jie, L., Riadh, M., Wenpo, Li. 2024. Pyracantha fortuneana alcohol extracts as biodegradable corrosion inhibitors for copper in H_2SO_4 media, Journal of Molecular Liquids., 397,124117, doi: https://doi.org/10.1016/j.molliq.2024.124117

[230] Noor, E.A., Al-Moubaraki, A.H. 2008. Corrosion behavior of mild steel in hydrochloric acid solutions. Int. J. Electrochem. Sci., 3, 806–818, doi:

[231] Tan, B., Xiang, B., Zhang, S., Qiang, Y., Xu, L., Chen, S., He, J. 2021. Papaya leaves extract as a novel eco-friendly corrosion inhibitor for Cu in H_2SO_4 medium,

Journal of Colloid and Interface Sciences., 582, 918-931, doi: https://doi.org/10.1016/j.jcis.2020.08.093.7

[232] Jing, Z., Wang, Y., Gong, H., Huang, Y., Ma, H., Xie, H., Li, S., Zhang, F., Gao, A. 2018. Photo and thermally stable branched corrosion inhibitors containing two benzotriazole groups for copper in 3.5 wt% sodium chloride solution, Corros. Sci., 138, 353–371, doi: https://doi.org/10.1016/j.corsci.2018.04.027

[233] Sadeghi Erami, M., Amirnasr, S., Meghdadi, M., Talebian, H., Farrokhpour, K., Raeissi, M. 2019. Carboxamide derivatives as new corrosion inhibitors for mild steel protection in hydrochloric acid solution, Corros. Sci. 151, 190–197, doi: https://doi.org/10.1016/j.corsci.2019.02.019

[234] Quy Huong, D., Duong, T., & Nam, P. C. (2019). Effect of the Structure and Temperature on Corrosion Inhibition of Thiourea Derivatives in 1.0 M HCl Solution. *ACS Omega*, *4*(11), 14478–14489. https://doi.org/10.1021/acsomega.9b01599

[235] Titilayo, J., Ajayi, A. 2025. Corrosion Inhibition and Adsorption Characteristics for Mild steel by Extract of Kyllinga Erecta Plant in Acidic Medium, IJPSAT., 49, 414-424, ISSN: 2509-0119

[236] Fort, C.I., Pap, Z., Indrea, E. 2014. Pt/N–TiO_2 Aerogel Composites Used for Hydrogen Production Via Photocatalysis Process, Catal Lett., **144**, 1955–1961, doi: https://doi.org/10.1007/s10562-014-1353-y

[237] Pifferi, G., Cappelletti, C., Di Bari, D., Meroni, F., Spadavecchia, L., Falciola, L. 2014. Multi-walled carbon nanotubes (MWCNTs) modified electrodes: Effect of purification and functionalization on the electroanalytical performances, Electrochim. Acta, 146, 403-410, doi: https://doi.org/10.1016/j.electacta.2014.09.099

[238] Jankovics, H., Szekér, P., Tóth, E., Balázs, K., Lábadi, Z., Saftics, A., Kalas, B., Fried, M., Petrik, P., Vonderviszt, F. 2021. Flagellin-based electrochemical sensing layer for arsenic detection in water, Sci. Rep., 11, 3497, doi: https://doi.org/10.1038/s41598-021-83053-y

[239] Hidalgo, J., Fort, I.C., Galambos, I., Jankovics, H., Hidalgo, L., Turdean, G.L. 2024. TiO_2 aerogel − A sensing electrode matrix for the sensitive detection of diclofenac sodium, Microchemical Journal., 207, 111855, doi: https://doi.org/10.1016/j.microc.2024.111855

[240] Masson, O., Guinebretière, R. 1996. Size and shape characterization of TiO_2 aerogel nanocrystals, Nanostructured Materials., 7, 7, 725-731, doi: 10.1016/S0965-9773(96)00049-9

[241] Yanqiang, B., Li, Z., Dewei, M., Fei, Z. 2021. Low-temperature synthesis of micro–mesoporous TiO_2–SiO_2 composite film containing Fe–N Co-doped anatase nanocrystals for photocatalytic NO removal, Catal. Lett., 151, 2396–2407, https://doi.org/10.1007/s10562-020-03466-8

[242] Naika, B., Hemapa, M., Chandrashekhara, A., Iyera, V., Sivankutty, P., Narendra, G. 2013. Preparation of TiO_2, Ag-doped TiO_2 nanoparticle and TiO_2–SBA-15 nanocomposites using simple aqueous solution-based chemical method and study of their photocatalytical activity, Journal of Experimental Nanoscience, 8, 4, 462–479, doi: http://dx.doi.org/10.1080/17458080.2011.597435

[243] N. Dong, B. Gao, S. Chen, A. 2021. Selective electrochemical sensor based on TiO_2/ reduced graphene for efficient determination of methanol, Int. J. Electrochem. Sci., 16, 210351, doi: https://doi.org/10.20964/2021.03.28

[244] Davis, R., Mauer, J. L. 2010. Fourier transform infrared (FT-IR) spectroscopy: A rapid tool for detection and analysis of foodborne pathogenic bacteria, in A. Mendez-Vilas (ed), Current Research, Technology and Education Topics in Applied Microbiology and Microbial Biotechnology, Formatex Research Center, vol. 2, pp. 1582-1594, ISBN-8461461959

[245] Naumann, D. 2006. Infrared Spectroscopy in Microbiology. Encyclopedia of Analytical Chemistry., 2, 15, 28-41, doi:10.1002/9780470027318.a0

[246] D. Li-Vien, N.B. Colthup, W.G. Fateley, J.G. Grasselli, The Handbook of Infrared and Raman Characteristic Frequencies of Organic Molecules, Academic Press, Boston, 1991

[247] Chai, A., Wang, C., Chen, Y. 2024. Synthesis and characterization of modified centrifuged-electrospun carbon nanofibers for high-performance supercapacitor electrodes, Journal of the Taiwan Institute of Chemical Engineers., 156, 2024, 105329, doi: https://doi.org/10.1016/j.jtice.2023.105329

[248] Baig, N., Sajid, M., Tawfik, A. 2019. Recent trends in nanomaterial-modified electrodes for electroanalytical applications, TrAC Trends in Analytical Chemistry., 111, 47-61, https://doi.org/10.1016/j.trac.2018.11.044

[249] Bai, J., Zhou, B. 2014. Titanium dioxide nanomaterials for sensor applications, Chem. Rev., 114, 10131–10176, doi: https://doi.org/10.1021/cr400625j

[250] Baghayeri, M., Amiri, A., Fayazi, M., Nodehi, M., Esmaeelnia, A. 2021. Electrochemical detection of bisphenol a on a MWCNTs/CuFe2O4 nanocomposite modified glassy carbon electrode, Materials Chemistry and Physics., 261, 124247, doi: https://doi.org/10.1016/j.matchemphys.2021.124247

[251] Goyal, R. N., Chatterjee, S., Agrawal, B. 2010. Electrochemical investigations of diclofenac at edge plane pyrolytic graphite electrode and its determination in human urine, Sensors Actuators B Chem., 145, 743–748, doi: 10.1016/j.snb.2010.01.038

[252] Bai, J., Zhou, B. 2014. Titanium dioxide nanomaterials for sensor applications, Chem. Rev., 114, 10131–10176, doi: https://doi.org/10.1021/cr400625j

[253] Eteya, M., Rounaghi, M., Behjat Deiminiat, B. 2019. Fabrication of a new electrochemical sensor based on Au-Pt bimetallic nanoparticles decorated multi-walled carbon nanotubes for determination of diclofenac, Microchemical Journal, 144, 254-260, doi: https://doi.org/10.1016/j.microc.2018.09.009

[254] Vogt, S., Su, Q., Gutierrez-Sanchez, C., Noll, G. 2016. A critical view on electrochemical impedance spectroscopy (EIS) using the ferri/ferrocyanide redox couple at gold electrodes, Anal. Chem., 88, 4383−4390, doi: 10.1021/acs.analchem.5b04814

[255] Van Haeverbeke, M., Stock, M., De Baets, M. 2022. Equivalent Electrical Circuits and Their Use Across, IEEEAccess, Electrochemical Impedance SpectroscopyApplication Domains, 10, 25, 15-22, doi: 10.1109/ACCESS.2022.3174067

[256] Rusu, M., Fort, C. I., Cotet, L.C., Vulpoi, M., Todea, M., M., Turdean, G.L., Danciu, I., Popescu, I., Baia, C. 2018. Insights into the morphological and structural particularities of highly sensitive porous bismuth-carbon nanocomposites based electrochemical sensors, Sens. Actuators B Chem., 268, 398-410, doi: 10.1016/j.snb.2018.04.103

[257] Salvo-Comino, C., Rassas, I., Minot, S., Bessueille, F., Arab, M., Chevallier, V., Rodriguez-Mendez, M., Errachid, A., Jaffrezic-Renault, N. 2019. Voltammetric sensor based on molecularly imprinted chitosan-carbon nanotubes decorated with gold nanoparticles nanocomposite deposited on boron-doped diamond electrodes for catechol detection, Materials., 13, 1–11, doi: https://doi.org/10.3390/ma13030688

[258] Barsoukov, E., Macdonald, J.R. 2005. Impedance Spectroscopy Theory, Experiment, and Applications Second Edition, Published by John Wiley & Sons Inc Hoboken, New Jersey, doi: 10.1002/0471716243

[259] Yang, X., Wang, F., Hu, S. 2008. Enhanced oxidation of diclofenac sodium at a nano- structured electrochemical sensing film constructed by multi-wall carbon

nanotubes–surfactant composite, Mater. Sci. Eng. C., 28, 188–194, doi: https://doi.org/10.1016/j.msec.2006.11.006

[260] Wang, Q., Chen, G., Liu, N., Wang, S., Liu, C., Meng, X., Liu, G. 2006. Protonation constants of chitosan with different molecular weight and degree of deacetylation, Carbohydrate Polymers., 65, 194–201, doi: 10.1016/j.carbpol.2006.01.001

[261] Aranaz, I., Alcántara, A. R., Civera, M. C., Arias, C., Elorza, B., Heras Caballero, A., Acosta, N. 2021. Chitosan: An Overview of Its Properties and Applications, Polymers., 13, 19, 3256, doi: https://doi.org/10.3390/polym13193256

[262] Shalauddin, M., Akhter, S., Basirun, W., Bagheri, S., Anuar, N., Johan, M. 2019. Hybrid nanocellulose/f-MWCNTs nanocomposite for the electrochemical sensing of diclofenac sodium in pharmaceutical drugs and biological fluids, Electrochim. Acta., 304, 323–333, https://doi.org/10.1016/j.electacta.2019.03.003

[263] Tenno, R., Pohjoranta, A. 2012. Control of diffusion limited electrochemical redox processes: Simulation study, Journal of Process Control., 22, 1, 228-235, doi: https://doi.org/10.1016/j.jprocont.2011.08.004

[264] Killedar, L., Ilager, D., Shetti, N.P., Aminabhavi, T.M., Reddy, K. R. 2021. Synthesis of ruthenium doped titanium dioxide nanoparticles for the electrochemical detection of diclofenac sodium, J. Mol. Liq., 340, 116891, doi: https://doi.org/10.1016/j.molliq.2021.116891

[265] Harvey, D. 2000. Modern Analytical Chemistry, 1st ed.; McGraw-Hill: Boston, MA, USA, p. 95.

[266] Karuppiah, C., Cheemalapati, S.M., Chen, S.M., Palanisamy, S. 2014. Carboxyl-functionalized graphene oxide-modified electrode for the electrochemical determination of nonsteroidal anti-inflammatory drug diclofenac, Ionics., 21, 231–238, doi:

[267] Yu, H., Jiao, J., Li, Q., Li, Y. 2021. Electrochemical Determination of Diclofenac Sodium in Pharmaceutical Sample Using Copper Nanoparticles/Reduced Graphene Oxide Modified Glassy Carbon Electrode, International Journal of Electrochemical Science., 16, 10, 211024, doi: https://doi.org/10.20964/2021.10.19

[268] Hoa, N., Tu, N., Son, L., Son, T., Khieu, T.S., Le, T. Electrochemical determination of diclofenac by using ZIF-67/g-C3N4 modified electrode, Adsorp. Sci. Technol., 15, 45, 22, doi: 10.1155/2021/7896286

[269] Shalauddin, Md., Akhter, S., Bagheri, S., Karim, M., Kadri, N., Basirun, W. 2017. Immobilized copper ions on MWCNTS-Chitosan thin film: Enhanced amperometric

sensor for electrochemical determination of diclofenac sodium in aqueous solution, Int. J. Hydr. Ener., 42, 31, 19951-19960, doi: https://doi.org/10.1016/j.ijhydene.2017.06.163
[270] Shalauddin, Md., Akhter, S., Basirun, W., Bagheri, S., Anuar, N., Johan, M. 2019. Hybrid nanocellulose/f-MWCNTs nanocomposite for the electrochemical sensing of diclofenac sodium in pharmaceutical drugs and biological fluids, Electrochim. Acta., 304, 323-333, doi: https://doi.org/10.1016/j.electacta.2019.03.003
[271] Goodarzian, M., Khalilzade, M., Karimi, F., Gupta, V., Keyvanfard, M., Bagheri, H. 2014. Square wave voltammetric determination of diclofenac in liquid phase using a novel ionic liquid multiwall carbon nanotubes paste electrode, J. Mol. Liq., 197, 114-119, doi: https://doi.org/10.1016/j.molliq.2014.04.037
[272] Fard, G. P., Alipour, E., Sabzi, R. E. 2016. Modification of a disposable pencil graphite electrode with multiwalled carbon nanotubes: application to electrochemical determination of diclofenac sodium in some pharmaceutical and biological samples. Analytical Methods., 8, 19, 3966–3974, doi:10.1039/c6ay00441e
[273] Elbalkiny, H.T., Yehia, A.M., Riad, S.M., Elsaharty, Y.S. 2019. Potentiometric diclofenac detection in wastewater using functionalized nanoparticles, Microchem. J., 145, 90–95, doi: 10.1016/j.microc.2018.10.017
[274] Brennan, E., Futvoie, P., Cassidy, J., Schazmann, B. 2017. An ionic liquid-based sensor for diclofenac determination in water, International Journal of Environmental Analytical Chemistry., 97, 6, 588–596, doi:10.1080/03067319.2017.1333607
[275] Schirmer, C., Posseckardt, J., Schröder, M., Gläser, M., Howitz, S., Scharff, W., Mertig. M. 2019. Portable and low-cost biosensor towards on-site detection of diclofenac in wastewater, Talanta., 203, 242 247, doi: 10.1016/j.talanta.2019.05.058
[276] Sasal, A., Tyszczuk-Rotko, K., Wójciak, M., Sowa, I. 2020. First electrochemical sensor (Screen-printed carbon electrode modified with carboxyl functionalized multiwalled carbon nanotubes) for ultratrace determination of diclofenac, Materials., 13, 781, doi: https://doi.org/10.3390/ma13030781
[277] SCHEER (Scientific Committee on Health, Environmental and Emerging Risks), Final Opinion on Draft Environmental Quality Standards for Priority Substances under the Water Framework Directive - diclofenac, 2022.
[278] Honakeri, N., Malode, S., Kulkarni, P., Shetti, P. 2020. Electrochemical behavior of diclofenac sodium at coreshell nanostructure modified electrode and its analysis in human urine and pharmaceutical samples, Sens. Int., 1, 100002, doi: https://doi.org/10.1016/j.sintl.2020.100006

6. Supplementary tablets and figures

Table S1. EIS fitted parameter calculated for Ti/PEDOT-PA and Ti/PEDOT-2PA at scan rate, 5 or 10mV·s^{-1} tested in artificial saliva at pH 5. Equivalent circuit: ($R_{sol}(Q_{dl}(R_{ct}Q_{film}))$).

Parameter	Samples			
	PEDOT-PA/Ti v= 5 mV·s^{-1}	**PEDOT-2PA/Ti v= 5 mV·s^{-1}**	**PEDOT-PA/Ti v= 10 mV·s^{-1}**	**PEDOT-2PA/Ti v= 10 mV·s^{-1}**
	t=0 min			
R_{sol} (Ω·cm^{-2})	28.44 ± 1.12	27.93 ± 1.13	28.58 ± 1.35	15.65 ± 1.35
Q_{dl} ($S \cdot s^n \cdot cm^{-2}$)	0.01 ± 1×10^{-3}	0.01 ± 1.13	1.31×10^{-4} ± 0.11	3.31×10^{-3} ± 1.31
n	0.84	0.89	0.94	0.87
R_{ct} (Ω·cm^{-2})	59.17 ± 2.30	32.19 ± 0.47	35.28 ± 2.66	136.7 ± 2.36
Q_{film} ($S \cdot s^n \cdot cm^{-2}$)	1.11×10^{-4} ± 0.12	1.50×10^{-4} ± 0.12	8.77×10^{-4} ± 0.01	4.60×10^{-6} ± 0.81
n_1	0.88	0.75	0.90	0.92
chi^2	1.80×10^{-4}	8.12×10^{-4}	1.15×10^{-4}	6.22×10^{-4}
t= 195 min				
R_{sol} (Ω·cm^{-2})	25.74 ± 1.47	24.52 ± 1.10	25.95 ± 3.17	14.99 ± 1.78
Q_{dl} ($mS \cdot s^n \cdot cm^{-2}$)	9.31 ± 4×10^{-4}	8.35 ± 0.97	0.12 ± 0.56	3.35 ± 1.72
n	0.86	0.8946	0.95	0.88
R_{ct} (Ω·cm^{-2})	53.35 ± 3.34	30.13 ± 1.17	28.62 ± 1.92	101.8 ± 3.37
Q_{film} ($S \cdot s^n \cdot cm^{-2}$)	1.09×10^{-4} ± 0.13	0.00015 ± 2.89	8.96×10^{-5} ± 0.15	4.79×10^{-5} ± 0.12
n_1	0.87	0.84	0.92	0.95
chi^2	1.90×10^{-4}	1.10×10^{-3}	2×10^{-4}	8.6×10^{-4}
t= 360 min				
R_{sol} (Ω·cm^{-2})	23.87 ± 1.84	21.49 ± 1.49	24.03 ± 1.11	14.12 ± 2.87
Q_{dl} ($mS \cdot s^n \cdot cm^{-2}$)	9.51 ± 4×10^{-4}	8.32 ± 0.75	1.25 ± 0.22	3.33 ± 0.74
n	0.87	0.90	0.95	0.88
R_{ct} (Ω·cm^{-2})	47.87 ± 2.22	27.82 ± 1.34	20.32 ± 2.26	90.27 ± 3.01
Q_{film} ($mS \cdot s^n \cdot cm^{-2}$)	1.01 ± 0.17	0.16 ± 0.3	9.10×10^{-2} ± 0.33×10^{-2}	4.69×10^{-2} ± 1.55×10^{-2}
n_1	0.94	0.91	0.98	0.92

chi^2	2×10^{-4}	1.10×10^{-4}	2×10^{-4}	9.10×10^{-4}

value ±is the relative standard error (RSD) expressed in percent (%)

Table S2. EIS fitted parameter calculated in Ti/PEDOT-PA and Ti/PEDOT-2PA at scan rate, 5 or 10 $mV\cdot s^{-1}$ tested in artificial saliva at pH 6. Equivalent circuit: ($R_{sol}(Q_{dl}(R_{ct}Q_{film}))$).

Parameter	**Samples**			
	PEDOT-PA/Ti v= 5 $mV\cdot s^{-1}$	**PEDOT-2PA/Ti v= 5 $mV\cdot s^{-1}$**	**PEDOT-PA/Ti v= 10 $mV\cdot s^{-1}$**	**PEDOT-2PA/Ti v= 10 $mV\cdot s^{-1}$**
	t=0 min			
R_{sol} ($\Omega\cdot cm^{-2}$)	28.44 ± 1.12	27.93 ± 1.13	28.58±1.35	29.84 ±1.74
Q_{dl} ($mS\cdot s^n\cdot cm^{-2}$)	9 ± 0.10	8.20 ± 1.10	0.13 ± 0.11	6.10×10^{-4} ± 0.13
n	0.84	0.89	0.94	0.83
R_{ct} ($\Omega\cdot cm^{-2}$)	59.17 ± 2.30	32.19 ± 0.47	35.28 ± 2.6	416 ± 5.36
Q_{film} ($S\cdot s^n\cdot cm^{-2}$)	1.11×10^{-4} ± 0.12	1.50×10^{-4} ± 0.12	8.77×10^{-4} ± 0.01	4.22×10^{-5} ± 0.08
n_1	0.88	0.75	0.90	0.88
chi^2	1.80×10^{-4}	8.80×10^{-4}	1.10×10^{-4}	2.60×10^{-4}
t= 195 min				
R_{sol} ($\Omega\cdot cm^{-2}$)	25.74 ± 1.47	24.52 ± 1.10	25.95 ± 3.17	26.85 ± 1.22
Q_{dl} ($mS\cdot s^n\cdot cm^{-2}$)	9.31 ± 0.40	8.32 ± 0.91	0.12 ± 0.56	0.57 ± 0.18
N	0.86	0.8946	0.95	0.81
R_{ct} ($\Omega\cdot cm^{-2}$)	53.35 ± 3.34	30.13 ± 1.17	28.62 ± 1.92	339.20 ± 4.02
Q_{film} ($mS\cdot s^n\cdot cm^{-2}$)	0.11 ± 0.01	0.15 ± 0.03	0.08 ± 0.01	4.29×10^{-2} ± 2.10×10^{-3}
n_1	0.87	0.84	0.97	0.83
chi^2	1.90×10^{-4}	1.80×10^{-4}	1.20×10^{-4}	1.85×10^{-4}
t= 360 min				
R_{sol} ($\Omega\cdot cm^{-2}$)	23.87 ± 1.84	21.49 ± 1.49	24.03 ± 1.11	25.12 ± 2.87
Q_{dl} ($mS\cdot s^n\cdot cm^{-2}$)	9.52 ± 0.02	8.33 ± 0.0007	1.25×10^{-4} ± 0.22	5.75×10^{-4} ± 0.47

N	0.87	0.90	0.95	0.82
R_{ct} ($\Omega \cdot cm^{-2}$)	47.87 ± 2.22	27.82 ± 1.34	20.32 ± 2.26	305 ± 4.25
Q_{film} ($S \cdot s^n \cdot cm^{-2}$)	1.01×10^{-4} ± 0.17	0.00016 ± 0.0003	9.10×10^{-5} ± 0.33	4.63×10^{-5} ± 1.65
n_1	0.94	0.91	0.98	0.83
chi^2	1.90×10^{-4}	1.95×10^{-4}	2×10^{-4}	2.12×10^{-4}

Table S3. EIS fitted parameter calculated in Ti/PEDOT-PA and Ti/PEDOT-2PA at scan rate, 5 or 10mV·s^{-1} tested in artificial saliva at pH 7. Equivalent circuit: ($R_{sol}(Q_{dl}(R_{ct}Q_{film}))$).

Parameter	**Samples**			
	Ti/PEDOT-PA	**Ti/PEDOT-2PA**	**Ti/PEDOT-PA**	**Ti/PEDOT-2PA**
	v = 5 mV·s^{-1}		**v = 10 mV·s^{-1}**	
	time = 0 minute			
R_s [ohm·cm^2]	28.70 ± 0.40	27.29 ± 0.18	28.91 ± 0.18	31.77 ± 0.75
Q_{dl}[mS·s^n·cm^{-2}]	5.16×10^{-2} ± 0.02	0.15±0.02	0.20 ± 0.03	0.77 ± 0.02
n	0.86	0.73	0.71	0.95
R_{ct}	108.20± 0.38	32.30± 0.28	9.87± 0.69	94.15± 4.74
Q_{filml} [mS·s^n·cm^{-2}]	0.12 ± 0.58	8.67 ± 0.10	9.15 ± 0.01	292.15 ± 0.03
n_1	0.95	0.89	0.95	0.80
chi^2	1.16×10^{-4}	8.79×10^{-4}	3.94×10^{-4}	1.71×10^{-3}
	time = 100 minutes			
R_s [ohm·cm^2]	26.46 ± 0.36	27.03 ± 0.84	28.70 ± 0.02	30.03 ± 0.84
Q_{dl}[mS·s^n·cm^{-2}]	$4.67 \cdot 10^{-2}$ ± 0.25	0.11 ± 0.18	0.19 ± 0.32	0.20 ± 0.18
n	0.87	0.77	0.72	0.77
Rct	104.41 ± 0.35	14.89 ± 2.59	8.58×10^{-3} ± 0.09	14.89 ± 2.59
Q_{filml} [mS·s^n·cm^{-2}]	15.12 ± 0.56	3.81 ± 0.58	9.85± 0.68	3.81± 0.58
n_1	0.96	0.92	0.95	0.92

chi^2	9.63×10^{-5}	1.30×10^{-4}	3.84×10^{-4}	1.30×10^{-4}
	time = 360 minutes			
R_s [ohm·cm^2]	24.09 ± 1.68	26.76 ± 1.68	24.33 ± 0.02	29.03 ± 0.84
Q_{dl}[mS·s^n·cm^{-2}]	15.11 ± 0.21	0.17 ± 0.21	0.18 ± 0.32	0.11 ± 0.18
n	0.94	0.77	0.72	0.77
R_{ct}	96.03 ± 3.22	12.93 ± 3.22	8.72 ± 0.70	14.89 ± 2.59
Q_{filml} [mS·s^n·cm^{-2}]	3.58×10^{-2} ± 0.72	3.66 ± 0.72	8.27± 0.10	3.81± 0.58
n_1	0.93	0.93	0.95	0.92
chi^2	9.25×10^{-5}	1.78×10^{-4}	4.32×10^{-4}	1.30×10^{-4}

value ± is the relative standard error (RSD) expressed in percent (%)

Table S4. Parameters of the zero-order release kinetic model of PA from the membrane film PEDOT-PA/Ti and PEDOT-2PA/Ti prepared by electropolymerization at 5mV·s^{-1} and 10mV·s^{-1}. Data recorded after 6h at saliva solution adjusted at different pH obtained by ZsimpWin 2.30 software

Variable	**R vs t (t>200 min)**			**R vs t (t<200 min)**		
	Intercept	**Slope**	**R^2**	**Intercept**	**Slope**	**R^2**
PA, v=5 mV·s^{-1}, pH= 5	27.91 ± 0.11	-0.02 ± 0.01	0.9551	27.74 ± 0.10	-0.02 ± 3.93×10^{-4}	0.9931
PA, v=10 mV·s^{-1}, pH= 5	27.77 ± 0.08	-0.02± 7.97×10^{-4}	0.9709	27.84 ± 0.22	-0.02 ± 7.78×10^{-4}	0.9795
PA, v=5 mV·s^{-1}, pH= 6	28.76 ± 0.04	-0.01 ± 4.14×10^{-4}	0.9887	28.54 ± 0.16	-0.01 ± 5.77×10^{-4}	0.9764
PA, v=10 mV·s^{-1}, pH= 6	28.44 ± 0.04	-0.02 ± 4.50×10^{-4}	0.9924	27.53 ± 0.04	-0.01 ± 1.62×10^{-4}	0.9973
PA, v=5 mV·s^{-1}, pH= 7	29.50 ± 0.03	-0.01± 2.75×10^{-4}	0.9953	29.29 ± 0.04	-0.01 ± 1.62×10^{-4}	0.9987
PA, v=10 mV·s^{-1}, pH= 7	27.01 ± 0.05	-0.02 ± 3.70×10^{-4}	0.9930	26.85 ± 0.14	-0.02 ± 4.74×10^{-4}	0.9908
2PA, v=5 mV·s^{-1}, pH= 5	27.91 ± 0.11	-0.02 ± 1.22×10^{-2}	0.9551	27.74 ± 0.10	-0.02 ± 3.93×10^{-4}	0.9931

2PA, v=10 mV·s^{-1}, pH= 5	13.38 ± 0.01	-0.01 ± 9.43×10^{-5}	0.9954	13.01 ± 0.05	-0.01 ± 1.73×10^{-4}	0.9840
2PA, v=5 mV·s^{-1}, pH= 6	22.31 ± 0.09	-0.009 ± 7.87×10^{-4}	0.9088	25.61 ± 0.48	-3×10^{-3} ± 10.2×10^{-4}	0.9677
2PA mV·s^{-1}, v=10, pH=6	29.89 ± 0.07	-0.01 ± 7.07×10^{-4}	0.9691	29.31 ± 0.17	-0.01 ± 6.68×10^{-4}	0.9730
2PA mV·s^{-1}, v=5 mV·s^{-1}, pH=7	28.3 0± 0.15	-0.02 ± 1.30×10^{-3}	0.9505	27.40 ± 0.18	-0.02 ± 6.18×10^{-4}	0.9875
2PA, v=10 mV·s^{-1}, pH=7	30.11 ± 0.03	-0.01 ± 2.51×10^{-4}	0.9926	29.85 ± 0.19	-0.01 ± 6.73×10^{-4}	0.9533

Table S5. Parameters of the Higuchi release kinetic model of PA from the membrane film PEDOT-PA/Ti and PEDOT-2PA/Ti prepared by electropolymerization at 5mV·s^{-1} and 10mV·s^{-1}. Data recorded after 6h at saliva solution adjusted at different pH

Variable	**R vs $\sqrt{t}$; (t>200 min)**			**R vs $\sqrt{t}$; (t<200 min)**		
	Intercept	**Slope**	**R^2**	**Intercept**	**Slope**	**R^2**
PA, v=5 mV·s^{-1}, pH= 5	28.65 ± 0.12	-0.24 ± 0.01	0.9721	31.84 ± 0.16	-0.54 ± 0.01	0.9946
PA, v=10 mV·s^{-1}, pH= 5	28.86 ± 0.15	-0.27 ± 0.02	0.9648	32.69 ± 0.37	-0.59 ± 0.02	0.9850
PA, v=5 mV·s^{-1}, pH= 6	29.79 ± 0.16	-0.25 ± 0.02	0.9519	31.85 ± 0.40	-0.41 ± 0.02	0.9634
PA, v=10 mV·s^{-1}, pH= 6	29.65 ± 0.13	-0.30 ± 0.01	0.9805	30.33 ± 0.07	-0.35 ± 0.01	0.9982
PA, v=5 mV·s^{-1}, pH= 7	30.41 ± 0.12	-0.24 ± 0.01	0.9730	33.41 ± 0.10	-0.49 ± 0.01	0.9980
PA, v=10 mV·s^{-1}, pH= 7	28.19 ± 0.14	-0.30 ± 0.02	0.9763	30.27 ± 0.22	-0.46±0.01	0,9890
2PA, v=5 mV·s^{-1}, pH= 5	28.65 ± 0.12	-0.24 ± 0.02	0.9730	31.84 ± 0.16	-0.54 ± 0.01	0.9945
2PA, v=10 mV·s^{-1}, pH= 5	25.65 ± 0.12	-4.9054 ± 0.05	0,9853	14.08 ± 0.07	-0.13 ± 0.01	0.9907
2PA, v=5 mV·s^{-1}, pH= 6	23.00 ± 0.10	-0.16 ± 0.01	0.9554	33.46 ± 1.02	-0.95 ± 0.06	0.9610
2PA, v=10 mV·s^{-1}, pH=6	30.29 ± 0.19	-0.18 ± 0.02	0.8700	32.44 ± 0.36	-0.40 ± 0.02	0.9700

2PA, v=5 mV·s^{-1}, pH=7	28.87 ± 0.22	-0.27 ± 0.03	0.9314	32.02 ± 0.16	-0.56 ± 0.01	0.9955
2PA, v=10 mV·s^{-1}, pH=7	30.88 ± 0.11	-0.19 ± 0.01	0.9603	32.66 ± 0.38	-0.33 ± 0.02	0.9504

Table S6. Parameters of the Korsmeyer–Peppas kinetic model of PA from the membrane film PEDOT-PA/Ti and PEDOT-2PA/Ti prepared by electropolymerization at 5mV·s^{-1} and 10mV·s^{-1}. Data recorded after 6h at saliva solution adjusted at different pH.

Variable	$\frac{ln\,R}{ln\,t}$ **; (t>200 min)**			$\frac{ln\,R}{ln\,t}$ **; (t<200 min)**		
	Intercept	**Slope**	**R^2**	**Intercept**	**Slope**	**R^2**
PA, v=5 mV·s^{-1}, pH= 5	1.48 ± 0.01	-0.03 ± 3×10^{-3}	0.9383	1.78 ± 0.02	-0.18 ± 0.01	0.9804
PA, v=10 mV·s^{-1}, pH= 5	1.49 ± 9×10^{-3}	-0.04 ± 4×10^{-3}	0.8938	-0.21 ± 0.01	-0,178 ± 0.01	0.9866
PA, v=5 mV·s^{-1}, pH= 6	1.50 ± 8×10^{-3}	-0.03 ± 5×10^{-3}	0.8364	1.72 ± 0.02	-0.13 ± 0.01	0.9420
PA, v=10 mV·s^{-1}, pH= 6	1.50 ± 1×10^{-3}	-0.04 ± 4×10^{-3}	0.8949	1.67 ± 0.01	-0.11 ± 0.01	0.9925
PA, v=5 mV·s^{-1}, pH= 7	1.54 ± 8×10^{-3}	-0.05 ± 4×10^{-3}	0.9157	1.79 ± 0.01	-0.16 ± 0.01	0.9894
PA, v=10 mV·s^{-1}, pH= 7	1.47 ± 7×10^{-3}	-0.04 ± 4×10^{-3}	0.9160	1.69 ± 0.02	-0.14 ± 0.01	0.9581
2PA mV·s^{-1}, v=5, pH= 5	1.48 ± 5×10^{-3}	-0.03 ± 3×10^{-3}	0.9383	1.78 ± 0.02	-0.17 ± 0.01	0.9804
2PA, v=10 mV·s^{-1}, pH= 5	1.16 ± 6×10^{-3}	-0.03 ± 3×10^{-3}	0.8507	1.31 ± 0.01	-0.10 ± 0.01	0.9812
2PA, v=5, pH= 6	1.39 ± 4×10^{-3}	-0.03 ± 2×10^{-3}	0.9507	2.53 ± 0.13	-0.52 ± 0.1	0.9258
2PA, v=10 mV·s^{-1}, pH=6	1.51 ± 7×10^{-3}	-0.03 ± 4×10^{-3}	0.8434	1.70 ± 0.02	-0.12 ± 0.01	0.9617
2PA, v=5 mV·s^{-1}, pH=7	1.49 ± 9×10^{-3}	-0.04 ± 5×10^{-3}	0.8540	1.81 ± 0.01	-0.18 ± 0.01	0.9869
2PA, v=10 mV·s^{-1}, pH=7	1.51 ± 5×10^{-3}	-0.02 ± 3×10^{-3}	0.8715	1.67 ± 0.02	-0.01 ± 0.01	0.9110

Table S7. Mechanical characteristics of the Ti–6Al–4 V electrodes coating with PMMA + x IBU (where x is 0.2, 0.4 and 1 mM)

Measurement	**PMMA**	**0.2 mM IBU–PMMA**	**0.4 mM IBU–PMMA**	**1 mM IBU–PMMA**
Fracture stress (kPa)	4.93 ± 3×10^{-3}	9.59 ± 0.02	6.99 ± 3×10^{-3}	10.91 ± 4×10^{-3}

Fracture strain (mm/mm)	1.98 ± 0.03	1.44 ± 0.95	1.32 ± 0.04	1.50 ± 0.02
Young's modulus[a] (kPa)	3.29 ± 0.02	8.85 ± 0.06	3.62 ± 0.04	9.30 ± 0.12
Film thickness[b] (µm)	9.30 ± 1.17	11.15 ± 0.62	12.69 ± 1.86	12.86 ± 1.14

[a] Values estimated as the slope of the linear domain of the stress–strain curves

[b] Measurement using Elcometer instrument, expressed as mean ± 3 × std. dev. of 10 measurements.

Table S8. Electrochemical parameters for corrosion measurements (OCP, LP, PDP) on the bare Ti–6Al–4 V and xIBU–PMMA/Ti–6Al–4 V (x = 0, 0.2, 0.4, and 1 mM) coating electrodes immersed in 3.5% NaCl

Measurement	**Ti–6Al–4 V**	**0 IBU–PMMA/ Ti–6Al–4 V**	**0.2 IBU–PMMA/ Ti–6Al–4 V**	**0.4 IBU–PMMA/ Ti–6Al–4 V**	**1 IBU–PMMA/ Ti–6Al–4 V**
OCP					
OCP (V)	$-0.26 \pm 2\times10^{-3}$	$0.09 \pm 7\times10^{-5}$	-0.02 ± 0.01	$-0.18 \pm 6\times10^{-3}$	-0.20 ± 0.01
Linear polarization (LP)					
R_p (kohm)	101.91 ± 0.26	164.27 ± 2.16	183.15 ± 0.28	**194.50 ± 1.21**	188.03 ± 2.12
IER_p (%)	-	-	10.28 ± 1.32	**15.54 ± 1.65**	12.62 ± 1.97
Tafel data (PDP)					
i_{corr} (A/cm^2)	$9.79\times10^{-8} \pm 0.19\times10^{-8}$	$3.26\times10^{-8} \pm 0.01\times10^{-8}$	$1.83\times10^{-8} \pm 0.01\times10^{-8}$	$1.01\times10^{-8} \pm 0.04\times10^{-8}$	$1.07\times10^{-8} \pm 0.06\times10^{-8}$
E_{corr} (V) vs. Ag/AgCl, KCl*sat*	$-0.21 \pm 4\times10^{-3}$	$0.01 \pm 1.41\times10^{-4}$	$-0.08 \pm 1.44\times10^{-3}$	$-0.18 \pm 3\times10^{-3}$	$-0.20 \pm 2\times10^{-3}$
b_c (V/dec)	$0.05 \pm 1\times10^{-3}$	$0.05 \pm 1.45\times10^{-3}$	$0.04 \pm 3\times10^{-3}$	$0.04 \pm 4\times10^{-3}$	$0.03 \pm 4\times10^{-3}$
b_a (V/dec)	$0.05 \pm 1\times10^{-3}$	$0.04 \pm 1.42\times10^{-3}$	$0.03 \pm 4.22\times10^{-3}$	$0.03 \pm 3\times10^{-3}$	$0.03 \pm 3\times10^{-3}$
Corrosion rate (CR) (mm/ year)	$1.20\times10^{-3} \pm 0.04\times10^{-3}$	$7.55\times10^{-4} \pm 0.18\times10^{-4}$	$4.02\times10^{-4} \pm 0.40\times10^{-4}$	**$2.41\times10^{-4} \pm 0.05\times10^{-4}$**	$2.53\times10^{-4} \pm 0.01\times10^{-4}$
IE_p (%)	-	-	43.86 ± 4.03	**69.02 ± 0.76**	67.17 ± 0.58

Mean ± standard deviations of 3 measurements.

Table S9. EIS fitted data on the bare Ti–6Al–4 V and xIBU–PMMA/Ti–6Al–4 V (x = 0, 0.20, 0.40, and 1 mM) coating electrodes immersed in 3.5% NaCl

Measurement	Ti–6Al–4 V	0 IBU–PMMA/ Ti–6Al–4 V	0.2 IBU–PMMA/ Ti–6Al–4 V	0.4 IBU–PMMA/ Ti–6Al–4 V	1 IBU–PMMA/ Ti–6Al–4 V
R_s (ohm × cm^2)	15.81 ± 1.23	171.44 ± 3.08	115.12 ± 9.18	119.33 ± 5.22	64.24 ± 7.11
Q_f (μS·sn/cm^2)	1.10 ± 5.16	5.26 ± 1.16	8.44 ± 0.54	4.88 ± 0.55	6.60 ± 0.35
n_1	0.82	0.77	0.80	0.79	0.75
R_f (ohm × cm^2) × 10^{-3}	1739 ± 3.66	1734 ± 1.82	2548 ± 4.63	3776 ± 2.89	2449 ± 2.75
Q_{dl} (μS·sn/cm^2)	2.48 ± 7.79	11.94 ± 3.32	11.03 ± 6.88	0.37 ± 2.28	26.78· ± 7.35
n_2	0.96	0.53	0.52	0.53	0.51
Rct (ohm × cm^2) × 10^3	1.74 ± 15.17	2.45 ± 1.19	5.92 ± 4.99	23.41 ± 5.41	2.84 ± 8.78
|Z|a (ohm × cm^2) × 10^{-3}	405.31	1041.14	889.62	1466.95	1040.63
R_{pb} (ohm × cm^2) × 10^{-3}	1756.35	1736.45	2553.92	3776.93	3476.91
$\chi^2 \times 10^{-3}$	0.23	0.20	0.43	0.14	0.18
IER_{ct} (%)	-	-	58.61 ± 2.22	**89.53** ± 1.37	13.73±0.55

Mean ± standard deviations of 3 measurements.

Table S10. Mechanical resistances for mild steel in 0.1 M HNO_3 solution without and with different concentrations of the Tara-x-SE, Tara-x-ME, and Guayusa-x-SE extracts (where x = 200, 600, 1000 ppm)

Formulation	Fracture Stress (GPa)	Fracture Strain (mm/mm)	Young's Modulus (GPa)	Percentage of Elongation (%)
Mild Steel at room conditions	193.98 ± 2.40	0.92 ± 0.02	210.84 ± 13.10	34.85 ± 0.33
Blank	183.91 ± 2.95	1.04 ± 0.04	175.14 ± 25.69	12.17 ± 1.46
Tara-200-SE	190.43 ± 0.96	1.05 ± 0.01	181.38 ± 16.57	21.96 ± 1.49
Tara-600-SE	191.44 ± 1.15	1.03 ± 0.02	185.86 ± 9.23	32.95 ± 0.60
Tara-1000-SE	191.65 ± 1.68	1.01 ± 0.02	189.56 ± 13.06	23.77 ± 0.45
Tara-200-ME	184.95 ± 2.11	1.02 ± 0.01	181.85 ± 16.46	14.41 ± 0.35

Tara-600-ME	187.55 ± 2.10	1.03 ± 0.01	182.08 ± 14.18	23.41 ± 2.31
Tara-1000-ME	188.46 ± 1.05	1.03 ± 0.04	182.97 ± 12.50	25.83 ± 0.54
Guayusa-200-SE	138.71 ± 1.58	0.77 ± 0.01	176.39 ± 12.35	10.81 ± 0.26
Guayusa-600-SE	155.67 ± 1.56	0.85 ± 0.01	181.13 ± 10.64	19.43 ± 1.73
Guayusa-1000-SE	134.75 ± 0.79	0.74 ± 0.03	180.82 ± 9.38	18.47 ± 0.41

Values are expressed as mean ± standard deviations of 3 measurements

Table S11. Electrochemical parameters from Tafel plots for mild steel samples in 0.10 M HNO_3 solution in the absence and presence of different concentrations of the Tara-x-SE, Tara-x-ME, and Guayusa-x-SE extracts (where: x = 200, 600, 1000 ppm)

Parameter	Blank	Tara-200-SE	Tara-600-SE	Tara-1000-SE	Tara-200-ME	Tara-600-ME	Tara-1000-ME	Guayusa-200-SE	Guayusa-600-SE	Guayusa-1000-SE
-OCP / V	0.43 ± 0.07	0.32 ± 0.01	0.36 ± 0.07	0.38 ± 0.05	0.29 ± 0.02	0.31 ± 0.16	0.34 ± 0.03	0.28 ± 0.17	0.30 ± 0.22	0.23 ± 0.18
–Ecorr / mV vs. Ag/AgCl, KCl_{sat}	444.77 ± 0.87	338.50 ± 0.74	345.62 ± 1.87	451.22 ± 0.52	299.40 ± 3.45	344.05 ± 1.22	471.95 ± 4.37	386.76 ± 1.00	344.05 ± 1.22	352.31 ± 1.25
–bc / $mV \cdot dec^{-1}$	43.78 ± 5.21	72.10 ± 4.46	96.13 ± 3.21	75.05 ± 1.77	54.11 ± 0.73	20.27 ± 0.60	20.91 ± 0.56	38.07 ± 4.53	16.22 ± 0.48	25.95 ± 0.77
ba / $mV \cdot dec^{-1}$	50.91 ± 1.45	64.10 ± 1.28	64.42 ± 3.54	30.27 ± 1.07	46.30 ± 0.48	10.85 ± 0.93	20.65 ± 1.87	44.27 ± 1.26	8.68 ± 0.74	20.76 ± 0.61
icorr / $\mu A \cdot cm^{-2}$	10182 ± 36.23	4821.33 ± 0.87	619.17 ± 8.01	267.24 ± 3.12	7279.00 ± 18.06	3057.32 ± 10.21	402.54 ± 12.16	8853.91 ± 31.50	2445.61 ± 8.17	1912.14 ± 13.07
IE / %	-	52.65 ± 2.02	93.91 ± 1.48	97.38 ± 2.04	28.51 ± 0.15	69.98 ± 1.11	96.05 ± 0.68	13.04 ± 0.14	69.98 ± 1.11	81.22± 1.42

Values are expressed as mean ± standard deviations of 3 measurements.

Table S11. EIS parameters for mild still in 0.10 M HNO_3 solution in the absence and the presence of different concentrations (x) of the Tara-x-SE, Tara-x-ME, and Guayusa-x-SE extracts (where: x = 200, 600, 1000 ppm).

Parameter	Blank	Tara-200-SE	Tara-600-SE	Tara-1000-SE	Tara-200-ME	Tara-600-ME	Tara-1000-ME	Guayusa-200-SE	Guayusa-600-SE	Guayusa-1000-SE
Rs / Ω·cm²	20.22±0.05	19.22 ± 0.58	19.18 ± 0.44	20.01 ± 0.28	20.10 ± 0.54	20.24 ± 0.51	19.94 ± 0.19	19.22 ± 0.51	20.05 ± 0.03	20.14 ± 0.15
CPE × 10^5/ S·secn/cm²	8.63±0.25	1.82±0.06	1.07±0.05	1.66±0.04	2.59±0.07	2.55±0.01	1.55±0.05	7.50±0.22	3.06±0.01	3.00±0.08
Rct / Ω·cm²	95.23±3.42	494.80± 14.47	699.95± 33.66	1027.44±10.27	442.70 ± 14.60	560.45 ± 16.81	831.70± 19.94	109.51± 3.93	448.36± 13.45	753.90± 12.45
n	0.73	0.80	0.84	0.88	0.83	0.81	0.84	0.70	0.75	0.82
Cdl / µF·cm⁻²	14.61±0.85	5.60±0.03	7.10±0.07	3.41±0.02	10.37±0.05	11.31±0.01	5.58±0.02	12.70± 0.98	9.048± 0.01	11.58± 0.04
Rp / Ω·cm²	115.45± 1.73	514.02± 7.52	719.13± 17.21	1047.01± 5.27	462.80± 7.57	580.69± 8.66	851.64± 10.65	128.73± 2.04	468.41± 6.74	774.04± 6.30
χ2	8.22×10^{-4}	7.44×10^{-4}	9.12×10^{-4}	1.01×10^{-3}	8.08×10^{-4}	9.57×10^{-4}	8.42×10^{-4}	9.37×10^{-4}	1.21×10^{-3}	9.82×10^{-4}
τ / mS	1.69± 0.05	2.88± 0.01	5.11 ± 0.06	3.57 ± 0.01	4.80 ± 0.02	6.57 ± 0.04	4.75 ± 0.06	1.89± 0.04	5.26± 0.03	6.73± 0.01
IE/ %	-	80.75 ± 0.05	86.39 ± 0.15	90.73 ± 0.03	78.49 ± 1.09	83.01 ± 0.37	88.55± 0.15	13.04± 0.21	78.46± 0.15	87.70± 0.12

Values are expressed as mean ± standard deviations of 3 measurements. Errors expressed in %

Table S12. Calculated **values of the adsorption parameters for Tara-SE, Tara-ME inhibitors**

T / K	Tara-SE					Tara-ME				
	K_{ads}^{*}	1/n	ΔG_{ads} (kJ·mol^{-1})	R /n	red Chi^2	K_{ads}^{*}	1/n	ΔG_{ads} (kJ·mol^{-1})	R /n	red Chi^2
Langmuir model										
305	1.89			0.9894/4	2.78×10^{-3}	2.45			0.9840/4	7.14×10^{-3}
315	3.54			0.9911/4	7.69×10^{-3}	4.72			0.9552/4	72.52×10^{-3}
325	3.18			0.9913/4	13.46×10^{-3}	4.17			0.9619/4	105.31×10^{-3}
335	2.60			0.9768/4	4.05	3.24			0.9737/4	7.07
Freundlich model										
305	0.62	0.58	-8.97	0.9890/4	0.75×10^{-3}	0.51	0.48	-8.46	0.9911/4	0.42×10^{-3}
315	0.39	0.38	-8.07	0.9962/4	0.15×10^{-3}	0.30	0.24	-7.33	0.8294/4	2.73×10^{-3}
325	0.29	0.42	-7.50	0.9979/4	0.07×10^{-3}	0.22	0.29	-6.80	0.9021/4	1.95×10^{-3}
335	0.03	0.47	-1.05	0.9867/4	0.62×10^{-3}	0.02	0.39	-0.55	0.9645/4	1.16×10^{-3}
Temkin model										
305	15.85		-17.20	0.9935/4	0.31×10^{-3}	20.83		-17.89	0.9821/4	0.50×10^{-3}
315	34.44		-19.79	0.9865/4	0.17×10^{-3}	124.31		-23.15	0.8211/4	0.99×10^{-3}
325	28.62		-19.20	0.9894/4	0.08×10^{-3}	69.85		-22.33	0.8869/4	0.40×10^{-3}
335	21.80		-19.77	0.9765/4	0.01×10^{-3}	32.29		-20.87	0.9544/4	0.02×10^{-3}
Flory Huggins model										
305	1.67	0.83	.	0.9634/4	1.38×10^{-3}	1.87	0.50		0.9453/4	2.99×10^{-3}
315	2.52	0.26		0.9690/4	2.38×10^{-3}	2.40	0.19		0.6784/4	33.18×10^{-3}
325	1.68	0.19		0.9778/4	1.54×10^{-3}	1.86	0.13		0.7784/4	21.24×10^{-3}
335	0.12	0.02		0.9339/4	3.47×10^{-3}	0.15	0.01		0.8891/4	16.57×10^{-3}
El Awady model										

305	10.83	0.29	-16.23	0.9877/4	0.30×10^{-3}	13.90	4.11	-16.86	0.9761/4	0.30×10^{-3}
315	22.80	0.66	-18.71	0.9810/4	0.09×10^{-3}	69.65	12.08	-21.63	0.8177/4	0.35×10^{-3}
325	22.01	0.97	-19.21	0.9857/4	0.03×10^{-3}	22.01	9.56	-19.21	0.9857/4	0.03×10^{-3}
335	21.54	0.22	-19.74	0.9761/4	0.03×10^{-4}	21.54	121.21	-19.74	0.9761/4	0.03×10^{-4}

* K_{ads} values have different units in the function of the used model, ΔG_{ads} was calculated using equation (35)

Table S13. Calculated **values of the adsorption parameters for Guayusa inhibitors**

Guayusa-SE				
K_{ads}*	**1/n**	**ΔG_{ads} (kJ·mol^{-1})**	**R /n**	**red Chi^2**
Langmuir model				
1.62			0.848/4	2.11×10^{-3}
3.04			0.849/4	7.42×10^{-3}
2.73			0.850/4	12.23×10^{-3}
2.23			0.837/4	3.47
Freundlich model				
0.40	0.38	-6.63	0.877/4	3.33×10^{-3}
0.23	0.19	-5.75	0.8650/4	2.14×10^{-3}
0.18	0.23	-5.33	0.8707/4	1.53×10^{-3}
0.02	0.31	-0.43	0.8756/4	9.15×10^{-3}
Temkin model				
14.28		-15.50	0.9893/4	2.81×10^{-3}
31.03		-17.83	0.9852/4	1.52×10^{-3}
25.79		-17.30	0.9824/4	7.33×10^{-4}
19.64		-17.81	0.9722/4	0.02×10^{-3}
Flory Huggins model				
1.68	0.45		0.9396/ 4	2.74×10^{-3}

2.15	0.17		0.6743/ 4	3.07×10^{-3}
1.67	0.64		0.7737/ 4	1.93×10^{-3}
0.13	0.01		0.8838/ 4	1.48×10^{-3}
El Awady model				
12.68	3.74	-15.38	0.9713/4	2.77×10^{-3}
63.52	11.02	-19.73	0.8152/4	3.23×10^{-3}
20.07	8.72	-17.52	0.9843/4	3.22×10^{-4}
19.65	11.05	-18.01	0.9783/4	4.04×10^{-4}

Table 17. Electric equivalent circuit parameters obtained by fitting the experimental data at GCE, Chit/GCE, Chit+bioF/GCE, Chit+TiO_2/GCE, Chit+TiO_2AG/GCE, Chit+f-MWCNTs/GCE, Chit+bioF+TiO_2/GCE, Chit+bioF+TiO_2AG/GCE, and Chit+bioF+f-MWCNTs/GCE modified electrodes. Equivalent circuit $R_{el}(Q(R_{ct}W))$

Type of Electrode	**R_{el} (ohm·cm^2)**	**Q (μS·s^n/cm^2)**	**n**	**R_{ct} (ohm·cm^2)**	**W (mS·s$^{1/2}$/cm^2)**	**C (μF/cm^2)**	**k_s (cm/s)**	**χ^2**
GCE	2.71 ± 3.79	16.79 ± 4.1	0.82	**121.37 ± 0.63**	28.51 ± 2.56	**4.38**	4.39×10^{-4}	$5\cdot10^{-4}$
Chit/GCE	4.26 ± 0.65	13.64 ± 1.91	0.85	**128.25 ± 0.67**	37.04 ± 2.08	**4.45**	4.15×10^{-4}	$3\cdot10^{-4}$
Chit+bioF/GCE	3.85 ± 0.71	10.66 ± 2.61	0.92	**88.89 ± 0.39**	32.78 ± 1.10	**5.82**	6.04×10^{-4}	$2\cdot10^{-4}$
Chit+TiO_2/GCE	5.22 ± 2.44	4.66 ± 0.01	0.93	**91.4 ± 0.70**	30.93 ± 0.31	**6.86**	4.52×10^{-4}	$6\cdot10^{-4}$

Chit+TiO_2AG/GCE	4.99 ± 3.51	108.70 ± 7.07	0.89	**67.81 ± 0.78**	30.03 ± 1.61	**97.08**	7.94×10^{-4}	$8\cdot10^{-4}$
Chit+f-MWCNTs/GCE	4.96 ± 0.32	8.40 ± 0.78	0.94	**73.44 ± 0.85**	34.96 ± 0.03	**12.66**	4.52×10^{-4}	$9\cdot10^{-4}$
Chit+bioF+TiO_2/GCE	6.51 ± 0.25	4.20 ± 0.22	0.92	**102.15 ± 2.12**	27.64 ± 0.12	**7.11**	5.13×10^{-4}	$8\cdot10^{-4}$
Chit+bioF+TiO_2AG/GCE	3.59 ± 0.59	142.5 ± 2.16	0.92	**77.73 ± 0.33**	33.68 ± 0.92	**96.33**	6.91×10^{-4}	$1\cdot10^{-3}$
Chit+bioF+f-MWCNTs/GCE	3.23 ± 0.20	7.80 ± 0.03	0.90	**71 ± 0.25**	34.46 ± 0.02	**16.53**	5.22×10^{-4}	$1\cdot10^{-3}$

± the relative standard deviations (%); capacitance calculated as $C = (Q \times R_{ct})^{1/n} / R_{ct}$, $k_s = RT/(n^2F^2 R_{ct}C)$, where where R is the ideal gas constant (8.31 J/mol K), F is the Faraday number, (96485C/ mol), T is the temperature (298 K), n is the number of electrons transferred, and C is the iron concentration in the electrolyte solution (in mol/cm^3

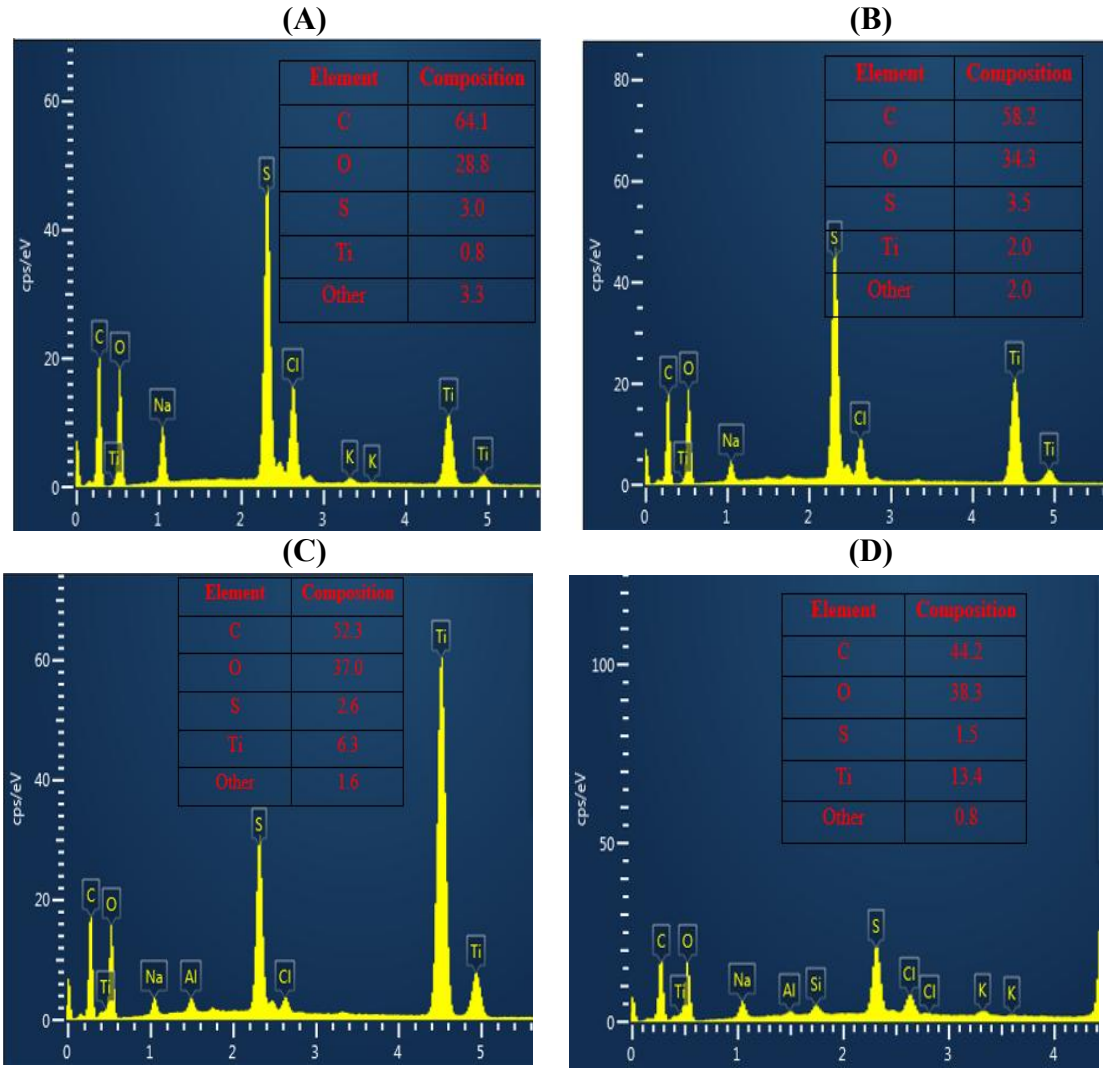

Figure S1. EDX spectra of PEDOT/Ti prepared at 5 mV·s^{-1} (A), PEDOT/Ti prepared at 10 mV·s^{-1} (B), PEDOT+PA/Ti prepared at 5 mV·s^{-1} (C), and PEDOT+2PA/Ti prepared at 10 mV·s^{-1} (D) at a magnification equal to 50 nm

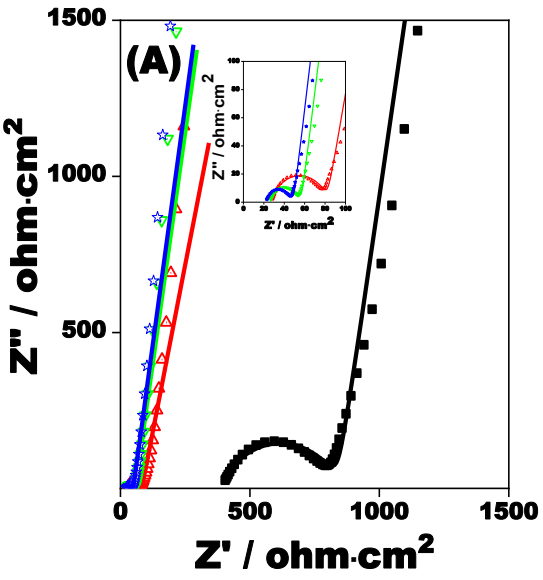

Figure S2. Nyquist plot for Ti/PEDOT-PA (A) and Ti/PEDOT-2PA (B) composite modified electrode. Experimental conditions: scan rate of electropolymerization, v = 10 $mV \cdot s^{-1}$ (A, C); test solution, artificial saliva pH 5; time of experiment, 0 h (■), 1 h (△), 3 h (▽), 6 h (★)

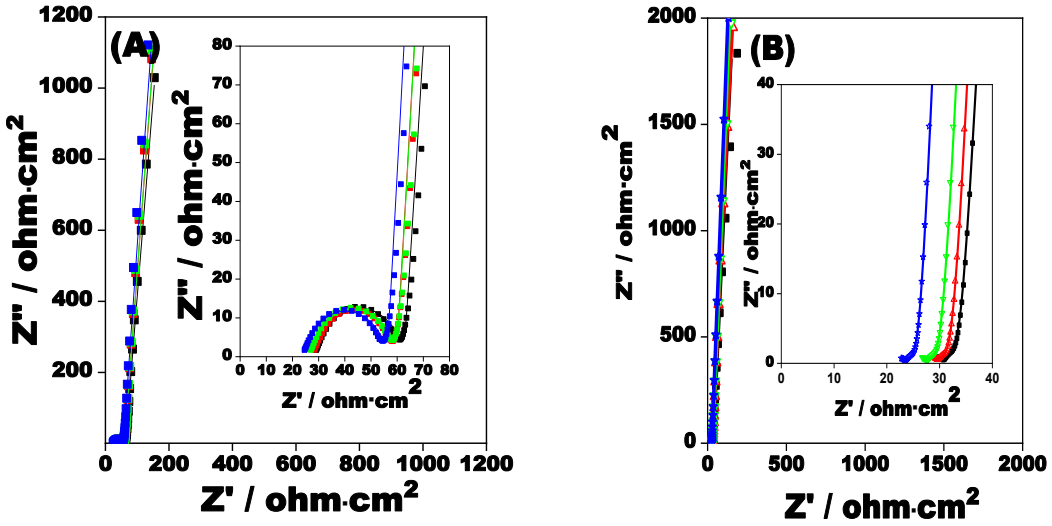

Figure S3. Nyquist diagram for Ti/PEDOT-PA (A) and Ti/PEDOT-2PA (B) composite modified electrode. Experimental conditions: scan rate of electropolymerization, v = 5 $mV \cdot s^{-1}$ (A, C); test solution, artificial saliva pH 6; time of experiment, 0 h (■), 1 h (△), 3 h (▽), 6 h (★)

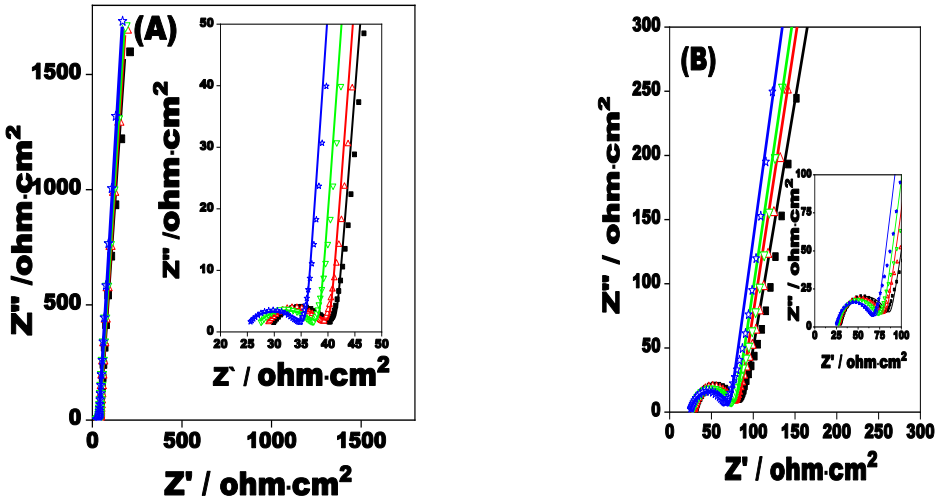

Figure S4. Nyquist (A, B) and Bode (C, D) diagram for Ti/PEDOT-PA (A, C) and Ti/PEDOT-2PA (B, D) composite modified electrode. Experimental conditions: scan rate

of electropolymerization, v = 10 mV·s^{-1} (A, C); test solution, artificial saliva pH 6; time of experiment, 0 h (■), 1 h (△), 3 h (▽), 6 h (★)

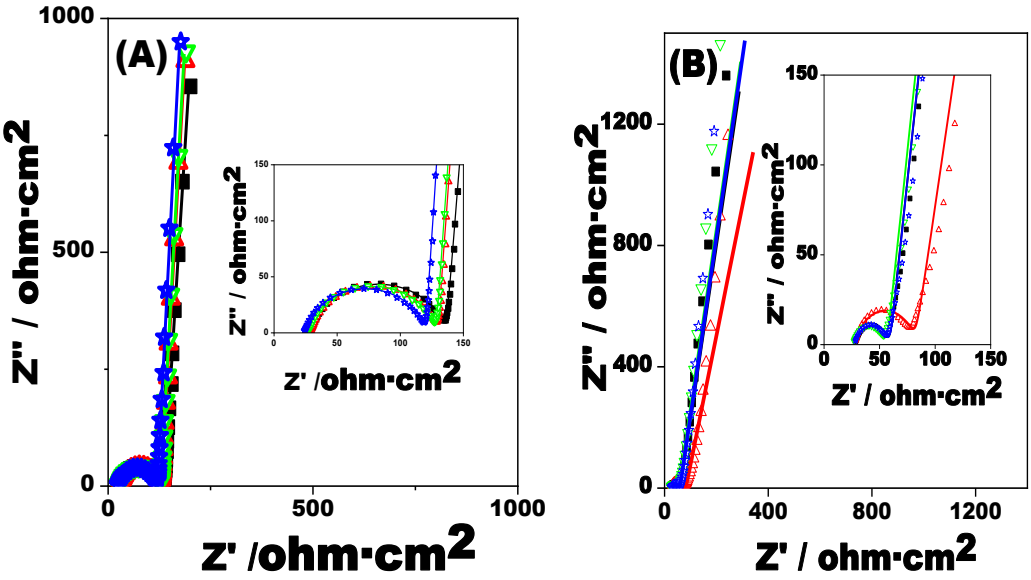

Figure S5. Nyquist (A, B) and Bode (C, D) diagram for Ti/PEDOT-PA (A, C) and Ti/PEDOT-2PA (B, D) composite modified electrode. Experimental conditions: scan rate of electropolymerization, v = 5 mV·s^{-1} (A, C); test solution, artificial saliva pH 7; time of experiment, 0 h (■), 1 h (△), 3 h (▽), 6 h (★).

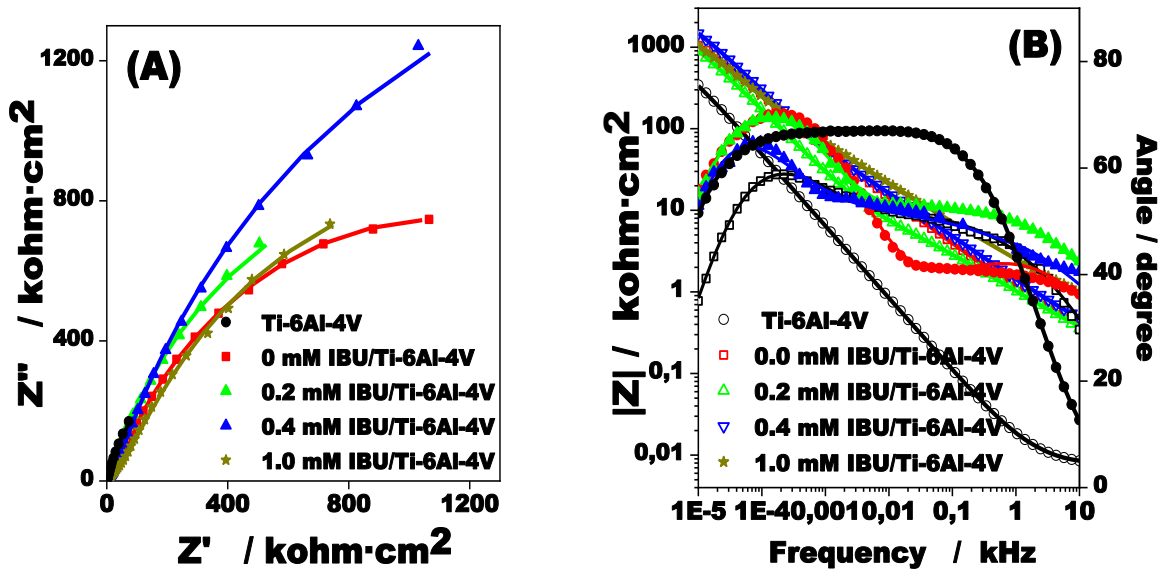

Figure S6. Nyquist (A) and Bode (B) plots recorded at the x IBU-PMMA/ Ti–6Al–4V (where: x = 0 (red, ■), 0.20 mM (green, ▲), 0.40 mM (blue, ▼), and 1 mM (dark

brown, ★) IBU) modified surfaces. Experimental conditions: 3.50 % NaCl; frequency range, 10 mHz to 10 kHz.

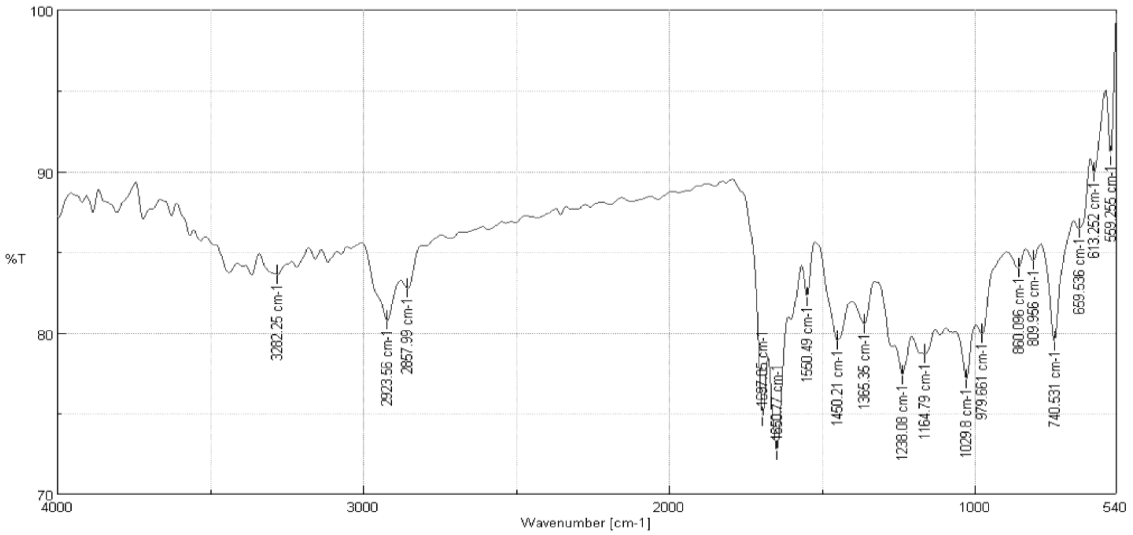

Figure S7. FTIR spectra for Guayusa plant extracts

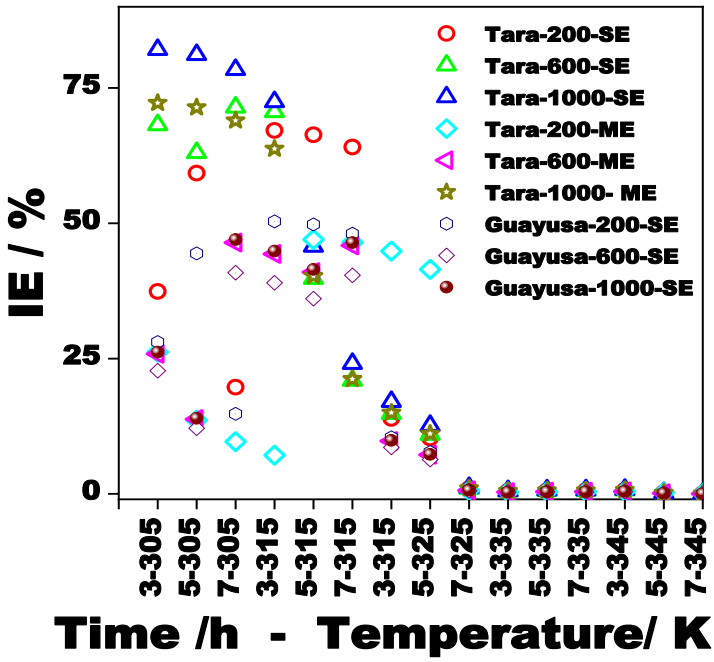

Figure S8. Study of the inhibition efficiency at mild steel samples in 0.10 M HNO_3 in the presence of Tara-x-SE, Tara-x-ME, and Guayusa extracts (where: x = 200, 600, 1000 ppm) at different concentrations (see inset), temperature and immersion times

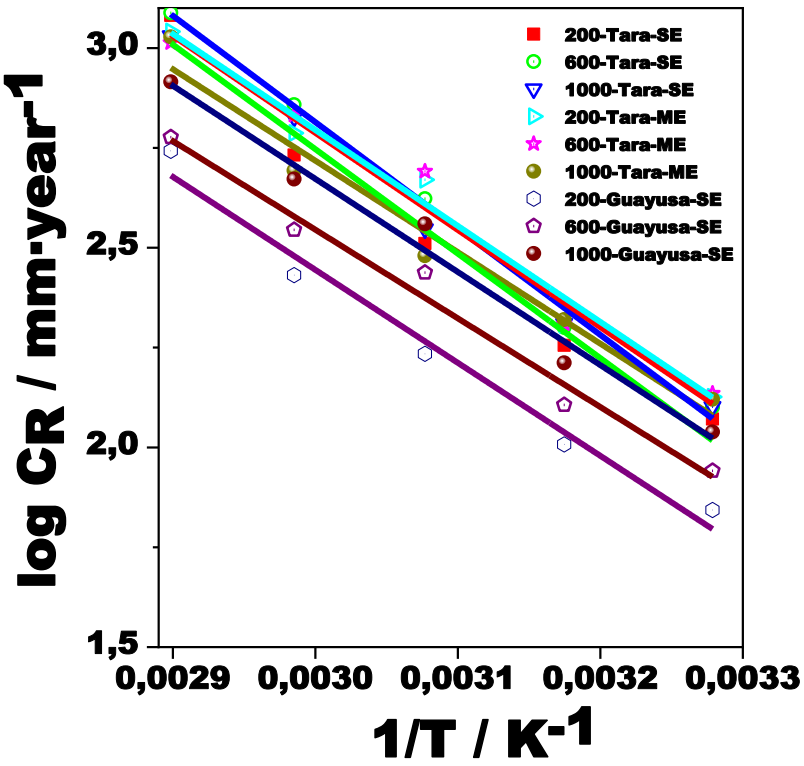

Figure S9. Relation of the log CR vs. 1/T in mild steel samples in 0.10 M HNO_3 in the presence of Tara-SE extract, Tara-x-ME, and Guayusa-x-SE extract (where x= 200, 600, 1000 ppm), after 3 hours of immersion.